


New books for the kid
scientist's library *p. 1222*

Expanding financial
services in Kenya *p. 1288*

Designer cells to correct
insulin deficiency *p. 1296*

Science

\$15
9 DECEMBER 2016
sciencemag.org

 AAAS

FAMILY TIES

Saudi Arabia strives to prevent genetic diseases *p. 1217*



CONTENTS

9 DECEMBER 2016 • VOLUME 354 • ISSUE 6317



1235

What drives
the ice ages?

INSIGHTS

BOOKS ET AL.

1222 CALLING ALL KID SCIENTISTS

PERSPECTIVES

1230 A FAST RADIO BOOM

Bright distant radio bursts are excellent probes of the intergalactic medium

By V. M. Kaspi

► REPORT P. 1249

1231 WHY DOES TIME SEEM TO FLY WHEN WE'RE HAVING FUN?

Increased dopamine may cause our internal clock to slow down, creating a sense of speeding time

By P. Simen and M. Matell

► REPORT P. 1273

1232 SWIMMING IN POLLUTED WATERS

Genomic data provide insights into the molecular basis for pollution tolerance of Atlantic killifish

By M. Tobler and Z. W. Culumber

► REPORT P. 1305

1234 ENCODING VOCAL CULTURE

Neuronal encoding of birdsong promotes learning and species specificity

By O. Tchernichovski and D. Lipkind

► REPORTS PP. 1278 & 1282

1235 THE SMOKING GUN OF THE ICE AGES

Forty years ago, a seminal paper showed that small changes in Earth's orbit are key to understanding ice age cycles

By D. A. Hodell

DEPARTMENTS

1207 EDITORIAL

Timeline for refugee scholars

By Allan Goodman

1346 WORKING LIFE

Following my lucky star

By Nancy Grace Roman

Science Staff	1204
New Products	1309
Science Careers	1310



1210

NEWS

IN BRIEF

1208 News at a glance

IN DEPTH

1210 CORALS TIE STRONGER EL NIÑOS TO CLIMATE CHANGE

Much-debated link gains support from long record of ocean temperatures

By C. Pala

1211 WORRIES, CONFUSION AFTER CANCER TRIAL DEATHS

Experimental immune treatment linked to fatal brain swelling

By J. Couzin-Frankel

1212 U.S. CONGRESS WANTS TO KNOW THE WEATHER WEEKS AHEAD

Bill targets seasonal forecasts and NOAA's pricey satellites

By P. Voosen

1213 AIDS EPIDEMIC NEARS CONTROL IN THREE AFRICAN COUNTRIES

Massive new surveys show stunning progress

By J. Cohen

1214 PEROVSKITE SOLAR CELLS GEAR UP TO GO COMMERCIAL

In tandem with silicon, low-cost photovoltaic crystals make electricity more efficiently

By R. F. Service

1215 CARBON MONOXIDE, THE SILENT KILLER, MAY HAVE MET ITS MATCH

Repurposed molecule saves rodents from gas poisoning

By W. Yan

► SCI. TRANSL. MED. RESEARCH ARTICLE BY I. AZAROV ET AL. 10.1126/scitranslmed.aah6571

1216 CURATOR RESIGNS AFTER SEXUAL MISCONDUCT INVESTIGATIONS

Long-running case sparks debate about collaboration

By A. Gibbons

FEATURES

1217 WHEN DNA AND CULTURE CLASH

Saudi Arabia is making a big push into human genomics, hoping to prevent inherited diseases

By J. Kaiser

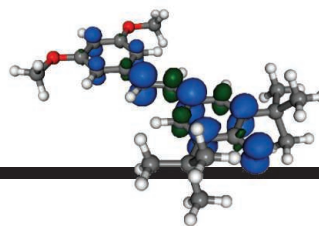
1220 Qatar's genome effort slowly gears up

By J. Kaiser



1222

CONTENTS



1260

Radically enabled
synthesis

9 DECEMBER 2016 • VOLUME 354 • ISSUE 6317

POLICY FORUMS

1237 WHAT LIFE SCIENTISTS SHOULD KNOW ABOUT SECURITY THREATS

Considerable information is publicly available to help research institutions understand and counter potential threats *By K. M. Berger*

1240 ENHANCING REPRODUCIBILITY FOR COMPUTATIONAL METHODS

Data, code, and workflows should be available and cited *By V. Stodden et al.*

LETTERS

1242 EDITORIAL EXPRESSION OF CONCERN

By J. Berg

1242 INSTILLING INTEGRITY

By J. M. DuBois

1242 LIFE IN SCIENCE: RESPECT FOR THE ANCIENTS

By F. Beardsley

1243 NOW IS THE TIME TO PROTECT THE ARCTIC

By N. E. Hussey et al.

1243 ERRATA

RESEARCH

IN BRIEF

1245 From *Science* and other journals

REVIEW

1248 CHEMISTRY

The broadening reach of frustrated Lewis pair chemistry *D. W. Stephan*

REVIEW SUMMARY; FOR FULL TEXT:

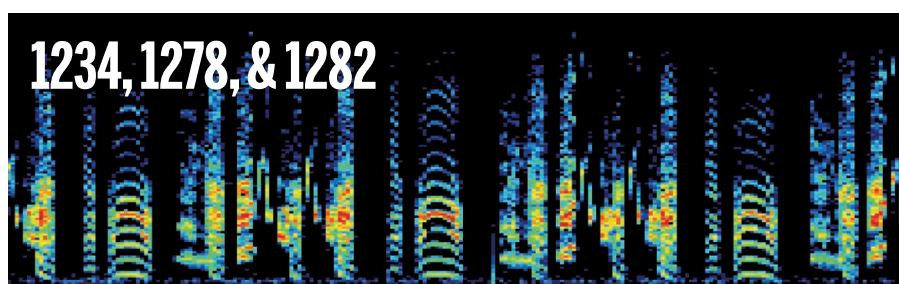
dx.doi.org/10.1126/science.aaf7229

REPORTS

1249 RADIO ASTRONOMY

The magnetic field and turbulence of the cosmic web measured using a brilliant fast radio burst *V. Ravi et al.*

► PERSPECTIVE P. 1230



1252 MICROFLUIDICS

How boundaries shape chemical delivery in microfluidics *M. Aminian et al.*

1257 COMPOSITES

Sensitive electromechanical sensors using viscoelastic graphene-polymer nanocomposites *C. S. Boland et al.*

► VIDEO

1260 ORGANIC CHEMISTRY

Synthesis of resveratrol tetramers via a stereoconvergent radical equilibrium *M. H. Keylor et al.*

1265 ASYMMETRIC CATALYSIS

A general, modular method for the catalytic asymmetric synthesis of alkylboronate esters *J. Schmidt et al.*

1269 TOPOLOGICAL MATTER

Robust spin-polarized midgap states at step edges of topological crystalline insulators *P. Sessi et al.*

1273 BRAIN RESEARCH

Midbrain dopamine neurons control judgment of time *S. Soares et al.*

► PERSPECTIVE P. 1231; PODCAST

NEUROSCIENCE

1278 Dopamine neurons encode

performance error in singing birds *V. Gadagkar et al.*

1282 Mind the gap: Neural coding of species identity in birdsong prosody *M. Araki et al.*

► PERSPECTIVE P. 1234

1288 DEVELOPMENT ECONOMICS

The long-run poverty and gender impacts of mobile money *T. Suri and W. Jack*

1293 ORIGIN OF LIFE

Transient compartmentalization of RNA replicators prevents extinction due to parasites *S. Matsumura et al.*

1296 SYNTHETIC BIOLOGY

β-cell-mimetic designer cells provide closed-loop glycemic control *M. Xie et al.*

1301 VIRAL EVOLUTION

Ecological speciation of bacteriophage lambda in allopatry and sympatry *J. R. Meyer et al.*

1305 ECOLOGICAL GENOMICS

The genomic landscape of rapid repeated evolutionary adaptation to toxic pollution in wild fish *N. M. Reid et al.*

► PERSPECTIVE P. 1232

ON THE COVER



Arab families such as this one by the Red Sea in Jeddah, Saudi Arabia, are often at higher risk of genetic diseases because of the tradition of close cousins marrying. Saudi Arabia has boosted

genomics research as part of an effort to help diagnose and prevent such diseases. See page 1217.

Photo: © Reuters Photographer/Reuters

SCIENCE (ISSN 0036-8075) is published weekly on Friday, except the last week in December, by the American Association for the Advancement of Science, 1200 New York Avenue, NW, Washington, DC 20005. Periodicals mail postage (publication No. 484460) paid at Washington, DC, and additional mailing offices. Copyright © 2016 by the American Association for the Advancement of Science. The title SCIENCE is a registered trademark of the AAAS. Domestic individual membership and subscription (51 issues): \$165 (\$74 allocated to subscription). Domestic institutional subscription (51 issues): \$1522. Foreign postage extra: Mexico, Caribbean (surface mail) \$55; other countries (air assist delivery) \$89. First class, airmail, student, and emeritus rates on request. Canadian rates with GST available upon request. GST #R1254 88122. Publications Mail Agreement Number 1069624. Printed in the U.S.A. Change of address: Allow 4 weeks, giving old and new addresses and 8-digit account number. Postmaster: Send change of address to AAAS, P.O. Box 96178, Washington, DC 20090-6178. Single-copy sales: \$15.00 current issue, \$20.00 back issue prepaid includes surface postage; bulk rates on request. Authorization to photocopy material for internal or personal use under circumstances not falling within the fair use provisions of the Copyright Act is granted by AAAS to libraries and other users registered with the Copyright Clearance Center (CCC) Transactional Reporting Service, provided that \$35.00 per article is paid directly to CCC, 222 Rosewood Drive, Danvers, MA 01923. The identification code for Science is 0036-8075. Science is indexed in the Reader's Guide to Periodical Literature and in several specialized indexes.

Editor-in-Chief Jeremy Berg

Executive Editor Monica M. Bradford **News Editor** Tim Appenzeller

Deputy Editors Lisa D. Chong, Andrew M. Sugden(UK), Valda J. Vinson, Jake S. Yeston

Research and Insights

DEPUTY EDITOR, EMERITUS Barbara R. Jasny **SR. EDITORS** Caroline Ash(UK), Gilbert J. Chin, Julia Fahrenkamp-Uppenbrink(UK), Pamela J. Hines, Stella M. Hurlley(UK), Paula A. Kiberstis, Marc S. Lavine(Canada), Ian S. Osborne(UK), Beverly A. Purnell, L. Bryan Ray, Guy Riddihough, H. Jesse Smith, Jelena Stajic, Peter Stern(UK), Phillip D. Szuranyi, Sacha Vignieri, Brad Wible, Laura M. Zahn
ASSOCIATE EDITORS Brent Grocholski, Priscilla Kelly, Keith T. Smith **ASSOCIATE BOOK REVIEW EDITOR** Valerie B. Thompson **LETTERS EDITOR** Jennifer Sills **LEAD CONTENT PRODUCTION EDITORS** Harry Jach, Lauren Kmec **CONTENT PRODUCTION EDITORS** Amelia Beyna, Jeffrey E. Cook, Chris Filialetau, Cynthia Howe, Barbara P. Ordway, Catherine Wolner **SR. EDITORIAL COORDINATORS** Carolyn Kyle, Beverly Shields **EDITORIAL COORDINATORS** Aneera Dobbins, Joi S. Granger, Jeffrey Hearn, Lisa Johnson, Maryrose Madrid, Anita Wynn
PUBLICATIONS ASSISTANTS Nida Masliulis, Dona Mathieu, Le-Toya Mayne Flood, Shannon McMahon, Scott Miller, Jerry Richardson, Alice Whaley(UK), Gwen Grant(UK), Brian White **EXECUTIVE ASSISTANT** Anna Bashkirova **ADMINISTRATIVE SUPPORT** Janet Clements(UK), Lizanne Newton(UK), Sarah Harrison(UK)

News

NEWS MANAGING EDITOR John Travis **INTERNATIONAL EDITOR** Richard Stone **DEPUTY NEWS EDITORS** Elizabeth Culotta, David Grimm, Eric Hand, David Malakoff, Leslie Roberts **CONTRIBUTING EDITOR** Martin Enserink(Europe) **SR. CORRESPONDENTS** Daniel Clery(UK), Jeffrey Mervis, Elizabeth Pennisi **NEWS WRITERS** Adrian Cho, Jon Cohen, Jennifer Couzin-Frankel, Carolyn Gramling, Jocelyn Kaiser, Catherine Maticic, Kelly Servick, Robert F. Service, Erik Stokstad(Cambridge, UK), Paul Voosen, Meredith Wadman
INTERNS Jessica Boddy, Rachael Lallensack **CONTRIBUTING CORRESPONDENTS** John Bohannon, Warren Cornwall, Ann Gibbons, Mara Hvistendahl, Sam Kean, Eli Kintisch, Kai Kupferschmidt(Berlin), Andrew Lawler, Mitch Leslie, Eliot Marshall, Virginia Morell, Dennis Normile(Shanghai), Tania Rabesandratana(London), Emily Underwood, Gretchen Vogel(Berlin), Lizzie Wade(Mexico City)
CAREERS Donisha Adams, Rachel Bernstein(Editor), Maggie Kuo **COPY EDITORS** Julia Cole, Dorie Cheylen, Jennifer Levin(Chief)
ADMINISTRATIVE SUPPORT Jessica Adams

Executive Publisher Rush D. Holt

Publisher Bill Moran **Chief Digital Media Officer** Rob Covey

DIRECTOR, BUSINESS STRATEGY AND PORTFOLIO MANAGEMENT Sarah Whalen **DIRECTOR, PRODUCT AND CUSTOM PUBLISHING** Will Schweitzer
PRODUCT DEVELOPMENT ASSOCIATE Hannah Heckner **BUSINESS SYSTEMS AND FINANCIAL ANALYSIS** DIRECTOR Randy Yi **SENIOR SYSTEMS ANALYST** Nicole Mehmedovich **DIRECTOR, BUSINESS OPERATIONS & ANALYSIS** Eric Knott **MANAGER, BUSINESS OPERATIONS** Jessica Tierney
SENIOR BUSINESS ANALYST Cory Lipman **BUSINESS ANALYSTS** David Garrison, Michael Hardesty Meron Kebede, Sandy Kim
FINANCIAL ANALYST Drew Sher **DIRECTOR, COPYRIGHTS LICENSING SPECIAL PROJECTS** Emilie David **PERMISSIONS ASSOCIATE** Elizabeth Sandler **RIGHTS, CONTRACTS, AND LICENSING ASSOCIATE** Lili Kiser **RIGHTS & PERMISSIONS ASSISTANT** Alexander Lee

MARKETING DIRECTOR Elise Swinehart **ASSOCIATE MARKETING DIRECTOR** Stacey Burke Bowers **MARKETING ASSOCIATE** Steven Goodman
CREATIVE DIRECTOR Scott Rodgersen **SENIOR ART ASSOCIATES** Paula Fry **ART ASSOCIATE** Kim Huynh

FULFILLMENT SYSTEMS AND OPERATIONS membership@aaas.org **MANAGER, MEMBER SERVICES** Pat Butler **SPECIALISTS** Terrance Morrison, Latashia Russell **MANAGER, DATA ENTRY** Mickie Napoleoni **DATA ENTRY SPECIALISTS** Brenden Aquilino, Fiona Giblin
MARKETING ASSOCIATE Isa Sesay-Bah

DIRECTOR, INSTITUTIONAL LICENSING David Celano **PUBLISHER RELATIONS, EASTERN REGION** Keith Layson **PUBLISHER RELATIONS, WESTERN REGION** Ryan Rexroth **ASSOCIATE DIRECTOR, INSTITUTIONAL LICENSING OPERATIONS** Iquo Edim **SENIOR OPERATIONS ANALYST** Lana Guzman
MANAGER, AGENT RELATIONS & CUSTOMER SUCCESS Judy Lillibridge

WEB TECHNOLOGIES PORTFOLIO MANAGER Trista Smith **TECHNICAL MANAGER** Chris Coleman **PROJECT MANAGER** Nick Fletcher
DEVELOPERS Elissa Heller, Ryan Jensen, Jimmy Marks, Brandon Morrison

DIGITAL MEDIA DIRECTOR OF ANALYTICS Enrique Gonzales **DIGITAL REPORTING ANALYST** Eric Hossinger **SR. MULTIMEDIA PRODUCER** Sarah Crespi
MANAGING DIGITAL PRODUCER Alison Crawford **PRODUCER** Liana Birke **VIDEO PRODUCER** Chris Burns, Nguyễn Khởi Nguyễn
DIGITAL SOCIAL MEDIA PRODUCER Brice Russ

DIRECTOR OF OPERATIONS PRINT AND ONLINE Lizabeth Harman **DIGITAL/PRINT STRATEGY MANAGER** Jason Hillman
QUALITY TECHNICAL MANAGER Marcus Spiegler **PROJECT ACCOUNT MANAGER** Tara Kelly **DIGITAL PRODUCTION MANAGER** Lisa Stanford
ASSISTANT MANAGER DIGITAL/PRINT Rebecca Doshi **SENIOR CONTENT SPECIALISTS** Steve Forrester, Antoinette Hodal, Lori Murphy, Anthony Rosen **CONTENT SPECIALISTS** Jacob Hedrick, Kimberley Oster **ADVERTISING OPERATIONS SPECIALIST** Ashley Jeter

DESIGN DIRECTOR Beth Rakouskas **DESIGN EDITOR** Marcy Atarod **SENIOR DESIGNER** Chrystal Smith **DESIGNER** Christina Aycock
GRAPHICS MANAGING EDITOR Alberto Cuadra **GRAPHICS EDITOR** Garvin Grullón **SENIOR SCIENTIFIC ILLUSTRATORS** Chris Bickel, Katharine Sutliff **SCIENTIFIC ILLUSTRATOR** Valerie Altounian **INTERACTIVE GRAPHICS EDITOR** Jia You **SENIOR GRAPHICS SPECIALISTS** Holly Bishop, Nathalie Cary **PHOTOGRAPHY MANAGING EDITOR** William Douthitt **PHOTO EDITOR** Emily Petersen

DIRECTOR, GLOBAL COLLABORATION, CUSTOM PUBLICATIONS, ADVERTISING Bill Moran **EDITOR, CUSTOM PUBLISHING** Sean Sanders: 202-326-6430 **ASSISTANT EDITOR, CUSTOM PUBLISHING** Jackie Oberst: 202-326-6463 **ASSOCIATE DIRECTOR, ADVERTISING MARKETING** Justin Savyers: 202-326-7061 **science_advertising@aaas.org** **ADVERTISING SUPPORT MANAGER** Karen Foote: 202-326-6740 **ADVERTISING PRODUCTION OPERATIONS MANAGER** Deborah Tompkins **SR. PRODUCTION SPECIALIST/GRAPHIC DESIGNER** Army Hardcastle **SR. TRAFFIC ASSOCIATE** Christine Hall **SALES COORDINATOR** Shirley Young **ASSOCIATE DIRECTOR, COLLABORATION, CUSTOM PUBLICATIONS/CHINA/TAIWAN/KOREA/SINGAPORE** Xiaoying Chiu: +86-186 0082 9345, xchiu@aaas.org **COLLABORATION/CUSTOM PUBLICATIONS/JAPAN** Adarsh Sandhu: +81532-81-5142 asandhu@aaas.org **EAST COAST/E. CANADA** Laurie Faraday: 508-747-9395, FAX 617-507-8189 **WEST COAST/W. CANADA** Lynne Stickrod: 415-931-9782, FAX 415-520-6940
MIDWEST Jeffrey Dembksi: 847-498-4520 x3005, Steven Loecher: 847-498-4520 x3006 **UK EUROPE/ASIA** Roger Goncalves: TEL/FAX +41 43 243 1358 **JAPAN** Katsuyoshi Fukamizu(Tokyo): +81-3-3219-1777 kfukamizu@aaas.org **DIRECTOR, COLLABORATION AND PUBLISHING SERVICES CHINA/TAIWAN** Yan Xiang: +86-186 0082 9345, yxiang@aaas.org

DIRECTOR, GLOBAL ADVERTISING AND SALES Tracy Holmes: +44 (0) 1223 326525, FAX +44 (0) 1223 326532 tholmes@science-int.co.uk **CLASSIFIED** advertise@sciencecareers.org **U.S. SALES** Tina Burks: 202-326-6577, Nancy Toema: 202-326-6578 **EUROPE/ROW SALES** Sarah Lelarge
SALES ASSISTANT KCI Grace Japan Hirayuki Mashiki(Kyoto): +81-75-823-1109 hmashiki@aaas.org **CHINA/TAIWAN** Yan Xiang: +86-186 0082 9345 yxiang@aaas.org **MARKETING MANAGER** Allison Pritchard **MARKETING ASSOCIATE** Aimee Aponte

AAAS BOARD OF DIRECTORS, Chair Geraldine L. Richmond **PRESIDENT** Barbara A. Schaaf **PRESIDENT-ELECT** Susan Carol Field
Treasurer David Evans **Shaw Chief Executive Officer** Rush D. Holt **BOARD** Cynthia M. Beall, May R. Berenbaum, Charles J. Bustamante, Stephen P.A. Fodor, Claire M. Fraser, Michael S. Gazzaniga, Laura H. Greene, Elizabeth Loftus, Mercedes Pascual

SUBSCRIPTION SERVICES For change of address, missing issues, new orders and renewals, and payment questions: 866-434-AAAS (2227) or 202-326-6417, FAX 202-842-1065. Mailing addresses: AAAS, P.O. Box 96178, Washington, DC 20090-6178 or AAAS Member Services, 1200 New York Avenue, NW, Washington, DC 20005

INSTITUTIONAL SITE LICENSES 202-326-6730 **REPRINTS:** Author Inquiries 800-635-7181 **COMMERCIAL INQUIRIES** 803-359-4578 **PERMISSIONS** 202-326-6765, permissions@aaas.org **AAAS Member Services** 202-326-6417 or http://membercentral.aaas.org/discourts

Science serves as a forum for discussion of important issues related to the advancement of science by publishing material on which a consensus has been reached as well as including the presentation of minority of conflicting points of view. Accordingly, all articles published in Science—including editorials, news and comment, and book reviews—are signed and reflect the individual views of the authors and not official points of view adopted by AAAS or the institutions with which the authors are affiliated.

INFORMATION FOR AUTHORS See pages 624 and 625 of the 5 February 2016 issue or access www.sciencemag.org/authors/science-information-authors

SENIOR EDITORIAL BOARD

Gary King, *Harvard University*, Susan M. Rosenberg, *Baylor College of Medicine*, Ali Shilatfard, *Northwestern University Feinberg School of Medicine*

BOARD OF REVIEWING EDITORS

(Statistics board members indicated with \$)

Adriano Aguzzi, *U. of Hospital Zurich*
Takuzo Aida, *U. of Tokyo*
Leslie Aiello, *Wenner-Gren Foundation*
Judith Allen, *U. of Edinburgh*
Sonia Altizer, *U. of Georgia*
Sebastian Amigorena, *Institut Curie*
Meinrat O. Andreea, *Max-Planck Inst. Mainz*
Paola Arlotta, *Harvard U.*
Johan Auwerx, *EPFL*
David Awschalom, *U. of Chicago*
Clare Baker, *University of Cambridge*
Nenad Ban, *ETH Zurich*
Franz Bauer, *Pontificia Universidad Católica de Chile*
Ray H. Baughman, *U. of Texas, Dallas*
David Baum, *U. of Wisconsin*
Carlo Beenakker, *Leiden U.*
Kamran Behnia, *ESPCI-ParisTech*
Yasmine Belkaid, *NIAID, NIH*
Philip Benfey, *Duke U.*
May Berenbaum, *U. of Illinois*
Gabriele Bergers, *U. of California, San Francisco*
Bradley Bernstein, *Massachusetts General Hospital*
Peer Bork, *EMBL*
Bernard Bourdon, *Ecole Normale Supérieure de Lyon*
Chris Bowler, *Ecole Normale Supérieure*
Ian Boyd, *U. of St. Andrews*
Emily Brodsky, *U. of California, Santa Cruz*
Ron Brookmeyer, *U. of California Los Angeles (\$)*
Christian Büchel, *U. Hamburg-Eppendorf*
Joseph A. Burns, *Cornell U.*
Carter Tribble Butts, *U. of California, Irvine*
Gyorgy Buzsaki, *New York U. School of Medicine*
Blanche Capel, *Duke U.*
Mats Carlsson, *U. of Oslo*
Ib Chorkendorff, *U. of Denmark*
David Clapham, *Children's Hospital Boston*
Joel Cohen, *Rockefeller U., Columbia U.*
James J. Collins, *MIT*
Robert Cook-Deegan, *Duke U.*
Lisa Coussens, *Oregon Health & Science U.*
Alan Cowman, *Walter & Eliza Hall Inst.*
Robert H. Crabtree, *Yale U.*
Roberto Croce, *Vrije Universiteit*
Janet Currie, *Princeton U.*
Jeff L. Dangl, *U. of North Carolina*
Tom Daniel, *U. of Washington*
Frans de Waal, *Emory U.*
Stanislas Dehaene, *Collège de France*
Robert Desimone, *MIT*
Claude Desplan, *New York U.*
Sandra Diaz, *Universidad Nacional de Cordoba*
Dennis Discher, *U. of Pennsylvania*
Gerald W. Dorn II, *Washington U. School of Medicine*
Jennifer A. Doudna, *U. of California, Berkeley*
Bruce Dunn, *U. of California, Los Angeles*
William Dunphy, *Caltech*
Christopher Dye, *WHO*
Todd Ehlers, *U. of Tuebingen*
David Ehrhardt, *Carnegie Inst. of Washington*
Tim Elston, *U. of North Carolina at Chapel Hill*
Jennifer Elisseeff, *Johns Hopkins U.*
Gerhard Ertl, *Fritz-Haber-Institut, Berlin*
Barry Everitt, *U. of Cambridge*
Ernst Fehr, *U. of Zurich*
Anne C. Ferguson-Smith, *U. of Cambridge*
Michael Feuer, *The George Washington U.*
Toren Finkel, *NHLBI, NIH*
Kate Fitzgerald, *U. of Massachusetts*
Peter Fratzl, *Max-Planck Inst.*
Elaine Fuchs, *Rockefeller U.*
Daniel Geschwind, *UCLA*
Karl-Heinz Glassmeier, *TU Braunschweig*
Ramón González, *Rice U.*
Elizabeth Grove, *U. of Chicago*
Nicolas Gruber, *ETH Zurich*
Kip Guy, *St. Jude's Children's Research Hospital*
Teekjip Ha, *U. of Illinois at Urbana-Champaign*
Wolf-Dietrich Hardt, *ETH Zurich*
Christian Haass, *Ludwig Maximilians U.*
Sharon Hammes-Schiffer, *U. of Illinois at Urbana-Champaign*
Michael Hasselmo, *Boston U.*
Martin Heimann, *Max-Planck Inst. Jena*
Yka Helariutta, *U. of Cambridge*
James A. Hendler, *Rensselaer Polytechnic Inst.*
Janet G. Hering, *Swiss Fed. Inst. of Aquatic Science & Technology*
Kai-Uwe Hinrichs, *U. of Bremen*
David Hodell, *U. of Cambridge*
Lora Hooper, *UT Southwestern Medical Ctr. at Dallas*
Tamas Horvath, *Yale University*
Raymond Huey, *U. of Washington*
Fred Hughson, *Princeton U.*
Auke Ijspeert, *EPFL Lausanne*
Stephen Jackson, *USGS and U. of Arizona*
Steven Jacobsen, *U. of California, Los Angeles*
Seema Jayachandran, *Northwestern U.*
Kai Johnson, *EPFL Lausanne*
Peter Jonas, *Inst. of Science & Technology (IST) Austria*
Matt Kaeberlein, *U. of Washington*
William Kaelin Jr., *Dana-Farber Cancer Inst.*
Daniel Kahne, *Harvard U.*
Daniel Kammen, *U. of California, Berkeley*
Abby Kanner, *U. of California, Los Angeles*
Hitoshi Kawakatsu, *U. of Tokyo*
Masashi Kawasaki, *U. of Tokyo*
V. Naray Kim, *Seoul National U.*
Robert Kingston, *Harvard Medical School*
Etienne Kochlin, *Ecole Normale Supérieure*
Alexander Kolodkin, *Johns Hopkins U.*
Thomas Langer, *U. of Cologne*
Mitchell A. Lazar, *U. of Pennsylvania*
David Lazer, *Harvard U.*
Thomas Lecuit, *IDM*
Virginia Lee, *U. of Pennsylvania*
Stanley Lemon, *U. of North Carolina at Chapel Hill*
Ottoline Leyser, *Cambridge U.*
Wendell Lim, *U.C. San Francisco*
Marcia C. Linn, *U. of California, Berkeley*
Jianguo Liu, *Michigan State U.*
Luis Liz-Marzan, *CIC biomaGUNE*
Jonathan Losos, *Harvard U.*
Ke Lu, *Chinese Acad. of Sciences*
Christian Lüscher, *U. of Geneva*
Laura Machesky, *CRUK Beatson Inst. for Cancer Research*
Aime Magurran, *U. of St. Andrews*
Oscar Marin, *CSIC & U. Miguel Hernández*
Charles Marshall, *U. of California, Berkeley*
C. Robertson McClung, *Dartmouth College*
Rodrigo Medellín, *U. of Mexico*
Graham Medley, *U. of Warwick*
Jane Memmott, *U. of Bristol*
Tom Misteli, *NCI*
Yasushi Miyashita, *U. of Tokyo*
Mary Ann Moran, *U. of Georgia*
Richard Morris, *U. of Edinburgh*
Alison Moutter-Reif, *NC State U. (\$)*
Thomas Murray, *The Hastings Center*
Daniel Neuman, *U. of California, Berkeley*
Kitty Nijmeijer, *U. of Twente*
Helga Nowotny, *European Research Advisory Board*
Rachel O'Reilly, *Warwick U.*
Joe Orenstein, *U. of California Berkeley & Lawrence Berkeley National Lab*
Harry Orr, *U. of Minnesota*
Pilar Ossorio, *U. of Wisconsin*
Andrew Oswald, *U. of Warwick*
Isabella Pagano, *Istituto Nazionale di Astrofisica*
Margaret Palmer, *U. of Maryland*
Steve Palumbi, *Stanford U.*
Jane Parker, *Max-Planck Inst. of Plant Breeding Research*
Giovanni Parmigiani, *Dana-Farber Cancer Inst. (\$)*
John H. J. Petrini, *Memorial Sloan-Kettering Cancer Center*
Samuel Pfaff, *Salk Institute for Biological Studies*
Kathrin Plath, *U. of California, Los Angeles*
Joshua Plotkin, *U. of Pennsylvania*
Albert Polman, *FOM Institute AMOLF*
Philippe Poulin, *CNRS*
Jonathan Pritchard, *Stanford U.*
Wim van der Putten, *Netherlands Institute of Ecology*
David Randall, *Colorado State U.*
Sarah Reisman, *Caltech*
Felix Rey, *Institut Pasteur*
Trevor Robbins, *U. of Cambridge*
Jim Roberts, *Fred Hutchinson Cancer Research Ctr.*
Amy Rosenzweig, *Northwestern University*
Mike Ryan, *U. of Texas, Austin*
Mitsunori Saitoku, *Kyoto U.*
Shimon Sakaguchi, *Kyoto U.*
Miguel Salmeron, *Lawrence Berkeley National Lab*
Jürgen Sandkühler, *Medical U. of Vienna*
Alexander Schier, *Harvard U.*
Vladimir Shalaev, *Purdue U.*
Robert Siliciano, *Johns Hopkins U.*
Denis Simon, *Arizona State U.*
Uri Simonsohn, *U. of Pennsylvania*
Alison Smith, *John Innes Centre*
Richard Smith, *U. of North Carolina (\$)*
John Speakman, *U. of Aberdeen*
Allan C. Spradling, *Carnegie Institution of Washington*
Jonathan Sprent, *Garvan Inst. of Medical Research*
Eric Steig, *U. of Washington*
Paula Stephan, *Georgia State U. and National Bureau of Economic Research*
Molly Stevens, *Imperial College London*
Ira Tabas, *Columbia U.*
Sarah Teichmann, *Cambridge U.*
John Thomas, *North Carolina State U.*
Shubha Tole, *Jata Institute of Fundamental Research*
Christopher Tyler-Smith, *The Wellcome Trust*
Sanger Inst.
Herbert Virgin, *Washington U.*
Berth Vogelstein, *Johns Hopkins U.*
David Wallace, *Weizmann Inst. of Science*
Ian Walsmley, *U. of Oxford*
Jane-Ling Wang, *U. of California, Davis (\$)*
David Waxman, *Fudan U.*
Jonathan Weissman, *U. of California, San Francisco*
Chris Wikle, *U. of Missouri (\$)*
Ian A. Wilson, *The Scripps Res. Inst. (\$)*
Timothy D. Wilson, *U. of Virginia*
Rosemary Wyse, *Johns Hopkins U.*
Jan Zaenen, *Leiden U.*
Kenneth Zaret, *U. of Pennsylvania School of Medicine*
Jonathan Zehr, *U. of California, Santa Cruz*
Len Zon, *Children's Hospital Boston*
Maria Zuber, *MIT*

BOOK REVIEW BOARD

David Bloom, *Harvard U.*, Samuel Bowring, *MIT*, Angela Creager, *Princeton U.*, Richard Swedder, *U. of Chicago*, Ed Wasserman, *DuPont*

Lifeline for refugee scholars

The global refugee crisis now stands at 65 million forcibly displaced people, according to the United Nations. Could the world ever have imagined a number exceeding that produced by the Nazis and World War II? The conflict over Syria alone, raging since 2011, has so far resulted in more than 11 million refugees and internally displaced persons. Over the past year, international summits have convened to address this global crisis, including the United Nations Summit in September. There is a growing view that the world must recognize these individuals not as part of a temporary emergency, but as a long-term challenge, and one where higher education can play a major role.

The immediate challenges of refugee management can, understandably, overshadow taking stock of the vast scope of people who are displaced. Among those who have had their education, or their career in academia, interrupted are the many scholars and scientists whose lives and work serve thousands more. If you consider the decades of study and training, the ripple effect of published work, and the numbers of students taught, each scholar represents the compounded potential to deliver life-saving innovations and ground-breaking scientific discovery that could reach countless others. Many of these scholars will have no safe home to return to in the foreseeable future.

During and after World War II, efforts were made to help scholars who were dismissed from German universities on racial and political grounds. Initiatives such as the Academic Assistance Council [now known as the Council for At-Risk Academics (CARA)] and the Emergency Committee for Displaced German and European Scholars of the Institute of International Education (IIE) helped scholars who were forced out of Germany.

Today, organizations including CARA, IIE, the Alexander von Humboldt Foundation's Philipp Schwartz Initiative, and the Scholars at Risk network continue to

build lifelines for academics at risk. For example, the IIE Scholar Rescue Fund has provided fellowships to nearly 700 professors and senior researchers from 56 countries, including Syria and other war-torn countries such as Iraq and Yemen—nearly twice as many academics as the organization helped during World War II. These rescued scholars have joined universities, teaching hospitals, research institutions, and laboratories around the world that have

not only accepted them as their own, but have gained in return. One scholar, who was forced out of Belarus, now leads research in nanotechnology in the United States where he continues to pioneer diagnostic techniques for chronic diseases. Another refugee scholar from Nigeria, well known in the field of immunology, continued her research on infectious diseases in South Africa and Kenya before returning home to an improved security situation. Recognizing such outcomes, students at Rockefeller University in New York, along with postdoc-led organizations such as INet NYC, have committed to help displaced scientists adapt to a new academic culture and a long-term career path in the United States.

Displaced scholars, whether refugees or in exile, need the support of institutions large and small, in countries large and small, to break through the barriers that prevent them from academic engagement and employment—fears that they will take jobs away, require more help than they give, or not make the transition to teaching students in the host country. In succumbing to this backlash, we forget that the world's great universities became great because they welcomed refugees, exiles, and thinkers in distress. With support from the international academic community, threatened scholars and scientists can be saved. Let us all ensure that academic training is not wasted, knowledge for present and future generations is preserved, and that the next Albert Einstein or Felix Bloch is not lost in the painful currents of forced emigration.

—Allan Goodman



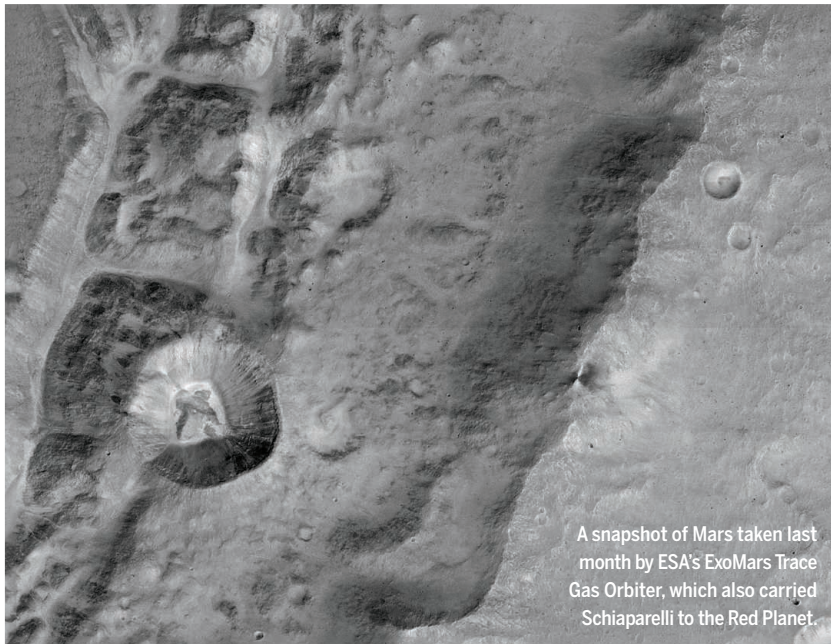
Allan Goodman is President of the Institute of International Education, New York, New York. agoodman@iie.org



“Displaced scholars...need the support of...the international academic community...”

IN BRIEF

Mars mission a go; asteroid lander killed



A snapshot of Mars taken last month by ESA's ExoMars Trace Gas Orbiter, which also carried Schiaparelli to the Red Planet.

The European Space Agency's (ESA's) funders last week decided to press ahead with the ExoMars 2020 lander, despite the failure of the test-run Schiaparelli lander, which crashed on Mars in October and cast a pall over the mission. Ministers from ESA's 22 member states approved the €440 million still needed for the mission, a collaboration with Russia, but determined that €97 million of that must come from ESA's internal funds. "Today I am very confident we will do it. We have some contingency," ESA Director General Jan Wörner said at a 2 December press conference. In total, the ministers approved €10.3 billion for ESA projects; the agency had requested €11 billion, so some belt tightening will be required. A suite of science missions will go ahead, including studies of exoplanets, the sun, Mercury, and dark energy. But with only a 1% annual increase to ESA's central funding, there may be a squeeze if inflation increases or ExoMars goes over budget. The Asteroid Impact Mission was the sole casualty. It planned to study and land on a near-Earth asteroid in preparation for a NASA-led impact mission in 2022 that aimed to alter its orbit. <http://scim.ag/ESAmnist>

AROUND THE WORLD

Global science scores flat

PARIS | The rapid growth of technology hasn't made the world's teenagers any smarter in science. That's the overarching message from the 2015 Programme for International Student Assessment (PISA), which focused on the scientific aptitude of 15-year-olds in some 72 countries and political jurisdictions. Singaporean students continue to lead the world, followed by Japan, Estonia, Taiwan, Finland, and Canada. But scores have changed little since the 2006 science test. U.S. students are once again mired in the middle of the pack. The silver lining for U.S. policymakers is a narrowing gap between the performance of the least and most advantaged students, which PISA officials call the equity index. But some of that narrowing was due to a retreat at the high end of the scale. The results refute conventional wisdom that more spending on education leads to better outcomes and that recent immigrants pull down a country's performance. But the test also finds that students who enjoy science and want to pursue it as a career don't necessarily do better than their peers.

Fires blaze in mountain forests

GATLINBURG, TENNESSEE | A firestorm that raged through Gatlinburg on 28 November, killing at least 14 people, is part of a record-shattering wildfire season in the southern Appalachian Mountains. Fall wildfires aggravated by a months-long drought across much of the southeastern United States scorched more than 40,000 hectares of federal land in Tennessee, North Carolina,



Fires scorched Gatlinburg, a Smoky Mountain resort.

South Carolina, and Georgia—more than four times the area burned by wildfires in 2007, the previous record setter of the past 45 years, says U.S. Forest Service (USFS) ecologist Steve Norman, in Asheville, North Carolina. The region's forests were shaped by frequent, low-intensity fires, prior to European settlement, but thanks to modern firefighting techniques there have been few wildfires in recent decades. "We don't see fires like this. I've never seen one in my career," says Joe O'Brien, a USFS ecologist in Athens, Georgia. "We really don't know what the impact is going to be." O'Brien says he expects scientists will use satellite imagery to first assess how intense and widespread the fires were. Researchers will next scrutinize aftereffects on mountain ecosystems, such as survival of different tree species.

Gravitational wave hunt resumes

HANFORD, WASHINGTON, AND LIVINGSTON, LOUISIANA | Fourteen months after scoring a monumental discovery, physicists are back in the hunt for gravitational waves—ripples in spacetime set off by some of the cosmos's most violent events. On 14 September 2015, experimenters working with the Laser Interferometer Gravitational-Wave Observatory (LIGO), a pair of gigantic instruments in Hanford and Livingston, spotted a pulse of waves from two massive black holes spiraling into each other 1.3 billion light-years away (http://scim.ag/_gravwaves). Researchers spotted a second black-hole merger before ending that observation run in January. On 30 November, after 11 months of tuning, LIGO began taking data again, with roughly 10% better sensitivity than before. LIGO physicists hope eventually to double the instruments' sensitivity and spot as many as one black hole merger per day.

Indonesia protects peatlands

JAKARTA | The Indonesian government is strengthening restrictions on converting peatlands for agricultural use. In the last 2 decades, companies have turned thousands of hectares of virgin forest into palm oil plantations by draining the swampy soil and burning the vegetation. The World Resources Institute (WRI) says peat drainage in Indonesia and Malaysia releases annual emissions equivalent to nearly 70 coal-fired power plants. The conversion reduces habitat for endangered species such as the orangutan—and the burning creates a toxic haze that has caused human respiratory problems across much of southeast Asia (*Science*, 15 January, p. 209). Starting in 2011, Indonesia introduced a



The dino's tail plumage has fine filamentous "barbules" that spring from the barbs, or feather shafts (rachis not shown.)

Tail feathers in amber

While hunting through an amber market in Myanmar, paleontologist Lida Xing of China University of Geosciences in Beijing made a startling discovery: a small golden chunk about 99 million years old that contained, along with the usual scattering of insects, a 36-millimeter-long section of a flexible, finely feathered tail. Prehistoric feathers have been found in amber before—but not at the level of 3D detail found in this specimen, Xing and co-authors report this week in *Current Biology*. Using photomicrographs and computerized tomography scanning, the team studied the eight preserved vertebrae and their feathers. Unlike archaeopteryx or modern birds, the vertebrae were not fused into a solid rod at the tip of the tail; instead, the tail is whiplike and flexible—suggesting that its owner was in fact a dinosaur, likely a member of a group of small theropods called coelurosaurs. The amber also preserved plumage pigments that suggest the theropod was colored chestnut brown along its back and lighter on its belly. The structure of the plumage, meanwhile, may answer a lingering question about feather evolution: The tail feathers lack a well-developed central shaft, or rachis, but have fine tiers of branching as in modern feathers, suggesting that those branching barbs and barbules evolved first.

series of 2-year moratoria, renewed three times by presidential decree, on conversions of primary forest resting on peat formations more than 1 meter deep. The new regulation goes further: It covers all peatlands regardless of the thickness of the peat layer, and is permanent. The ban "is a bold move," says Arief Wijaya, senior manager for forests and climate for WRI in Jakarta. WRI, which says the ban is "a huge win in the fight against climate change," estimates that over the next 15 years, the new rules could keep up to 7.8 gigatons of carbon dioxide out of the atmosphere.

Congress makes deal on NSF bill

WASHINGTON, D.C. | There may be a truce in the fiercely partisan 3-year war between Republican leaders in the House of Representatives and the scientific community over how the National Science Foundation (NSF) should operate. A compromise struck with the Senate and pending

this week in Congress preserves NSF's criteria for selecting the best research proposals and is something researchers think they can live with. The battleground is a reauthorization of the 2010 America Creating Opportunities to Meaningfully Promote Excellence in Technology, Education, and Science Act, which sets out policies governing NSF, the National Institute of Standards and Technology, and federal programs on innovation, manufacturing, and science and math education. Since 2013, the House has adopted a succession of bills containing language that scientists interpreted as telling NSF to favor applied research with obvious payoffs. Their Senate counterparts, in contrast, united behind a single, bipartisan piece of legislation crafted by senators Cory Gardner (R-CO) and Gary Peters (D-MI) that scientists preferred, and that approach seems to have largely prevailed when legislators from both houses sat down to reconcile their differences. <http://scim.ag/NSFbilldeal>



Paleoclimatologist Kim Cobb samples coral, which preserves a record of water temperature in the ratio of oxygen isotopes in its skeleton.

CLIMATE

Corals tie stronger *El Niños* to climate change

Much-debated link gains support from long record of ocean temperatures

By **Christopher Pala**, on Christmas Island, in Kiribati

Kim Cobb and two team members, clad in black scuba gear, have been scouring the coral-studded seabed near the equatorial Pacific's Christmas Island here for nearly an hour. Then Cobb emerges with a victorious "Yes!"

A few minutes later, Cobb, a paleoclimatologist at the Georgia Institute of Technology in Atlanta, dives back to the bottom and, from under a coral head, extracts the prize: two small containers encrusted with coralline algae. Inside are recorders of salinity and temperature that captured in excruciating detail the 2015–16 El Niño event, which brought a pulse of abnormally warm water to the tropical Pacific. The recorders showed that during the disturbance, which wreaked climatic havoc around the globe, the warming here set a record: 3°C above normal. The extreme warmth, Cobb says, reflected not just the natural El Niño cycle, but a new factor: global warming caused by human activity.

As she will report next week at the American Geophysical Union meeting in San Francisco, California, a detailed, long-term temperature record derived from corals on Christmas and other Pacific islands shows that over the last 7000 years, El Niños waxed and waned. Then, during the 20th century, with global warming taking hold, their intensity began to climb. The trend is likely to continue, boding ever more destructive El Niños,

she says. "It's yet another impact of global warming that we'd like to avoid."

Gavin Schmidt, director of NASA's Goddard Institute for Space Studies in New York City, says Cobb's temperature archive offers the first historical picture of El Niño and its changes. "It's unique and gives a fascinating window into an otherwise totally obscure, but vitally important, part of climate history."

El Niños arrive every 3 to 7 years when winds fail in the tropical Pacific, allowing warm water to pool in the eastern part of the ocean. The oceanic warmth disrupts fisheries and can bleach and kill corals—85% of Christmas Island's corals may have died in the latest El Niño, which ended in May. El Niños also trigger widespread floods and droughts that, during the extreme El Niño of 1997–98, caused \$35 billion in damage and claimed an estimated 23,000 lives.

Yet no one knew whether the gradual warming of the globe is intensifying these events, in part because records are short and spotty in the remote parts of the Pacific where El Niño hits hardest. To get the long view, Cobb and her collaborators gathered hundreds of lumps of old coral washed up on beaches on Christmas and Fanning islands (both part of the Republic of Kiribati) and the U.S. island of Palmyra. By applying uranium-thorium dating to the corals and measuring ratios of oxygen isotopes in their skeletons, her lab reconstructed ocean temperatures for much of the last 7000 years.

During that time, Cobb says, "all kinds of stuff was going on in the climate, but it had

no discernible effect on El Niño events." But the corals, supplemented by sensors like the one Cobb recovered off Christmas, show that over the past century El Niño intensity has increased by 25%. "There is no century even remotely resembling the 20th in the record for at least 5000 years," she says.

Cobb's finding is consistent with a 2013 study of tree rings suggesting that El Niño-related weather havoc has intensified across much of the globe in recent decades, notes Wenju Cai, a climate modeler at the Commonwealth Scientific and Industrial Research Organisation in Melbourne, Australia. But the tree ring record is too short, he says, to show whether global warming is to blame. Cobb's 7000-year archive, in contrast, "clearly shows that 20th century El Niños are more extreme and intense than they were before the industrial era, and that points to global warming as a cause."

Eric Guilyardi, a climate scientist at the Pierre Simon Laplace Institute in Paris, hopes Cobb's results will inspire others to develop similar temperature records elsewhere in the equatorial Pacific. "This will give us the spatial view needed to be sure El Niño is indeed changing."

Now, Cobb plans to push her temperature record into the future. "We're now tracking 30 corals that have survived this latest El Niño," she says. They're waiting to record the next one—and even hotter seas to come. ■

Christopher Pala is a freelance journalist based in Washington, D.C.

CANCER IMMUNOTHERAPY

Worries, confusion after cancer trial deaths

Experimental immune treatment linked to fatal brain swelling

By Jennifer Couzin-Frankel

An experimental cancer therapy is facing its biggest setback yet, after an unexpected complication killed seven people over about a year, five of them in a single clinical trial. The company, Seattle, Washington-based Juno Therapeutics, has its most troubled trial on hold and is racing to figure out why patients suffered fatal brain swelling. Researchers elsewhere are grappling with possible ramifications for the breakthrough treatment, which goes up for drug approval next year.

"Why would we see this now? We don't know, period," says Stephan Grupp, a pediatric oncologist at the Children's Hospital of Philadelphia in Pennsylvania. In several trials, he has treated more than 100 children with the experimental approach, in which a patient's own immune cells are genetically engineered to fight cancer. None experienced the fluid buildup, known as cerebral edema, that killed adults in Juno's trials. Grupp and others speculate that the explanation may lie in the specific product tested and the patient population, rather than in the overall strategy itself. Still, they are mostly in the dark. Cerebral edema "wasn't on anybody's radar," Grupp admits. Company officials declined to comment, saying only that they are investigating.

Several hundred people with advanced blood cancers, from toddlers to senior citizens, have received the treatment, called chimeric antigen receptor (CAR)-T cell therapy, with remarkable results (*Science*, 28 June 2013, p. 1514). Many have now been cancer free for years, and the therapy is part of a new arsenal of immune-based cancer therapies (*Science*, 20 December 2013, p. 1432). Doctors are beginning to test CAR-T therapy in solid tumors like lung cancer. Results there are mixed (*Science*, 2 September, p. 983).

Like other cancer immunotherapies, CAR-T therapy can overstimulate the immune system, triggering an out-of-control proliferation of immune cells that can shut down vital organs. The first child treated with CAR-T therapy, a 6-year-old girl with leuke-

mia, nearly died from this. "The community recognized this as a huge threat to our patients and to the therapy" and found drugs to manage it, says Crystal Mackall, who heads the cancer immunology and immunotherapy program at Stanford University in Palo Alto, California. The therapy was also known to carry neurological risks, including confusion, delirium, seizures, and even a temporary inability to speak. But they have not been fatal.

Juno reported the first death about a year

edema is essentially an extreme version of the brain issues doctors were already recording or is something else. Either way, the cause could lie in one or several specific features of the Juno trial. For one, most of the deaths are in adults with acute leukemia; people with this disease tend to have more side effects from CAR-T therapy, in part because the T cells can expand more quickly for reasons that are not well understood. This increases effectiveness but also risks.

Other variables include the age of trial participants—children often have fewer side effects—and the chemotherapy given before the T cells.

Finally, there's the design of the CAR-T cells themselves. All incorporate a "costimulatory molecule" that encourages proliferation. The five deaths occurred in Juno's trial that uses a molecule called CD28. The company's other trial, with two edema deaths, relies on a different molecule, called 4-1BB. Novartis, which is also running trials in acute leukemia and has not reported cerebral edema, relies on 4-1BB, too.

A third company, Kite Pharma, based in Santa Monica, California, is using CD28 but is treating adults with advanced lymphoma, not leukemia; it hasn't seen any cases of cerebral edema, executives say. Kite and Novartis plan to apply for FDA approval next year.

Better animal models could help solve the mystery. The most popular CAR-T therapy model, in mice, failed to predict any neurotoxicity. Earlier this week, a team at the Seattle Children's Research Institute in Washington reported at the ASH meeting that they had tested a CAR-T therapy in rhesus monkeys, and that the animals developed abnormal behaviors and tremors, suggesting neurologic effects.

"It's clearly sobering," Mackall says of the Juno deaths. "I've lived, eaten, and breathed" this therapy, and "you think you understand it." Still, she points out, all cancer drugs come with huge risks, and that's something patients, their doctors, and drug regulators generally accept given the severity of the disease. "Let's get rid of the hype here: This is a new therapy that is very promising," Mackall says, "but we still have a lot to learn about it." ■



A new cancer treatment genetically engineers T cells (blue) to attack malignant cells like this lymphocyte cell (orange).

ago, but it didn't trigger alarm bells. Then in July, the company revealed a cluster of three more deaths in a different trial, for acute leukemia. Juno suggested these were due to a chemotherapy drug called fludarabine that the patients also received. Juno eliminated fludarabine from its protocol, and the U.S. Food and Drug Administration (FDA) allowed the trial to resume.

But late last month, edema killed two more patients in the same trial, which is now back on hold. Neither the company nor FDA has released much information since, including the total number of patients treated. Last weekend at the annual American Society of Hematology (ASH) meeting, however, Juno reported that a seventh patient, with chronic leukemia, had also died from cerebral edema.

Mackall and others wonder whether the



FORECASTING

U.S. Congress wants to know the weather weeks ahead

Bill targets seasonal forecasts and NOAA's pricey satellites

By **Paul Voosen**

Two winters ago, a pool of icy arctic air stalled over much of the United States. Snowstorms crippled the Midwest, snarling truck and rail freight. As accidents and financial losses piled up, lawmakers began to hear a refrain from soy farmers and ethanol shippers: It would have been great to know this was coming a few months earlier. Could they get the scientists on that?

Congress's response is a sweeping weather bill that passed the Senate on 1 December. The bill, expected to be approved by the House of Representatives and signed into law this month, aims to bolster the capacity of the National Oceanic and Atmospheric Administration (NOAA) to make seasonal weather predictions between 2 weeks and 2 years out. That would put within forecasters' reach events like the severe 2014–15 winter, when unusual Pacific temperatures, declining Arctic sea ice, or heavy autumn snowfall in Asia may have led the jet stream to dip drastically south across eastern North America. It would also require modeling skills that are now largely the province of climate scientists, who look years or decades ahead. Although the sponsors of the bill include representatives Lamar Smith (R-TX) and Frank Lucas (R-OK), both critics of the reality of human-driven climate change, no one seems to mind, if climate forecasting can improve the bottom line for business.

"If we can offer better predictions in these time frames, it's just going to help us with our economy, with our well-being, and with our defense," says Raymond Ban, a meteorologist and retired Weather Channel executive based in Marietta, Georgia, who led a 2016 U.S. National Academies report on long-range forecasting. He says such predictions could help the U.S. Navy anticipate Arctic sea ice extent, assist farmers in choosing crop varieties, and let emergency planners prepare for hazardous storms. "All we're talking about is benefit."

The first significant legislation to address weather in a generation, the bill covers plenty of ground beyond seasonal forecasts. It calls for NOAA to improve its hurricane and tornado research. It directs the agency to put sensors on subsea telecommunication cables to improve tsunami warnings, and expand its efforts in uncovering prehistoric tsunamis. It orders the agency to evaluate how well the public understands and responds to its cryptic system of "watch" and "warning" weather alerts.

The bill also offers a sharp response to NOAA's notoriously delayed and overbudget satellite missions, to the point of telling the agency which simulations it should run to judge the relative merits of sensors. It also requires NOAA to shift from relying exclusively on its own satellites and weather data and to look for commercial alternatives wherever possible. "It stops asking NOAA to think about this and starts telling them

A radar in the Maldives tracks the growing storms of a seasonal Madden-Julian Oscillation event.

how to do it," says David Titley, a director of the Center for Solutions to Weather and Climate Risk at Pennsylvania State University in State College.

The biggest boost to science, however, will likely come from the bill's emphasis on seasonal forecasts, for which it urges Congress to set aside \$26.5 million a year. Weather forecasters have tended to put more effort into ingesting data from satellites, weather balloons, and ocean buoys than improving the physics of their computer models, which simulate the behavior of the atmosphere and oceans by dividing them up into boxes and calculating how conditions evolve in each one. After 2 weeks, the weather models tend to stray, offering little predictive value. But over the past decade, climate scientists, who have far more accurate long-term models, have become interested in shorter timescales, aiming to predict ocean warming events like El Niño, which unfold over years rather than decades. Now, they are focusing on even shorter-term phenomena like the Madden-Julian Oscillation (MJO), storms that march east around the equator at 30- to 60-day intervals, with far-reaching effects on global weather patterns just a few weeks out.

The climate models are ripe for weather forecasters to exploit, says Scott Sandgathe, a meteorologist at the University of Washington in Seattle. "It's time the climate community and weather community came together," he says. "We are investing in experts in two separate communities doing close to the same thing."

NOAA's National Weather Service is already moving in these directions. Last year, for example, the service began publishing experimental 2- to 4-week forecasts. And in July, NOAA selected the system of boxes used for climate simulations at the Geophysical Fluid Dynamics Laboratory in Princeton, New Jersey, to be the basis for its next-generation weather model.

But the agency's forecasts are widely seen to lag behind those from the European Centre for Medium-Range Weather Forecasts in Reading, U.K., Sandgathe says. One reason for the Europeans' success is their models' talent in conjuring up the MJO, thanks to better physics, more detailed initial conditions, and better calibration—which give their models predictive skill beyond 20 days.

The United States is not yet able to match that skill. But as it begins to fold in the lessons of its climate models, it may yet, as Representative Lucas put it, "reclaim superior weather prediction." ■

GLOBAL HEALTH

AIDS epidemic nears control in three African countries

Massive new surveys show stunning progress

By Jon Cohen

Amidst the reams of statistics that pour out on every World AIDS Day on 1 December came one surprising bit of good news this year. Three neighboring, cash-strapped countries in hard-hit southern Africa—Malawi, Zambia, and Zimbabwe—have had remarkable success against the virus, according to the most comprehensive study done to date.

The new study, coordinated out of the Columbia University Mailman School of Public Health and led by epidemiologist Wafaa El-Sadr, collected massive amounts of on-the-ground data by visiting 80,000 randomly selected households in the three countries. The upshot: HIV-infected people in the region are getting treated and sticking with their drug regimen in numbers that have surprised and delighted experts. The survey found that up to two-thirds of HIV-infected people in the three countries have fully suppressed the virus, slashing the rate of new infections. (In the United States, the comparable figure is 30%.) “We’re getting very close to the number that shuts down epidemics,” says Deborah Birx, who heads the U.S. President’s Emergency Plan for AIDS Relief (PEPFAR) in Washington, D.C.

Until now, the most authoritative estimates of new HIV infection rates, or incidence, and prevalence have come from the Joint United Nations Programme on HIV/

AIDS (UNAIDS). Those are based on mathematical models that largely extrapolate from clinics and nonrandomized surveys. The UNAIDS estimates do not include the level of virus in each infected person, a key indication of how well interventions are working.

The new population-based HIV impact assessments (PHIAs), which began in 2015 and are funded by PEPFAR, fill that gap. In addition to going door-to-door in cities, teams traveled to the remote countryside, often pulling up to thatch-roofed homes and erecting pop-up tents in which nurses did blood draws. Social scientists also interviewed participants about their health and lifestyle. Blood was assessed on the spot for HIV and syphilis, with counseling and treatment referrals made for anyone in need. Then the teams took the vials back to cities to analyze viral levels. “We have to reach people we haven’t reached and know exactly where the crusade is failing,” El-Sadr said during a survey in Zimbabwe.

The results, released in press releases and fact sheets, mostly confirm the UNAIDS estimates of HIV’s reach in the three countries—which each have a prevalence of more than 10% of the adult population. But they showed an annual rate of new infections in Zimba-

bwe and Zambia that was substantially lower than expected (see table, below). Peter Ghys, who directs strategic information and evaluation at UNAIDS in Geneva, Switzerland, says his team will incorporate the PHIA data in future modeling estimates.

Across the region, the PHIA results suggest, the rate of new infections has fallen by half since 2003. Data on viral levels point to one factor: At least 86% of people in each country receiving antiretroviral treatment had “fully suppressed” HIV. This means they had such low levels of virus in their blood that the drugs not only are staving off AIDS, but making it highly unlikely that they will infect others. “We were amazed when we saw this,” El-Sadr says.

The result helps assuage worries that many infected people in those countries are not sticking with their treatment. PEPFAR surveys of clinics had suggested that more than 20% of people who started treatment ended up dropping it. “We were misled at the program level about retention,” Birx says. The PHIA data’s high level of viral suppression suggests that instead, “people were moving from one clinic to another and it looked like they were lost to follow-up.”

All three countries have received substantial international assistance for HIV/AIDS prevention and treatment: Since 2004, PEPFAR has invested \$4 billion, and the Global Fund to Fight AIDS, Tuberculosis and Malaria has provided \$2 billion more. But funding alone does not explain the gains against the virus, Birx says. “These programs and the people implementing them have done an extraordinary job of working with the community and the individual clients.”

The new data have important implications for the global push to end HIV/AIDS epidemics by 2030. To achieve that, UNAIDS has set what is known as the 90-90-90 goal for 2020. UNAIDS modeling shows that epidemics will peter out if 90% of infected people know their HIV status, 90% of that group receives antiretrovirals, and 90% on treatment have undetectable viral levels. This translates to undetectable viral levels in 73% of all HIV-infected people in a population—including those who don’t know their status and have uncontrolled infections. The PHIA numbers suggest the goal is within reach: Malawi is already at 67.6%, Zimbabwe is at 60.4%, and Zambia is at 59.8%. The preliminary findings are “pretty doggone amazing,” Birx says. “This really shows why it is so important to get community-level survey data.” ■

Vital statistics

A new study in southern Africa reveals a lower than expected annual rate of new HIV infections.

COUNTRY	PREVALENCE	NEW INFECTIONS
Malawi	10.6%	0.37%
Zambia	12.3%	0.66%
Zimbabwe	14.6%	0.45%



An HIV survey in Zimbabwe revealed that 86% of treated people are sticking with it.

PHOTO: ICAP AT COLUMBIA UNIVERSITY



Michael McGehee (right), a materials scientist at Stanford University in Palo Alto, California, examines a tandem perovskite cell.

MATERIALS SCIENCE

Perovskite solar cells gear up to go commercial

In tandem with silicon, low-cost photovoltaic crystals make electricity more efficiently

By **Robert F. Service**, in Boston

Cheap materials called perovskites are insinuating themselves into silicon solar cells—a first step toward ultimately usurping the reigning cell material. Last week, at a meeting here of the Materials Research Society (MRS), researchers announced that “tandem” cells, in which perovskites are layered on top of silicon and other photovoltaic materials, have achieved record-setting efficiencies at turning sunlight into electricity. Now, researchers are moving fast to surmount the lack of durability and other problems that have hindered the commercialization of perovskites.

“I think perovskites are going to make it to market,” says Aslihan Babayigit, a perovskite researcher at Hasselt University in Diepenbeek, Belgium. The progress has been “amazing,” adds David Cahen, a materials scientist at the Weizmann Institute of Science in Rehovot, Israel. “Even if all the problems are not solved, most look solvable.”

Known since the 1830s, perovskites are a class of crystals with a common 3D structure. It wasn’t until 2009 that researchers in Japan first realized their potential as a photovoltaic material. The first perovskite devices converted only 3.8% of light energy into electricity, far less than crystalline silicon, today’s dominant commercial technology, which tops out at 25.3% efficiency for the best research cells. (Commercial cells usually vary between 16%–20%.) But researchers tinkered with their perovskite recipes, and the efficiencies of the cells quickly skyrocketed. The record now stands at 22.1%, demonstrated earlier this year by researchers in South Korea.

Tandems, which combine cells optimized to capture different parts of the solar spectrum, can do even better. Silicon, for instance, preferentially absorbs reddish light, whereas perovskites tend to soak up blue and green photons. Slapping a perovskite cell on top of silicon need not cost much because the ingredients are dirt cheap, and the crys-

tals can be grown easily at low temperatures. Tandems also allow perovskites to piggyback on the entrenched silicon industry.

At the MRS meeting, Michael McGehee, a materials scientist at Stanford University in Palo Alto, California, reported that by growing a perovskite on silicon, he and his colleagues had created a tandem cell with an efficiency of 23.6%, better than the efficiencies of either component. Another group led by Christophe Ballif of the Federal Polytechnic School of Lausanne in Neuchâtel, Switzerland, reported in July that a silicon-perovskite tandem with a more complex architecture had reached an efficiency of 25.2%.

Tandems are likely to continue improving for years. Researchers have yet to build in all the finer tricks of the trade, such as optimizing the electricity-carrying layers in the cells and adding coatings that minimize surface reflections. Even with current perovskite materials, over the next couple years silicon-perovskite tandems could reach efficiencies of 30%, McGehee predicts. At that threshold, says Henry Snaith, a physicist at the University of Oxford in the United Kingdom, solar companies will start to add perovskites into their commercial panels, driving further improvements in the materials that could ultimately help them supplant silicon altogether.

At the MRS meeting, some researchers foreshadowed that day. Giles Eperon, a materials scientist at the University of Washington in Seattle, explained that when getting his Ph.D. at Oxford, he made a perovskite that strongly absorbs reddish light—the wavelengths that silicon has specialized in. Partnering with McGehee’s group, Eperon layered his red absorber on top of a more

Stronger together

By stacking perovskite solar cells in tandem with others, researchers are nearing the record efficiency of single crystal silicon, the industry’s commercial standard. Two-terminal (2T) devices layer the materials into a single cell; four-terminal (4T) devices stack together two electrically independent cells.

SOLAR CELL TYPE	RECORD EFFICIENCY (%)
Silicon (single crystal)	25.3
Perovskite-perovskite (2T)	17
Perovskite-perovskite (4T)	20.3
Silicon-perovskite (2T)	23.6
Silicon-perovskite (4T)	25.2

standard blue absorber, achieving an efficiency of 20.3% in a pure perovskite tandem. Although not yet as good as perovskite-silicon tandems, the perovskite components in the cells are still rapidly improving, whereas silicon has flatlined.

For all their gains in efficiency, perovskites have faced lingering problems. Water vapor, high temperatures, or even prolonged sun exposure can dissolve or degrade perovskites within hours. But at the MRS meeting, McGehee reported exceptional stability for new perovskite recipes that replace an organic component called methylammonium with formamidinium or the element cesium. When encapsulated to protect them from moisture, these cells showed no sign of degradation for 6 weeks, even when exposed to temperatures of 85°C and a relative humidity of 85%, a standard test of durability. “Panels that pass it usually will not fail due to heat and humidity over 25 years outside,” McGehee says.

Others are reporting improvements in manufacturing commercial-sized cells rather than the small, bespoke crystals used for setting records. Christopher Case, the chief technology officer for Oxford Photovoltaics (Oxford PV) in the United Kingdom, a perovskite solar cell company launched by Snaith, says the company has scaled up the postage stamp-sized research cells to ones that are 10 centimeters square and that have passed industry durability standards. Last month, the company acquired a former photovoltaic pilot facility in Germany. It is now gearing up to produce perovskite cells atop full-sized commercial silicon wafers, 15 centimeters on a side, Case says. Oxford PV also recently announced that they raised an additional £26 million (\$33 million) over the last 18 months from investors, and Case says the company has inked partnerships with several of the top 10 silicon solar cell producers to investigate adding perovskites to their cells. If all goes well, he says, the first pilot products could appear in 2018.

That leaves safety as the major outstanding roadblock to commercialization. The most efficient perovskites contain a highly soluble form of lead, a dangerous neurotoxin that could leach into homes, soil, or groundwater if the cells degrade. Babayigit says there are potential solutions, such as encapsulating the perovskite in protective shells or adding sulfides around the cell, which would bind and quarantine any lead that managed to escape. For now, she says, “it’s a heavily underresearched field that needs attention.” Given how quickly perovskites are moving to market, it’s a safe bet that someone will soon take on the project. ■

BIOMEDICINE

Carbon monoxide, the silent killer, may have met its match

Repurposed molecule saves rodents from gas poisoning

By Wudan Yan

On 26 January, Ling Wang and Qinzi Xu, two biomedical scientists at the University of Pittsburgh in Pennsylvania, placed a mouse under a chemical hood, anesthetized it, and hooked it up to monitors. Wang closed the hood and Xu turned on a switch to deliver 3% carbon monoxide (CO)—a concentration so high that it would kill most humans almost immediately—for 4.5 minutes. The mouse’s blood pressure dropped precipitously and its heart rate turned irregular. Then, through an intravenous tube, they delivered a molecule their lab had developed. Moments later, the animal’s blood pressure began to rise and it recovered. This was a first: There are no known antidotes for CO poisoning.

Given off by engines, heaters, and fireplaces, the tasteless, odorless gas sends more than 50,000 Americans to the emergency room—and kills approximately 500—every year. CO poisons in at least two ways. First, it binds tightly to the hemoglobin in blood and prevents it from delivering oxygen throughout the body. Second, it inhibits the process of respiration in mitochondria, cells’ powerhouses. About the best physicians can now offer in cases of poisoning is a treatment developed more than 50 years ago: high-pressure oxygen.

“People have attempted some biochemical tricks to free carbon monoxide from hemoglobin, but they don’t really work. That’s why we literally have a therapy that’s as old as oxygen,” says Lance Becker, a physician at the Hofstra Northwell School of Medicine in Manhasset, New York. “So the idea of finding something that might work better, faster, and stronger is very appealing.”

That something, described in this week’s issue of *Science Translational Medicine*, is neuroglobin—a protein typically found in the brain and retina that protects cells from injury by binding oxygen and nitric oxide—repurposed into a CO scavenger.

The Pittsburgh research team, led by critical care physician Mark Gladwin, was originally studying its function when they noticed that isolated neuroglobin molecules almost always had CO, a natural byproduct of hemoglobin breakdown, bound to them. “I thought this was bad news at the time, because we needed to get the CO off the neuroglobin in an extra experimental step,”

Gladwin said. But when a colleague asked in 2012 whether there was any antidote for CO poisoning, he realized that his lab might already have an answer.

In the mouse study, the group engineered a mutated version of neuroglobin that binds CO 500 times more tightly than it binds hemoglobin. The CO-laden molecules are excreted through the kidneys. When given within 5 minutes

of a lethal dose of CO, the neuroglobin saved 87% of mice, the group reports. “This agent is phenomenal: It can rip carbon monoxide right off the hemoglobin,” says Lindell Weaver, a doctor who treats patients with high-pressure oxygen at Intermountain Healthcare in Salt Lake City.

Weaver notes, however, that CO poisoning also activates a series of immunological pathways that cause lingering damage to the nervous and cardiovascular systems. “The long-term effects of carbon monoxide are complicated, so just removing [it] might not be enough,” he says. “But this agent could be life-saving if it’s administered immediately.”

Gladwin’s team now plans to further explore the efficacy and safety of the neuroglobin in rats, larger mammals, and, eventually, patients. One challenge will be making the neuroglobin scavenger in the amounts needed for use in the field and clinic. The U.S. Food and Drug Administration, Gladwin says, has already promised an expedited review of the treatment given that CO poisoning is a “serious unmet need.” ■

Wudan Yan is a freelance journalist based in Seattle, Washington.

SCIENTIFIC COMMUNITY

Curator resigns after sexual misconduct investigations

Long-running case sparks debate about collaboration

By Ann Gibbons

Paleoanthropologist Brian Richmond, who allegedly sexually assaulted a research assistant and harassed trainees in a field school, has resigned his prestigious position as curator of human origins at the American Museum of Natural History (AMNH) in New York City, the museum said this week. Richmond will continue to work off-site until 31 December, and will be paid 1 year of salary, as his contract, which included tenure, requires.

Museum spokesperson Anne Canty declined to say if Richmond resigned under

University of Illinois in Urbana-Champaign. Clancy co-led a high profile survey called SAFE, which reported numerous cases of sexual harassment at field sites (*Science*, 19 April 2013, p. 265). She and other anthropologists hope that the case marks a shift in how their field deals with harassment.

The formal complaint against Richmond was made by the research assistant. She alleged that he sexually assaulted her in his hotel room in Florence, Italy, in September, 2014, after sessions at a scientific meeting. Richmond has said the encounter was consensual. An initial investigation by the museum's human resources staff found that



The American Museum of Natural History investigated curator Brian Richmond for 2 years.

pressure, although he has been the subject of repeated investigations over the past 2 years for violating policies on sexual harassment. Earlier this year, Richmond wrote to *Science* that the museum asked him to resign in December 2015, but that he “had never assaulted anyone,” and that he had “sincerely apologized” to the assistant (*Science*, 12 February, p. 652). This week he told *Science* that the details of his departure are confidential and stressed that only one formal complaint had been lodged against him. “I plan to focus on my family and the next steps in my career,” he wrote in a statement, including “to publish the outstanding discoveries that my colleagues, former students, and I made.”

Richmond's case convulsed the field of paleoanthropology (*Science*, 29 April, p. 503), and reaction to the news of his resignation was swift. “Woo-hoo! This is a positive step in the direction of there being consequences for perpetrators,” said biological anthropologist Kathryn Clancy of the

Richmond “had violated the Museum's policy prohibiting inappropriate relationships between supervisors and their subordinates,” according to a memo obtained by *Science*. The research assistant was assigned a new supervisor, but she and Richmond both continued to work at the museum.

Unhappy with this outcome, the research assistant publicly shared her story at another meeting. This sparked paleoanthropologist Bernard Wood at George Washington University (GWU) in Washington, D.C., to explore Richmond's actions at that university, where Richmond worked until mid-2014, and at the Koobi Fora Field School in Kenya, which was jointly run by GWU. AMNH then did a second investigation, which uncovered allegations that Richmond had sexually harassed students at the field school. Richmond resigned from the field school but continued to work at the museum.

After Richmond refused to resign, the museum last December hired an outside

firm, T&M Protection Resources in New York City, to conduct a third investigation. The museum also asked Richmond to work offsite starting in January, according to the research assistant. The results of this third investigation, which concluded when Richmond resigned this week, have not been released. But Canty said the firm also helped the museum revise its sexual harassment policies and provide training for all employees, students and volunteers.

The research assistant, who remains employed by the museum, told *Science* the day after the resignation that she was “just glad it's over and that justice prevailed. The museum did the right thing.” Other museum employees echoed that sentiment, saying that the human origins program was without direction during the stressful investigations. The museum plans to eventually hire a new curator of human origins.

Although Richmond co-authored several high-profile papers last year and says he plans to continue publishing, researchers are fiercely divided over whether others should share authorship with him. Last April, at the annual meeting of the American Association of Physical Anthropologists in Atlanta, Clancy and others argued that researchers should stop all collaboration, including joint publication, with colleagues under investigation for sexual harassment or discrimination, or urge such colleagues to withdraw from joint papers. At least one young researcher mentored by Richmond says a journal editor reported recently that some researchers refused to review papers with Richmond's name on them.

But removing Richmond from publications after the work was done would be “plagiarism,” says paleoanthropologist David Strait of Washington University in St. Louis in Missouri, a long-time collaborator with Richmond. “I can't agree with removing someone from authorship on a paper that began in good faith before allegations of misconduct became known.”

There are no professional standards on how to proceed, notes paleoanthropologist Leslie Aiello of the Wenner-Gren Foundation for Anthropological Research in New York City, but she and journal editors agree that the priority should be to avoid penalizing junior scientists who need to publish their research.

The whole affair leaves Wood, who once mentored Richmond and later encouraged investigation of his actions, with an “overwhelming sense of sadness and some hope.” He regrets the harm done to women in science, and hopes the episode “will mark a watershed in all of our efforts to make the scientific workplace welcoming to all.” ■



Saudi geneticist Fowzan Alkuraya examines Muteb, a 6-year-old boy born with epilepsy and global developmental delay.

WHEN DNA AND CULTURE CLASH

Saudi Arabia is making a big push into human genomics, hoping to prevent inherited diseases

By Jocelyn Kaiser, in Riyadh

In a hospital conference room here in Saudi Arabia's capital, a lieutenant colonel in the Saudi army, dressed in fatigues and a black beret, stoically tells a story of genetic casualties. His and his wife's first child, born in 2004, seemed healthy at first, but at 6 months old the baby girl could not yet sit up and barely cried. Doctors in

France, where the family was living at the time, found no explanation. "We were sure that lack of oxygen" during delivery had caused brain damage, the father says.

Although their next baby, a boy, was healthy, a second girl born 5 years later had similar developmental delays. Meanwhile, the officer's sister had given birth to six children, two healthy but four with similar

medical problems: Each had crossed eyes and an IQ below 70, didn't talk, and didn't walk until about age 5.

Both the lieutenant colonel, who asked not to be identified, and his sister had married first cousins, who were also related. Suspicions that this close kinship played some role in their kids' problems led the two families to this clinic at King Faisal

Specialist Hospital and Research Centre (KFSHRC) and into the care of Fowzan Alkuraya, a young Saudi geneticist who had recently returned from the United States. Some months after the families gave him DNA samples, Alkuraya delivered the results: All four parents carried one copy of the exact same disease mutation, a change of a single DNA base in a gene called *ADAT3*. Although the mutation was harmless to the parents because each retained a working copy of the gene, their severely disabled children had inherited two faulty copies. As a result, their cells couldn't make an enzyme that helps translate DNA into proteins.

Alkuraya's news brought the families some measure of comfort, and hope. "It was a big relief for my wife, for me, for my sister, for everyone" to know what had gone wrong, the officer says. Hoping to break their bad genetic luck, he and his wife decided they would turn to in vitro fertilization (IVF) and use preimplantation genetic diagnosis to select embryos that inherited no *ADAT3* mutation. They now have 2-year-old twins, a boy and a girl. "And they are perfectly healthy," the father says.

The officer's family is one of hundreds that have come to Alkuraya, 39, who may be the country's leading genetics sleuth. His work is part of a boom in human genetics research in Saudi Arabia over the past decade, which has culminated in a Saudi version of a human genome project, called the Saudi Human Genome Program (SHGP). Largely because many Arabs marry cousins or other close relatives, the country, like others in the Middle East, has an increased rate of inherited genetic diseases—nearly double the rate in Europe and the United States and 10 times higher for certain disorders, according to some estimates (see map, p. 1221). As a result, the country has long drawn Western scientists eager to bag disease genes new to science. But Alkuraya and other geneticists here at KFSHRC are bringing such research home.

They are harnessing cheap, next-generation DNA sequencing to pin down mutations underlying unexplained diseases, cranking through more than 10,000 cases in the past 5 years. Although most of the solved cases involve known mutations, some have yielded novel disease genes—more than 200 from Alkuraya's group alone, including *ADAT3*. The output of the relatively small team rivals that of larger groups of disease gene hunters in the United States and Europe, colleagues say. "I am very impressed with what [Alkuraya] has achieved in Saudi Arabia," says Joris



Samel Al Samel and some of his children, three of whom have developmental problems. His eldest son, Mohammad (not pictured), is healthy, but after having a DNA test, learned that he is a carrier of the mutation that afflicted his siblings.

Veltman, a human geneticist at Radboud University Medical Center in Nijmegen, the Netherlands.

Alkuraya and his colleagues hope the growing catalog of disease mutations they have found will not only help individual families with inherited diseases have healthy babies, but lead to premarriage DNA tests for young people that could bring down the high rate of those diseases here. The broader sequencing effort could also have payoffs beyond the Middle East. The country's closely related population should make it easier to identify "healthy knockouts"—people who lack both copies of a specific gene yet remain healthy and even gain protection against disease, providing clues to new drugs. "If there's any place they should be discovered, it's here," Alkuraya says.

But first, Saudi geneticists will have to get past the worsening budget crisis here triggered by the global drop in oil prices. Funding is on hold for the next phase of the overall genome project, and even ongoing

research grants, including Alkuraya's, have been slashed this year. It's vital that his gene sleuthing and other genomics efforts in the country don't stall out, observers say. As human geneticist Daniel MacArthur of the Broad Institute in Cambridge, Massachusetts, notes, "There's no question the opportunities there are massive."

OUTSIDE THE RESEARCH WING of KFSHRC on the traffic-clogged streets here, women cannot mingle with unrelated men and must wear a loose black robe called an abaya. But in this surprisingly cosmopolitan space, women swap their abayas for lab coats and work side by side with male staff. Some take off their head scarves, but others retain their black face veils, known as niqabs, even in the lab.

Such adherence to tradition helps explain why about 40% or more of native Saudis—two-thirds of the country's 30 million people—still marry first cousins or other close relatives. The practice, once common in Europe, lives on in much



of the Middle East today, helping preserve wealth and tribal ties. But the downside of consanguineous marriage is a relatively high risk for recessive genetic diseases, which develop when both the maternal and paternal copy of a gene are faulty. If both parents carry the same recessive disease mutation, their children have a 25% chance of inheriting two copies and developing the disease; and in the large families still common in Saudi Arabia, the genetic dice are rolled repeatedly. By one estimate, 8% of babies in Saudi Arabia are born with a genetic or partly genetic disease, compared with 5% in most high-income countries.

Often the diseases have never been seen before. For decades, Middle Eastern clinicians puzzled by these cases have called in European or U.S. scientists, who collected DNA samples from the afflicted families and claimed lead authorship on papers describing new disease genes. After the draft human genome was unveiled in 2001, the country's homogeneous population—made up of about two dozen major tribes de-

scended from a small number of founders—also attracted broader genetics efforts. Brian Meyer, an Australian expat scientist who has long worked in Saudi Arabia and now chairs the KFSHRC genetics department, recalls a proposal from genome sequencing pioneer Craig Venter to launch a company modeled after Iceland's deCODE, which would have mined the DNA of Saudis for drug targets. The plan fizzled out because of local concerns about privacy and exporting genetic data for commercial purposes, however.

"The population wasn't ready," Meyer says. Saudi Arabia also declined to contribute DNA samples to HapMap, an international effort to map human genetic diversity that began in 2002. Middle Easterners are still virtually missing from human genome reference databases, a problem some Arab scientists are now trying to remedy (see sidebar, p. 1220).

In the late 1990s, however, the seeds of a Saudi genome effort began to take root. After finding that the mutations causing

cystic fibrosis in Saudis were different from those in Europeans, KFSHRC geneticists began to do their own disease gene hunting. Alkuraya soon joined the chase.

A star medical student from a small town in Saudi Arabia's north, Alkuraya says he realized that the nation's inherited diseases were a "major problem"—and an unparalleled research opportunity. After training in the United States in pediatrics and medical genetics, he completed a postdoc in developmental genetics at the Harvard University-affiliated Brigham and Women's Hospital in Boston and became first author on a 2006 paper in *Science* on a gene that controls palate formation.

Alkuraya could have found a U.S. faculty position and traveled to Saudi Arabia to collect disease cases, but he worried that "I would have felt like an opportunist." In 2007, he returned to launch his own research group at KFSHRC and nearby Alfaisal University. He's acutely aware of what he's missing compared with Boston: In Riyadh, he has no world-class experts from other disciplines down the hall with which to exchange ideas and faces long delays in getting reagents such as antibodies. To stay productive—he's published more than 270 papers since he got back—he juggles multiple projects. "You really need to anticipate everything ahead of time," he says.

In his gene hunt, Alkuraya takes advantage of a shortcut known as exome sequencing, which analyzes just the 1% of DNA in a genome that codes for proteins. Instead of scanning entire genomes for mutated genes, a disease hunter can just compare the exome of a sick child with one or two exomes of normal, healthy people, such as the child's parents—a process that takes weeks rather than years. In 2011, Alkuraya's team used that exome strategy for the first time to find a new disease gene: *DOCK6*, which causes limb malformations when mutated.

The team picked up its pace 3 years ago when Saudi Arabia announced plans for a 100,000-person genome project modeled after efforts in countries such as the United Kingdom and Iceland. Saudi leaders decided to focus a \$40 million pilot project on diagnosing patients with single-gene diseases who are recruited by physicians at Saudi research institutions. That proved to be a "wise decision," says Sultan Al-Sedairy, the project's principal investigator and executive director of KFSHRC.

The Saudi genome team uses two shortcuts to find the culprit mutations. In one, instead of sequencing a patient's full exome, the genome project analyzes only the genes most likely to be involved in the condition—genes already tied to facial mal-



In addition to having grip strength tested, participants in the Qatar Biobank may have DNA sequenced.

Qatar's genome effort slowly gears up

By **Jocelyn Kaiser**, in Doha

Like neighboring Saudi Arabia, the small, oil- and gas-rich country of Qatar has ambitious plans to sequence the DNA of many thousands of its citizens, hoping ultimately to provide them with better health care. A visit to this glittering seaside capital, where state-of-the-art biomedical research labs rise across town from futuristic skyscrapers, suggests Qatar has the financial resources to pull it off. But another requirement—policies and guidelines for accessing the DNA data—remains a work in progress and has hampered a pilot effort.

When the Qatar Genome Programme (QGP) was announced in late 2013, some researchers privately questioned the benefits of its stated goal: sequencing the complete genomes of all 300,000 native Qataris. But the project found solid footing by settling on a much smaller pilot project that will probe the population genetics of Arabs, who are missing from international DNA databases dominated by people of European and a few other ancestries. “We have different origins, different genomes, that will reflect on our diseases and our health challenges,” says virologist Asmaa Al-Thani, a member of the royal family who chairs the QGP Committee.

Earlier studies of Qatari genomes, by geneticists at Weill Cornell Medicine in New York City, which has a campus here, showed that the country's dozen tribes descended from three ancestral groups—Bedouins, Persians, and Africans—and carry many mutations not seen in other populations. Such information will aid the hunt for inherited disease

genes among Qataris and other Middle Easterners, by helping researchers find aberrant genes and avoid linking harmless mutations to an illness.

To add detail to the picture, QGP collaborators at the Sidra Medical and Research Center here have sequenced the full genomes of 3000 generally healthy citizens already being tracked as part of a long-term study called the Qatar Biobank. Local and expat researchers from Qatari institutions are now planning more than a dozen studies based on these initial DNA sequences, which were completed in June. A second round of at least 3000 genomes will come from Qataris with diseases.

But so far, no outside researchers have gotten their hands on the information, as QGP officials and scientists wrestle over data access issues. They include how to prevent the DNA sequences from being downloaded onto other computers or accessed from outside Qatar, and who should be liable if people's genetic or clinical information gets stolen.

Some say it's not surprising that Qatar, which is still building a scientific infrastructure, is running into these roadblocks. “A country that has never done anything like this suddenly faces the challenge of a global-level project,” says former U.S. National Institutes of Health cancer immunologist Francesco Marincola, who has been chief research officer at Sidra for the past 4 years.

Still, the scientific—and perhaps medical—payoff will be worth the struggle, says Khalid Fakhro, a Qatari geneticist who was part of the Weill Cornell effort and is now based at Sidra. “There is so much unappreciated diversity in this part of the world.” ■

formations for those with facial abnormalities, for example. The project assembled a team of some 90 geneticists, clinicians, and others, who developed 13 panels of known disease genes for conditions such as deafness, vision loss, heart disease, and metabolic disorders.

This “Mendeliome” approach, the SHGP reported in *Genome Biology* last year, diagnosed 43% of 2357 cases for about \$75 to \$150 a person within days. That success rate, from a cut-rate approach, impresses observers. (The team solved another 11% using costlier exome sequencing.) Although clinical geneticists in other countries have begun using gene panels before turning to exome sequencing, “people haven't systematically done it the way they have in Riyadh,” says geneticist James Lupski of Baylor College of Medicine in Houston, Texas. “I think we can learn things from them.”

If the Mendeliome strategy doesn't pinpoint the responsible mutation, the team can also try to take advantage of the second shortcut. When the child of a consanguineous union develops a recessive disease, the responsible mutation usually lies within a larger identical block of DNA inherited from both parents. Researchers can therefore ignore most of the child's exome and look for the mutation at fault by only probing these shared parental regions, which they find by scanning the DNA for known markers. “That gives us x-ray vision,” Alkuraya says. “You know just where to look.”

BEYOND THE PRACTICAL PAYOFF of diagnosing genetic diseases, the Saudi team is excited by the science it's generating. Among the more than 200 genes newly linked to human illness by Alkuraya's team is one called *DNASE1L3* that causes an inherited form of lupus and is being pursued as a drug target for the immune disorder. The group has found dozens of additional genes that cause intellectual disability. Other genes are among the first known to be fatal in early embryonic development. Identifying mutations behind such failed pregnancies is difficult because it requires DNA from the lost embryo, but Alkuraya has enrolled pregnant mothers with a history of miscarriage and collects a fetal tissue sample when they show signs of miscarriage again.

He acknowledges that some of his published connections between genes and a disease are preliminary—often a mutation has only been found in one family so far—and that he doesn't do much of the functional work needed to pin down what these genes do. “My philosophy is always to get the genes out” so that other geneti-

cists can build on them, Alkuraya says. The SHGP group soon plans to publish the full database of its genome data on more than 10,000 individuals.

Some of these data may also challenge previously reported gene-disease links. In a paper last month in *Genome Biology*, Alkuraya reports that hundreds of gene variants labeled as pathogenic in other databases are commonly found in Saudis without the relevant disease.

In the next phase of the SHGP, researchers want to study common disorders such as heart disease and diabetes—a rare inherited form of diabetes afflicts some Saudis—and personalize cancer therapies based on a person's DNA. Alkuraya also

lab has been unable to replace equipment for the past 2 years.

But Alkuraya says that for the moment, he's not too worried about his science. "I'm sitting on so much data. If I were to shut my lab down now, I could continue to write papers for the next 3 years."

WHILE THE GENOMICS RESEARCH SLOWS, what has been learned so far is starting to pay off for Saudi families. There is often little to be done for children who inherit a recessive disease, but genetic knowledge can save future children from a similar outcome. In addition to selecting IVF embryos without disease mutations, potential Saudi parents can turn to prenatal diagnosis if the wife is

ing were done instead, "the same sample could be used for thousands of diseases," Meyer says. He says that the SHGP's next phase includes a plan to begin using a custom, chiplike device, known as a genotyping array, to screen couples' DNA samples for the 2300 most common disease mutations in the Saudi population.

Earlier screening, perhaps in high school before a marriage is arranged or a couple falls in love, might be even more effective, Alkuraya says. "We can't change the culture, but just by screening and prevention we can help people," adds his colleague Dorota Monies, a Polish expat researcher who has lived in Riyadh for more than a decade and who runs the DNA sequencers for the genome project.

Such a compulsory national test for that many genetic diseases would be "unparalleled in scale," says Stephen Kingsmore, a geneticist at Rady Children's Hospital in San Diego, California. The country would also have to greatly expand its cadre of genetic counselors—it now has just nine. "If you have proper counseling in the clinic, then they understand and stop the marriage," says Ayman Alsulaiman, a genetic counselor at KFSHRC who consults for the Ministry of Health's current premarital screening program. "With no proper counseling, they don't listen."

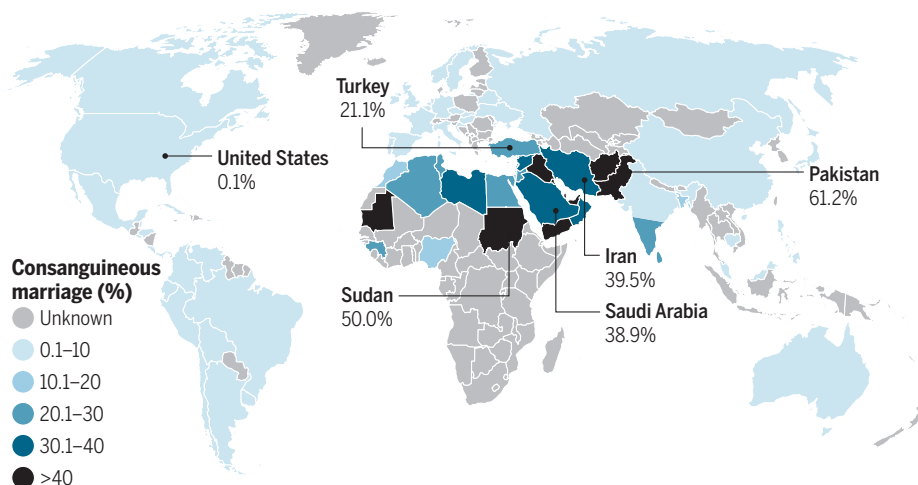
In the meantime, the Saudi team encourages parents who have a child with a genetic disorder to have their immediate and extended family tested, to reduce the risk in future births. This can be a sensitive matter, says Shatha Al Rasheed, a research genetic counselor with KACST. A mother may worry that her husband will take a second wife if he learns they both carry a disease gene. Or families may fear that their sons and daughters will never get married. But most families end up sharing the information: "I feel success stories are much more common than negative ones," Al Rasheed says.

Mohammad Al Samel, a 27-year-old medical student in his residency in Jeddah, Saudi Arabia, grew up with three siblings severely disabled by a mutation identified by Alkuraya's lab. After their diagnosis, Al Samel agreed to have his DNA tested and learned that he is a carrier of the same genetic flaw. His fiancée is also being tested, even though the two aren't related and she's unlikely to have the mutation. If she does, Al Samel says, they will still marry but consider "other solutions" such as IVF to avoid having a sick child.

"I didn't have brothers or sisters who were healthy enough to play with me, and we had to stay in the hospital for long times," he says. "I don't want my kids to have the same memories. You cannot imagine." ■

Marital problems

Thanks to a culture that encourages marriages between first cousins, Saudi Arabia has one of the higher rates of consanguinity in the world, which has elevated its incidence of many inherited genetic diseases.



aims to recruit up to 10,000 people who receive health care at KFSHRC in hopes of finding healthy knockouts, a potential boon to drug developers. A Texas woman lacking the gene *PCSK9*, for example, led to a new class of drugs that drastically reduces cholesterol by mimicking the effect of the gene knockout (*Science*, 16 May 2014, p. 687). The hunt should be easier in Saudi Arabia's consanguineous population. "I'm really optimistic that we're going to find something like" *PCSK9*, Alkuraya says.

All of this will depend on funding, however. The Saudi government has approved \$200 million in the budget of the country's main science agency, King Abdulaziz City for Science and Technology (KACST) here, to fund the next 5 years of the SHGP, including the purchase of the latest DNA sequencers, which Alkuraya hopes to use. But the money hasn't yet been released, and existing funds dwindled this year. Alkuraya's own grants have been cut by 50% and his

already pregnant. (Islamic law allows abortion to save the mother's life, and clerics in Saudi Arabia have ruled that this also applies before 120 days of gestation if she is likely to have a severely malformed fetus.)

Five years ago, about 80 families a year came to KFSHRC's prenatal diagnostics lab for genetic testing. Now, about 500 families annually seek testing, and as a result as many as 125 pregnancies have been terminated because the babies would have had severe or fatal diseases. "That's a huge economic burden on the country that we have eliminated," says geneticist Faiqa Imtiaz, who heads the hospital's prenatal testing lab.

Ultimately, the Saudi genome team would like to screen all 150,000 Saudi couples who plan to marry each year for disease genes. Each couple is now required by the Ministry of Health to have their blood biochemically analyzed for signs they are carriers of sickle cell anemia and thalassemia, two genetic diseases that are common here. If DNA test-



In addition to having grip strength tested, participants in the Qatar Biobank may have DNA sequenced.

Qatar's genome effort slowly gears up

By **Jocelyn Kaiser**, in Doha

Like neighboring Saudi Arabia, the small, oil- and gas-rich country of Qatar has ambitious plans to sequence the DNA of many thousands of its citizens, hoping ultimately to provide them with better health care. A visit to this glittering seaside capital, where state-of-the-art biomedical research labs rise across town from futuristic skyscrapers, suggests Qatar has the financial resources to pull it off. But another requirement—policies and guidelines for accessing the DNA data—remains a work in progress and has hampered a pilot effort.

When the Qatar Genome Programme (QGP) was announced in late 2013, some researchers privately questioned the benefits of its stated goal: sequencing the complete genomes of all 300,000 native Qataris. But the project found solid footing by settling on a much smaller pilot project that will probe the population genetics of Arabs, who are missing from international DNA databases dominated by people of European and a few other ancestries. “We have different origins, different genomes, that will reflect on our diseases and our health challenges,” says virologist Asmaa Al-Thani, a member of the royal family who chairs the QGP Committee.

Earlier studies of Qatari genomes, by geneticists at Weill Cornell Medicine in New York City, which has a campus here, showed that the country's dozen tribes descended from three ancestral groups—Bedouins, Persians, and Africans—and carry many mutations not seen in other populations. Such information will aid the hunt for inherited disease

genes among Qataris and other Middle Easterners, by helping researchers find aberrant genes and avoid linking harmless mutations to an illness.

To add detail to the picture, QGP collaborators at the Sidra Medical and Research Center here have sequenced the full genomes of 3000 generally healthy citizens already being tracked as part of a long-term study called the Qatar Biobank. Local and expat researchers from Qatari institutions are now planning more than a dozen studies based on these initial DNA sequences, which were completed in June. A second round of at least 3000 genomes will come from Qataris with diseases.

But so far, no outside researchers have gotten their hands on the information, as QGP officials and scientists wrestle over data access issues. They include how to prevent the DNA sequences from being downloaded onto other computers or accessed from outside Qatar, and who should be liable if people's genetic or clinical information gets stolen.

Some say it's not surprising that Qatar, which is still building a scientific infrastructure, is running into these roadblocks. “A country that has never done anything like this suddenly faces the challenge of a global-level project,” says former U.S. National Institutes of Health cancer immunologist Francesco Marincola, who has been chief research officer at Sidra for the past 4 years.

Still, the scientific—and perhaps medical—payoff will be worth the struggle, says Khalid Fakhro, a Qatari geneticist who was part of the Weill Cornell effort and is now based at Sidra. “There is so much unappreciated diversity in this part of the world.” ■

formations for those with facial abnormalities, for example. The project assembled a team of some 90 geneticists, clinicians, and others, who developed 13 panels of known disease genes for conditions such as deafness, vision loss, heart disease, and metabolic disorders.

This “Mendeliome” approach, the SHGP reported in *Genome Biology* last year, diagnosed 43% of 2357 cases for about \$75 to \$150 a person within days. That success rate, from a cut-rate approach, impresses observers. (The team solved another 11% using costlier exome sequencing.) Although clinical geneticists in other countries have begun using gene panels before turning to exome sequencing, “people haven't systematically done it the way they have in Riyadh,” says geneticist James Lupski of Baylor College of Medicine in Houston, Texas. “I think we can learn things from them.”

If the Mendeliome strategy doesn't pinpoint the responsible mutation, the team can also try to take advantage of the second shortcut. When the child of a consanguineous union develops a recessive disease, the responsible mutation usually lies within a larger identical block of DNA inherited from both parents. Researchers can therefore ignore most of the child's exome and look for the mutation at fault by only probing these shared parental regions, which they find by scanning the DNA for known markers. “That gives us x-ray vision,” Alkuraya says. “You know just where to look.”

BEYOND THE PRACTICAL PAYOFF of diagnosing genetic diseases, the Saudi team is excited by the science it's generating. Among the more than 200 genes newly linked to human illness by Alkuraya's team is one called *DNASE1L3* that causes an inherited form of lupus and is being pursued as a drug target for the immune disorder. The group has found dozens of additional genes that cause intellectual disability. Other genes are among the first known to be fatal in early embryonic development. Identifying mutations behind such failed pregnancies is difficult because it requires DNA from the lost embryo, but Alkuraya has enrolled pregnant mothers with a history of miscarriage and collects a fetal tissue sample when they show signs of miscarriage again.

He acknowledges that some of his published connections between genes and a disease are preliminary—often a mutation has only been found in one family so far—and that he doesn't do much of the functional work needed to pin down what these genes do. “My philosophy is always to get the genes out” so that other geneti-



PERSPECTIVES

ASTRONOMY

A fast radio boom

Bright distant radio bursts are excellent probes of the intergalactic medium

By **Victoria M. Kaspi**^{1,2}

The mystery of the fast radio bursts (FRBs) continues to deepen. First reported in 2007 (1), FRBs are a few-millisecond-duration flashes of radio waves that appear to be coming from far outside our Milky Way galaxy, possibly from cosmological distances. Astronomers estimate, from the nearly two dozen FRBs seen thus far, that these events occur several thousands of times per day across the whole sky, implying that the phenomenon is surprisingly common in the universe. Of those published, only one has been seen to repeat (2). Although there are presently more published theories on the physical nature of FRBs than there are published sources, the origin of FRBs is still a curious cosmic conundrum. On page 1249 of this issue, Ravi *et al.* (3) report on the brightest FRB yet detected, FRB 150807, and on its utility for placing constraints on properties of the intergalactic medium. Using the Parkes radio telescope in Australia, the team observed an “exceptionally intense” FRB, weighing in at a booming 120 janskys

[the unit of 1 jansky, a favorite of radio astronomers, honors American Karl Jansky (1905–1950), one of the fathers of the field, and amounts to 10^{-26} watts per square meter per hertz of bandwidth].

“Exceptionally intense” is a relative term; the power radiated by a single cell phone signal is over a billion times the power detected by Ravi *et al.* in FRB 150807. Nevertheless, by radio astronomy standards the event was remarkable, briefly outshining nearly every persistent radio source in the sky. Not only was it bright, FRB 150807 was also 80% linearly polarized, clearly announcing some strong preferential direction within the unknown emitter. Magnetic fields in interstellar space are known to scramble polarized signals by rotating the plane of polarization as the signal propagates, a radio frequency-dependent effect known as Faraday rotation. Yet the burst Ravi *et al.* detected, in spite of apparently arriving from far outside the Milky Way, shows only a tiny amount of Faraday rotation, enabling the authors to set one of the very few constraints on the magnetization of the intergalactic medium.

With so few FRBs detected, yet one being as bright as this newly detected event, it could well be that such bright FRBs are fairly common. Indeed, a recent analysis (4) of the statistics of the known FRBs, including

FRB 150807, concluded that the distribution of FRB brightnesses is skewed toward more intense bursts relative to what one would expect for a uniform population in a universe having Euclidean (that is, flat) geometry. If this is correct, it would mean that even small (and hence low-sensitivity) radio telescopes have a good chance of detecting FRBs, a possibility that suggests an opportunity for a quick and relatively inexpensive solution to help solve the FRB puzzle. On the other hand, another very recent similar statistical analysis of FRB brightnesses came to the opposite conclusion (5), namely that current data are fully consistent with a nonevolving FRB population in a Euclidean universe. Those authors, however, did not yet know about FRB 150807. Can a single boom really make such a difference?

A team at the California Institute of Technology (Caltech), which includes some of the Ravi *et al.* team, is gambling that the answer to that question is yes. They are currently building a low-cost FRB detection system out of commercial parts, using a handful of 5-m radio dishes. They are hoping to be fully online in the next few months and able to spot an FRB as bright as FRB 150807 every 2 to 3 weeks. Their instrument enables them to automatically localize on the sky to within a few arc seconds any detection, something that has yet to be done for any FRB because, thus far, all have been seen by telescopes with poor angular resolution. An unambiguous FRB localization could lead to the identification of a host galaxy, which could be a major clue to the origins of FRBs. Such a coup would be a scientific “bada-bing, bada-boom” for the Caltech team.

Meanwhile, our Canadian-led collaboration is taking no chances in the FRB game.

¹Department of Physics, McGill University, 3600 University Street, Montreal, QC H3A 2T8, Canada. ²McGill Space Institute, 3550 University Street, Montreal, QC H3A 2A7, Canada. Email: vkaspi@physics.mcgill.ca



The CHIME radio telescope consists of four fixed 20- by 100-m semicylinders. Along the axis of each cylinder, 256 dual-polarization feeds will be installed that will provide sensitivity in the range of 400 to 800 MHz. The full combination of all the feeds will be done by a correlator that will be far larger than any previously built and will provide over 200 square degrees of instantaneous sky coverage. This, together with a back-end burst searching instrument that will detect short radio signals in real time, will enable CHIME to detect many FRBs per day.

The CHIME (Canadian Hydrogen Intensity Mapping Experiment) radio telescope, currently being built in Penticton, British Columbia (see the photo), will be several orders more sensitive than the Caltech instrument and, depending on the true brightness distribution, could detect dozens of FRBs per day, even in the conventional, nonevolving Euclidean scenario. CHIME should thus blow the field open, enabling a wide variety of different FRB statistical analyses and a large number of localization opportunities. The CHIME FRB project is expected to come online in the latter half of 2017 and is eagerly awaited by the community.

Regardless of the brightness distribution, one thing is sure: FRBs are proving themselves to be truly useful probes on the extragalactic universe, hence providing a great boon—not just a boom—for all of astronomy. ■

REFERENCES

1. D.R. Lorimer *et al.*, *Science* **318**, 777 (2007).
2. L. Spitler *et al.*, *Nature* **531**, 202 (2016).
3. V. Ravi *et al.*, *Science* **354**, 1249 (2016).
4. H. K. Vedantham, V. Ravi, G. Hallinan, R. M. Shannon, <https://arxiv.org/abs/1606.06795> (2016).
5. N. Oppermann, L. Connor, U. Pen, *Mon. Not. R. Astron. Soc.* **461**, 984 (2016).

10.1126/science.aag1600

NEUROSCIENCE

Why does time seem to fly when we're having fun?

Increased dopamine may cause our internal clock to slow down, creating a sense of speeding time

By Patrick Simen¹ and Matthew Matell²

Animals use the neurotransmitter dopamine to encode the relationship between their responses and reward. Reinforcement learning theory (1) successfully explains the role of phasic bursts of dopamine in terms of future reward maximization. Yet, dopamine clearly plays other roles in shaping behavior that have no obvious relationship to reinforcement learning, including modulating the rate at which our subjective sense of time grows in real time. On page 1273 of this issue, Soares *et al.* (2) closely examine the role of dopamine in mice performing a task in which they keep track of the time between two events and make decisions about this temporal duration. The results suggest the need to reassess the leading theory of dopamine function in timing—the dopamine clock hypothesis (3). They may also help explain empirical phenomena that challenge the reinforcement learning account of dopamine function.

Reinforcement learning theory posits that reward prediction errors inform animals about which behaviors to engage in so as to maximize future reward. Time is the key factor in the experiments that have linked reinforcement learning to dopamine (4). These experiments demonstrate that behavior is shaped by bursts of activity (“phasic activity”) in midbrain dopamine-secreting neurons. When a reward occurs at an unexpected time, a positive reward prediction error is generated (increased dopamine release signals that “things are better than expected”). Consequently, communication from cortical neurons to neurons in the striatum is altered to change behavior in ways that maximize reward. Conversely, a negative reward prediction error signaled by a decrease in dopamine release occurs when a reward is not provided when expected. In addition, if delivery of a reward reliably occurs at the predicted time, it produces no burst of dopamine release at that moment,

but instead begins to produce a phasic dopamine signal in response to the earliest reward-predicting cue. Thus, future choices can be made so as to obtain the cue, and thereafter the reward. Eventually this process yields a temporally extended chain of cues and behaviors terminating in reward. However, time itself has typically been of less interest to reinforcement learning-dopamine researchers than the mechanisms that link these elements into chains of expected sensory inputs and planned motor outputs.

Yet, dopamine plays a key role in interval timing. The dopamine clock hypothesis holds that increased dopamine release speeds up an animal's subjective sense of time—its internal clock. For example, rats treated with amphetamine, which enhances dopamine release, respond earlier than when they are tested without the drug. Curiously, a simple prediction of the dopamine clock hypothesis would seem to be that time doesn't fly, but rather crawls, when you're having fun. Unexpectedly pleasurable events boost dopamine release, which should cause your internal clock to run faster. Your subjective sense of time in that case grows faster than time itself, so that short intervals seem longer than they are. The dopamine clock hypothesis accounts for this counterintuitive prediction by an additional assumption about attention: When things are good, attention to time is reduced, such that intervals seem shorter than they are (5).

To clarify the role of dopamine in interval timing, Soares *et al.* investigated midbrain dopamine neuron activity in the substantia nigra pars compacta (SNc) of mice performing a timing task. They presented mice with two brief tones, and trained them to classify the interval between the tones as shorter or longer than a standard criterion. They then observed calcium influx into dopaminergic SNc neurons, which signals activity. Consistent with standard reinforcement learning theory, the authors observed bursts of activity in dopamine-synthesizing neurons that were locked to the second tone, reflecting the probability of an upcoming reward. This probability was greatest when the in-

¹Department of Neuroscience, Oberlin College, Oberlin, OH, USA. ²Department of Psychology, Villanova University, Villanova, PA, USA. Email: psimen@oberlin.edu



The CHIME radio telescope consists of four fixed 20- by 100-m semicylinders. Along the axis of each cylinder, 256 dual-polarization feeds will be installed that will provide sensitivity in the range of 400 to 800 MHz. The full combination of all the feeds will be done by a correlator that will be far larger than any previously built and will provide over 200 square degrees of instantaneous sky coverage. This, together with a back-end burst searching instrument that will detect short radio signals in real time, will enable CHIME to detect many FRBs per day.

The CHIME (Canadian Hydrogen Intensity Mapping Experiment) radio telescope, currently being built in Penticton, British Columbia (see the photo), will be several orders more sensitive than the Caltech instrument and, depending on the true brightness distribution, could detect dozens of FRBs per day, even in the conventional, nonevolving Euclidean scenario. CHIME should thus blow the field open, enabling a wide variety of different FRB statistical analyses and a large number of localization opportunities. The CHIME FRB project is expected to come online in the latter half of 2017 and is eagerly awaited by the community.

Regardless of the brightness distribution, one thing is sure: FRBs are proving themselves to be truly useful probes on the extragalactic universe, hence providing a great boon—not just a boom—for all of astronomy. ■

REFERENCES

1. D.R. Lorimer *et al.*, *Science* **318**, 777 (2007).
2. L. Spitler *et al.*, *Nature* **531**, 202 (2016).
3. V. Ravi *et al.*, *Science* **354**, 1249 (2016).
4. H. K. Vedantham, V. Ravi, G. Hallinan, R. M. Shannon, <https://arxiv.org/abs/1606.06795> (2016).
5. N. Oppermann, L. Connor, U. Pen, *Mon. Not. R. Astron. Soc.* **461**, 984 (2016).

10.1126/science.aag1600

NEUROSCIENCE

Why does time seem to fly when we're having fun?

Increased dopamine may cause our internal clock to slow down, creating a sense of speeding time

By Patrick Simen¹ and Matthew Matell²

Animals use the neurotransmitter dopamine to encode the relationship between their responses and reward. Reinforcement learning theory (1) successfully explains the role of phasic bursts of dopamine in terms of future reward maximization. Yet, dopamine clearly plays other roles in shaping behavior that have no obvious relationship to reinforcement learning, including modulating the rate at which our subjective sense of time grows in real time. On page 1273 of this issue, Soares *et al.* (2) closely examine the role of dopamine in mice performing a task in which they keep track of the time between two events and make decisions about this temporal duration. The results suggest the need to reassess the leading theory of dopamine function in timing—the dopamine clock hypothesis (3). They may also help explain empirical phenomena that challenge the reinforcement learning account of dopamine function.

Reinforcement learning theory posits that reward prediction errors inform animals about which behaviors to engage in so as to maximize future reward. Time is the key factor in the experiments that have linked reinforcement learning to dopamine (4). These experiments demonstrate that behavior is shaped by bursts of activity (“phasic activity”) in midbrain dopamine-secreting neurons. When a reward occurs at an unexpected time, a positive reward prediction error is generated (increased dopamine release signals that “things are better than expected”). Consequently, communication from cortical neurons to neurons in the striatum is altered to change behavior in ways that maximize reward. Conversely, a negative reward prediction error signaled by a decrease in dopamine release occurs when a reward is not provided when expected. In addition, if delivery of a reward reliably occurs at the predicted time, it produces no burst of dopamine release at that moment,

but instead begins to produce a phasic dopamine signal in response to the earliest reward-predicting cue. Thus, future choices can be made so as to obtain the cue, and thereafter the reward. Eventually this process yields a temporally extended chain of cues and behaviors terminating in reward. However, time itself has typically been of less interest to reinforcement learning-dopamine researchers than the mechanisms that link these elements into chains of expected sensory inputs and planned motor outputs.

Yet, dopamine plays a key role in interval timing. The dopamine clock hypothesis holds that increased dopamine release speeds up an animal's subjective sense of time—its internal clock. For example, rats treated with amphetamine, which enhances dopamine release, respond earlier than when they are tested without the drug. Curiously, a simple prediction of the dopamine clock hypothesis would seem to be that time doesn't fly, but rather crawls, when you're having fun. Unexpectedly pleasurable events boost dopamine release, which should cause your internal clock to run faster. Your subjective sense of time in that case grows faster than time itself, so that short intervals seem longer than they are. The dopamine clock hypothesis accounts for this counterintuitive prediction by an additional assumption about attention: When things are good, attention to time is reduced, such that intervals seem shorter than they are (5).

To clarify the role of dopamine in interval timing, Soares *et al.* investigated midbrain dopamine neuron activity in the substantia nigra pars compacta (SNc) of mice performing a timing task. They presented mice with two brief tones, and trained them to classify the interval between the tones as shorter or longer than a standard criterion. They then observed calcium influx into dopaminergic SNc neurons, which signals activity. Consistent with standard reinforcement learning theory, the authors observed bursts of activity in dopamine-synthesizing neurons that were locked to the second tone, reflecting the probability of an upcoming reward. This probability was greatest when the in-

¹Department of Neuroscience, Oberlin College, Oberlin, OH, USA. ²Department of Psychology, Villanova University, Villanova, PA, USA. Email: psimen@oberlin.edu

tertone duration was much shorter or much longer than the criterion—i.e., when the duration could be easily discriminated from the intermediate, criterion duration.

Reward prediction errors are only prediction errors to the extent that they are surprising, however. An animal's surprise about the arrival time of the second tone ought, therefore, to modulate the reward prediction error, and it did. The intertone interval was picked from a set of six durations, so that a mouse's surprise about the second tone should become smaller as the intertone interval becomes longer—a longer wait for the second tone makes its imminent arrival more likely. The animal's surprise ought therefore to decrease to 0 at the maximum intertone duration. Soares *et al.*



The dopamine clock hypothesis of how we sense the passing of time is challenged by the findings of Soares *et al.*

demonstrate that dopamine bursts locked to the second tone were modulated by both reward probability and temporal surprise. Further, they found ramping dopaminergic neuron activity during the intertone interval that declined in the same way as the surprise function.

A faster subjective sense of time should produce a more rapidly declining surprise function, by definition. However, this seems to conflict with the dopamine clock hypothesis: Faster clocks should lead to more rapid declines in dopamine, but declines in dopamine should slow down the clock. This apparent inconsistency may rest on a lack of knowledge about how (6–8) or where (9–11) time is represented in the brain. Does a subjective time estimate computed outside the SNc drive the surprise function (12)? Or does the midbrain dopamine surprise signal drive a timer outside the SNc, as the dopamine clock hypothesis suggests? Soares *et al.* observed that lower intertone dopaminergic neuron activity correlated with a faster clock, not a slower clock, in contrast to the predictions of the

dopamine-timing hypothesis. Purely observational methods cannot establish causality, so the authors also used optogenetic methods that allow precise timing of perturbations to manipulate dopamine neuron activity on a subset of timing trials. Their results were unambiguous: Dopaminergic neuron activity did indeed appear to modulate internal clock speed, supporting a causal role for dopamine in regulating the subjective time sense. However, rather than speeding up the internal clock, increased dopaminergic neuron activity appeared to slow it down.

How can these results be reconciled with the large body of data on dopamine's role in subjective time estimation? One possibility is that, in contrast to the spatially and cell type-specific targeting of Soares *et al.*, systemic dopamine manipulation alters cortical timing processes (13) in a different direction and to a greater degree than the SNc-striatum effects.

Although phasic dopamine release seems to fit the reinforcement learning story, tonic dopamine release seems to do something rather different than encoding a reward prediction error. Instead, it seems to control overall response vigor or motivation (14). These findings can be accommodated within a theory in which tonic and phasic dopamine represent different kinds of information. Yet findings of “quasi-tonic” ramping signals within individual trials of nontiming tasks (15) pose a challenge even to this compromise theory. Soares *et al.* similarly see “quasi-tonic” surprise signals that challenge the dopamine clock hypothesis. These results suggest that upward- and downward-ramping dopamine signals may prove essential to unifying the reinforcement learning and interval-timing literatures, resolving their internal inconsistencies, and clarifying dopamine's true role in shaping behavior. ■

REFERENCES

1. P.R. Montague *et al.*, *J. Neurosci.* **16**, 1936 (1996).
2. S. Soares *et al.*, *Science* **354**, 1273 (2016).
3. W.H. Meck, *J. Exp. Psychol. Anim. Behav. Process.* **9**, 171 (1983).
4. J.R. Hollerman, W. Schultz, *Nat. Neurosci.* **1**, 304 (1998).
5. J.I. Lake, W.H. Meck, *Neuropsychologia* **51**, 284 (2013).
6. R. Laje, D. V. Buonomano, *Nat. Neurosci.* **16**, 925 (2013).
7. M. Matell, W.H. Meck, *Cogn. Brain Res.* **21**, 139 (2004).
8. P. Simen *et al.*, *Timing Time Percept.* **1**, 159 (2013).
9. A.A. Chubykin *et al.*, *Neuron* **77**, 723 (2013).
10. M. Wiener *et al.*, *NeuroImage* **49**, 1728 (2010).
11. M. Jazayeri, M.N. Shadlen, *Curr. Biol.* **25**, 2599 (2015).
12. Y.K. Takahashi *et al.*, *Neuron* **91**, 182 (2016).
13. K.L. Parker *et al.*, *J. Neurosci.* **34**, 16774 (2014).
14. Y. Niv *et al.*, *Psychopharmacology (Berl.)* **191**, 507 (2007).
15. M.W. Howe *et al.*, *Nature* **500**, 575 (2013).

10.1126/science.aal4021

EVOLUTION

Swimming in polluted waters

Genomic data provide insights into the molecular basis for pollution tolerance of Atlantic killifish

By Michael Tobler and Zachary W. Cumber

Human activities alter ecosystems around the planet, often rendering environmental conditions unfavorable for plant and animal survival. In the salt marshes along North America's Atlantic coast, the influx of industrial waste has caused chemical pollutants to accumulate at lethal levels, causing the disappearance of many species from affected sites. Yet, multiple populations of the Atlantic killifish (*Fundulus heteroclitus*) have adapted to cope with levels of pollution orders of magnitude higher than those that members of the same species from unaffected habitats can tolerate. On page 1305 of this issue, Reid *et al.* (1) provide strong evidence that adaptation has occurred rapidly and through similar genetic changes in multiple populations of killifish that have independently colonized polluted habitats.

Large population sizes and high levels of genetic diversity help to explain why killifish can rapidly adapt to anthropogenic pollution. Standing genetic variation facilitated rapid adaptation to toxic environments by recruiting existing, beneficial genetic variants, avoiding potential time lags that could occur if evolutionary responses were dependent on de novo beneficial mutations (2). Consequently, abundant species with high levels of genetic diversity may have the greatest ability to adapt to anthropogenic environmental change, whereas those lacking a standing stock of potentially beneficial mutations may be at risk of disappearing before evolution has a chance of rescuing them through adaptation.

In their study, Reid *et al.* compared whole-genome sequences from multiple pairs of tolerant and nontolerant populations. This

Division of Biology, Kansas State University, 116 Ackert Hall, Manhattan, KS 66506, USA. Email: tobler@ksu.edu

tertone duration was much shorter or much longer than the criterion—i.e., when the duration could be easily discriminated from the intermediate, criterion duration.

Reward prediction errors are only prediction errors to the extent that they are surprising, however. An animal's surprise about the arrival time of the second tone ought, therefore, to modulate the reward prediction error, and it did. The intertone interval was picked from a set of six durations, so that a mouse's surprise about the second tone should become smaller as the intertone interval becomes longer—a longer wait for the second tone makes its imminent arrival more likely. The animal's surprise ought therefore to decrease to 0 at the maximum intertone duration. Soares *et al.*



The dopamine clock hypothesis of how we sense the passing of time is challenged by the findings of Soares *et al.*

demonstrate that dopamine bursts locked to the second tone were modulated by both reward probability and temporal surprise. Further, they found ramping dopaminergic neuron activity during the intertone interval that declined in the same way as the surprise function.

A faster subjective sense of time should produce a more rapidly declining surprise function, by definition. However, this seems to conflict with the dopamine clock hypothesis: Faster clocks should lead to more rapid declines in dopamine, but declines in dopamine should slow down the clock. This apparent inconsistency may rest on a lack of knowledge about how (6–8) or where (9–11) time is represented in the brain. Does a subjective time estimate computed outside the SNc drive the surprise function (12)? Or does the midbrain dopamine surprise signal drive a timer outside the SNc, as the dopamine clock hypothesis suggests? Soares *et al.* observed that lower intertone dopaminergic neuron activity correlated with a faster clock, not a slower clock, in contrast to the predictions of the

dopamine-timing hypothesis. Purely observational methods cannot establish causality, so the authors also used optogenetic methods that allow precise timing of perturbations to manipulate dopamine neuron activity on a subset of timing trials. Their results were unambiguous: Dopaminergic neuron activity did indeed appear to modulate internal clock speed, supporting a causal role for dopamine in regulating the subjective time sense. However, rather than speeding up the internal clock, increased dopaminergic neuron activity appeared to slow it down.

How can these results be reconciled with the large body of data on dopamine's role in subjective time estimation? One possibility is that, in contrast to the spatially and cell type-specific targeting of Soares *et al.*, systemic dopamine manipulation alters cortical timing processes (13) in a different direction and to a greater degree than the SNc-striatum effects.

Although phasic dopamine release seems to fit the reinforcement learning story, tonic dopamine release seems to do something rather different than encoding a reward prediction error. Instead, it seems to control overall response vigor or motivation (14). These findings can be accommodated within a theory in which tonic and phasic dopamine represent different kinds of information. Yet findings of “quasi-tonic” ramping signals within individual trials of nontiming tasks (15) pose a challenge even to this compromise theory. Soares *et al.* similarly see “quasi-tonic” surprise signals that challenge the dopamine clock hypothesis. These results suggest that upward- and downward-ramping dopamine signals may prove essential to unifying the reinforcement learning and interval-timing literatures, resolving their internal inconsistencies, and clarifying dopamine's true role in shaping behavior. ■

REFERENCES

1. P.R. Montague *et al.*, *J. Neurosci.* **16**, 1936 (1996).
2. S. Soares *et al.*, *Science* **354**, 1273 (2016).
3. W.H. Meck, *J. Exp. Psychol. Anim. Behav. Process.* **9**, 171 (1983).
4. J.R. Hollerman, W. Schultz, *Nat. Neurosci.* **1**, 304 (1998).
5. J.I. Lake, W.H. Meck, *Neuropsychologia* **51**, 284 (2013).
6. R. Laje, D. V. Buonomano, *Nat. Neurosci.* **16**, 925 (2013).
7. M. Matell, W.H. Meck, *Cogn. Brain Res.* **21**, 139 (2004).
8. P. Simen *et al.*, *Timing Time Percept.* **1**, 159 (2013).
9. A.A. Chubykin *et al.*, *Neuron* **77**, 723 (2013).
10. M. Wiener *et al.*, *NeuroImage* **49**, 1728 (2010).
11. M. Jazayeri, M.N. Shadlen, *Curr. Biol.* **25**, 2599 (2015).
12. Y.K. Takahashi *et al.*, *Neuron* **91**, 182 (2016).
13. K.L. Parker *et al.*, *J. Neurosci.* **34**, 16774 (2014).
14. Y. Niv *et al.*, *Psychopharmacology (Berl.)* **191**, 507 (2007).
15. M.W. Howe *et al.*, *Nature* **500**, 575 (2013).

EVOLUTION

Swimming in polluted waters

Genomic data provide insights into the molecular basis for pollution tolerance of Atlantic killifish

By Michael Tobler and Zachary W. Cumber

Human activities alter ecosystems around the planet, often rendering environmental conditions unfavorable for plant and animal survival. In the salt marshes along North America's Atlantic coast, the influx of industrial waste has caused chemical pollutants to accumulate at lethal levels, causing the disappearance of many species from affected sites. Yet, multiple populations of the Atlantic killifish (*Fundulus heteroclitus*) have adapted to cope with levels of pollution orders of magnitude higher than those that members of the same species from unaffected habitats can tolerate. On page 1305 of this issue, Reid *et al.* (1) provide strong evidence that adaptation has occurred rapidly and through similar genetic changes in multiple populations of killifish that have independently colonized polluted habitats.

Large population sizes and high levels of genetic diversity help to explain why killifish can rapidly adapt to anthropogenic pollution. Standing genetic variation facilitated rapid adaptation to toxic environments by recruiting existing, beneficial genetic variants, avoiding potential time lags that could occur if evolutionary responses were dependent on de novo beneficial mutations (2). Consequently, abundant species with high levels of genetic diversity may have the greatest ability to adapt to anthropogenic environmental change, whereas those lacking a standing stock of potentially beneficial mutations may be at risk of disappearing before evolution has a chance of rescuing them through adaptation.

In their study, Reid *et al.* compared whole-genome sequences from multiple pairs of tolerant and nontolerant populations. This

Division of Biology, Kansas State University, 116 Ackert Hall, Manhattan, KS 66506, USA. Email: tobler@ksu.edu

10.1126/science.aal4021

approach provides insights into whether organisms evolve similar or unique adaptations in response to the same environmental challenges. Given high levels of standing genetic variation across the genome, there may be multiple ways for killifish populations to adapt to environmental pollution. However, the authors show that, in all populations, selection acted on variants in genes associated with the aryl hydrocarbon receptor (AHR) signaling pathway. This pathway is well known for its role in responding to pollutants, and its components directly interact with the aromatic hydrocarbon pollutants found in affected killifish habitats.

Repeated loss-of-function mutations in components of the AHR signaling pathway prevent unfavorable interactions between AHR and pollutants, facilitating normal embryonic development in tolerant populations. Consequently, adaptation to pollutants in different killifish populations appears to involve modification of similar genomic regions (see the figure). Such convergent evolution indicates that selection from pollutants can lead to repeatable and predictable evolutionary outcomes (3). Consistent modification of AHR signaling

may in fact be the only tangible way by which the fish can mitigate the adverse consequences of exposure to pollution. Predictability may thus be particularly high if constraints limit the number of evolutionary solutions to a shared problem (4). Such limitations can arise when selection is mediated by stressors that have specific biochemical targets and physiological consequences. Convergent molecular modi-

“...abundant species with high levels of genetic diversity may have the greatest ability to adapt to anthropogenic environmental change...”

fications have been documented in other systems exposed to naturally occurring physiochemical stressors (5–7).

Mutations in components of the AHR signaling pathway protect fish from the toxic effects of pollutants, but they also have adverse effects on other physiological processes regu-

lated by this pathway. Reid *et al.* document compensatory mutations that may mitigate loss of function in AHR signaling. The consequences of adaptive modification of toxicity targets may thus percolate through the genome, leading to coordinated evolution in multicomponent pathways and resulting in complex genomic changes (8). Despite widespread convergence in the AHR pathway, some genetic modifications were unique to specific population pairs, perhaps reflecting differences in the stressors experienced by the populations under study (see the figure).

The patterns of genome evolution in killifish provide insight into the molecular basis of adaptation to anthropogenic pollution and rapid, contemporary evolution. The study suggests that evolution may be predictable at the molecular level, at least when populations are adapting to similar physiochemical stressors with specific targets of selection. However, it also highlights potential limits to our predictive power. Knowledge of the physiological consequences of specific selective forces may enable us to predict in which genomic regions changes will occur, but not the specific modifications within those regions, because alternative genetic variants occur at the same loci of different tolerant killifish populations. Studies in other systems have shown that alternative genetic changes in the same genomic regions can have equivalent functional consequences (9).

Future studies should test the robustness of inferences from studies on single species and investigate whether such findings are applicable at broader phylogenetic scales. Extreme environments with clearly defined and replicated selective regimes—whether created by human effects or natural physiochemical stressors—provide unique opportunities to explore the predictability of evolutionary change, enabling hypothesis-driven tests of organismal responses at all levels of biological organization (10). It is only through examination of the molecular underpinnings of adaptation to specific sources of selection in diverse phylogenetic and ecological contexts that we can develop a predictive framework for evolutionary change. ■

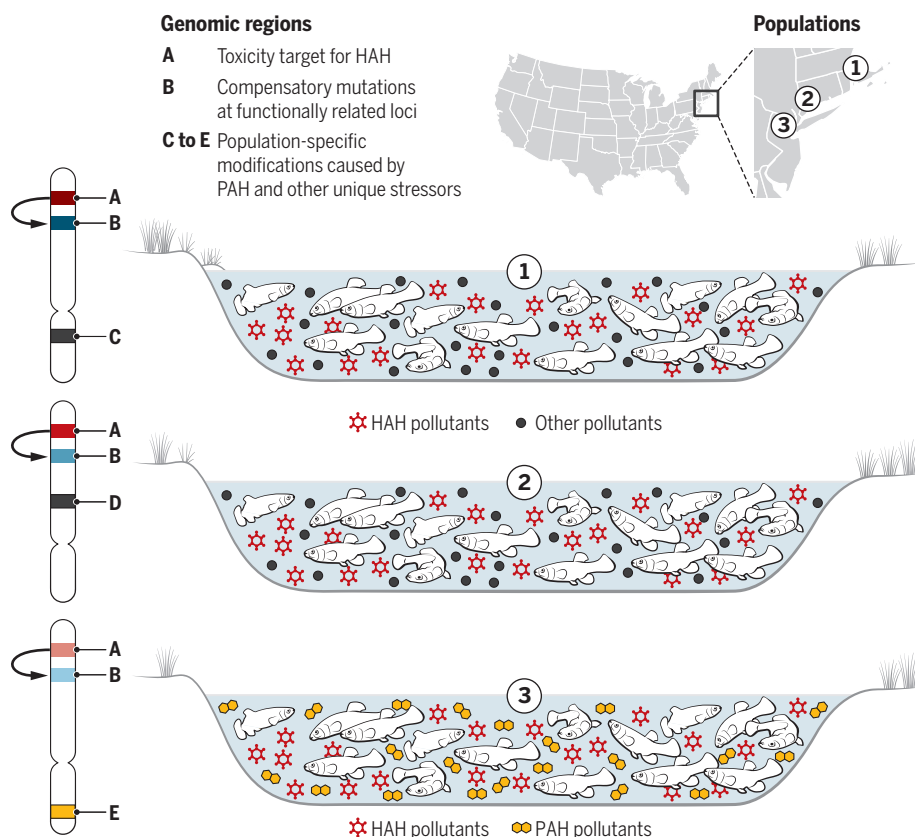
REFERENCES

1. N. M. Reid *et al.*, *Science* **354**, 1305 (2016).
2. R. D. Barrett, D. Schluter, *Trends Ecol. Evol.* **23**, 38 (2008).
3. D. L. Stern, V. Orgogozo, *Science* **323**, 746 (2009).
4. J. B. Losos, *Evolution* **65**, 1827 (2011).
5. J. L. Kelley *et al.*, *Mol. Biol. Evol.* **33**, 1419 (2016).
6. S. Dobler, S. Dalla, V. Wagschal, A. A. Agrawal, *Proc. Natl. Acad. Sci. U.S.A.* **109**, 13040 (2012).
7. R. D. Tarvin, J. C. Santos, L. A. O'Connell, H. H. Zakon, D. C. Cannatella, *Mol. Biol. Evol.* **33**, 1068 (2016).
8. D. Juan, F. Pazos, A. Valencia, *FEBS Lett.* **582**, 1225 (2008).
9. C. Natarajan *et al.*, *Science* **354**, 336 (2016).
10. M. Tobler, R. Riesch, M. Plath, in *Extremophile Fishes: Ecology, Evolution, and Physiology of Teleosts in Extreme Environments*, R. Riesch, M. Tobler, M. Plath, Eds. (Springer, Heidelberg, Germany, 2015), pp. 279–296.

10.1126/science.aal3211

Rapid adaptation of pollution tolerance in killifish

Multiple genomic regions are involved in adapting to environmental pollution during rapid evolution. PAH, polycyclic aromatic hydrocarbons; HAH, halogenated aromatic hydrocarbons.





NEUROSCIENCE

Encoding vocal culture

Neuronal encoding of birdsong promotes learning and species specificity

By Ofer Tchernichovski and Dina Lipkind

How does an inexperienced young animal acquire proper communication skills that will serve it well as an adult in a complex social environment? Juvenile songbirds acquire their vocal repertoire by imitating songs from adults. But song imitation per se is not the ultimate goal of their vocal development (1). Birdsong may carry information about species identity, group identity (local culture), individual identity, and—perhaps most important—about a bird's qualities as a potential mate (2, 3). There is some tension between these developmental goals: Because birds can imitate songs very accurately, local song convergence could compromise individual identity. Similarly, the accumulation of geographical drifts in song structure could potentially compromise the species-specific “signature” of the song. On pages 1278 and 1282 of this issue, Gadagkar *et al.* (4) and Araki *et al.* (5), respectively, discover neuronal coding of singing performance error and

of species song identity. Together, their findings reveal an elegant natural solution that alleviates the tension between cultural transmission and retaining a species-specific “signature” in songs over generations.

Gadagkar *et al.* identified an important component of a circuit that carries out vocal imitation: The authors recorded from dopaminergic neurons in the midbrain ventral tegmental area (VTA) that project into a basal ganglia song-learning nucleus called Area X in adult zebra finches, while they were singing. Using real-time song-analysis software, they targeted specific song syllables and produced auditory interference, designed to trick the bird into believing that it produced a distorted syllable. The authors found that the dopaminergic signal from VTA to Area X encodes singing performance error. Interestingly, the error signal was not absolute, but highly sensitive to the statistics of previous singing performance, indicating continuous dopaminergic monitoring of motor performance in reference to an internally generated goal. This dopaminergic error signal for evaluating singing behaviors in adult birds could plausibly account also for the ability of juveniles to precisely imitate the song of

Zebra finches learn to sing from each other, but their songs retain a “signature” of their species identity.

their tutor. But what mechanism accounts for protecting the species-specific song signature from random drifts associated with cultural transmission through imitation? The Araki *et al.* study offers a possible solution.

Araki *et al.* monitored vocal learning in juvenile zebra finches that were raised by foster Bengalese finch parents. The authors found that birds imitated the foreign-species song syllables, but adjusted the durations of intersyllabic gaps toward their own species-specific rhythm signature—which they had never heard. This difference in imitation fidelity was reflected in two distinct types of neurons in the birds' auditory cortex. One type encodes the morphology of song syllables—that is, it encodes acoustic features such as pitch and timbre. The other type encodes the rhythm of the song, independently of its acoustic detail, like a barcode. Interestingly, this latter type of neuron responded preferentially to species-typical gap durations, suggesting a possible mechanism for biasing imitation toward an innate species-typical song rhythm “barcode.”

Together, the findings of Gadagkar *et al.* and Araki *et al.* may provide a natural solution to alleviating the tension between cultural transmission and retaining a species-specific signature in songs over generations. The two neuronal populations in the auditory cortex transform a song input into two orthogonal channels: a syllable morphology channel and a rhythm (barcode)

Department of Psychology, Hunter College, The City University of New York, New York, NY, USA. Email: tchernichovski@gmail.com

channel. During vocal practice, the input from the bird's own song (auditory feedback) through the rhythm channel could encode the error from the species-specific song rhythm. Projecting that error signal to the VTA could set a performance goal of approximating the innate song rhythm pattern. In parallel, song input via the syllable morphology channel, which faithfully encodes syllable structure, could set a second performance goal of approximating the tutor song's syllables (6). Because the two channels are orthogonal, the two putative error signals are additive, and can be combined in real time into a single VTA dopaminergic signaling of singing performance error. However, Area X is not involved in correcting rhythm errors (7), suggesting the possibility that the VTA projects deviation from different developmental performance goals into different motor song production brain centers. Further, song rhythm is not entirely innate, and syllable morphology is not entirely learned. Within their species-specific range, birds do imitate gap durations, and beyond their species-specific range, imitation of syllable morphology becomes biased toward the species-specific range (8). Therefore, a more realistic scenario would include multiple performance goals where the balance between innate and acquired performance targets (9) varies across channels, with syllable morphology being more sensitive to cultural input and rhythm being tuned more strongly toward innate templates.

The studies of Gadagkar *et al.* and Araki *et al.* are only early steps in identifying neuronal mechanisms for encoding ecologically valid singing performance targets, and for guiding motor performance toward multiple developmental goals without conflict. Such "split" encoding may enable cultural transmission while retaining species-specific signature over generations (8). Beyond vocal culture in songbirds, the synchronous approximation of multiple developmental goals is relevant to many animal communication systems, and perhaps even to the retention of stable cultures in humans (9, 10). ■

REFERENCES

1. T. Marler, M. Tamura, *Condor* **64**, 368 (1962).
2. O. Tchernichovski, G. Marcus, *Curr. Opin. Neurobiol.* **28**, 42 (2014).
3. B. Ballentine *et al.*, *Behav. Ecol.* **15**, 163 (2004).
4. V. Gadagkar *et al.*, *Science* **354**, 1278 (2016).
5. M. Araki *et al.*, *Science* **354**, 1282 (2016).
6. T. W. Troyer, A. J. Doupe, *J. Neurophysiol.* **84**, 1204 (2000).
7. F. Ali *et al.*, *Neuron* **80**, 494 (2013).
8. O. Fehér, H. Wang, S. Saar, P. P. Mitra, O. Tchernichovski, *Nature* **459**, 564 (2009).
9. J. W. Carr, K. Smith, H. Cornish, S. Kirby, *Cogn. Sci.* **10.1111/cogs.12371** (2016).
10. D. Centola, A. Baronchelli, *Proc. Natl. Acad. Sci. U.S.A.* **112**, 1989 (2015).

10.1126/science.aal3205

CLIMATE

The smoking gun of the ice ages

Forty years ago, a seminal paper showed that small changes in Earth's orbit are key to understanding ice age cycles

By David A. Hodell

Forty years ago, Hays, Imbrie, and Shackleton in a paper in *Science* tested the hypothesis that small changes in Earth's orbital geometry—namely precession, obliquity, and eccentricity—were responsible for the waxing and waning of the great continental ice sheets during the Quaternary period, which began about 2.58 million years ago (1). The paper is considered to be the "smoking gun" in support of the astronomical hypothesis of the Ice Ages, which is over a century old and most often ascribed to Milutin Milankovitch (2).

Hays, Imbrie, and Shackleton studied two marine sediment cores from the sub-Antarctic Indian Ocean. Hays counted radiolaria to produce a record of past sea surface temperature and stratification; Shackleton measured oxygen isotopes in the shells of foraminifera as a proxy of changing continental ice volume; and Imbrie did the statistical analysis. The strategy was to use time-series analysis to identify cycles present in the paleoclimate records and compare them with the most accurate periodicities of Earth's orbit available at the time (3).

John Imbrie, who passed away earlier this year, described his "Eureka moment" in a 1997 interview for the American Institute of Physics (4). After collecting the spectral analysis output from the mainframe computer at Brown University, he took the results home. Later that evening, he examined the results and found that the periodicities in the paleoclimate record were 42,000, 23,500, and 19,000 years. These periods matched the predicted orbital periods of obliquity (42,000 years) and precession (23,500 and 19,000 years) almost exactly, and Imbrie knew straight away that this could not have occurred by chance alone. "My golly," he thought, "Milankovitch is right." He rushed to the phone to ring Hays and Shackleton.

The authors found that the dominant rhythm in the paleoclimate record was approximately 100,000 years ($\pm 20,000$ years), which matches Earth's eccentricity cycle. But

whereas the 42,000-, 23,500-, and 19,000-year cycles could be explained by a linear response to obliquity and precession, the negligible effect of eccentricity on Earth's incoming energy could not directly account for the large amplitude of the climate signal near 100,000 years. To describe the process, the authors used the analogy of a pacemaker that sets the rhythm of the Ice Ages but does not necessarily directly account for the amplitude of the signal (see the figure). In Hays's words, "A colleague of mine at Lamont...had recently had a pacemaker implanted to control his heart's timing. We were all young at the time so pacemakers were not common among us so his was of special interest. I thought the action of this

"...Imbrie knew straight away that this could not have occurred by chance alone. 'My golly,' he thought, 'Milankovitch is right.'"

pacemaker on his heartbeat could be analogous to that of the orbital variations on the timing of Ice Age climate changes. I suggested the title to Nick and John and they agreed that it would work" (5).

Hays, Imbrie, and Shackleton purposely avoided identifying the specific mechanisms by which changes in orbital geometry result in the advance and retreat of the ice sheets. Instead, they tested the general astronomical hypothesis. In so doing, they framed many of the questions that paleoclimatologists have sought to answer since then. For example, how do orbitally induced changes in the seasonal distribution of insolation get amplified by global radiative feedbacks to result in the pervasive glacial-interglacial changes in Earth's climate? What is the origin of the quasiperiodic 100,000-year cycle? And how might future climate respond to Earth's changing orbit (in the absence of anthropogenic greenhouse gases)?

Efforts to address these questions included the Spectral Mapping Project (SPEC-MAP), created in the 1980s to produce long, continuous records from ocean sediments that could be used to study the timing and

The Godwin Laboratory for Palaeoclimate Research, Department of Earth Sciences, University of Cambridge, Downing Street, Cambridge CB2 3EQ, UK. Email: dah73@cam.ac.uk

phasing of key parts of the climate system. Parallel advances in the recovery and analysis of ice cores produced long records of variations in greenhouse gases in the atmosphere, which proved to be a vital feedback needed to explain glacial–interglacial cycles. In 2000, Shackleton (6) combined data from ice and marine sediment cores to argue that the global carbon cycle was responsible for the 100,000-year signal through changing atmospheric carbon dioxide concentrations.

In the original paper, Hays, Imbrie, and Shackleton identified two main obstacles to testing the Milankovitch hypothesis that still challenge paleoclimatologists today. First, it remains unclear which aspects of the climate system are most sensitive to changes in seasonal insolation anomalies induced by orbital geometry. Second, uncertainties associated with geological chronology limit our ability to determine the exact timing and phasing of events, which are needed to work out cause-effect relationships.

To address this second limitation, we need an absolute time scale for the marine record that is independent of astronomical tuning (in which time is derived by correlating sedimentary signals to orbital variations). Without accurate time control, paleoclimate observations and interpretations remain ambiguous or circular, limiting our ability to infer past mechanisms of climate change. Correlation of marine cores

to radiometrically dated speleothems (cave deposits) offers the best prospects for developing an absolute time scale.

Another challenge is that the oxygen isotope signal of benthic foraminifera, which is commonly used as a proxy for global ice volume, contains a significant temperature component (6, 7). Thus, it becomes difficult to evaluate the relative timing of the responses of temperature and ice sheets to orbital forcing (7). It is also important to know the history of individual ice sheets—in the Northern Hemisphere (European, Asian, Laurentide, Cordilleran, Greenland) and Antarctica, especially before the Middle Pleistocene Transition (1.25 to 0.65 million years ago) (8).

Much attention has been paid to glacial terminations because they represent the times of the greatest and most abrupt climate change. However, deglaciations may be an inevitable consequence of the instability of very large, isostatically depressed ice sheets (9–11). The ice growth phase of the glacial cycle may also be a crucial time for understanding how the climate system is paced by orbital variations. Furthermore, many have suggested that the quasiperiodic 100,000-year cycle does not result directly from eccentricity forcing but rather consists of multiples of precession and/or obliquity beats (9, 12). The key to explaining the quasiperiodic 100,000-year cycle may be to understand how the climate system, once it is in a glacial state, manages to avoid deglaciation

and permits ice to continue to accumulate, thereby skipping orbital beats.

Another important missing piece of the Ice Age puzzle may be how shorter (millennial) and longer (10,000 to 100,000 years) orbital climate variability interact to produce the observed patterns of Quaternary glacial–interglacial cycles. The transitions into and out of glacial periods are marked by increased millennial-scale variability. This short-term variability may serve as a mechanism to trigger transitions as a bifurcation point is approached in a dynamical climate system with multiple stable states (13, 14).

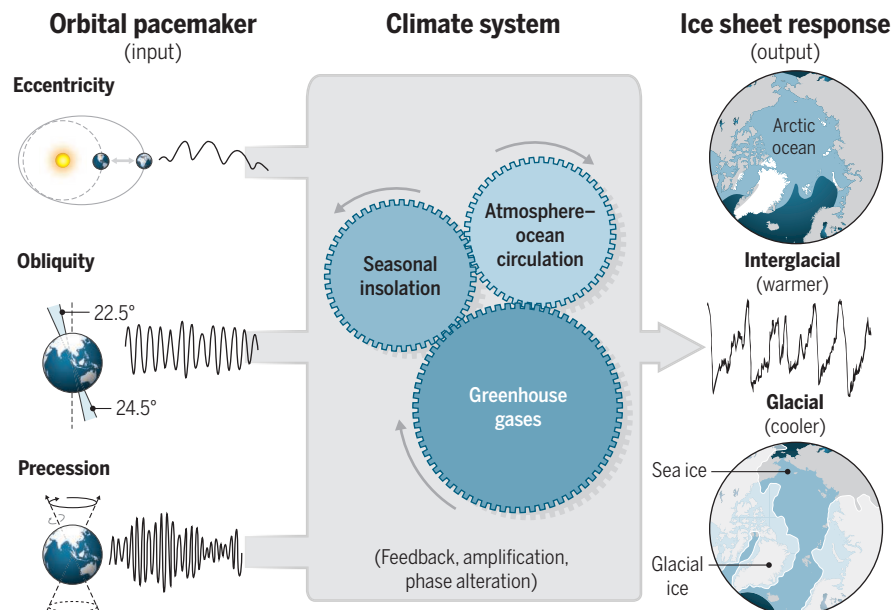
There has been a natural tendency for paleoclimatologists to focus on the past million years, because sediment of this age is readily accessible by piston coring. Yet, this time period is probably one of the most difficult times in which to test the Milankovitch hypothesis, because the response of the cryosphere–climate system to orbital forcing has been highly nonlinear. The Early Pleistocene (2.58 to 0.78 million years ago) provides a simpler test bed because the response of Earth's climate system to obliquity forcing was more linear.

Lastly, coupled climate–ice sheet models that can run long, transient experiments will continue to improve and provide insight to the growth and decay of ice sheets under changing boundary conditions.

The paper by Hays, Imbrie, and Shackleton (7) is often said to have solved the mystery of the Ice Ages. But, in fact, it raised more questions than it answered. Although progress has been made over the past four decades, we still lack a unified mechanistic understanding that links changes in Earth's orbit to the Ice Ages (15). This is a vibrant area of current research, and I trust we will have made more progress by the 50th anniversary of this seminal paper in 2026. ■

Pacemaker of the Ice Ages

Hays, Imbrie, and Shackleton treated secular changes in the orbit as a forcing function (input) of the climate system. The output is the geological record of glacial–interglacial cycles. In the pacemaker analogy, the pacemaker is the cyclic variations in Earth's orbital geometry, the heart is the climate system, and the heartbeat is the resulting glacial–interglacial cycles.



REFERENCES

1. J. D. Hays, J. Imbrie, N. J. Shackleton, *Science* **194**, 1121 (1976).
2. M. Milankovitch, *Kanon der Erdbeistrahlung und seine Anwendung auf das Eiszeitenproblem*, Royal Serbian Academy of Sciences Spec. Publ. 132, Sect. Math. Nat. Sci., vol. 33 (1941).
3. A. L. Berger, *Astron. Astrophys.* **51**, 127 (1976).
4. Interview of John Imbrie by Ronald Doel on 21 May 1997, Niels Bohr Library and Archives, American Institute of Physics, College Park, MD, USA; www.aip.org/history-programs/niels-bohr-library/oral-histories/6924.
5. Personal communication in an email to D.A.H. on 11 November 2016.
6. N. J. Shackleton, *Science* **289**, 1897 (2000).
7. H. Elderfield *et al.*, *Science* **337**, 704 (2012).
8. M. E. Raymo *et al.*, *Science* **313**, 492 (2006).
9. M. E. Raymo, *Paleoceanography* **12**, 577 (1997).
10. G. H. Denton *et al.*, *Science* **328**, 1652 (2010).
11. T. Hughes, *Quat. Sci. Rev.* **30**, 1829 (2011).
12. P. Huybers, C. Wunsch, *Nature* **434**, 491 (2005).
13. D. Paillard, *Rev. Geophys.* **39**, 325 (2001).
14. M. Crucifix, *Philos. Trans. R. Soc. A* **370**, 1140 (2012).
15. M. E. Raymo, P. Huybers, *Nature* **451**, 284 (2008).

10.1126/science.aal4111



POLICY FORUM

BIOSECURITY

What life scientists should know about security threats

Considerable information is publicly available to help research institutions understand and counter potential threats

By **Kavita M. Berger**

Although concerns about biological weapons and terrorism were discussed by a few scientists before 2001, the broader life-sciences community was not engaged until after the 2001 anthrax-laced letters. The events of 2001 led to efforts in the United States to strengthen biological security for pathogens that could adversely affect public health and safety (i.e., Biological Select Agents and Toxins) and research that could be directly misapplied for harmful purposes (i.e., Dual Use Life Sciences Research of Concern). Resulting policy and practices required scientists to assess security risks of certain types of pathogen research and to identify and implement risk reduction measures. However, scientists have argued for years that their lack of access to or knowledge about malicious actors limits effective assessment and communication of security risks (1–3). How much information is available in the public domain for scientists to understand, evaluate, and communicate plausible biosecurity risks; and what can be done to prevent such threats?

A comprehensive assessment of plausible threats facing research institutions in the

United States was conducted as part of the biosecurity risk assessment of the U.S.-sponsored *Risk and Benefit Assessment for Gain of Function Research* concerning influenza, severe acute respiratory syndrome (SARS) coronavirus, and Middle East respiratory syndrome (MERS) coronavirus (4). The information contained in this assessment exists in a variety of places, from documents describing offensive biological weapons efforts of nation-states and nonstate actors to criminal activities perpetrated by individuals and extremist groups. In addition to these data, other relevant incidents are listed in the supplementary tables.

The 93 publicly described incidents fall into three main categories. First, and the largest, category includes attempts and actual use of pathogens and toxins to cause harm (56 incidents). Of the incidents involving malicious use of biological agents, 21 were criminal acts perpetrated by individuals, 17 were domestic terrorists targeting people in their own country, and 18 were transnational terrorists (table S1). Although threats from outsiders cannot be ruled out, analysis of these incidents indicates that the greatest security risk to research institutions came from insiders.

Groups targeting life-science facilities and

In a laboratory, individuals in various positions could harm the institution, their co-workers, or the broader community by negligent or harmful actions.

hospitals were identified in 26 incidents (table S2). The incidents involved attacks on research and health care facilities, including theft of research animals, arson in laboratories, and explosions at clinics. Domestic extremist organizations (for example Animal Liberation Front or Earth Liberation Front) have vandalized research facilities, stolen or released research animals, stolen research documents, perpetrated arson attacks, or harmed researchers and institutional officials. Although a majority of incidents were attacks perpetrated by violent animal rights or eco-radical organizations (i.e., domestic extremists), several incidents involving individuals are described. A subset of incidents describes malicious acts involving insiders sabotaging or destroying others' experiments.

Ten incidents involving other harmful acts caused primarily by individuals (table S3) were identified. These were acts perpetrated by individual scientists or health professionals and involved negligence or deliberate harm. Negligent acts include theft of a pathogen before legal transfer to a colleague, transport of an undocumented pathogen on a commercial flight, and employment of a drug addict who used hospital supplies and replaced contaminated supplies for reuse by unsuspecting patients. Deliberate acts have involved scientists or health professionals physically harming individuals and, in some cases, shooting one or more people.

The role that insiders play in a majority of these incidents is striking. Malicious actors seeking access to the laboratories, animal facilities, research data, or experimental samples require assistance from insiders to gain knowledge about the research being conducted, security practices, and locations of research samples and animals. Insiders were sometimes knowingly recruited by malicious organizations, perpetrated crimes themselves for various reasons, or unknowingly provided information and materials to malicious actors. To many in the scientific community, this conclusion may seem unbelievable or not representative of their environments. Although the overall number of cases is low, harmful acts continue to take place, which suggests the need to develop and implement systems to identify and stop incidents from occurring at the individual, institutional, community, and federal levels (see the photo).

This Policy Forum describes several practices that can be implemented at research

Gryphon Scientific, LLC, Takoma Park, MD 20912, USA.
Email: kberger@gryphonscientific.com

institutions to identify early and to prevent potential threats from affecting individuals, laboratories, and the entire institution. A list of resources is included in the supplementary materials.

PREVENTING THREATS

Research institutions use a variety of methods to prevent threats facing their institutions. These measures are like layers of an onion, providing points at which malicious actors could be stopped from causing harm.

The suite of physical security measures implemented at several U.S. research institutions includes key card or biometric controls, gates, security guards, security cameras, and training. Although these measures may seem draconian, many academic and nonprofit research institutions use a combination of these measures to prevent violent extremists from gaining access to research facilities and vandalizing, stealing animals, or destroying experiments and results. At some institutions, all of these measures are implemented for certain facilities, such as those that conduct research with non-human primates. Private industry often uses these measures to protect intellectual property and trade secrets.

Although physical security measures can deter malicious outsiders from gaining access to laboratories, they do not address potential harms caused by insiders who intentionally or unintentionally seek to damage the reputation, financial status, physical structure, or research of institutions and affiliated individuals (see the chart). Insiders might use the materials to which they have special access to harm others or enable external entities to gain access to sensitive information or materials. Often, discussions about insider threats focus on harms caused by scientists. However, research institutions employ and educate many types of individuals, any one of whom could divulge information, provide access to facilities, or carry out malicious acts. Thus, measures that raise awareness about potential security risks and are applied equally to all relevant individuals could promote norms around safeguarding research and the institutional environment from harm. Also, broad inclusion of stakeholders enables individuals to look out for each other (in a positive way),

which is a key component of some biosecurity programs (5, 6).

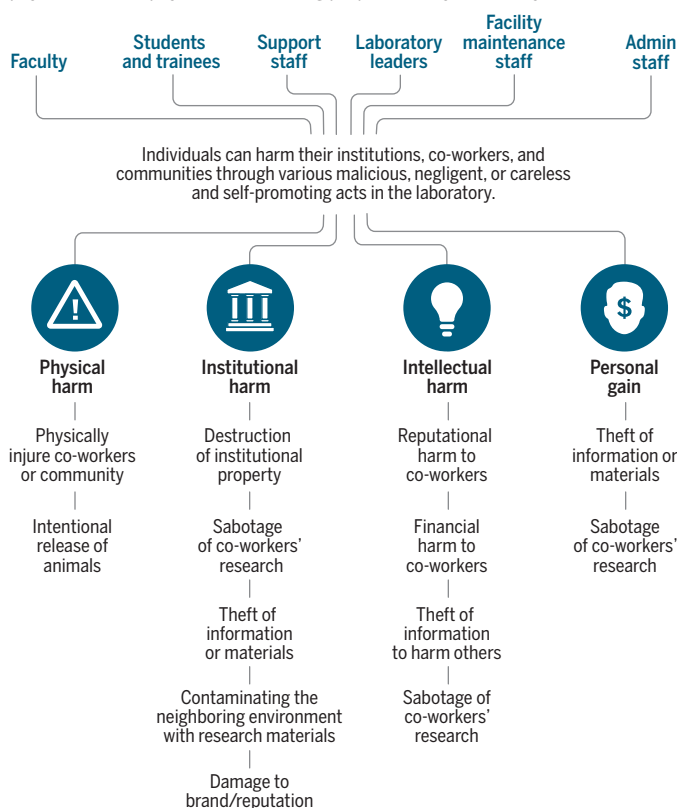
For decades, individuals who have access to sensitive information and materials have been targeted by malicious actors of all kinds, from foreign intelligence officers seeking information about scientific activities to extremists intent on attacking a research or health care facility. In some cases, insiders do not know they are providing information or materials to malicious actors; in these cases, individuals may be sharing their research at a conference, interviewing for a nonexistent job, or sharing a biological sample with a colleague. In other cases, insiders are coerced

No single driver can be attributed to individuals who intend to harm others. A review of literature suggests that harmful behaviors can be triggered by several factors, such as disillusionment with one's career or work and/or educational environment, a devastating life experience, and a predisposition to certain behaviors, such as antisocial behavior, existing belief structure, ideology, some serious mental health issues, abuse, isolation, and struggle with power dynamics. Potential drivers for negligent behavior, which could harm others or enable unauthorized access to sensitive materials or information by outsiders,

range from deliberate noncompliance with rules, narcissism, and arrogance to distraction from one's tasks, fatigue, and inadequate training.

Personnel security in academia

Personnel security at universities is highly complex, with the potential for various physical and nonphysical harms being perpetrated by a diversity of stakeholders.



into providing information or materials through various means, including romantic relationships, flattery, or money. In addition to federal requirements on export control, deemed exports, and restricted persons, measures most often used to prevent these types of incidents include (i) training about institutional policy and procedures; (ii) training on potential threats, their elicitation tactics, and appropriate actions when discovered; (iii) a structure that enables nonpunitive and/or anonymous reporting of suspicious activity; and (iv) a process for evaluating and mitigating suspicious activity.

ADDRESSING THE THREAT

Despite the wide variety of potential drivers for malicious or negligent behavior, prevention measures are similar. Several U.S. research universities use different combinations of measures to prevent harmful behavior from insiders (see supplementary materials).

Behavioral risk assessment committees have been established to vet employees at hiring and periodically thereafter. For example, University of Wisconsin and Boston University have created committees to comply with personnel security requirements issued in the 2012 final rule on regulation of biological select agents and toxins [see (3)].

Nonpunitive and/or anonymous reporting structures for communicating suspicious incidents or violations have been proposed. Several research institutions have ombudsman services that empower employees and/or students to report

incidents of concern. These services were explored as possible avenues for reporting personnel security violations or suspicious events in a 2010 National Research Council report (7). However, concerns about policing peers or having the appropriate whistleblower protections have been raised by the scientific community for more than a decade. Although these concerns persist, the increased awareness of violence on campuses and in workplaces and communities during the past few years seems to have shifted the discussion toward empowering bystander reporting. In addition, organizations that

support high-containment research, for example, Galveston National Laboratory, have supported the development of nonpunitive self-reporting mechanisms (8).

Strong vertical and horizontal leadership helps to promote safe and secure research and educational environments by empowering individuals to share their experiences and knowledge with others and to think creatively about productive approaches to solve problems. The concept of a “just culture,” wherein individuals (regardless of seniority, position, or other potential distinguishing factors) are treated equally, has been raised by legal experts at research universities as an approach for reducing the ability for individuals to bend or disregard rules (9). Ongoing mentorship helps individuals develop professional, trusted relationships with one another and provides opportunities for early identification and resolution of potential acts of harm caused by feelings of depression, isolation, disillusionment, or other similar feelings. Vanderbilt University has a formalized mentoring program for Women in Science and Engineering to support both personal and professional development of its members (10); this has enabled the development of trusted relationships through which women can seek advice and guidance on difficult career-related issues. The University of Illinois Urbana-Champaign and Yale University offer mentorship resources for graduate students and postdoctoral fellows career and social interactions (11, 12).

Employee and student assistance and career development programs provide useful services to faculty, staff, and students to ensure that they are able to seek help with professional difficulties, personal events, or other stressful situations. These programs exist at most, if not all, major research institutions in the United States.

Finally, executive-level committees, such as the All-Hazards Risk Leadership Council at the University of Texas MD Anderson Cancer Center, provide high-level support for assessing and remediating potential threats (13, 14). Several universities established threat assessment teams in the early 2000s to identify, evaluate, and resolve potential threats on campus (15).

Preventing misapplication of experimental protocols and research results presents a different problem with which the security community has been struggling for decades. Recently, the focus has been primarily on misapplication of biotechnology and pathogen research. The inherent complexity associated with determining the potential that

legitimate or beneficial research could be misapplied by a malicious actor has led security experts to focus approaches on education, review of research, and communication. In 2008, the AAAS identified 15 U.S. universities that created training programs on the dual use issue (16, 17), several of which are not offered today. However, different universities (e.g., University of North Carolina (<http://bit.ly/dualuseself-study>)) have established training programs that include dual use research, whereas others reference the Collaborative Institutional Training Initiative (CITI) biosafety and biosecurity training program (<http://bit.ly/CITI-BB>) in which dual use research is taught or the Department of Health and Human Services training presentation on U.S. government policy (<http://bit.ly/DHHS-DU>). Internationally, several efforts have been initiated to establish a code of conduct for responsible use of biology (18, 19), train scientists about dual use issues (20), and enable scientists to develop their own curricula (21, 22).

Whether and to what degree training programs, codes of conduct, expert reviews, and responsible communication efforts are effective are unclear. Including training in public affairs and risk communication; better defined procedures for any dual use life sciences review; case studies for training that are appropriate for the threats, risks, and scientific environment; and programs that are generalizable to nonselect agent or pathogen research will be important. Periodically updating the curricula to remain current would further improve training programs and reduce the risk of alarmism and stereotyping.

The amount of information publicly available about malicious incidents is vastly greater than what many previously thought. With these data in mind, scientists, institutional administrators, regulators, and funders can identify and synthesize information on possible threats to their institutions; evaluate which of the threats pose substantial risk, based on the policy and practices of the institution; and implement practices to raise awareness of and prevent security threats. Furthermore, these data might provide opportunities to bring together experts from across security disciplines, the legal system, and research institutions to develop measures that simultaneously draw on practical experience and academic evaluations to address institutional needs. ■

Although the overall number of cases is low, harmful acts continue....”

REFERENCES AND NOTES

1. K. M. Berger et al., *Bridging Science and Security for Biological Research: Implementing the Revised Select Agents and Toxin Regulations: Meeting Report*, Washington, DC, 22 to 23 April 2013 (AAAS, Washington, DC, 2013).
2. K. M. Berger et al., *Bridging Science and Security for Biological Research: International Science and Security: Meeting Report*, Washington, DC, 4 to 5 February 2013 (AAAS, Washington, DC, 2013).
3. K. M. Berger et al., *Bridging Science and Security for Biological Research: Personnel Security Programs: Meeting Report*, Washington, DC, 21 to 23 April 2013 (AAAS, Washington, DC, 2014).
4. Gryphon Scientific, *Risk and Benefit Analysis of Gain of Function Research* (Gryphon Scientific, Takoma Park, MD, 2015).
5. J. J. Higgins, P. Weaver, J. P. Fitch, B. Johnson, R. M. Pearl, *Biosec. Bioterr.* **11**, 130 (2013).
6. C. Skvorc, D. E. Wilson, *Biosec. Bioterr.* **9**, 23 (2011).
7. National Research Council, *Responsible Research with Biological Select Agents and Toxins* (National Academies Press, Washington, DC, 2009).
8. K. M. Berger, K. Luke, J. Sta. Ana, M. Frankel, *Biological Safety Training Programs as a Component of Personnel Reliability: Workshop Report*, Washington, DC, 17 March 2009 (AAAS, Washington, DC, 2009).
9. AAAS, Gryphon Scientific, Federal Bureau of Investigation (FBI), discussions regarding personnel security in academia for a meeting (3).
10. Vanderbilt University, Women in Science and Engineering Program (2016); <https://anchorlink.vanderbilt.edu/organization/vuwise>.
11. University of Illinois Urbana-Champaign, Faculty and Staff Toolkits for Mentoring (2016); www.grad.illinois.edu/faculty-staff/toolkits/mentor.
12. Office for Graduate Student Development and Diversity, Yale University, 4-Tiered Mentoring Program (2016); <http://bit.ly/4-TieredMP>.
13. W. Adcox, chief of police for MD Anderson Cancer Center of the University of Texas System, pers. commun.
14. Security Executive Council, “Driving results by communicating your value story” (Security State of the Industry February 2016 Briefing, Security Executive Council, 2016); <http://bit.ly/2gbtXNw>.
15. K. M. Berger, T. Smith, J. Poulakidas, *Competing Responsibilities: Addressing the Security Risks of Biological Research in Academia. Workshop Report*, Washington, DC, 20 to 21 January 2010 (AAAS, Washington, DC, 2010).
16. K. M. Berger, M. K. Mohlman, J. Sta. Ana, M. Frankel, *Professional and Graduate-level Programs on Dual Use Research and Biosecurity for Scientists Working in the Biological Sciences: Workshop Report*, Washington, DC, 21 November 2008 (AAAS, Washington, DC, 2008).
17. J. L. Sta. Ana, M. S. Frankel, K. M. Berger, *Science* **326**, 1193 (2009).
18. World Health Organization, *Responsible Life Sciences Research for Global Health Security: A Guidance Document* (WHO, Geneva, 2010); <http://bit.ly/WHO2fVq>.
19. Koninklijke Nederlandse Akademie Van Wetenschappen, *A Code of Conduct for Biosecurity* (2009); <https://www.knaw.nl/en/news/publications/a-code-of-conduct-for-biosecurity>.
20. The AAAS Center for Science, Technology, and Security Policy has designed a set of 10 practical training exercises for life scientists throughout the broader Middle East and North Africa (BMENA) region AAAS (2014). These exercises are based on high-quality, published life sciences research from BMENA region. They are freely available for use. See www.aaas.org/report/BMENA-risk-analysis-training.
21. National Research Council, *Research in the Life Sciences with Dual Use Potential: An International Faculty Development Project on Education About the Responsible Conduct of Science* (National Academies Press, Washington, DC, 2011), p. 54.
22. National Research Council, *Developing Capacities for Teaching Responsible Science in the MENA Region: Refashioning Scientific Dialogue* (National Academies Press, Washington, DC, 2013), p. 137.

ACKNOWLEDGMENTS

I thank P. Mauger, who conducted the research on malicious incidents for the biosecurity risk assessment of the gain-of-function risk and benefit assessment; R. Casagrande and R. Stephens from Gryphon Scientific for their review of the manuscript; and T. Wang from AAAS, who approved inclusion of unpublished discussions from a 2015 workshop on personnel security.

SUPPLEMENTARY MATERIALS

www.sciencemag.org/content/354/6316/1237/suppl/DC1

10.1126/science.aaf9334

REPRODUCIBILITY

Enhancing reproducibility for computational methods

Data, code, and workflows should be available and cited

By **Victoria Stodden**,¹ **Marcia McNutt**,² **David H. Bailey**,³ **Ewa Deelman**,⁴ **Yolanda Gil**,⁴ **Brooks Hanson**,⁵ **Michael A. Heroux**,⁶ **John P.A. Ioannidis**,⁷ **Michela Tauber**⁸

Over the past two decades, computational methods have radically changed the ability of researchers from all areas of scholarship to process and analyze data and to simulate complex systems. But with these advances come challenges that are contributing to broader concerns over irreproducibility in the scholarly literature, among them the lack of transparency in disclosure of computational methods. Current reporting methods are often uneven, incomplete, and still evolving. We present a novel set of Reproducibility Enhancement Principles (REP) targeting disclosure challenges involving computation. These recommendations, which build upon more general proposals from the Transparency and Openness Promotion (TOP) guidelines (1) and recommendations for field data (2), emerged from workshop discussions among funding agencies, publishers and journal editors, industry participants, and researchers representing a broad range of domains. Although some of these actions may be aspirational, we believe it is important to recognize and move toward ameliorating irreproducibility in computational research.

Access to the computational steps taken to process data and generate findings is as important as access to data themselves. Computational steps can include information that details the treatment of outliers and missing values or gives the full set of model parameters used. Unfortunately, reporting of and access to such information is not routine in the scholarly literature (3). Although independent reimplementations of an experiment can provide important scientific evidence regarding a discovery and is a practice we wish to encourage, access to the underlying software and data is key

to understanding how computational results were derived and to reconciling any differences that might arise between independent replications (4). We thus focus on the ability to rerun the same computational steps on the same data the original authors used as a minimum dissemination standard (5, 6), which includes workflow information that explains what raw data and intermediate results are input to which computations (7). Access to the data and code that underlie discoveries can also enable downstream scientific contributions, such as meta-analyses, reuse, and other efforts that include results from multiple studies.

RECOMMENDATIONS

Share data, software, workflows, and details of the computational environment that generate published findings in open trusted repositories. The minimal components that enable independent regeneration of computational results are the data, the computational steps that produced the findings, and the workflow describing how to generate the results using the data and code, including parameter settings, random number seeds, make files, or function invocation sequences (8, 9).

Often the only clean path to the results is presented in a publication, even though many paths may have been explored. To minimize potential bias in reporting, we recommend that negative results and the relevant spectrum of explored paths be reported. This places results in better context, provides a sense of potential multiple comparisons in the analyses, and saves time and effort for other researchers who might otherwise explore already traversed, unfruitful paths.

Persistent links should appear in the published article and include a permanent identifier for data, code, and digital artifacts upon which the results depend. Data and code underlying discoveries must be discoverable from the related publication, accessible, and reusable. A unique identifier should be assigned for each artifact by the article publisher or repository. We recommend digital object identifiers (DOIs) so that it is possible to discover related data sets and code through the DOI structure itself, for example, using a hierarchical schema. We advocate sharing digital scholarly objects in open trusted repositories that are crawled by search engines.

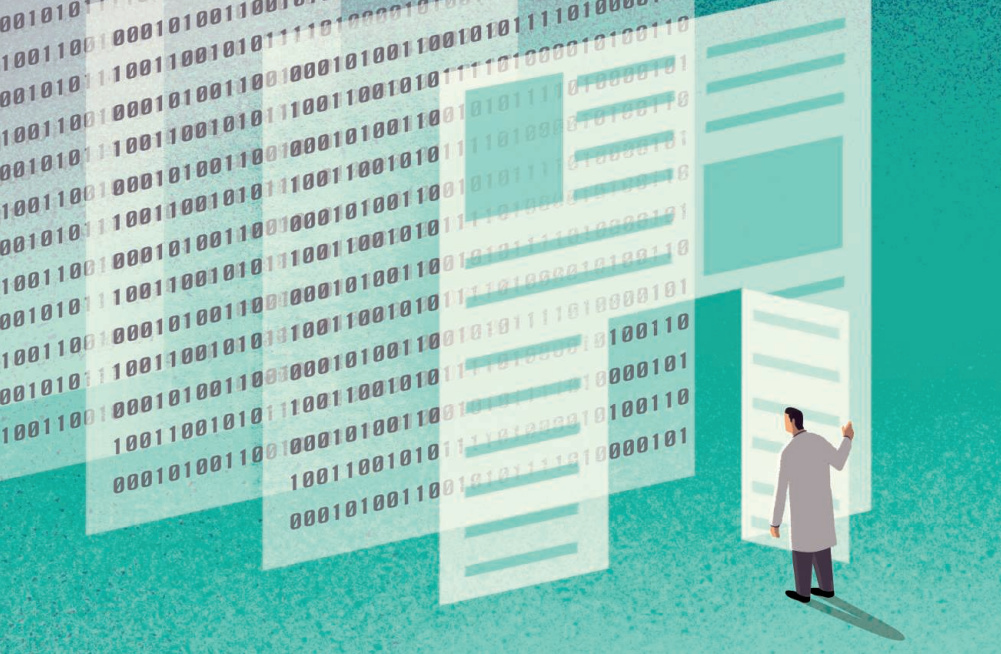
Sufficient metadata should be provided for someone in the field to use the shared digital scholarly objects without resorting to contacting the original authors (i.e., <http://bit.ly/2fVwjPH>). Software metadata should include, at a minimum, the title, authors, version, language, license, Uniform Resource Identifier/DOI, software description (including purpose, inputs, outputs, dependencies), and execution requirements.

To enable credit for shared digital scholarly objects, citation should be standard practice. All data, code, and workflows, including software written by the authors, should be cited in the references section (10). We suggest that software citation include software version information and its unique identifier in addition to other common aspects of citation.

To facilitate reuse, adequately document digital scholarly artifacts. Software and data should include adequate levels of documentation to enable independent reuse by someone skilled in the field. Best practice suggests that software include a test suite that exercises the functionality of the software (10).

Use Open Licensing when publishing digital scholarly objects. Intellectual property laws typically require permission from the authors for artifact reuse or reproduction. As author-generated code and workflows fall under copyright, and data may as well, we recommend using the Reproducible Research Standard (RRS) to maximize utility to the community and to enable verification of findings (11). The RRS recommends attribution-only licensing, e.g., the MIT License or the modified Berkeley Software Distribution (BSD) License for software and workflows; the Creative Commons Attribution (CC-BY) license for media; and public domain dedication for data. The RRS and principles of open licensing should be clearly explained to authors by journals, to ensure long-term open access to digital scholarly artifacts.

¹University of Illinois at Urbana-Champaign, Champaign, IL 61801, USA. ²National Academy of Sciences, Washington, DC 20418, USA. ³University of California, Davis, CA 95616, USA. ⁴University of Southern California, Los Angeles, CA 90007, USA. ⁵American Geophysical Union, Washington, DC 20009, USA. ⁶Sandia National Laboratories, Avon, MN 56310, USA. ⁷Stanford University, Stanford, CA 94305, USA. ⁸University of Delaware, Newark, DE 19716, USA. Email: vcs@stodden.net



Journals should conduct a reproducibility check as part of the publication process and should enact the TOP standards at level 2 or 3. Such a check asks whether the data, code, and computational steps upon which findings depend are available in an open trusted repository in a discoverable and persistent way, with links provided in the publication. And have all digital artifacts been openly licensed? Is documentation and workflow information available for a reader to follow the discovery process? Are all digital scholarly objects used in the discovery process cited in the manuscript's reference section? Could the published computational findings be reproduced on an independent system by using the data and code provided?

The last item is arguably the most time-consuming for reviewers and difficult to carry out, and many journals may choose not to adopt it or may perform partial reproduction for only some of the computational findings. The journal article should specify which of these items have been checked and, if so, whether they are fully or partially fulfilled.

Journals should strive to enact level 2 or 3 of the TOP standards on "Data transparency" and "Analytic methods (code) transparency." Level 3 recommends an independent reproduction of findings. Some journals are already taking steps in this direction (12, 13).

To better enable reproducibility across the scientific enterprise, funding agencies should instigate new research programs and pilot studies. Resolving some barriers to reproducibility may be straightforward; however, others may take time and community effort to overcome. We recommend enacting research programs to advance our understanding of reproducibility in computationally enabled research. Topics might include methods for verifying queries on confidential data; extending validation, verification, and uncertainty quantification to encompass reproducibility;

numerical reproducibility and sensitivity to small variations in computation (14); testing standards for code, including closed or proprietary codes; cyberinfrastructure that supports reproducibility, as well as innovative computational work; pilot efforts to create "instruction manuals" for manuscript submission (e.g., <http://libguides.caltech.edu/authorcarpentry>); policy research on intellectual property law and software patenting; costs and benefits to reproducibility in different settings, for example, in industry collaboration; provenance and workflow repositories; and exploring how to make investments regarding the preservation of various digital artifacts. Funding bodies could support efforts to reproduce results in different computational settings to better understand sources of error in computational findings.

BARRIERS, EXCEPTIONS, ONGOING EFFORTS

We recognize that there are challenges to the implementation of these recommendations. There will necessarily be exceptions in the near term and possibly indefinitely, for example, analysis and data involving human subjects or proprietary codes. However, we believe that creative ways to manage exceptions could be developed in such cases and that exceptions should be explained in the article. For example, if data or code cannot be made publicly accessible, the research team or journals could have infrastructure, policies, and procedures in place for rapidly giving reviewers access to information necessary to perform a review (13, 15).

It may not be possible to fully disclose, or even license, all proprietary software used in the discovery pipeline. However, scripts designed to be executed by propriety software such as MATLAB may be openly licensed by the script authors under the RRS. We also feel there are broad benefits to code release, for example, allowing for inspection, even if

the code cannot be executed (16).

Beyond the reproducibility check described above, journals can improve review of computational findings by rewarding reviewers who take extra effort to verify computational findings. Authors that facilitate such a review could be rewarded with badging of their published article (e.g., <http://bit.ly/Badging2gP>). Best practices for reviewers of reproducible publications need to be formulated. Funding agencies may encourage, request, and reward reproducible research practices in the scientific investigations that they review and fund.

Appropriate methodology to facilitate reproducibility should be taught to students who will use computational techniques in research. Best practices of digital scholarship should be required and incorporated into curricula and should include discussions of ethics, use of repositories, and version control, for example. Key societies or communities should consider short courses, best practices publications, and awards to promote these skills. Groups or research areas with limited experience in reproducible research practices could focus initially on a few seminal articles to demonstrate and promote reproducibility.

We believe that as these efforts become commonplace, practices and tools will continue to emerge that reduce the amount of time and resource investment necessary to facilitate reproducibility and support increasingly ambitious computational research. ■

REFERENCES AND NOTES

1. B. A. Nosek et al., *Science* **348**, 1422 (2015).
2. M. McNutt et al., *Science* **351**, 1024 (2016).
3. A. A. Alsheikh-Ali et al., *PLOS ONE* **6**, e24357 (2011).
4. D. Donoho et al., *IEEE Comput. Sci. Eng.*, **11**, 8 (2009).
5. V. Stodden, *JMS Bull. Online*, 17 November (2013); <http://bit.ly/BullJMS2013>.
6. D. H. Bailey, J. M. Borwein, V. Stodden, *Notices Amer. Math. Soc.* **60** (6), 679 (2013).
7. D. Garijo et al., *PLOS ONE* **8**, e80278 (2013).
8. D. Donoho, V. Stodden, in *The Princeton Companion to Applied Mathematics*, N. J. Higham, Ed. (Princeton Univ. Press, Princeton, NJ, 2016), pp. 916–925.
9. R. Gentleman, D. Temple Lang, *J. Comput. Graph. Stat.* **16**, 1 (2007).
10. V. Stodden, S. Miguez, *J. Open Res.* **2**, e21 (2014).
11. V. Stodden, *Comput. Sci. Eng.* **11**, 35 (2009).
12. V. Stodden, P. Guo, Z. Ma, *PLOS ONE* **8**, e67111 (2013).
13. M. Heroux, *ACM Trans. Math. Softw.* **41**(3), art13 (2015).
14. D. H. Bailey, J. M. Borwein, V. Stodden, in *Reproducibility: Principles, Problems, Practices*, H. Atmanspacher and S. Maasen, Eds. (Wiley, New York, 2015), pp. 205–232.
15. M. Fuentes, *AMSTAT News*, July 2016; <http://bit.ly/JASA2gb>.
16. R. J. LeVeque, *SIAM News* **46**, April 2013.

ACKNOWLEDGMENTS

These recommendations emerged from a workshop held at the American Association for the Advancement of Science (AAAS), Washington, DC, 16 and 17 February 2016, funded by the Laura and John Arnold Foundation (<http://bit.ly/AAAS2016Arnold>). Workshop participants are identified in the supplementary materials.

SUPPLEMENTARY MATERIALS

www.sciencemag.org/content/354/6317/1240/suppl/DC1

10.1126/science.aah6168

LETTERS

Edited by **Jennifer Sills**

Editorial expression of concern

IN THE 3 June issue, *Science* published the Report “Environmentally relevant concentrations of microplastic particles influence larval fish ecology” by Oona M. Lönnstedt and Peter Eklöv (*1*). The authors have notified *Science* of the theft of the computer on which the raw data for the paper were stored. These data were not backed up on any other device nor deposited in an appropriate repository. *Science* is publishing this Editorial Expression of Concern to alert our readers to the fact that no further data can be made available, beyond those already presented in the paper and its supplement, to enable readers to understand, assess, reproduce, or extend the conclusions of the paper.

Jeremy Berg

Editor in Chief

REFERENCE

1. O. M. Lönnstedt, P. Eklöv, *Science* **352**, 1213 (2016).

Published online 1 December
10.1126/science.aah6990

Instilling integrity

I AM WRITING to correct the record on the Professionalism and Integrity in Research Program (PI Program), which J. Mervis discussed in his News Feature “After the fall” (28 October, p. 408). Our workshop and follow-up program help researchers to operate professionally and with integrity after persistent or serious noncompliance or lapses of research integrity in their labs. All program faculty are funded researchers with training in research ethics and doctoral degrees in psychology. (I am not a sociologist, as asserted in the article.) The article states that “DuBois says he doesn’t always know what his clients have done.” In fact, we always discuss what they have done—superficially during enrollment interviews and in depth during the workshop—and we design professional development plans to help them avoid such difficulties in the future.

The article also states that “DuBois admits that it’s hard to judge the efficacy of his program, especially because recidivism of any sort would be highly unlikely in such a small sample.” However, we have documented the efficacy of the program, and preliminary



Sunset on the island of Kosrae.

LIFE IN SCIENCE

Respect for the ancients

I am finishing the day’s field notes by the light of a kerosene lamp on the Micronesian island of Kosrae, home of the archaeological site of Safonfok, when two Micronesians on my field crew approach my tent and ask me to escort them to the latrine. These local men, who are fishermen in their village when not working on my project, know that this remote terrain was abandoned long ago by their ancestors. They have a deep respect for the ancient history of archaeological sites and the ghosts and spirits that inhabit them.

It is common to ask permission of the local spirits for safe entry into an archaeological site or passage through a remote area. The men do this quietly, sometimes under their breath, sometimes with a ritual. (One man removed his shoes when we entered the jungle.) The night, it is believed, belongs to the spirits and ghosts—you don’t walk around without a purpose, you don’t whistle (the language of ghosts is heard as a whistle), you don’t call out someone’s name (a ghost may take the name and use it to trick you by luring you into a treacherous place), and you don’t walk in the center of a path (this is where ghosts walk).

Because I work in ancient places filled with ghosts, I have developed a reputation on this island as someone who is not afraid of anything. The men who have come to my tent trust me to provide safe passage between camp and the latrine. As we walk through the darkness, we are serenaded by night birds, croaking frogs, and buzzing insects. We quietly talk about the coral fish hooks for which Safonfok is known, and they share the island’s traditional lore as told to them by their grandfathers. I spend my days uncovering ancient artifacts, but sometimes it is at night when history seems to come alive.

Felicia Beardsley

Department of Sociology and Anthropology University of La Verne,
La Verne, CA 91750, USA. Email: fbeardsley@laverne.edu

10.1126/science.aal5071

LIFE IN SCIENCE is an occasional feature highlighting some of the humorous or unusual day-to-day realities that face our readers. Can you top this? Submit your story to www.submit2science.org

data indicate improvements in the use of evidence-based decision-making strategies, attitudes toward compliance, and the use of best practices within labs (such as creating and using standard operating procedures, holding regular meetings, and developing transparent data management procedures). To our knowledge, no other program has such data on positive outcomes.

Most crucially, the stories of the researchers who attend our program are often cautionary tales for other researchers. In most cases, participants are productive researchers whose lapses did

not involve a decision to engage in serious wrongdoing—which is why institutions chose to refer them to a professional development workshop rather than terminate their employment (*1*).

James M. DuBois

Washington University School of Medicine, St. Louis,
MO 63110, USA. Email: duboisjm@wustl.edu

REFERENCE

1. J. M. DuBois, J. T. Chibnall, R. Tait, J. Vander Wal, *Nature* **534**, 173 (2016).

10.1126/science.aal3844

Now is the time to protect the Arctic

WE WELCOME THE recent designation of the Ross Sea Marine Protected Area (MPA) as an important step forward in international protection of our polar seas (1). Yet there is a reluctance to take similar steps in the Arctic. We acknowledge that increased scientific effort and collaboration as recommended by C. Tesar *et al.* ("Toward strategic, coherent, policy-relevant arctic science," Policy Forum, 23 September, p. 1368) are much-needed steps for improved Arctic governance. But we are concerned that these steps provide policy-makers with an excuse to stall the protection of the Arctic marine ecosystem, under the premise of insufficient data.

A protected area network in the Arctic was initiated 20 years ago, based on best principles (2, 3). Yet, in 2015 the U.S. Chairmanship of the Arctic Council solicited yet another desktop study of Arctic MPAs (4). Are the policy-makers purposely dragging their feet because of the bountiful natural gas and oil reserves, fisheries potential, and expansion of shipping routes in the Arctic?

Management of marine resources at both poles faces similar issues of complicated multinational agreements and resource-exploitation conflicts. But unlike Antarctica, the Arctic hosts both local peoples, who play an important role and rely on the unique environment, and vast natural resources in an area that remains relatively undeveloped. Based on the Antarctic MPA designation process, the unquestionable growth of exploitative activities in the Arctic will only complicate the designation of an Arctic MPA network in the future (C. M. Brooks *et al.*, "Science-based management in decline in

the Southern Ocean," Policy Forum, 14 October, p. 185).

Given rapid environmental changes and the expansion of lucrative human activities in the Arctic, immediate implementation of an MPA network is essential. We implore the U.S. Chairmanship to proactively lead the Arctic member states to enact an Arctic MPA Network now to protect this increasingly vulnerable ecosystem and the people who inhabit it.

Nigel E. Hussey,^{1*} Robert G. Harcourt,² Marie Auger-Méthé³

¹Department of Biological Sciences, University of Windsor, Windsor, ON, N9B 3P4, Canada.

²Department of Biological Sciences, Macquarie University, Sydney, NSW 2109, Australia. ³Department of Mathematics and Statistics, Dalhousie University, Halifax, NS, B3H 4R2, Canada.

*Corresponding author. Email: nehussey@uwindsor.ca

REFERENCES

1. U.S. Department of State, "On the New Marine Protected Area in Antarctica's Ross Sea" (2016); www.state.gov/secretary/remarks/2016/10/263763.htm.
2. Conservation of Arctic Flora and Fauna, "Circumpolar Protected Areas Network (CPAN)—Strategy and action plan: CAFF habitat conservation report 6" (Directorate for Nature Management, 1996).
3. Conservation of Arctic Flora and Fauna, "Proposed protected areas in the circumpolar Arctic 1996: CAFF habitat conservation report 2" (Directorate for Nature Management, 1996).
4. Protection of the Arctic Marine Environment, "Framework for a pan-Arctic Network of marine protected areas" (2015); www.pame.is/images/03_Projects/MPA/MPA_Report.pdf.

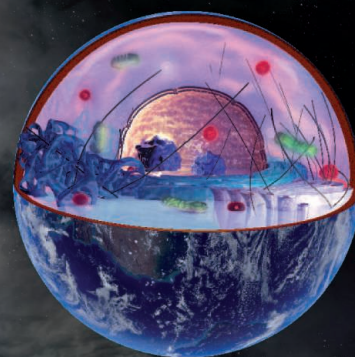
10.1126/science.aah6603

ERRATA

Erratum for the Editorial: "A comprehensive nuclear test ban" by E. J. Moniz, *Science* 354, 1081 (2016). Published online 9 December 2016; 10.1126/science.aam5318. In the print version, reference to the time frame of the effect of the international nuclear agreement with Iran was misstated. The online version of the Editorial contains the correct text.

Explore A World of Cellular Information

The human cell like never before.
A protein atlas of high-resolution microscopy images for you to explore for free.



THE CELL ATLAS
Created by researchers
for researchers

THE HUMAN PROTEIN ATLAS
www.proteinatlas.org

Inupiaq Eskimo hunters depend on Alaska's fragile ecosystem.

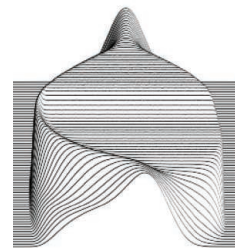


PHOTO: DESIGN PICS INC./ALAMY STOCK PHOTO

RESEARCH

Understanding solute mixing in microfluidic channels

Aminian et al., p. 1252



IN SCIENCE JOURNALS

Edited by **Stella Hurtley**



DEVELOPMENT ECONOMICS

Substituting minutes for money

In developing countries, bank branches and fixed-line telecommunications are scarce, whereas mobile phones are plentiful. These factors have led to the use of mobile money, whereby money can be used to purchase minutes, which can then be converted back into money. Suri and Jack show that increased access to mobile money has increased long-term consumption in Kenya and reduced the number of households in extreme poverty. —GJC

Science, this issue p. 1288

Two African women complete a mobile money transaction.

NEUROSCIENCE

Birds of a feather sing together

How do birds know that a song that they hear is from a member of their own species, and how do they learn their songs in the first place? Araki *et al.* identified two types of brain cells involved in how finches learn their songs (see the Perspective by Tchernichovski and Lipkind). When zebra finches were raised by Bengalese finch foster parents, they learned a song whose morphology resembled that of their foster father. However, the temporal structure remained zebra finch-specific, suggesting that it is innate. Gadagkar *et al.* recorded activity in specific dopamine neurons in singing zebra finches while controlling perceived song quality with

distorted auditory feedback. This distorted feedback represented worse performance than predicted and resulted in negative prediction errors. These findings suggest again that finches have an innate internal goal for their learned songs. —PRS

Science, this issue p. 1282, p. 1234;
see also p. 1278

ORGANIC CHEMISTRY

Catching a break in polyphenol synthesis

Chemical synthesis is usually rather different from playing with a modeling kit. If two large fragments of a molecule are not properly oriented, it is not typically possible to break them apart, rotate one, and then paste them back together. Yet that is precisely the trick that

Keylor *et al.* used to synthesize two plant-derived polyphenols. Resveratrol forms a variety of dimers, trimers, and tetramers. When one central carbon-carbon bond links the fragments, it is weak enough to break spontaneously and reversibly at room temperature. The authors leveraged this equilibrium to generate an efficient route to two of the tetramers, nepalensinol B and vateriaphenol C. —JSY

Science, this issue p. 1260

TOPOLOGICAL MATTER

An edge that is hard to get rid of

A distinguishing characteristic of topological insulators (TIs) is that they have conducting states on their boundary—a surface for a three-dimensional (3D) TI or a

line edge for a 2D TI. Sessi *et al.* used scanning tunneling spectroscopy to discover unusual 1D states in a 3D crystalline TI. The states appeared on the edge of a particular kind of step in the crystal and survived large magnetic fields and increased temperatures. This robustness bodes well for the potential use of these states in practical applications. —JS

Science, this issue p. 1269

ECOLOGICAL GENOMICS

Mapping genetic adaptations to pollution

Many organisms have evolved tolerance to natural and human-generated toxins. Reid *et al.* performed a genomic analysis of killifish, geographically separate and independent populations

of which have adapted recently to severe pollution (see the Perspective by Tobler and Culumber). Sequencing multiple sensitive and resistant populations revealed signals of selective sweeps for variants that may confer tolerance to toxins, some of which were shared between resistant populations. Thus, high genetic diversity in killifish seems to allow selection to act on existing variation, driving rapid adaptation to selective forces such as pollution. —LMZ

Science, this issue p. 1305;
see also p. 1232

SYNTHETIC BIOLOGY

Engineering cells to regulate glucose

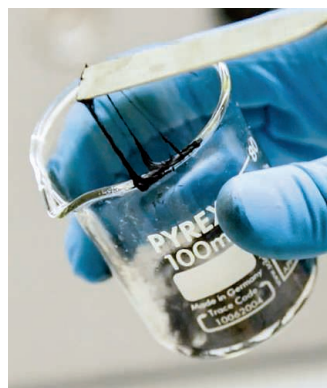
Diabetes mellitus affects hundreds of millions of people worldwide. Blood glucose levels are chronically deregulated in diabetics, and this can lead to many serious disorders, including cardiovascular disease and renal failure. Xie *et al.* engineered a synthetic circuit into human cells that can sense the glucose concentration and respond to correct deregulation. Implants containing designer cells improved glucose regulation in diabetic mice. —VV

Science, this issue p. 1296

COMPOSITES

Super sensitive, not so silly, putty

Many composites blend stiff materials, such as glass or carbon fibers, into a softer elastic polymer matrix to generate



Mixing graphene into Silly Putty

a material with better overall mechanical toughness. Boland *et al.* added graphene to a lightly cross-linked silicone polymer (also known as Silly Putty). The resulting composite has unusual mechanical properties, allowing the manufacture of strain sensors that can detect respiration and the footsteps of spiders. —MSL

Science, this issue p. 1257

PARKINSON'S DISEASE

A mitochondrial target for slowing PD

At present, there are no disease-modifying treatments to stall the progression of Parkinson's disease (PD). A drug in development to treat diabetes might provide a way to slow it down. The drug, MSDC-0160, targets a recently identified carrier of pyruvate (a major substrate for energy production) into mitochondria. Ghosh *et al.* successfully used the drug to block neurodegeneration in several different cellular and animal models of PD. Furthermore, in two mouse models of PD, cellular autophagy was restored and neuroinflammation was reduced. —OMS

Sci. Transl. Med. **8**, 368ra174 (2016).

INFECTIOUS DISEASE

Diseases emerge when forests degrade

Why emerging infectious diseases originate in tropical habitats remains a mystery, but habitat degradation may play a role. *Mycobacterium ulcerans* causes the tropical skin disease Buruli ulcer. Morris *et al.* looked for the presence of *M. ulcerans* in invertebrates and fish that they collected from 17 aquatic sites in French Guiana. They used molecular probes to quantify the mycobacterium and stable isotopes to quantify food web structure. Their findings linked habitat degradation to increases in the abundance of species lower down on the food chain—species more likely to carry the mycobacterium. —SN

Sci. Adv. 10.1126/sciadv.1600387 (2016).

IN OTHER JOURNALS

Edited by **Sacha Vignieri**
and **Jesse Smith**

METALLURGY

Steel goes for the quick draw

Steel is an important engineering material with properties that change with different processing techniques. Djaziri *et al.* found a new route for strengthening steel by using severe mechanical deformation. The improved strength comes from regions of Fe-C martensite, a known strengthening phase that normally requires quenching from high temperature. Extremely quick drawing of steel wires seems to have a similar effect without requiring high-temperature processing. —BG

Adv. Mater. 10.1002/adma.201601526 (2016).



DNA EVENTS

mRNA quality control

DNA is packaged into chromatin, and it must be actively unpacked, or remodeled, for genes to be transcribed into mRNA. That mRNA, synthesized in the nucleus, is also packed onto proteins, forming mRNA ribonucleoproteins (mRNPs). mRNPs are then shunted into the cytoplasm. Babour *et al.* show that one of the chromatin remodeling machines, the enzyme complex ISW1, has a second role in checking that mRNPs are properly packaged and competent to be exported to the cytoplasm. The ISW1 complex binds directly to the premature mRNPs, retaining them in proximity to their transcription sites. —GR

Cell **167**, 1201 (2016).

potential reason is the presence of immunosuppressive macrophages in the tumor microenvironment. Kaneda *et al.* and De Henau *et al.* now show in mice that inhibiting the lipid kinase phosphoinositide 3-kinase γ (PI3K γ), or deleting the gene that encodes it, turns immunosuppressive macrophages into immunostimulatory ones in a cell-intrinsic manner. Inhibiting PI3K γ in tumor-bearing mice led to greater T cell activation within tumors and, when combined with clinically available immunotherapies, to reduced tumor growth and improved overall survival. Clinical trials testing whether this strategy will also work in people are ongoing. —KLM

Nature **539**, 437, 443 (2016).

CANCER IMMUNOTHERAPY

Blocking PI3K γ makes cold tumors hot

Immunotherapy has changed the face of cancer treatment. However, despite some success, most individuals do not respond to this type of treatment. One

MICROBIOME

How fiber feeds a healthy gut

Starving bacteria in the gut may turn a beneficial microbial community into one that enhances disease susceptibility. Desai *et al.* explored the effects of eating adequate dietary fiber in a model



Strong steel is important for infrastructure such as the Golden Gate Bridge.

in which 14 well-characterized strains of human gut bacteria were inoculated into germ-free mice. A diet deficient in fiber increased the abundance of bacteria that digest the polysaccharides in the mucin layer that lines the gut. Thus, instead of helping digest the polysaccharides in dietary fiber, the microbiota attacked the protective layer of the intestinal wall. This allowed an introduced bacterial pathogen to grow and cause lethal colitis. The results may help establish the amounts and types of fiber that best maintain the protective mucin layer in the colon. —LBR

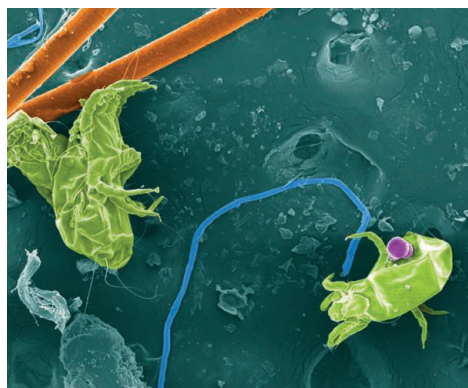
Cell **167**, 1339 (2016).

BIODIVERSITY Housemates

Whether we recognize it or not, we share our homes with a remarkable diversity of arthropods. Classifying the species that share our space is a challenging task. Madden *et al.* identified over 600 of these species by genotyping house dust collected by citizen scientists from over 700 homes across

the United States, revealing the presence of both expected species, such as cockroaches, and unexpected species, such as parasitic wasps. The characteristics of the home or the home occupants were more important for predicting occurrence than were climatic or regional factors, suggesting that home arthropod distributions cannot reliably be predicted from outdoor arthropod predictions but may represent groups of species that are well adapted to human environments. —SNV

Mol. Ecol. **10.1111/mec.13900** (2016).



Genetic screening of dust allows us to identify the arthropods that share our homes.

METROLOGY An on-chip cold-atom gravimeter

Gravimeters sense tiny changes in the local gravitational field and are used in geological studies, mineral exploration, and civil engineering to detect underground voids. Typically the size and weight of a small microwave oven, their operation is mechanical: A test mass pulls on a sensitive spring, and any difference in extension is compared with a reference point. Cold atoms cooled to their quantum ground state offer a quantum

mechanical approach for detecting gravity. Abend *et al.* have developed an on-chip cold-atom interferometer in which the active part of the sensor, including atom cooling and interference, takes up less than a cubic centimeter. The on-chip approach offers the prospect of

compact and sensitive gravimeters for field deployment. —ISO
Phys. Rev. Lett. **117**, 203003 (2016).

MATERIALS CHEMISTRY Forcing iron to bond to bismuth

Iron-bismuth compounds are of interest for extending the series of superconducting iron-pnictide materials, but the Fe–Bi bond has been elusive. One problem is the immiscibility of Bi in Fe. Walsh *et al.* report that the formation of FeBi₂ can be observed under extreme pressure conditions created with diamond anvils. Previous work was unsuccessful with the lower-pressure (body-centered cubic) phase of iron, so pressures sufficient to create its face-centered cubic phase were needed. At pressures above 30 GPa and temperatures of ~1500°C, a phase was observed in x-ray diffraction in which each iron atom coordinated to eight Bi atoms, along with stabilizing Bi–Bi interactions. Once formed, the material was stable down to 2.9 GPa. —PDS

ACS Central Sci. **10.1021/acscentsci.6b00287** (2016).

ALSO IN SCIENCE JOURNALS

Edited by Stella Hurtley

CHEMISTRY

Cooperation between frustrated partners

What might you do with a hat that had so many decorations dangling from the brim that you couldn't put it on? Lewis acids and bases are the molecular versions of hats and heads. Stephan reviews the surprising chemistry of so-called frustrated Lewis pairs (FLPs), which cannot form their natural complex together. Over the past decade, such systems (most often comprising a borane with a nitrogen or phosphorus partner) have been used to catalyze hydrogenation reactions, activate a number of other small molecules, and generally promote a wide range of cooperative chemical reactivity. —JSY

Science, this issue p. 1248

MICROFLUIDICS

Aspects of the design

In microfluidics systems, the small size of the channels ensures that the flow profiles are laminar, so solute mixing is largely governed by diffusion in the absence of active mixing. Aminian *et al.* revisited the classic phenomenon of Taylor diffusion to investigate the effects that the aspect ratio of the conduit has on the long-time axial distribution of solutes. They show both numerically and experimentally that the aspect ratio controls the skewness of this distribution, and thus pipe design alone is enough to control mixing profiles. —MSL

Science, this issue p. 1252

ASYMMETRIC CATALYSIS

Crafting chiral boron building blocks

Carbon-boron bonds are easily transformed into a wide variety of C–C, C–N, and C–O bonds. With that flexibility in mind, Schmidt *et al.* show that nickel complexes can catalyze asymmetric alkylation of carbon centers adjacent to boron. This protocol creates chiral

alkylboronates that function as stable precursors to numerous complex molecules. The reaction proceeds in stereoconvergent fashion—forming a single product from either mirror image of the α -haloboronate reagent. Successive reactions can also create chains of adjacent chiral alkyl centers with stereochemistry set by the configuration of the ligand bound to nickel. —JSY

Science, this issue p. 1265

RADIO ASTRONOMY

Probing the intergalactic magnetic field

Fast radio bursts (FRBs) are powerful flashes of astronomical radio waves that last just milliseconds and whose origins are a matter of debate. Ravi *et al.* discovered a FRB that is exceptionally bright (see the Perspective by Kaspi). This allowed them to measure how the polarization of the signal varies with wavelength (Faraday rotation). Combining this with the time delay of the flash at different wavelengths revealed the mean magnetic field along the line of sight. Assuming that the FRB originates from a colocated galaxy, the results constrain the intergalactic magnetic field and will inform models of galaxy formation and cosmology. —KTS

Science, this issue p. 1249;

see also p. 1230

ORIGIN OF LIFE

Beating the curse of the parasite

The evolution of molecular replicators was a critical step in the origin of life. Such replicators would have suffered from faster-replicating “molecular parasites” outcompeting the parental replicator. Compartmentalization of replicators inside protocells would have helped ameliorate the effect of parasites. Matsumura *et al.* show that transient compartmentalization in nonbiological

materials is sufficient to tame the problem of parasite takeover. They analyzed viral replication in a droplet-based microfluidic system, which revealed that as long as there is selection for a functional replicator, the population is not overwhelmed by the faster-replicating parasite genomes. —GR

Science, this issue p. 1293

VIRAL EVOLUTION

A laboratory model of viral speciation

New species arise through the evolution of barriers to reproduction. This process is well understood where the emerging species are spatially isolated from one another. But the process of sympatric speciation—where the diverging species co-occur—is more enigmatic. Bacterial viruses make good models for addressing such questions because of their rapid generation times. Meyer *et al.* took bacteriophage λ and grew it on a mix of two strains of *Escherichia coli*. The virus duly split its host preferences into lineages with differing affinity for their respective *E. coli* hosts. In some experiments, the phages diverged to the extent that they became reproductively restricted to one strain of *E. coli*, even when the other was present. —LMZ

Science, this issue p. 1301

BRAIN RESEARCH

Time is a subjective experience

Time, like space, is one of the fundamental dimensions of all our experiences. However, organisms do not work like clocks, and our judgment about the passage of time is variable, depending on circumstances. Soares *et al.* systematically investigated midbrain dopaminergic neurons during timing behavior in mice (see the Perspective by Simen and Matell). When measuring and manipulating mouse activity, the authors

observed that dopaminergic neurons controlled temporal judgments on a time scale of seconds. —PRS

Science, this issue p. 1273;

see also p. 1231

CLIMATE

Pacemaker of the ice ages, 40 years on

In a *Science* paper published 40 years ago, geoscientists Hays, Imbrie, and Shackleton provided evidence that small changes in Earth's orbit around the Sun are behind the ice age cycles of the past ~2.5 million years. They thus provided observational support for the Milankovitch theory that until then had been difficult to verify. In a Perspective, Hodel explores the history of this influential discovery and the continuing challenges in understanding the underlying mechanisms. Focusing on ice growth phases rather than deglaciations and exploring the period before 0.8 million years ago may be particularly helpful for understanding these mechanisms. —JFU

Science, this issue p. 1235

CALCIUM SIGNALING

Inhibiting calcium uptake ubiquitously

The membrane transporter SERCA keeps cytoplasmic calcium levels low. Micropeptides that inhibit SERCA in muscle have been characterized. Anderson *et al.* sought to identify micropeptides that could perform this inhibitory function in nonmuscle tissues. Like their muscle-specific counterparts, ELN (endoregulin) and ALN (another-regulin) inhibited the activity of SERCA isoforms that are abundant in nonmuscle tissues. Thus, micropeptides may regulate other membrane transporters that are structurally related to SERCA. —WW

Sci. Signal. **9**, ra119 (2016).

REVIEW SUMMARY

CHEMISTRY

The broadening reach of frustrated Lewis pair chemistry

Douglas W. Stephan

BACKGROUND: Since the work of Sabatier 100 year ago, chemists have turned almost exclusively to metals to activate H_2 by weakening or cleaving its central bond. This paradigm changed with a 2006 report of a metal-free molecule that reversibly activated H_2 across sterically encumbered Lewis acidic boron and Lewis basic phosphorus sites. Shortly thereafter, similar reactions were mediated by systems described as “frustrated Lewis pairs” (FLPs) that were derived from simple combinations of electron donors and acceptors in which steric demands precluded dative bond formation. The variety of such systems has since been expanded to include a wide range of donors and acceptors. Moreover, FLP reactivity has been shown to result when equilibria governing the

formation of Lewis acid-base adducts provides access to free acid and base. Mechanistic studies have demonstrated that the FLP activation of H_2 proceeds via a mechanism directly analogous to the Piers mechanism for borane-mediated hydrosilylation of ketones, first described in 1996. Nonetheless, the discovery of these metal-free reactions of H_2 has prompted considerable interest in this concept and its application to various chemical systems.

ADVANCES: The application of FLP reactivity with H_2 to metal-free hydrogenation catalysis rapidly led to reductions of polar substrates. Over the past decade, the range of reducible substrates has been expanded to a variety of unsaturated compounds, including imines, enamines,

olefins, polyaromatics, alkynes, ketones, and aldehydes. Efforts have also extended this technology to asymmetric hydrogenations, with a number of recent systems achieving high selectivity.

Early on, it was recognized that the reactivity of FLPs was not limited to H_2 . FLPs have shown the capacity to capture and react with a variety

ON OUR WEBSITE

Read the full article at <http://dx.doi.org/10.1126/science.aaf7229>

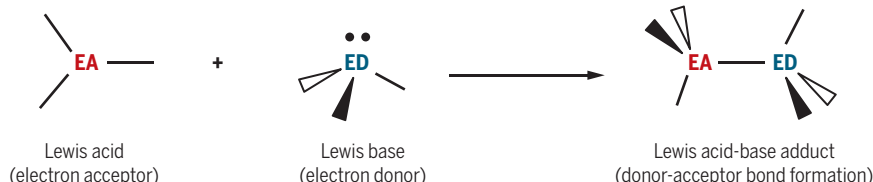
of small molecules, including olefins, alkynes, CO_2 , SO_2 , NO , CO , N_2O , and *N*-sulfinyltolylamines (*p*-tol)NSO (*p*-tol, *para*-tolyl). This has led to metal-free strategies for CO and CO_2 reduction and SO generation and new avenues to transient, persistent, or stable radicals. FLP chemistry has been further extended to new strategies in synthetic organic chemistry, including FLP-mediated approaches to hydroamination, hydroboration, cyclization, and boration reactions.

Because transition metals may also be acidic or basic, the reactivity of FLP systems in which one or both of the constituents are metal centers has been reported. Further, metal components can also be ancillary fragments for ligand-based FLP chemistry, or they can act as a scaffold, allowing the cooperative action of an FLP and a metal center on a substrate. In related developments, the notion of FLPs has been applied to the design of model systems for the active sites of the [Ni-Fe], [Fe-Fe], or [Fe] hydrogenase enzymes.

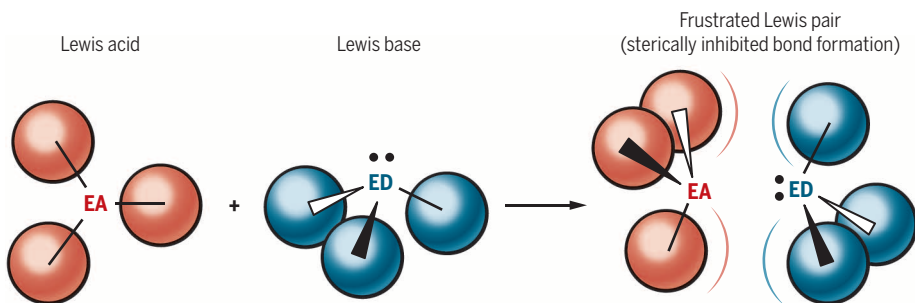
Reaching beyond main-group and organic chemistry into polymers and materials chemistry, FLP catalysts have been used to prepare lactone-derived polymers, cyanamide oligomers, and Te-containing heterocycles for applications in photoactive materials. In addition, heterogeneous FLP hydrogenation catalysts have emerged, and the concept also provides a new mechanistic perspective on CO_2 reduction on the surface of indium oxide nanocrystals.

OUTLOOK: Applications of FLP chemistry to metal-free reductions, asymmetric hydrogenations, C–C bond formation, and C–H bond functionalization are continuing to evolve. Such advances offer strategies for reduced costs and the elimination of toxic contaminants that will undoubtedly garner interest from the synthetic chemistry communities in academia and industry. The expanding range of main-group and transition metal-based FLPs continues to demonstrate the generality of this concept and its broadening utility. However, the innovative synthetic strategies, reactivity, and new perspectives derived from the application of this simple concept to other areas of chemistry are perhaps the most exciting prospect. ■

Classical Lewis acid-base chemistry



Frustrated Lewis pair chemistry



A recent paradigm for chemical reactivity, designated “frustrated Lewis pairs,” is based on impeded dative bonding between a Lewis acid and a Lewis base. For almost 100 years, the combination of electron acceptors (Lewis acids) and electron donors (Lewis bases) has been known to give Lewis acid-base adducts that incorporate donor-acceptor bonds. However, research over the past decade has shown that the introduction of steric demands or a dissociative equilibrium provides access to free donors and acceptors, allowing them to interact with a third molecule and leading to distinct reactivity. This concept has been applied to a broadening range of chemical problems.

Department of Chemistry, University of Toronto, 80 St. George Street, Toronto, Ontario M5S3H6, Canada.

Email: dstephan@chem.utoronto.ca

Cite this article as D. W. Stephan, *Science* **354**, aaf7229 (2016). DOI: [10.1126/science.aaf7229](https://doi.org/10.1126/science.aaf7229)

REVIEW

CHEMISTRY

The broadening reach of frustrated Lewis pair chemistry

Douglas W. Stephan

The revelation that combinations of Lewis acids and bases for which dative bonding is impeded can activate dihydrogen led to the concept of “frustrated Lewis pairs” (FLPs). Over the past decade, a range of FLP systems and substrate molecules have precipitated a paradigm change in main-group chemistry and metal-free catalysis. The FLP motif has also found application in a growing body of chemical problems in organic synthesis, transition metal and free radical chemistry, materials, enzymatic models, and surface chemistry. The current state of FLP chemistry is assessed herein, and the outlook for the future considered.

Lewis classified electron-accepting and electron-donating molecules as acids and bases, respectively, in the 1920s. This axiom predicts that combinations of a donor phosphine and an acceptor borane should react to form a P–B bonded adduct. Although this is generally observed, geometric constraints and/or sterically demanding substituents can deter such bonding. Probing the reactivity of such “frustrated” systems led to the discovery of the reversible activation of H₂ by the main-group compound *p*-(Mes₂P)C₆F₄[B(C₆F₅)₂] (**1**) (Mes, mesityl) in 2006 (Fig. 1A) (*1*). The ability of the combination of unquenched Lewis acid and base to cleave H₂ contravened 100 years of chemical dogma, which had asserted that such reactions required a metal. Studies the next year (*2, 3*) replaced the initial esoteric phosphine and borane with simpler combinations of electron donors (Lewis bases) and acceptors (Lewis acids) for which steric demands precluded classical adduct formation, leading to the formulation of a new paradigm for chemical reactivity arising from frustrated Lewis pairs (FLPs).

Since this early work, the scope of Lewis acids and bases that generate FLPs has been expanded by multiple research groups. Systematic studies have probed electrophilic Lewis acids (derived from groups 13 to 15 in the periodic table) in combination with Lewis basic nucleophiles (groups 14 to 16) in both inter- and intramolecular FLP systems, demonstrating exceptional capacities to activate H₂ and other substrates (*4, 5*). Although steric frustration is typically used to access FLP reactivity, classical Lewis acid-base adducts for which dissociative equilibria provide free acid and base also exhibit similar reactivity, illustrating the continuum of the FLP paradigm (*4–7*).

FLP reactions typically involve three components: two reagents cooperatively acting on a substrate molecule. The reactivity of FLPs has been demonstrated with a broad range of electron-rich

and electron-deficient reagents and a variety of small-molecule substrates, affording new avenues to catalysis. In addition, the notion of FLPs has been applied in fields disparate from main-group chemistry. This Review highlights the major advances over the past decade and the areas where applications are emerging, illustrating the broadening reach of the FLP concept.

Hydrogenation catalysis

An obvious application of FLP activation of H₂ is metal-free hydrogenation catalysis, and a 2007 report (*8*) demonstrated the FLP-mediated reductions of imines, aziridines, and protected nitriles. The scope of polar substrates has since been expanded dramatically to include enamines, silylenol-ethers (*4, 5*), enones (*9*), oximes (*10*), olefins (*11*), and polyaromatics (*12*) (Fig. 1B). In the latter two cases, a weak base is required so that the conjugate acid can protonate the substrate, generating a transient carbocation that captures hydride from the hydridoborate. Dissociation of the diethylether-B(C₆F₅)₃ adduct provides a free donor and acceptor that together act on H₂, effecting such reductions (*13*). This mechanism illustrates that FLP reactivity is accessible across a continuum spanning classical adducts to sterically frustrated pairs.

Reactions in which FLPs activate H₂ appear termolecular but occur at rates greater than expected from entropic considerations. Ten years before the articulation of the FLP concept, Parks and Piers established the mechanism of seemingly termolecular reactions in which a borane catalyzes the hydrosilylation of carbonyl species (*14*). Subsequent computational and experimental work has shown that the FLP activation of H₂ proceeds via a modified Piers mechanism (*7*). The computational studies (*15–19*) showed that the sterically frustrated Lewis acid and base generate an “encounter complex,” in which steric demands preclude dative bonding but are stabilized by van der Waals interactions. The encounter complex then reacts in a bimolecular fashion with H₂. Intramolecular FLPs follow a similarly

concerted pathway to H₂ cleavage. Recent calorimetric studies for FLP H₂ activation by (Mes₂P)C₂H₄[B(C₆F₅)₂] (**2**) afforded a reaction enthalpy of –43(4) kJ mol^{–1}, and time-resolved calorimetry under varying H₂ pressures showed pseudo first-order kinetics in H₂, suggesting that H₂ activation by the FLP is rate-limiting. The free energy for heterolytic splitting of H₂ was estimated to be –29.8(1.3) kJ mol^{–1} at 295 K in toluene (*20*).

Recent advances have broadened the substrate scope for FLP reductions. Repo and co-workers (*21*) exploited the intramolecular FLP C₆H₄(NMe₂)[B(C₆F₅)₂] (**3**) to selectively cis-hydrogenate nonfunctionalized internal alkynes (Fig. 1B). This reaction proceeds via initial protodeborylation of the catalyst precursor to generate C₆H₄(NMe₂)[BH(C₆F₅)] with liberation of C₆F₅H. Alkynes undergo hydroboration by this species to afford an FLP that activates H₂. Subsequent protonolysis liberates the *cis*-alkene and regenerates the active catalyst.

Initial attempts to reduce ketones in toluene by using H₂ and B(C₆F₅)₃ at 110°C led to the stoichiometric formation of borinic esters of the form RCH₂OB(C₆F₅)₂ and C₆F₅H (*22*). In contrast, performing reactions in ethereal solvents showed that catalytic borane effected the hydrogenation of carbonyl substrates (*23, 24*). Solvent participates in hydrogen bonding to the carbonyl, enhancing its electrophilicity and precluding loss of C₆F₅H. Molecular sieves or cyclodextrins achieved similar stabilization of transiently protonated carbonyl species in toluene, allowing for borane-catalyzed reduction of ketones (*25*).

FLP reductions of sterically hindered anilines to cyclohexylammonium salts have also been achieved (Fig. 1B) (*26*). These reductions consume four equivalents of H₂ but sequester the FLP in the product salt. Similar reductions of pyridines, quinolones, and quinoxalines (*27, 28*) afforded routes to the corresponding saturated heterocycles. Few homogeneous transition metal-based catalysts effect such transformations.

Modifications of FLP catalysts for asymmetric reduction began with seminal work from Chen and Klankermeyer (*29*), who demonstrated imine reduction with a pinene-derived borane (**4**) in 13% enantiomeric excess (ee) (Fig. 1C). Subsequently, modified chiral camphor-derived boranes (**5** and **6**) improved stereoselectivity to greater than 80% ee (*30*). Liu and Du (*31*) have developed a chiral *bis*-borane (**7**) derived from in situ hydroboration of axially chiral-substituted divinylbinaphthyl species that catalyzed asymmetric imine hydrogenation with stereoselectivities as high as 89% ee. Repo and co-workers (*32*) developed a chiral aminoborane catalyst (**8**) for enamine and unhindered imine reductions that yielded amines with stereoselectivities of up to 99% ee. Computational studies show the importance of steric repulsion and stabilization of intermolecular noncovalent forces in determining stereoselectivity. Using *bis*-borane catalysts related to **7**, Du and colleagues achieved the reduction of silylenol-ethers (*33*), pyridines (*28*), and a range of 2,3-disubstituted quinoxalines

Department of Chemistry, University of Toronto, 80 St. George Street, Toronto, Ontario M5S3H6, Canada.
Email: dstephan@chem.utoronto.ca

to give chiral alcohols, *cis*-piperidines, and tetrahydroquinoxalines (34), respectively, with selectivities up to 96% ee. Most recently, chiral *bis*-boranes in combination with PCy₃ (Cy, cyclohexyl) have been used to hydrogenate a series of 1,2-dicarbonyl compounds to give chiral α -hydroxy ketones and esters with 86 to 99% ee (35).

FLP catalysts have been broadened beyond electrophilic boranes. For example, borenium cations (e.g., 9) accessed via hydride abstraction from NHC-borane adducts (36, 37) yield cations that are sufficiently electrophilic to effect H₂ activation with imines and enamines (Fig. 1D). Subsequent work by Crudden and colleagues (38) extended such catalysis to mesoionic borenium cations. In related work, the borenium cation [(acridine)BCl₂][AlCl₄], in combination with (2,4,6-*t*Bu)pyridine (*t*Bu, *tert*-butyl), heterolytically activated H₂ at 100°C, delivering hydride to C-9 of the acridine (39). More recently, Clark and Ingleson

demonstrated that *N*-methylacridinium salts form FLPs with 2,6-lutidine, activating H₂ even in the presence of H₂O. With judicious choice of the anion, such cations catalyze transfer hydrogenation and hydrosilylation of aldimines (40).

In an alternative approach, electrophilic phosphonium cations, which derive Lewis acidity from a low-lying σ^* orbital (41), have been exploited in hydrodefluorination, dehydrocoupling, hydrosilylation (42), and C-F arylation catalysis (43, 44). In proof-of-principle experiments, [FP(C₆F₅)₃][B(C₆F₅)₄] (10) and a bulky amine gave rise to FLP hydrogenation of olefins (45).

Small-molecule activation

Beyond the activation of H₂, a variety of other small molecules are captured by FLPs (Fig. 2) (4, 5). For example, Ashley *et al.* (46) showed the potential of FLPs to effect the reduction of CO₂ to methanol. This result spurred investigation

of a variety of FLPs for CO₂ capture (47) and reduction. Catalytic reduction to CO was achieved with excess phosphine, mediated by in situ-generated *bis*-phosphaylide and Zn-halide (48). FLP-mediated hydroboration of CO₂ affords methoxyboranes, ultimately a source of methanol (49, 50). In an advance that could facilitate catalyst design, Kumacheva and co-workers developed an innovative microfluidic approach to measure thermodynamic data for the rapid capture of CO₂ by the *t*Bu₃P/CIB(C₆F₅)₂ FLP (51).

In addition to CO₂, FLPs can capture SO₂, N₂O, NO, and CO (Fig. 2, 11 to 16) (47). Whereas SO₂ binds in a fashion analogous to CO₂, N₂O forms a linear PN₂OB linkage. The FLP adduct of NO is a persistent radical (Fig. 2, 15). FLPs also mediate the stoichiometric reduction of CO in the presence of HB(C₆F₅)₂ (52) or H₂ (53).

Previously unknown reactions of FLPs with small molecules continue to emerge. For example,

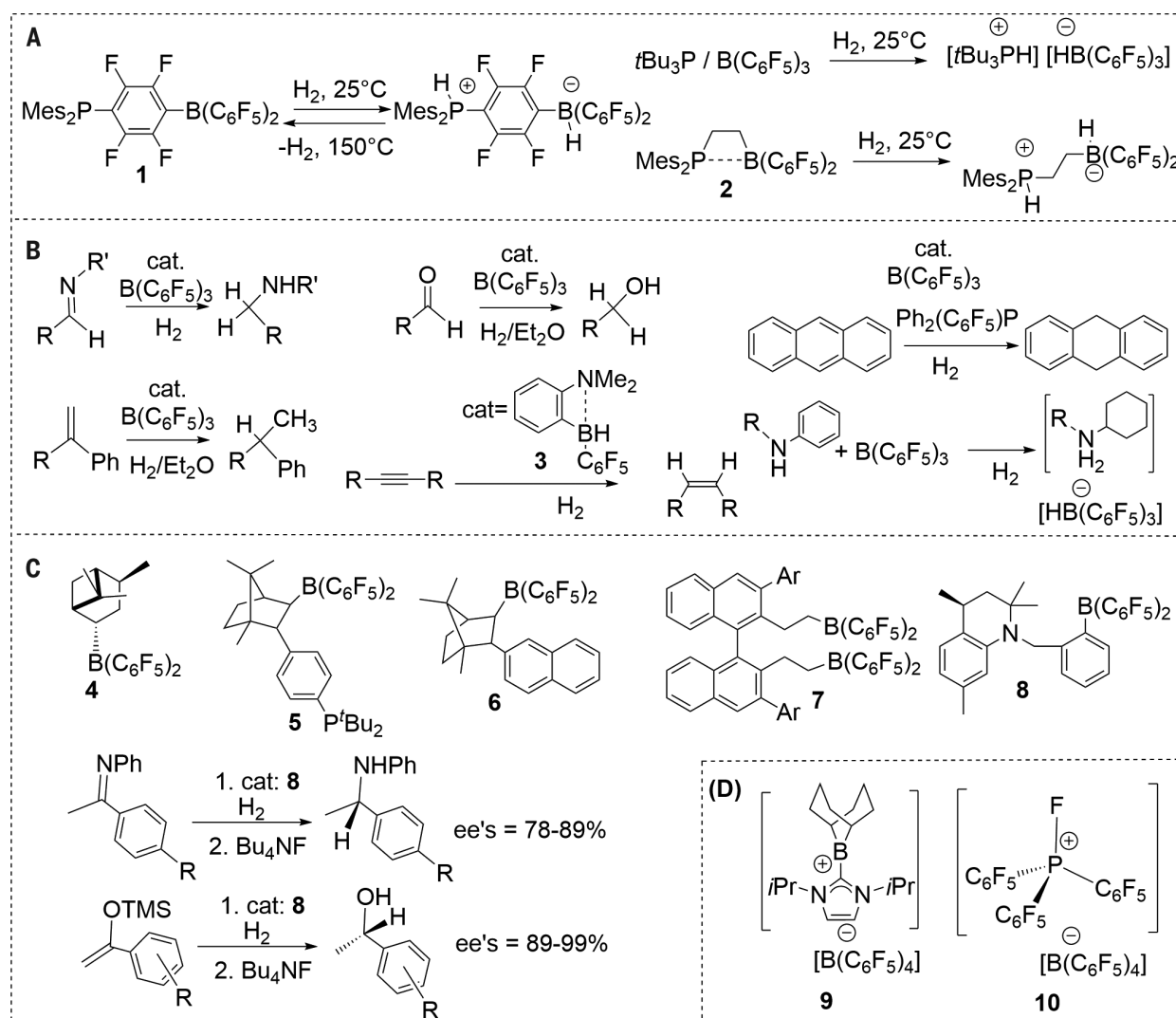


Fig. 1. Reactions of frustrated Lewis pairs (FLPs) with H₂. (A) Stoichiometric reaction of FLPs with H₂. (B) Catalytic and stoichiometric hydrogenations. (C) Asymmetric FLP catalysts and examples of stereoselective reductions. (D) Cationic FLP Lewis acid catalysts used in hydrogenations. cat., catalyst; ee, enantiomeric excess; Et, ethyl; *i*Pr, iso-propyl; Mes, mesityl; Ph, phenyl; *t*Bu, *tert*-butyl; TMS, trimethylsilyl. R and R' indicate various alkyl or aryl substituents.

FLP reaction with *N*-sulfinyltolylamine (*p*-tol)NSO (*p*-tol, *para*-tolyl), leads to binding via P–N and B–O bonds (Fig. 2, **17**). These products, formulated as phosphinimine-borane adducts of sulfur monoxide, effect the transfer of SO to several other reagents (**54**). Erker and co-workers (**55**) described the reaction of a FLP with CO, HB(C₆F₅)₂, and NO, resulting in CO–NO coupling to give a C=N double bond (Fig. 2, **18**) via a radical pathway.

Organic chemistry

The reactivity of FLPs with organic molecules was first demonstrated with reactions of P/B FLPs with olefins (**56**), alkynes (**57**), and cyclopropanes (**4**, **5**) giving zwitterionic addition products. Such reactivity has been exploited to generate heterocycles and to functionalize pyrroles (**4**, **5**). More recently, B(C₆F₅)₃ was shown to catalyze the addition of arylamines to terminal alkynes to give the corresponding enamines (Fig. 3A). Such hydroaminations were also performed in tandem with FLP hydrogenations, providing a one-pot synthesis of arylamine derivatives (**58**).

FLP reactions of alkynes have also been exploited to induce intramolecular cyclizations of sterically encumbered amines (**4**, **5**), propargyl amides, ureas, carbamates, and carbonates under mild conditions (**59**, **60**). These reactions amount to FLP addition to alkyne. Cyclic intermediates can be isolated, but secondary propargyl amides are catalytically converted to oxazoles (Fig. 3B) (**59**). Propargyl esters yield 1,3-carboboration allyl boron products via an initial cyclization and subsequent ring opening with C₆F₅-group migration (**61**). Conversely, internal propargyl esters provide stable zwitterionic 1,3-dioxolium compounds (**62**). Allenes react with FLPs to give 1,4-addition products, but allenyl ketones and esters react with B(C₆F₅)₃ to give 1,2-carboboration products. In each case, the Lewis acid activates the allene, prompting either C₆F₅ migration or nucleophilic attack by base, respectively (**63**).

Borenium cations have also been exploited as Lewis acids in stoichiometric synthetic chemistry, giving rise to syn-1,2-carboboration of alkynes (Fig. 3C) (**64**). More recently, Ingleson and co-workers (**65**) developed a catalytic process using B(C₆F₅)₃ in the presence of a borane-carbene adduct to achieve alkyne hydroboration. These reactions proceed by hydride abstraction from the borane-carbene adduct, generating a borenium cation and the nucleophilic borohydride [HB(C₆F₅)₃][−]. This latter species interacts with the activated alkyne, affording trans-hydroboration. Crudden and colleagues (**66**) generated borenium salts by B–H bond cleavage in pinacolborane by using B(C₆F₅)₃ or [Ph₃C]⁺ and 1,4-diazabicyclo[2.2.2]octane, leading to imine hydroboration.

In a major advance, Fontaine and co-workers (**67**) used the intramolecular FLP 1-TMP-2-BH₂-C₆H₄ (TMP, tetramethylpiperidine) to activate heteroarene C–H bonds, catalyzing the borylation of furans, pyrroles, and electron-rich thiophenes (Fig. 3D). Repo and colleagues further expanded the reaction scope to include arene and alkyne C–H bonds (**68**). Mechanistically, these reactions

involve the cleavage of a heterocycle C–H bond by the Lewis acid and base. Subsequent reaction of the B–C bond with HBpin (pin, pinacolate) affords the borylated product, whereas liberation of H₂ regenerates the catalyst.

Radical chemistry

FLPs derived from R₃P (R = *t*Bu, Mes, naphthyl) and two equivalents of Al(C₆F₅)₃ and N₂O provide a route to the transient frustrated radical pair (R₃P)^{•+}{[μ-O•][Al(C₆F₅)₃]₂}[−] (**19**) (**69**), which

affects C–H bond activation of either phosphine substituents or solvent to give salts including {*t*Bu₂PMe[C(Me)=CH₂]}{[μ-HO][Al(C₆F₅)₃]₂} (Me, methyl) and [(naphthyl)₃PCH₂Ph]{[μ-HO][Al(C₆F₅)₃]₂}. The analogous reaction of Mes₃P, Al(C₆F₅)₃•toluene, and N₂O in toluene gives the purple salt (Mes₃P)^{•+}{[μ-HO][Al(C₆F₅)₃]₂}[−] (**20**), a rare example of a P(IV) radical cation salt (Fig. 4A).

An ethylene-bridged P/B FLP captures NO to yield the persistent radical Mes₂P(CH₂)₂B(C₆F₅)₂(NO)[•] (**15**) (**70**), which reacts with toluene to give

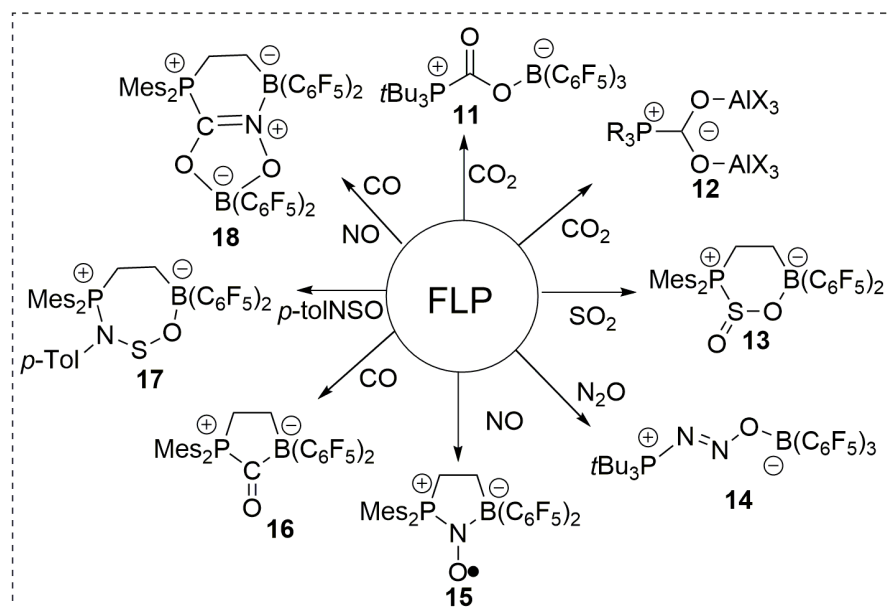


Fig. 2. Examples of FLP reactions with small molecules.

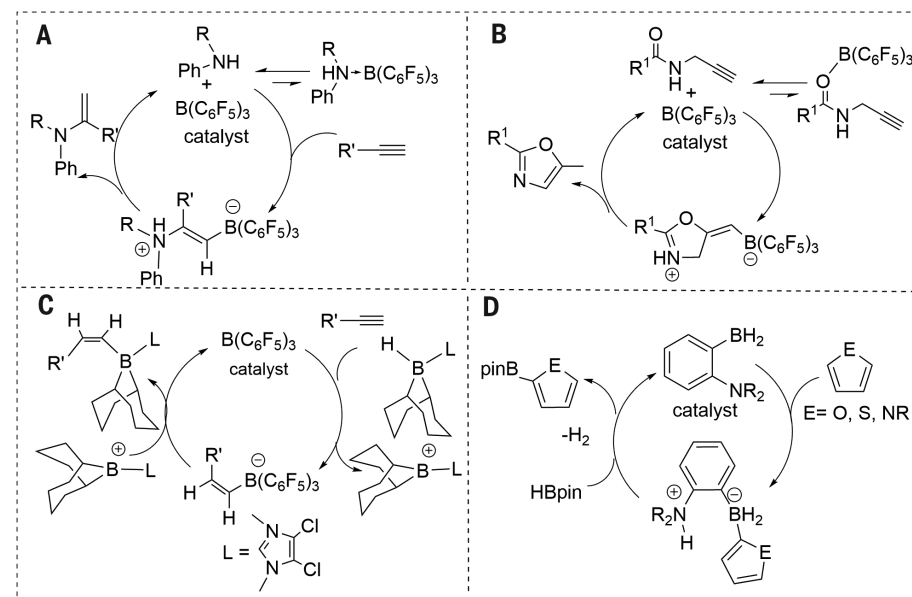


Fig. 3. Catalytic routes to organic derivatives. (A) Catalytic hydroamination. (B) Catalytic intramolecular cyclization. (C) Stoichiometric syn-1,2-carboboration of alkynes. (D) Catalytic C–H bond borylation.

$\text{Mes}_2\text{P}(\text{CH}_2)_2\text{B}(\text{C}_6\text{F}_5)_2(\text{NOH})$ and $\text{Mes}_2\text{P}(\text{CH}_2)_2\text{B}(\text{C}_6\text{F}_5)_2(\text{NOCH}_2\text{Ph})$ (Fig. 4B). Related NO-radical FLP species behave as oxygen-centered radicals to give rise to radical polymerizations of styrene (70).

More recently, efforts to reduce phenanthrene- or pyrene-diones with H_2 and $\text{B}(\text{C}_6\text{F}_5)_3$ led to the isolation of boron-derived radicals (Fig. 3C, 21) (71). These species are air-stable and undergo facile one-electron reductions to give related borate anions.

Transition metal chemistry

The FLP paradigm has also provided a strategy for the activation of small molecules by transition metal-based systems. Erker, Wass, and others (4, 5, 72) demonstrated that sterically frustrated combinations of a donor with electron-deficient metal centers such as Ti, Zr, or Hf react with a variety of small molecules including H_2 , CO_2 , alkenes, and alkynes, in direct analogy to main-group FLPs (Fig. 5A, 22). Subsequently, a Ru complex with pendant phosphine donor (23) was shown to stoichiometrically capture and catalytically hydroborate CO_2 (Fig. 5A) (73). Such combinations of a metallic acid and a donor base are conceptually reminiscent of the Noyori bifunctional catalysts (74). Ozerov and co-workers noted this analogy in describing three-coordinate Pd- and Pt-amide-chelate cations that effect aromatic C-H, alkynyl C-H, B-H, and B-B bond activations as FLPs (75).

The inverse situation, in which an electron-rich metal center acts as a Lewis base in concert with a Lewis acid, has drawn less attention. Berke and colleagues (76) investigated the action of a ReH

species and $\text{B}(\text{C}_6\text{F}_5)_3$ on CO_2 , whereas Wass and co-workers (77) described the activation of H_2 , CO_2 , and ethylene by the FLP composed of the three-coordinate complex $\text{CH}_2(\text{CH}_2\text{PtBu}_2)_2\text{PtCO}$ (24) and $\text{B}(\text{C}_6\text{F}_5)_3$ (Fig. 5B). Similarly, Lin and Peters (78) developed the chemistry of a Ni(0) complex, $\text{PhB}(\text{C}_6\text{H}_4\text{PPh}_2)_2\text{Ni}$ (25), where the electron-rich metal and electron-deficient boron act in concert to activate H_2 , giving $\text{PhBH}(\text{C}_6\text{H}_4\text{PPh}_2)_2\text{NiH}$ (Fig. 5B). The authors noted the conceptual analogy to FLPs and subsequently extended the chemistry to hydrogenation catalysis.

In recent work from Mankad (79), the chemistry of bimetallic complexes of the form $(\text{NHC})\text{MM}'\text{Cp}(\text{CO})_2$ (M, Ag, Cu; M', Fe, Ru) (80) were shown to catalyze the hydrogenation of alkynes. The proposed mechanism involves the cooperative activation of H_2 , and computations showed a transition state encompassing interactions of H_2 with the Lewis acidic Cu and basic Ru, in direct analogy to that computed for P/B FLPs (Fig. 5C, 26) (15). Mankad and colleagues used related bimetallic complexes in stoichiometric B-H activations (81) and catalytic arene borylations (82).

Metal centers can also be ancillary to either Lewis acidic or Lewis basic fragments involved in FLP chemistry. For example, in the Ru complex $\{[(\text{Ph}_2\text{PC}_6\text{H}_4)_2\text{B}(\eta^6\text{-Ph})]\text{RuCl}\}[\text{B}(\text{C}_6\text{F}_5)_4]$ (27) (83, 84), the η^6 interaction of the phenyl ring with Ru generates Lewis acidic carbon atoms that participate in FLP hydrogenation of imines (Fig. 5D). In contrast, combinations of the β -carbon of Ru acetylides and $\text{B}(\text{C}_6\text{F}_5)_3$ act as FLPs, reacting with alkynes, CO_2 , and aldehydes to effect FLP addition across the substrate molecule (85). Most

recently, Ison and co-workers (86) reported the formation of Lewis acid-base adducts of an oxo-Re complex (28) with $\text{B}(\text{C}_6\text{F}_5)_3$ (Fig. 5D). Heating to 100°C prompts dissociation, allowing catalytic FLP hydrogenation of unactivated olefins. Kinetic and mechanistic data are consistent with a mechanism in which H_2 is split between the terminal oxo atom and boron.

In a creative strategy to exploit FLPs, Szymczak and colleagues (87) developed a V terpyridine complex with a donor and an acceptor positioned in the secondary coordination sphere (29) so as to allow for cooperative action of the metal center and the FLP on the substrate molecule, $[\text{N}_2\text{H}_3]^+$ (Fig. 5E).

Enzyme models

One function of protein scaffolds in enzymes is to create separated environments for electron-rich and electron-poor sites. This function is conceptually analogous to the role of steric bulk in FLPs. This analogy has been furthered in the case of hydrogenases, enzymes that effect the reversible oxidation of H_2 to protons, via $[\text{Ni-Fe}]$, $[\text{Fe-Fe}]$, or $[\text{Fe}]$ active sites. In these enzymes, both the metal centers and protein matrix are engaged in the reactivity. DuBois, Bullock, and co-workers (88) developed enzyme model systems that combine a metal center with pendant noncoordinating amine donors, as in the Ni(II) complex $[\text{L}_2\text{Ni}]^{2+}$ (30) (Fig. 6A). The pendant amine groups act in concert with the Ni center to give rise to electrochemical oxidation of H_2 . The mechanism involves coordination of H_2 to Ni, proton transfers to the pendant amine groups, and electrochemical reduction of the transient Ni(0) species. The authors noted the direct analogy to FLPs and have extended this strategy to related Fe and Mn electrocatalysts for H_2 oxidations (89).

The $[\text{Fe}]$ -hydrogenase involves a mononuclear Fe-guanylylpyridinol cofactor (90) that catalyzes the reduction of methenyltetrahydromethanopterin (31) to methylenetetrahydromethanopterin (Fig. 6B). Using a strategy directly analogous to FLP chemistry, Meyer and colleagues (91) combined Lewis basic Ru metalates with an imidazolium salt (32) to split H_2 heterolytically, prompting hydride addition to the imidazolium and protonation of the Ru metalate in a manner that mimics hydrogenase reactivity (Fig. 6C).

Polymers and materials

In a creative application of FLP reactivity, Chen and co-workers (92–94) used $\text{Al}(\text{C}_6\text{F}_5)_3$ and phosphines or carbenes to polymerize methyl methacrylate (MMA), methylene butyrolactones, α -methylene- γ -butyrolactone, and γ -methyl- α -methylene- γ -butyrolactone. Such polymerizations proceed via zwitterionic phosphonium or imidazolium enolaluminate intermediates. MMA polymerization is zero-order in monomer after an induction period, supporting a bimolecular, activated-monomer propagation mechanism (93). In a similar fashion, 2-vinyl pyridine and 2-isopropenyl-2-oxazoline are polymerized by FLPs (95). Although P/B FLPs are inactive for the polymerization of MMA, they do polymerize γ -methyl- α -methylene- γ -butyrolactone

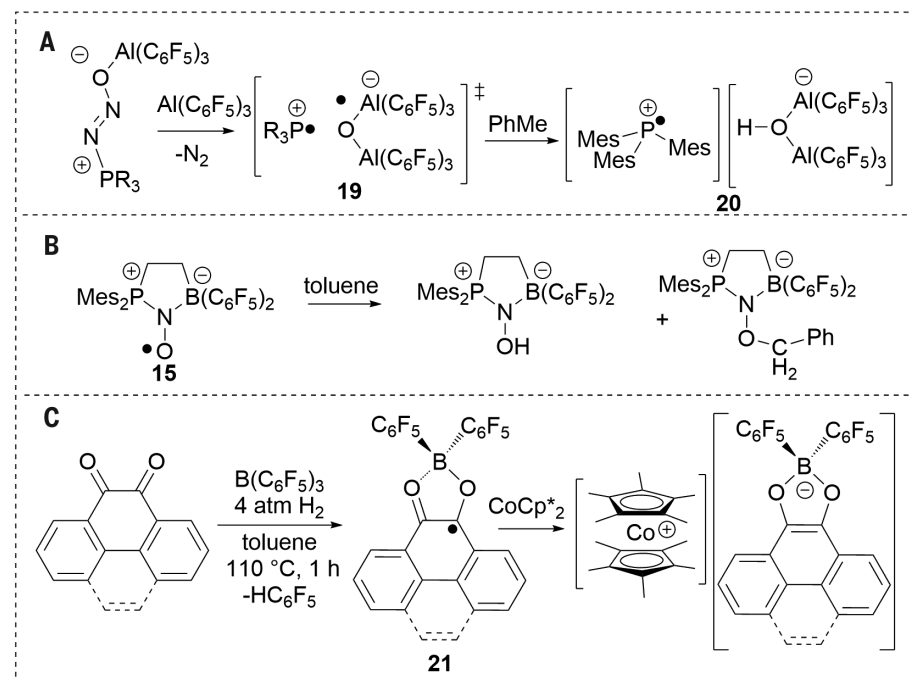


Fig. 4. FLP-derived radicals and their reactivity. (A) Generation of a transient radical. (B) Reaction of persistent radical with toluene. (C) Synthesis and oxidation of a stable radical. Cp^* , pentamethylcyclopentadienyl.

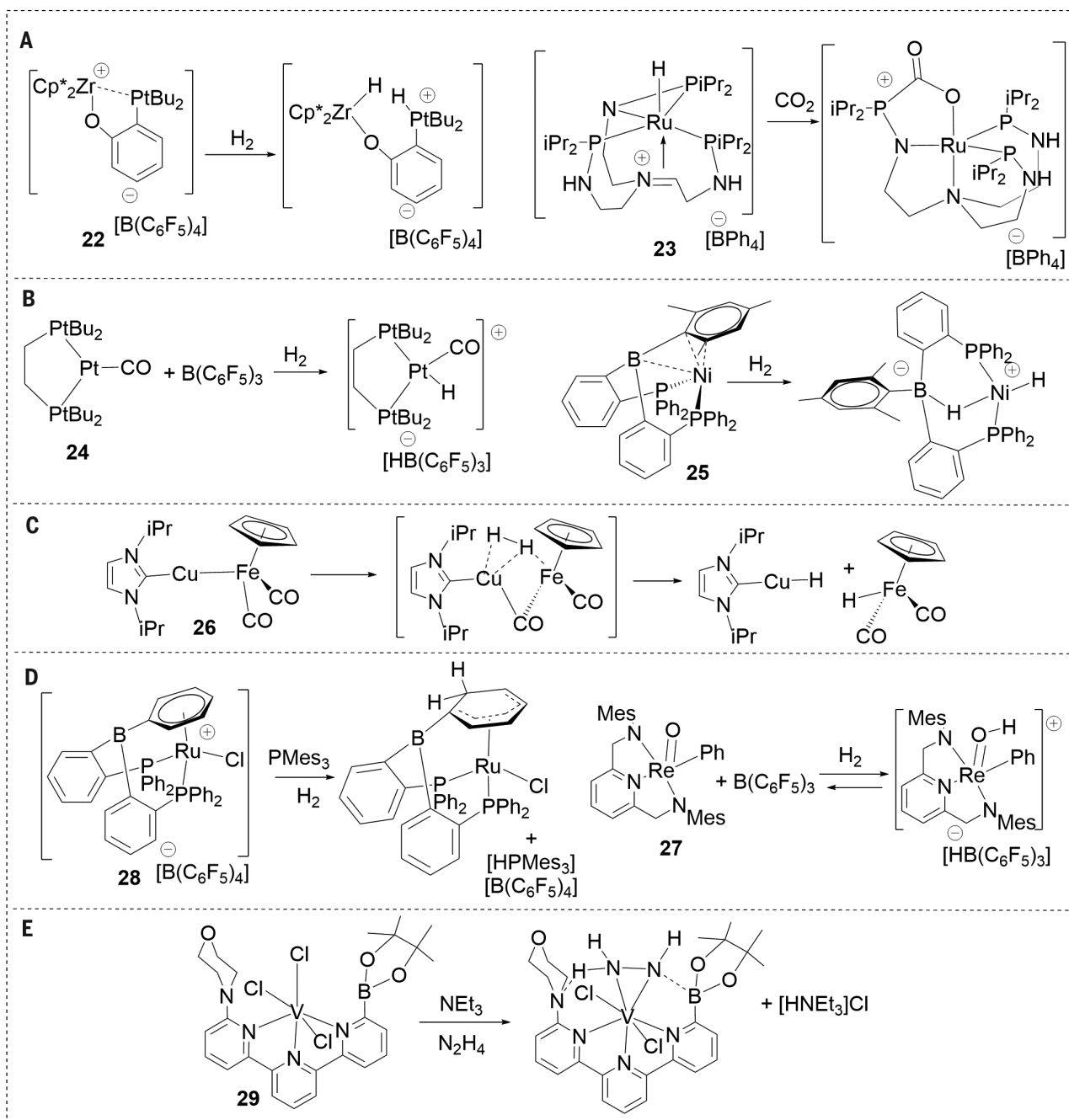


Fig. 5. Transition metal-based FLPs. (A) Zr and Ru species as Lewis acids in FLP reactions with H_2 and CO_2 , respectively. (B) The Pt(0) and Ni(0) centers act as Lewis bases in FLP activation of H_2 . (C) Metal-based analog of FLP reaction with H_2 . (D) Systems in which metal centers are ancillary to FLP reactivity. (E) FLP on a metal scaffold for cooperative interaction with the substrate.

(92). Würthwein and colleagues have reported the use of Al/N FLPs to oligomerize cyanamides (96). In a further innovation, Erker, Studer, Warren, and others developed the chemistry of FLP radicals derived from NO (97) for the polymerization of acrylates and vinyl monomers.

FLP chemistry is also developing toward further photoactive polymeric materials. For example, a synthetic route to six-membered B/Te heterocycles, $\text{RB}(\text{RC}=\text{CR})_2\text{Te}$, via a double-alkyne exchange process (98) offers the potential for convenient access to photoactive polymers. In

another effort, the inclusion of FLPs in metal-organic frameworks has been suggested. Such solid-state systems offer potential for CO_2 and H_2 capture and the possibility of CO_2 reduction (99). Targeting electrochemical H_2 oxidation, Wildgoose and co-workers (100, 101) showed that FLPs allow for fast hydrogen cleavage, providing a “hydride shuttle” that can be recycled multiple times.

Surface chemistry

Heterogeneous FLP catalysts have also emerged from the groups of Guo and Wang (102). This

team showed that although a clean gold surface is unreactive to H_2 , its combination with an imine or nitrile in solution results in the hydrogenation of C–N multiple bonds. Because these donors do not bind to the surface, the Au and N donor act as an FLP to activate H_2 , representing the first biphasic FLP catalyst.

In recent work, Ozin and colleagues (103) studied the catalytic conversion of CO_2 to carbon-based fuels by using nanostructured materials as catalysts. CO_2 was converted to CO via the reverse water-gas shift reaction catalyzed by hydroxylated

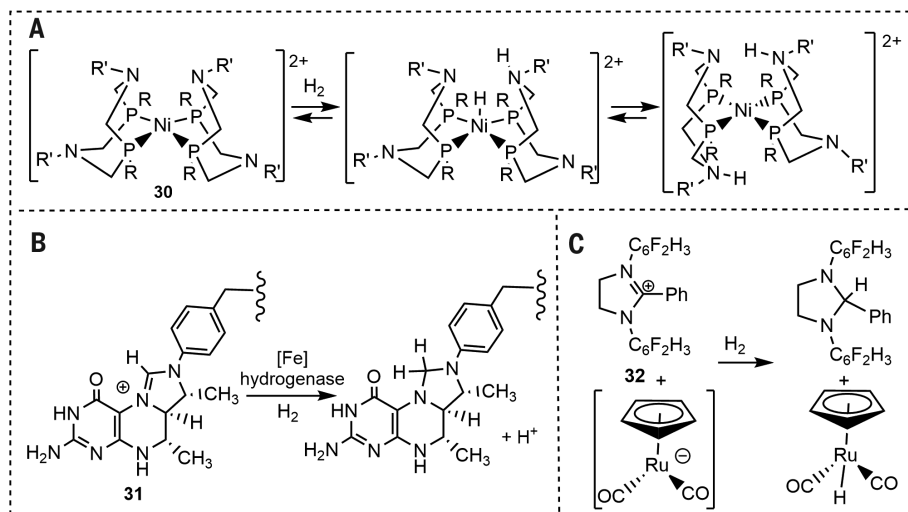


Fig. 6. Small-molecule models for hydrogenase enzyme active sites. (A) Reaction of Ni model compound with H₂. **(B)** Ezymatic reduction of methenyltetrahydromethanopterin. **(C)** Ru-imidazolium model reaction of [Fe]-hydrogenase.

indium oxide nanocrystals [In₂O_{3-x}(OH)_y]. Spectroscopic, kinetic, and density functional theory data support a mechanism in which Lewis basic hydroxide and Lewis acidic indium act cooperatively to heterolytically split H₂, prompting reaction with CO₂, yielding CO and H₂O. In a subsequent study (104) of the photochemistry of such indium oxide surfaces, Ozin and others described the mechanism in terms of surface FLPs. Although the cooperativity of acidic and basic sites is well established in surface catalysis, considering such systems in terms of the FLP paradigm may provide a new perspective for the design of improved photocatalysts.

Outlook

The observation that FLPs effect metal-free activation of H₂ has led to many subsequent studies, shifting our perspectives on main-group chemistry, the activation of small molecules, and catalysis. FLPs offer routes to hydrogenations, asymmetric reductions, organic synthesis, and radical chemistry. Further, the articulation of the FLP concept is influencing developments in transition metal, materials, and surface chemistry, as well as enzymatic models and heterogeneous catalysis. Commercial interest in FLP reactivity stems from reduced catalyst and product purification costs, lower toxicity, and distinct functional group tolerances. FLP reactivity has also prompted fundamental questions regarding the role of equilibria, van der Waals interactions, and molecular dynamics. Thus, this reactivity paradigm is stimulating studies across the full span of chemical science.

REFERENCES AND NOTES

- G. C. Welch, R. R. San Juan, J. D. Masuda, D. W. Stephan, Reversible, metal-free hydrogen activation. *Science* **314**, 1124–1126 (2006). doi: [10.1126/science.1134230](https://doi.org/10.1126/science.1134230); pmid: [17110572](https://pubmed.ncbi.nlm.nih.gov/17110572/)
- G. C. Welch, D. W. Stephan, Facile heterolytic cleavage of dihydrogen by phosphines and boranes. *J. Am. Chem. Soc.* **129**, 1880–1881 (2007). doi: [10.1021/ja067961j](https://doi.org/10.1021/ja067961j); pmid: [17260994](https://pubmed.ncbi.nlm.nih.gov/17260994/)
- P. Spies *et al.*, Rapid intramolecular heterolytic dihydrogen activation by a four-membered heterocyclic phosphane-borane adduct. *Chem. Commun. (Camb.)* **2007**, 5072–5074 (2007). doi: [10.1039/b710475h](https://doi.org/10.1039/b710475h); pmid: [18049757](https://pubmed.ncbi.nlm.nih.gov/18049757/)
- D. W. Stephan, G. Erker, Frustrated Lewis pairs: Metal-free hydrogen activation and more. *Angew. Chem. Int. Ed. Engl.* **49**, 46–76 (2010). doi: [10.1002/anie.200903708](https://doi.org/10.1002/anie.200903708); pmid: [20025001](https://pubmed.ncbi.nlm.nih.gov/20025001/)
- D. W. Stephan, G. Erker, Frustrated Lewis pair chemistry: Development and perspectives. *Angew. Chem. Int. Ed. Engl.* **54**, 6400–6441 (2015). doi: [10.1002/anie.201409800](https://doi.org/10.1002/anie.201409800); pmid: [25974714](https://pubmed.ncbi.nlm.nih.gov/25974714/)
- D. W. Stephan, G. Erker, Eds., *Frustrated Lewis Pairs I*, vol. 332 of *Topics in Current Chemistry* (Springer Press, 2013).
- D. W. Stephan, G. Erker, Eds., *Frustrated Lewis Pairs II, Expanding the Scope*, vol. 334 of *Topics in Current Chemistry* (Springer Press, 2013).
- P. A. Chase, G. C. Welch, T. Jurca, D. W. Stephan, Metal-free catalytic hydrogenation. *Angew. Chem. Int. Ed. Engl.* **46**, 8050–8053 (2007). doi: [10.1002/anie.200702908](https://doi.org/10.1002/anie.200702908); pmid: [17696181](https://pubmed.ncbi.nlm.nih.gov/17696181/)
- G. Erős *et al.*, Catalytic hydrogenation with frustrated Lewis pairs: Selectivity achieved by size-exclusion design of Lewis acids. *Chemistry* **18**, 574–585 (2012). doi: [10.1002/chem.201102438](https://doi.org/10.1002/chem.201102438); pmid: [22161804](https://pubmed.ncbi.nlm.nih.gov/22161804/)
- J. Mohr, M. Oestreich, B(C₆F₅)₃-catalyzed hydrogenation of oxime ethers without cleavage of the N–O bond. *Angew. Chem. Int. Ed. Engl.* **53**, 13278–13281 (2014). doi: [10.1002/anie.201407324](https://doi.org/10.1002/anie.201407324); pmid: [25283891](https://pubmed.ncbi.nlm.nih.gov/25283891/)
- J. Paradies, Metal-free hydrogenation of unsaturated hydrocarbons employing molecular hydrogen. *Angew. Chem. Int. Ed. Engl.* **53**, 3552–3557 (2014). doi: [10.1002/anie.201309253](https://doi.org/10.1002/anie.201309253); pmid: [24519904](https://pubmed.ncbi.nlm.nih.gov/24519904/)
- Y. Segawa, D. W. Stephan, Metal-free hydrogenation catalysis of polycyclic aromatic hydrocarbons. *Chem. Commun. (Camb.)* **48**, 11963–11965 (2012). doi: [10.1039/c2cc37190a](https://doi.org/10.1039/c2cc37190a); pmid: [23128319](https://pubmed.ncbi.nlm.nih.gov/23128319/)
- L. J. Hounjet *et al.*, Combinations of ethers and B(C₆F₅)₃ function as hydrogenation catalysts. *Angew. Chem. Int. Ed. Engl.* **52**, 7492–7495 (2013). doi: [10.1002/anie.201303166](https://doi.org/10.1002/anie.201303166); pmid: [23775686](https://pubmed.ncbi.nlm.nih.gov/23775686/)
- D. J. Parks, W. E. Piers, Tris(pentafluorophenyl)boron-catalyzed hydrosilylation of aromatic aldehydes, ketones, and esters. *J. Am. Chem. Soc.* **118**, 9440–9441 (1996). doi: [10.1021/ja961536g](https://doi.org/10.1021/ja961536g)
- S. Grimme, H. Kruse, L. Goerigk, G. Erker, The mechanism of dihydrogen activation by frustrated Lewis pairs revisited. *Angew. Chem. Int. Ed. Engl.* **49**, 1402–1405 (2010). doi: [10.1002/anie.200905484](https://doi.org/10.1002/anie.200905484); pmid: [20091722](https://pubmed.ncbi.nlm.nih.gov/20091722/)
- T. A. Rokob, A. Hamza, A. Stirling, T. Soós, I. Pápai, Turning frustration into bond activation: A theoretical mechanistic study on heterolytic hydrogen splitting by frustrated Lewis pairs. *Angew. Chem. Int. Ed. Engl.* **47**, 2435–2438 (2008). doi: [10.1002/anie.200705586](https://doi.org/10.1002/anie.200705586); pmid: [18288665](https://pubmed.ncbi.nlm.nih.gov/18288665/)
- T. A. Rokob, A. Hamza, I. Pápai, Rationalizing the reactivity of frustrated Lewis pairs: Thermodynamics of H₂ activation and the role of acid-base properties. *J. Am. Chem. Soc.* **131**, 10701–10710 (2009). doi: [10.1021/ja903878z](https://doi.org/10.1021/ja903878z); pmid: [19722636](https://pubmed.ncbi.nlm.nih.gov/19722636/)
- T. A. Rokob, A. Hamza, A. Stirling, I. Pápai, On the mechanism of B(C₆F₅)₃-catalyzed direct hydrogenation of imines: Inherent and thermally induced frustration. *J. Am. Chem. Soc.* **131**, 2029–2036 (2009). doi: [10.1021/ja809125r](https://doi.org/10.1021/ja809125r); pmid: [19159259](https://pubmed.ncbi.nlm.nih.gov/19159259/)
- T. A. Rokob, I. Bakó, A. Stirling, A. Hamza, I. Pápai, Reactivity models of hydrogen activation by frustrated Lewis pairs: Synergistic electron transfers or polarization by electric field? *J. Am. Chem. Soc.* **135**, 4425–4437 (2013). doi: [10.1021/ja312387q](https://doi.org/10.1021/ja312387q); pmid: [23432375](https://pubmed.ncbi.nlm.nih.gov/23432375/)
- S. M. Whittmore *et al.*, Catalytic reduction of polar substrates without metals: A thermodynamic and kinetic study of heterolytic activation of hydrogen by vacancies in frustrated Lewis pairs. *Catal. Today* **251**, 28–33 (2015). doi: [10.1016/j.cattod.2014.10.040](https://doi.org/10.1016/j.cattod.2014.10.040)
- K. Chernichenko *et al.*, A frustrated-Lewis-pair approach to catalytic reduction of alkynes to *cis*-alkenes. *Nat. Chem.* **5**, 718–723 (2013). doi: [10.1038/nchem.1693](https://doi.org/10.1038/nchem.1693); pmid: [23881505](https://pubmed.ncbi.nlm.nih.gov/23881505/)
- L. E. Longobardi, C. Tang, D. W. Stephan, Stoichiometric reductions of alkyl-substituted ketones and aldehydes to borinic esters. *Dalton Trans.* **43**, 15723–15726 (2014). doi: [10.1039/C4DT02648A](https://doi.org/10.1039/C4DT02648A); pmid: [25250629](https://pubmed.ncbi.nlm.nih.gov/25250629/)
- T. Mahdi, D. W. Stephan, Enabling catalytic ketone hydrogenation by frustrated Lewis pairs. *J. Am. Chem. Soc.* **136**, 15809–15812 (2014). doi: [10.1021/ja508829x](https://doi.org/10.1021/ja508829x); pmid: [25333657](https://pubmed.ncbi.nlm.nih.gov/25333657/)
- D. J. Scott, M. J. Fuchter, A. E. Ashley, Nonmetal catalyzed hydrogenation of carbonyl compounds. *J. Am. Chem. Soc.* **136**, 15813–15816 (2014). doi: [10.1021/ja5088979](https://doi.org/10.1021/ja5088979); pmid: [25333722](https://pubmed.ncbi.nlm.nih.gov/25333722/)
- T. Mahdi, D. W. Stephan, Facile protocol for catalytic frustrated Lewis pair hydrogenation and reductive deoxygenation of ketones and aldehydes. *Angew. Chem. Int. Ed. Engl.* **54**, 8511–8514 (2015). doi: [10.1002/anie.201503087](https://doi.org/10.1002/anie.201503087); pmid: [26038152](https://pubmed.ncbi.nlm.nih.gov/26038152/)
- T. Mahdi, Z. M. Heiden, S. Grimme, D. W. Stephan, Metal-free aromatic hydrogenation: Aniline to cyclohexyl-amine derivatives. *J. Am. Chem. Soc.* **134**, 4088–4091 (2012). doi: [10.1021/ja300228a](https://doi.org/10.1021/ja300228a); pmid: [22335795](https://pubmed.ncbi.nlm.nih.gov/22335795/)
- T. Mahdi, J. N. del Castillo, D. W. Stephan, Metal-free hydrogenation of *N*-based heterocycles. *Organometallics* **32**, 1971–1978 (2013). doi: [10.1021/om4000727](https://doi.org/10.1021/om4000727)
- Y. Liu, H. Du, Metal-free borane-catalyzed highly stereoselective hydrogenation of pyridines. *J. Am. Chem. Soc.* **135**, 12968–12971 (2013). doi: [10.1021/ja406761j](https://doi.org/10.1021/ja406761j); pmid: [23944383](https://pubmed.ncbi.nlm.nih.gov/23944383/)
- D. Chen, J. Klankermayer, Metal-free catalytic hydrogenation of imines with tris(perfluorophenyl)borane. *Chem. Commun. (Camb.)* **2008**, 2130–2131 (2008). doi: [10.1039/b801806e](https://doi.org/10.1039/b801806e); pmid: [18438491](https://pubmed.ncbi.nlm.nih.gov/18438491/)
- D. Chen, Y. Wang, J. Klankermayer, Enantioselective hydrogenation with chiral frustrated Lewis pairs. *Angew. Chem. Int. Ed. Engl.* **49**, 9475–9478 (2010). doi: [10.1002/anie.201004525](https://doi.org/10.1002/anie.201004525); pmid: [21031385](https://pubmed.ncbi.nlm.nih.gov/21031385/)
- Y. Liu, H. Du, Chiral dienes as “ligands” for borane-catalyzed metal-free asymmetric hydrogenation of imines. *J. Am. Chem. Soc.* **135**, 6810–6813 (2013). doi: [10.1021/ja4025808](https://doi.org/10.1021/ja4025808); pmid: [23607669](https://pubmed.ncbi.nlm.nih.gov/23607669/)
- M. Lindqvist *et al.*, Chiral molecular tweezers: Synthesis and reactivity in asymmetric hydrogenation. *J. Am. Chem. Soc.* **137**, 4038–4041 (2015). doi: [10.1021/ja512658m](https://doi.org/10.1021/ja512658m); pmid: [25636083](https://pubmed.ncbi.nlm.nih.gov/25636083/)
- S. Wei, H. Du, A highly enantioselective hydrogenation of silyl enol ethers catalyzed by chiral frustrated Lewis pairs. *J. Am. Chem. Soc.* **136**, 12261–12264 (2014). doi: [10.1021/ja507536g](https://doi.org/10.1021/ja507536g); pmid: [25133975](https://pubmed.ncbi.nlm.nih.gov/25133975/)
- Z. Zhang, H. Du, A highly *cis*-selective and enantioselective metal-free hydrogenation of 2,3-disubstituted quinoxalines. *Angew. Chem. Int. Ed. Engl.* **54**, 623–626 (2015). doi: [10.1002/anie.201505484](https://doi.org/10.1002/anie.201505484); pmid: [25393413](https://pubmed.ncbi.nlm.nih.gov/25393413/)
- X. Ren, H. Du, Chiral frustrated Lewis pairs catalyzed highly enantioselective hydrosilylations of 1,2-dicarbonyl

- compounds. *J. Am. Chem. Soc.* **138**, 810–813 (2016). doi: [10.1021/jacs.5b13104](https://doi.org/10.1021/jacs.5b13104); pmid: [26750998](https://pubmed.ncbi.nlm.nih.gov/26750998/)
36. J. M. Farrell, R. T. Posaratnanathan, D. W. Stephan, A family of N-heterocyclic carbene-stabilized borenium ions for metal-free imine hydrogenation catalysis. *Chem. Sci. (Camb.)* **6**, 2010–2015 (2015). doi: [10.1039/C4SC03675A](https://doi.org/10.1039/C4SC03675A)
 37. J. M. Farrell, J. A. Hatnean, D. W. Stephan, Activation of hydrogen and hydrogenation catalysis by a borenium cation. *J. Am. Chem. Soc.* **134**, 15728–15731 (2012). doi: [10.1021/ja307995f](https://doi.org/10.1021/ja307995f); pmid: [22931196](https://pubmed.ncbi.nlm.nih.gov/22931196/)
 38. P. Eisenberger, B. P. Bestvater, E. C. Keske, C. M. Crudden, Hydrogenations at room temperature and atmospheric pressure with mesoionic carbene-stabilized borenium catalysts. *Angew. Chem. Int. Ed. Engl.* **54**, 2467–2471 (2015). doi: [10.1002/anie.201409250](https://doi.org/10.1002/anie.201409250); pmid: [25586407](https://pubmed.ncbi.nlm.nih.gov/25586407/)
 39. E. R. Clark, M. J. Ingleson, [(acridine)BCl₂]⁺: A borenium cation that is a strong boron- and carbon-based Lewis acid. *Organometallics* **32**, 6712–6717 (2013). doi: [10.1021/om400463r](https://doi.org/10.1021/om400463r)
 40. E. R. Clark, M. J. Ingleson, N-methylacridinium salts: Carbon Lewis acids in frustrated Lewis pairs for α -bond activation and catalytic reductions. *Angew. Chem. Int. Ed. Engl.* **53**, 11306–11309 (2014). doi: [10.1002/anie.201406122](https://doi.org/10.1002/anie.201406122); pmid: [25195917](https://pubmed.ncbi.nlm.nih.gov/25195917/)
 41. C. B. Caputo, L. J. Hounjet, R. Dobrovetsky, D. W. Stephan, Lewis acidity of organofluorophosphonium salts: Hydrodefluorination by a saturated acceptor. *Science* **341**, 1374–1377 (2013). doi: [10.1126/science.1241764](https://doi.org/10.1126/science.1241764); pmid: [24052304](https://pubmed.ncbi.nlm.nih.gov/24052304/)
 42. J. M. Bayne, D. W. Stephan, Phosphorus Lewis acids: Emerging reactivity and applications in catalysis. *Chem. Soc. Rev.* **45**, 765–774 (2016). doi: [10.1039/C5SC00516G](https://doi.org/10.1039/C5SC00516G); pmid: [26255595](https://pubmed.ncbi.nlm.nih.gov/26255595/)
 43. J. Zhu, M. Pérez, C. B. Caputo, D. W. Stephan, Use of trifluoromethyl groups for catalytic benzylation and alkylation with subsequent hydrodefluorination. *Angew. Chem. Int. Ed. Engl.* **55**, 1417–1421 (2016). doi: [10.1002/anie.201510494](https://doi.org/10.1002/anie.201510494); pmid: [26663711](https://pubmed.ncbi.nlm.nih.gov/26663711/)
 44. J. Zhu, M. Pérez, D. W. Stephan, C–C coupling of benzyl fluorides catalyzed by an electrophilic phosphonium cation. *Angew. Chem. Int. Ed. Engl.* **55**, 8448–8451 (2016). doi: [10.1002/anie.201603627](https://doi.org/10.1002/anie.201603627); pmid: [27239806](https://pubmed.ncbi.nlm.nih.gov/27239806/)
 45. T. Vom Stein *et al.*, Electrophilic fluorophosphonium cations in frustrated Lewis pair hydrogen activation and catalytic hydrogenation of olefins. *Angew. Chem. Int. Ed. Engl.* **54**, 10178–10182 (2015). doi: [10.1002/anie.201504109](https://doi.org/10.1002/anie.201504109); pmid: [26178268](https://pubmed.ncbi.nlm.nih.gov/26178268/)
 46. A. E. Ashley, A. L. Thompson, D. O'Hare, Non-metal-mediated homogeneous hydrogenation of CO₂ to CH₃OH. *Angew. Chem. Int. Ed. Engl.* **48**, 9839–9843 (2009). doi: [10.1002/anie.200905466](https://doi.org/10.1002/anie.200905466); pmid: [19937890](https://pubmed.ncbi.nlm.nih.gov/19937890/)
 47. D. W. Stephan, G. Erker, Frustrated Lewis pair chemistry of carbon, nitrogen and sulfur oxides. *Chem. Sci. (Camb.)* **5**, 2625 (2014). doi: [10.1039/C4SC00395K](https://doi.org/10.1039/C4SC00395K)
 48. R. Dobrovetsky, D. W. Stephan, Catalytic reduction of CO₂ to CO by using zinc(II) and in situ generated carbodiphosphoranes. *Angew. Chem. Int. Ed. Engl.* **52**, 2516–2519 (2013). doi: [10.1002/anie.201208817](https://doi.org/10.1002/anie.201208817); pmid: [23364808](https://pubmed.ncbi.nlm.nih.gov/23364808/)
 49. M. A. Courtemanche, M. A. Légaré, L. Maron, F. G. Fontaine, Reducing CO₂ to methanol using frustrated Lewis pairs: On the mechanism of phosphine-borane-mediated hydroboration of CO₂. *J. Am. Chem. Soc.* **136**, 10708–10717 (2014). doi: [10.1021/ja5047846](https://doi.org/10.1021/ja5047846); pmid: [24948159](https://pubmed.ncbi.nlm.nih.gov/24948159/)
 50. C. Chauvier, A. Tlili, C. Das Neves Gomes, P. Thuéry, T. Cantat, Metal-free dehydrogenation of formic acid to H₂ and CO₂ using boron-based catalysts. *Chem. Sci. (Camb.)* **6**, 2938–2942 (2015). doi: [10.1039/C5SC00394F](https://doi.org/10.1039/C5SC00394F)
 51. M. Abolhasani, A. Günther, E. Kumacheva, Microfluidic studies of carbon dioxide. *Angew. Chem. Int. Ed. Engl.* **126**, 8126–8136 (2014). doi: [10.1002/ange.201403719](https://doi.org/10.1002/ange.201403719); pmid: [24961230](https://pubmed.ncbi.nlm.nih.gov/24961230/)
 52. M. Sajid *et al.*, Facile carbon monoxide reduction at intramolecular frustrated phosphane/borane Lewis pair templates. *Angew. Chem. Int. Ed. Engl.* **52**, 2243–2246 (2013). doi: [10.1002/anie.201208750](https://doi.org/10.1002/anie.201208750); pmid: [23322704](https://pubmed.ncbi.nlm.nih.gov/23322704/)
 53. R. Dobrovetsky, D. W. Stephan, Stoichiometric metal-free reduction of CO in syn-gas. *J. Am. Chem. Soc.* **135**, 4974–4977 (2013). doi: [10.1021/ja401492s](https://doi.org/10.1021/ja401492s); pmid: [23521150](https://pubmed.ncbi.nlm.nih.gov/23521150/)
 54. L. E. Longobardi, V. Wolter, D. W. Stephan, Frustrated Lewis pair activation of an N-sulfinylamine: A source of sulfur monoxide. *Angew. Chem. Int. Ed. Engl.* **54**, 809–812 (2015). doi: [10.1002/anie.201409969](https://doi.org/10.1002/anie.201409969); pmid: [25376102](https://pubmed.ncbi.nlm.nih.gov/25376102/)
 55. K.-Y. Ye *et al.*, Coupling of carbon monoxide with nitrogen monoxide at a frustrated Lewis pair template. *Angew. Chem. Int. Ed. Engl.* **55**, 9216–9219 (2016). doi: [10.1002/anie.201603760](https://doi.org/10.1002/anie.201603760); pmid: [27328914](https://pubmed.ncbi.nlm.nih.gov/27328914/)
 56. J. S. J. McCall, G. C. Welch, D. W. Stephan, Reactivity of “frustrated Lewis pairs”: Three-component reactions of phosphines, a borane, and olefins. *Angew. Chem. Int. Ed. Engl.* **46**, 4968–4971 (2007). doi: [10.1002/anie.200701215](https://doi.org/10.1002/anie.200701215); pmid: [17526043](https://pubmed.ncbi.nlm.nih.gov/17526043/)
 57. M. A. Dureen, D. W. Stephan, Terminal alkyne activation by frustrated and classical Lewis acid/phosphine pairs. *J. Am. Chem. Soc.* **131**, 8396–8397 (2009). doi: [10.1021/ja903650w](https://doi.org/10.1021/ja903650w); pmid: [19485368](https://pubmed.ncbi.nlm.nih.gov/19485368/)
 58. T. Mahdi, D. W. Stephan, Frustrated Lewis pair catalyzed hydroamination of terminal alkynes. *Angew. Chem. Int. Ed. Engl.* **52**, 12418–12421 (2013). doi: [10.1002/anie.201307254](https://doi.org/10.1002/anie.201307254); pmid: [24115279](https://pubmed.ncbi.nlm.nih.gov/24115279/)
 59. R. L. Melen, M. M. Hansmann, A. J. Lough, A. S. K. Hashmi, D. W. Stephan, Cyclisation versus 1,1-carbaboration: Reactions of B(C₆F₅)₃ with propargyl amides. *Chemistry* **19**, 11928–11938 (2013). doi: [10.1002/chem.201301899](https://doi.org/10.1002/chem.201301899); pmid: [23922200](https://pubmed.ncbi.nlm.nih.gov/23922200/)
 60. L. C. Wilkins *et al.*, Pathways to functionalized heterocycles: propargyl rearrangement using B(C₆F₅)₃. *Organometallics* **34**, 5298–5309 (2015). doi: [10.1021/acs.organomet.5b00753](https://doi.org/10.1021/acs.organomet.5b00753)
 61. M. M. Hansmann, R. L. Melen, F. Rominger, A. S. K. Hashmi, D. W. Stephan, Activation of alkynes with B(C₆F₅)₃–boron allylation reagents derived from propargyl esters. *J. Am. Chem. Soc.* **136**, 777–782 (2014). doi: [10.1021/ja4110842](https://doi.org/10.1021/ja4110842); pmid: [24354408](https://pubmed.ncbi.nlm.nih.gov/24354408/)
 62. M. M. Hansmann, R. L. Melen, F. Rominger, A. S. K. Hashmi, D. W. Stephan, B(C₆F₅)₃ promoted cyclisation of internal propargyl esters: Structural characterisation of 1,3-dioxolium compounds. *Chem. Commun. (Camb.)* **50**, 7243–7245 (2014). doi: [10.1039/c4cc01370k](https://doi.org/10.1039/c4cc01370k); pmid: [24817134](https://pubmed.ncbi.nlm.nih.gov/24817134/)
 63. R. L. Melen *et al.*, Diverging pathways in the activation of allenes with Lewis acids and bases: Addition, 1,2-carbaboration, and cyclization. *Organometallics* **34**, 4127–4137 (2015). doi: [10.1021/acs.organomet.5b00546](https://doi.org/10.1021/acs.organomet.5b00546)
 64. I. A. Cade, M. J. Ingleson, syn-1,2-carbaboration of alkynes with borenium cations. *Chemistry* **20**, 12874–12880 (2014). doi: [10.1002/chem.201403614](https://doi.org/10.1002/chem.201403614); pmid: [25138585](https://pubmed.ncbi.nlm.nih.gov/25138585/)
 65. J. S. McGough, S. M. Butler, I. A. Cade, M. J. Ingleson, Highly selective catalytic trans-hydroboration of alkynes mediated by borenium cations and B(C₆F₅)₃. *Chem. Sci. (Camb.)* **7**, 3384–3389 (2016). doi: [10.1039/C5SC004798F](https://doi.org/10.1039/C5SC004798F)
 66. P. Eisenberger, A. M. Bailey, C. M. Crudden, Taking the F out of FLP: Simple Lewis acid-base pairs for mild reductions with neutral boranes via borenium ion catalysis. *J. Am. Chem. Soc.* **134**, 17384–17387 (2012). doi: [10.1021/ja307374j](https://doi.org/10.1021/ja307374j); pmid: [23030065](https://pubmed.ncbi.nlm.nih.gov/23030065/)
 67. M. A. Légaré, M. A. Courtemanche, É. Rochette, F. G. Fontaine, Metal-free catalytic C–H bond activation and borylation of heteroarenes. *Science* **349**, 513–516 (2015). doi: [10.1126/science.1263591](https://doi.org/10.1126/science.1263591); pmid: [26228143](https://pubmed.ncbi.nlm.nih.gov/26228143/)
 68. K. Chernichenko *et al.*, Metal-free sp²–C–H borylation as a common reactivity pattern of frustrated 2-aminophenylboranes. *J. Am. Chem. Soc.* **138**, 4860–4868 (2016). doi: [10.1021/jacs.6b00819](https://doi.org/10.1021/jacs.6b00819); pmid: [27003334](https://pubmed.ncbi.nlm.nih.gov/27003334/)
 69. G. Ménard *et al.*, C–H bond activation by radical ion pairs derived from R₃P/Al(C₆F₅)₃ frustrated Lewis pairs and N₂O. *J. Am. Chem. Soc.* **135**, 6446–6449 (2013). doi: [10.1021/ja402964h](https://doi.org/10.1021/ja402964h); pmid: [23594345](https://pubmed.ncbi.nlm.nih.gov/23594345/)
 70. A. J. Cardenas *et al.*, Capture of NO by a frustrated Lewis pair: A new type of persistent N-oxyl radical. *Angew. Chem. Int. Ed. Engl.* **50**, 7567–7571 (2011). doi: [10.1002/anie.201101622](https://doi.org/10.1002/anie.201101622); pmid: [21726024](https://pubmed.ncbi.nlm.nih.gov/21726024/)
 71. L. E. Longobardi, L. Liu, S. Grimme, D. W. Stephan, Stable borocyclic radicals via frustrated Lewis pair hydrogenations. *J. Am. Chem. Soc.* **138**, 2500–2503 (2016). doi: [10.1021/jacs.5b12823](https://doi.org/10.1021/jacs.5b12823); pmid: [26846796](https://pubmed.ncbi.nlm.nih.gov/26846796/)
 72. A. M. Chapman, S. R. Flynn, D. F. Wass, Unexpected formation of early late heterobimetallic complexes from transition metal frustrated Lewis pairs. *Inorg. Chem.* **55**, 1017–1021 (2016). doi: [10.1021/acs.inorgchem.5b01424](https://doi.org/10.1021/acs.inorgchem.5b01424); pmid: [26756975](https://pubmed.ncbi.nlm.nih.gov/26756975/)
 73. M. J. Sgro, D. W. Stephan, Frustrated Lewis pair inspired carbon dioxide reduction by a ruthenium tris (aminophosphine) complex. *Angew. Chem. Int. Ed. Engl.* **51**, 11343–11345 (2012). doi: [10.1002/anie.201205741](https://doi.org/10.1002/anie.201205741); pmid: [23038414](https://pubmed.ncbi.nlm.nih.gov/23038414/)
 74. R. Noyori, Asymmetric catalysis: Science and opportunities (Nobel lecture). *Angew. Chem. Int. Ed. Engl.* **41**, 2008–2022 (2002). doi: [10.1002/1521-3773\(20020617\)41:12<2008::AID-ANIE2008>3.0.CO;2-4](https://doi.org/10.1002/1521-3773(20020617)41:12<2008::AID-ANIE2008>3.0.CO;2-4); pmid: [19746599](https://pubmed.ncbi.nlm.nih.gov/19746599/)
 75. J. C. DeMott, N. Bhuvanesh, O. V. Ozerov, Frustrated Lewis pair-like splitting of aromatic C–H bonds and abstraction of halogen atoms by a cationic [(PNP)-P-F] Pt⁺ species. *Chem. Sci. (Camb.)* **4**, 642–649 (2013). doi: [10.1039/C2SC21385K](https://doi.org/10.1039/C2SC21385K)
 76. Y. Jiang, O. Blacque, T. Fox, H. Berke, Catalytic CO₂ activation assisted by rhodium hydride/B(C₆F₅)₃ frustrated Lewis pairs—metal hydrides functioning as FLP bases. *J. Am. Chem. Soc.* **135**, 7751–7760 (2013). doi: [10.1021/ja402381d](https://doi.org/10.1021/ja402381d); pmid: [23617739](https://pubmed.ncbi.nlm.nih.gov/23617739/)
 77. S. J. K. Forrest *et al.*, Cooperative Lewis pairs based on late transition metals: Activation of small molecules by platinum(0) and B(C₆F₅)₃. *Angew. Chem. Int. Ed. Engl.* **54**, 2223–2227 (2015). doi: [10.1002/anie.201409872](https://doi.org/10.1002/anie.201409872); pmid: [25538001](https://pubmed.ncbi.nlm.nih.gov/25538001/)
 78. T. P. Lin, J. C. Peters, Boryl-metal bonds facilitate cobalt/nickel-catalyzed olefin hydrogenation. *J. Am. Chem. Soc.* **136**, 13672–13683 (2014). doi: [10.1021/ja504667f](https://doi.org/10.1021/ja504667f); pmid: [25181350](https://pubmed.ncbi.nlm.nih.gov/25181350/)
 79. N. P. Mankad, Selectivity effects in bimetallic catalysis. *Chemistry* **22**, 5822–5829 (2016). doi: [10.1002/chem.201505002](https://doi.org/10.1002/chem.201505002); pmid: [26879884](https://pubmed.ncbi.nlm.nih.gov/26879884/)
 80. M. K. Karunananda, N. P. Mankad, E-selective semi-hydrogenation of alkynes by heterobimetallic catalysis. *J. Am. Chem. Soc.* **137**, 14598–14601 (2015). doi: [10.1021/jacs.5b10357](https://doi.org/10.1021/jacs.5b10357); pmid: [26550848](https://pubmed.ncbi.nlm.nih.gov/26550848/)
 81. T. J. Mazzacano, N. P. Mankad, Thermal C–H borylation using a CO-free iron boryl complex. *Chem. Commun. (Camb.)* **51**, 5379–5382 (2015). doi: [10.1039/C4CC09180A](https://doi.org/10.1039/C4CC09180A); pmid: [25515057](https://pubmed.ncbi.nlm.nih.gov/25515057/)
 82. S. R. Parmelee, T. J. Mazzacano, Y. Q. Zhu, N. P. Mankad, J. A. Keith, A heterobimetallic mechanism for C–H borylation elucidated from experimental and computational data. *ACS Catal.* **5**, 3689–3699 (2015). doi: [10.1021/acscatal.5b00275](https://doi.org/10.1021/acscatal.5b00275)
 83. M. P. Boone, D. W. Stephan, A Ru- η^6 -arene complex as a C-based Lewis acid in the activation of hydrogen and hydrogenation catalysis. *J. Am. Chem. Soc.* **135**, 8508–8511 (2013). doi: [10.1021/ja403912n](https://doi.org/10.1021/ja403912n); pmid: [23718884](https://pubmed.ncbi.nlm.nih.gov/23718884/)
 84. M. P. Boone, D. W. Stephan, Ru- η^6 -arene cations [(Ph)₂PC₆H₄]⁺ B(η^6 -Ph)RuX]⁺ (X=Cl, H) as Lewis acids. *Chemistry* **20**, 3333–3341 (2014). doi: [10.1002/chem.201304289](https://doi.org/10.1002/chem.201304289); pmid: [24616079](https://pubmed.ncbi.nlm.nih.gov/24616079/)
 85. M. P. Boone, D. W. Stephan, Ancillary metal centers in frustrated Lewis pair chemistry: Ruthenium acetylide as a Lewis base in the activation of CO₂, aldehyde, and alkyne. *Organometallics* **33**, 387–393 (2014). doi: [10.1021/om401118n](https://doi.org/10.1021/om401118n)
 86. N. S. Lambic, R. D. Sommer, E. A. Ison, Transition-metal oxos as the Lewis basic component of frustrated Lewis pairs. *J. Am. Chem. Soc.* **138**, 4832–4842 (2016). doi: [10.1021/jacs.6b00705](https://doi.org/10.1021/jacs.6b00705); pmid: [27002927](https://pubmed.ncbi.nlm.nih.gov/27002927/)
 87. O. Tutusaus, C. Ni, N. K. Szymczak, A transition metal Lewis acid/base triad system for cooperative substrate binding. *J. Am. Chem. Soc.* **135**, 3403–3406 (2013). doi: [10.1021/ja400962h](https://doi.org/10.1021/ja400962h); pmid: [23421523](https://pubmed.ncbi.nlm.nih.gov/23421523/)
 88. S. Raugel *et al.*, The role of pendant amines in the breaking and forming of molecular hydrogen catalyzed by nickel complexes. *Chemistry* **18**, 6493–6506 (2012). doi: [10.1002/chem.201103346](https://doi.org/10.1002/chem.201103346); pmid: [22532421](https://pubmed.ncbi.nlm.nih.gov/22532421/)
 89. R. M. Bullock, M. L. Helm, Molecular electrocatalysts for oxidation of hydrogen using earth-abundant metals: Shoveling protons around with proton relays. *Acc. Chem. Res.* **48**, 2017–2026 (2015). doi: [10.1021/acs.accounts.5b00069](https://doi.org/10.1021/acs.accounts.5b00069); pmid: [26079983](https://pubmed.ncbi.nlm.nih.gov/26079983/)
 90. S. Shima *et al.*, The crystal structure of [Fe]-hydrogenase reveals the geometry of the active site. *Science* **321**, 572–575 (2008). doi: [10.1126/science.1158978](https://doi.org/10.1126/science.1158978); pmid: [18653896](https://pubmed.ncbi.nlm.nih.gov/18653896/)
 91. K. F. Kalz, A. Brinkmeier, S. Dechert, R. A. Mata, F. Meyer, Functional model for the [Fe] hydrogenase inspired by the frustrated Lewis pair concept. *J. Am. Chem. Soc.* **136**, 16626–16634 (2014). doi: [10.1021/ja509186d](https://doi.org/10.1021/ja509186d); pmid: [25353322](https://pubmed.ncbi.nlm.nih.gov/25353322/)
 92. T. Xu, E. Y. Chen, Probing site cooperativity of frustrated phosphine/borane Lewis pairs by a polymerization study. *J. Am. Chem. Soc.* **136**, 1774–1777 (2014). doi: [10.1021/ja412445n](https://doi.org/10.1021/ja412445n); pmid: [24417317](https://pubmed.ncbi.nlm.nih.gov/24417317/)
 93. Y. Zhang *et al.*, Lewis pair polymerization by classical and frustrated Lewis pairs: Acid, base and monomer scope and polymerization mechanism. *Dalton Trans.* **41**, 9119–9134 (2012). doi: [10.1039/c2dt30427a](https://doi.org/10.1039/c2dt30427a); pmid: [22614678](https://pubmed.ncbi.nlm.nih.gov/22614678/)
 94. Y. Zhang, G. M. Miyake, E. Y. X. Chen, Alane-based classical and frustrated Lewis pairs in polymer synthesis: Rapid polymerization of MMA and naturally renewable methylene

- butyrolactones into high-molecular-weight polymers. *Angew. Chem. Int. Ed. Engl.* **49**, 10158–10162 (2010). doi: [10.1002/anie.201005534](https://doi.org/10.1002/anie.201005534); pmid: [21108294](https://pubmed.ncbi.nlm.nih.gov/21108294/)
95. J. H. He, Y. T. Zhang, E. Y. X. Chen, Synthesis of pyridine- and 2-oxazoline-functionalized vinyl polymers by alane-based frustrated Lewis pairs. *Synlett* **25**, 1534–1538 (2014). doi: [10.1055/s-0033-1341248](https://doi.org/10.1055/s-0033-1341248)
 96. T. Holtrichter-Röbmann *et al.*, An aluminum-nitrogen based Lewis pair as an effective catalyst for the oligomerization of cyanamides: Formation of acyclic C–N oligomers instead of thermodynamically favored cyclic aromatic trimers. *Angew. Chem. Int. Ed. Engl.* **52**, 7135–7138 (2013). doi: [10.1002/anie.201301970](https://doi.org/10.1002/anie.201301970); pmid: [23740759](https://pubmed.ncbi.nlm.nih.gov/23740759/)
 97. M. Sajid *et al.*, *N,N*-addition of frustrated Lewis pairs to nitric oxide: An easy entry to a unique family of aminoxyl radicals. *J. Am. Chem. Soc.* **134**, 10156–10168 (2012). doi: [10.1021/ja302652a](https://doi.org/10.1021/ja302652a); pmid: [22548454](https://pubmed.ncbi.nlm.nih.gov/22548454/)
 98. F. A. Tsao, L. Cao, S. Grimme, D. W. Stephan, Double FLP-alkyne exchange reactions: A facile route to Te/B heterocycles. *J. Am. Chem. Soc.* **137**, 13264–13267 (2015). doi: [10.1021/jacs.5b09526](https://doi.org/10.1021/jacs.5b09526); pmid: [26447492](https://pubmed.ncbi.nlm.nih.gov/26447492/)
 99. J. Ye, J. K. Johnson, Design of Lewis pair-functionalized metal organic frameworks for CO₂ hydrogenation. *ACS Catal.* **5**, 2921–2928 (2015). doi: [10.1021/acscatal.5b00396](https://doi.org/10.1021/acscatal.5b00396)
 100. E. J. Lawrence, R. J. Blagg, D. L. Hughes, A. E. Ashley, G. G. Wildgoose, A combined “electrochemical-frustrated Lewis pair” approach to hydrogen activation: Surface catalytic effects at platinum electrodes. *Chemistry* **21**, 900–906 (2015). doi: [10.1002/chem.201404242](https://doi.org/10.1002/chem.201404242); pmid: [25382457](https://pubmed.ncbi.nlm.nih.gov/25382457/)
 101. E. J. Lawrence *et al.*, Metal-free electrocatalytic hydrogen oxidation using frustrated Lewis pairs and carbon-based Lewis acids. *Chem. Sci. (Camb.)* **7**, 2537–2543 (2016). doi: [10.1039/C5SC04564A](https://doi.org/10.1039/C5SC04564A)
 102. G. Lu *et al.*, Gold catalyzed hydrogenations of small imines and nitriles: Enhanced reactivity of Au surface toward H₂ via collaboration with a Lewis base. *Chem. Sci. (Camb.)* **5**, 1082 (2014). doi: [10.1039/c3sc52851k](https://doi.org/10.1039/c3sc52851k)
 103. K. K. Ghuman *et al.*, Illuminating CO₂ reduction on frustrated Lewis pair surfaces: Investigating the role of surface hydroxides and oxygen vacancies on nanocrystalline In₂O_{3-x}(OH)_y. *Phys. Chem. Chem. Phys.* **17**, 14623–14635 (2015). doi: [10.1039/C5CP02613J](https://doi.org/10.1039/C5CP02613J); pmid: [25971705](https://pubmed.ncbi.nlm.nih.gov/25971705/)
 104. K. K. Ghuman *et al.*, Photoexcited surface frustrated Lewis pairs for heterogeneous photocatalytic CO₂ reduction. *J. Am. Chem. Soc.* **138**, 1206–1214 (2016). doi: [10.1021/jacs.5b10179](https://doi.org/10.1021/jacs.5b10179); pmid: [26759919](https://pubmed.ncbi.nlm.nih.gov/26759919/)

ACKNOWLEDGMENTS

D.W.S. is grateful for the support of the Natural Sciences and Engineering Research Council of Canada and the award of a Canada Research Chair. L. Longobardi and T. Johnstone are thanked for helpful comments.

10.1126/science.aaf7229

REPORTS

RADIO ASTRONOMY

The magnetic field and turbulence of the cosmic web measured using a brilliant fast radio burst

V. Ravi,^{1*†} R. M. Shannon,^{2,3*†} M. Bailes,^{4,5} K. Bannister,² S. Bhandari,^{4,5}
N. D. R. Bhat,^{3,5} S. Burke-Spolaor,⁶ M. Caleb,^{4,5,7} C. Flynn,^{4,5} A. Jameson,^{4,5}
S. Johnston,² E. F. Keane,⁸ M. Kerr,² C. Tiburzi,⁹ A. V. Tuntsov,¹⁰ H. K. Vedantham¹

Fast radio bursts (FRBs) are millisecond-duration events thought to originate beyond the Milky Way galaxy. Uncertainty surrounding the burst sources, and their propagation through intervening plasma, has limited their use as cosmological probes. We report on a mildly dispersed (dispersion measure 266.5 ± 0.1 parsecs per cubic centimeter), exceptionally intense (120 ± 30 janskys), linearly polarized, scintillating burst (FRB 150807) that we directly localize to 9 square arc minutes. On the basis of a low Faraday rotation (12.0 ± 0.7 radians per square meter), we infer negligible magnetization in the circum-burst plasma and constrain the net magnetization of the cosmic web along this sightline to <21 nanogauss, parallel to the line-of-sight. The burst scintillation suggests weak turbulence in the ionized intergalactic medium.

A recently recognized population of fast radio bursts (FRBs) of likely extragalactic origin (1, 2) may revolutionize astrophysics and cosmology. Besides probing a heretofore-unknown astrophysical phenomenon, the bursts potentially carry imprints of propagation through inhomogeneous, magnetized plasma in the ionized interstellar media of other galaxies and the diffuse intergalactic medium (IGM). Simultaneous measurements of redshifts and line-of-sight free-electron column densities for FRBs can constrain the cosmological mass density and ionization history of baryons (3–5).

We detected FRB 150807 with the 64-m Parkes radio telescope, using the 21-cm multibeam receiver (6), while conducting timing observations of the millisecond pulsar PSR J2241–5236. This receiver is sensitive to 13 overlapping regions (beams) on

the sky within a 2° diameter circle. We performed a real-time search for FRBs commensally with the pulsar timing experiment using standard hardware (7) and search techniques (8–10).

The properties of FRB 150807 are given in Table 1, and calibrated burst data are shown in Fig. 1. The burst was detected in two adjacent beams. We used this two-beam detection and a model of the multibeam response (10) to constrain the position of the burst to a 9 arc min^2 region with 95% confidence (Fig. 2) and to correct the flux density and spectral shape of the burst owing to the telescope response relative to its off-axis localization. Over the 1182- to 1519.5-MHz band, the mean burst fluence is $50 \pm 20 \text{ Jy ms}$, and the bandwidth-averaged peak flux density is $120 \pm 30 \text{ Jy}$, with the uncertainties dominated by the telescope response at the burst position. Direct fluence measurements have not been possible for previous FRBs.

The line-of-sight free-electron column density for FRB 150807, measured in units of dispersion measure (DM), is $266.5 \pm 0.1 \text{ pc cm}^{-3}$. This substantially exceeds the expected foreground Milky Way DM, predicted to be $70 \pm 20 \text{ pc cm}^{-3}$ along the burst sightline (galactic longitude $l = 336.71 \pm 0.03^\circ$, latitude $b = -54.40 \pm 0.03^\circ$), which includes contributions from ionized plasma in both the Milky Way disk [$40 \pm 20 \text{ pc cm}^{-3}$ (11–13)] and

Table 1. Properties of FRB 150807.

Time of burst peak	Universal time	7 August 2015
	(Reference frequency 1207 MHz)	17:53:55.77991 \pm 0.00009
Position (J2000)	Right ascension	22:40:23 \pm 4
	Declination	-53.16 ± 2
	Galactic longitude (l)	$336.71 \pm 0.03^\circ$
	Galactic latitude (b)	$-54.40 \pm 0.03^\circ$
Peak flux (averaged over 1182 to 1519.5 MHz)	Measured	$12.2 \pm 0.1 \text{ Jy}$
	Implied (boresight)*	$120 \pm 30 \text{ Jy}$
Peak flux in dynamic spectrum	Measured	$128 \pm 5 \text{ Jy}$
	Implied (boresight)*	$1000 \pm 300 \text{ Jy}$
Fluence	Measured	$4.6 \pm 0.4 \text{ Jy ms}$
	Implied (boresight)*	$50 \pm 20 \text{ Jy ms}$
Spectral index α , for assumed spectral form proportional to f^α	Measured	-7 ± 2
	implied (boresight)*	-5 ± 2
Width	At half maximum amplitude	$0.35 \pm 0.05 \text{ ms}$
Dispersion measure (DM)	Total	$266.5 \pm 0.1 \text{ pc cm}^{-3}$
	Extra-galactic†	$200 \pm 20 \text{ pc cm}^{-3}$
Faraday rotation (RM)	Total	$12.0 \pm 7 \text{ rad m}^{-2}$
	Extra-galactic‡	$-1.3 \pm 7 \text{ rad m}^{-2}$
Mean line-of-sight parallel magnetic field, $B_{ }$	Total	$56 \pm 5 \text{ nG}$
	Extra-galactic‡† (2σ limit)	$<21 \text{ nG}$
Inferred scintillation bandwidth	Half-width at e^{-1} of the spectrum-autocorrelation peak	$100 \pm 50 \text{ kHz}$

*After correcting for the maximum-likelihood beam attenuation. †After removing the Milky Way DM contribution, estimated to be $70 \pm 10 \text{ pc cm}^{-3}$. ‡After removing the RM of the nearby pulsar PSR J2241–5236, adopted as the Milky Way RM contribution, and assuming a $|RM|$ of 2.7 rad m^{-2} and an extragalactic DM of 160 pc cm^{-3} .

¹Cahill Center for Astronomy and Astrophysics, MC249-17, California Institute of Technology, Pasadena, CA 91125, USA.

²Commonwealth Scientific and Industrial Research Organization (CSIRO) Astronomy and Space Science, Australia Telescope National Facility, Post Office Box 76, Epping, NSW 1710, Australia. ³International Centre for Radio Astronomy Research, Curtin University, Bentley, WA 6102, Australia. ⁴Centre for Astrophysics and Supercomputing, Swinburne University of Technology, Post Office Box 218, Hawthorn, VIC 3122, Australia. ⁵ARC Centre of Excellence for All-sky Astrophysics (CAASTRO), Australia. ⁶National Radio Astronomy Observatory, Array Operations Center, Post Office Box 0, Socorro, NM 87801-0387, USA. ⁷Research School of Astronomy and Astrophysics, Australian National University, ACT 2611, Australia. ⁸Square Kilometer Array (SKA) Organisation, Jodrell Bank Observatory, SK11 9DL, UK. ⁹Max-Planck-Institut für Radioastronomie, Auf dem Hügel 69, 53121 Bonn, Germany. ¹⁰Manly Astrophysics, 3/22 Cliff Street, Manly NSW 2095, Australia.

*Corresponding author. Email: vikram@caltech.edu (V.R.); ryan.shannon@csiro.au (R.M.S.) †These authors contributed equally to this work.

halo [$30 \pm 10 \text{ pc cm}^{-3}$ (14)] (15). The DM of FRB 150807 is the smallest hitherto reported for an FRB.

The spectrum of FRB 150807 is strongly enhanced between 1250 and 1300 MHz (Fig. 1D). This is reminiscent of the spectra of bursts from the repeating FRB 121102 (16) and may be intrinsic to the source. The enhancement could also be due to diffractive scintillation caused by scattering in the Milky Way; the expected scintillation bandwidth induced by Milky Way plasma density fluctuations is expected to be $>8 \text{ MHz}$ at these frequencies (17). The transient nature of scattering-induced magnifications (17) may explain the general absence of repeated bursts, if FRBs represent frequent bursts from compact objects (18–20). However, it is also possible that our follow-up observations, totaling 215 hours (10), were insufficiently sensitive to detect repeat bursts.

The localization of FRB 150807 can be used to estimate the distance at which it was emitted, if we can associate the FRB with a star or a galaxy. The deepest archival images of the sky-localization area (Fig. 2) contain nine objects brighter than a *Ks*-band magnitude of 19.2 (21): three stars and six galaxies. The brightest galaxy is at a distance between 1 and 2 Gpc (95% confidence), estimated from its photometric redshift (supplementary text S2) (10). The other galaxies are factors of >6 fainter than the brightest. Through a comparison of their infrared magnitudes with empirical and theoretical distributions of galaxy luminosities at different

distances, they are all expected to be $>500 \text{ Mpc}$ distant (22). Additionally, a similar analysis yields a low probability ($<5\%$) of a fainter undetected galaxy with a mass $>10^9$ solar masses (M_\odot) closer than 500 Mpc. If FRB 150807 originated in a galaxy, a distance of $>500 \text{ Mpc}$ is therefore likely unless the galaxy was $<10^9 M_\odot$.

The $80 \pm 1\%$ linear-polarization fraction of FRB 150807 enabled us to measure the Faraday rotation induced by magnetization of the dispersing plasma. The pulse-averaged rotation measure (RM) is $12.0 \pm 0.7 \text{ rad m}^{-2}$ (10). The nearby millisecond pulsar PSR J2241–5236, located 0.5° away on the sky, has a RM of $13.3 \pm 0.1 \text{ rad m}^{-2}$ despite a low DM of $11.41 \pm 0.01 \text{ pc cm}^{-3}$ (23). The Milky Way contributions to extragalactic source RMs vary by $\lesssim 10 \text{ rad m}^{-2}$ on degree angular scales at high Galactic latitudes (24–26). The pulsar RM is consistent with expectations for the Milky Way contribution along this sightline (25, 26); hence, we adopted it as such. We constrained the net extragalactic line-of-sight magnetic field $\langle B_{\parallel} \rangle$, weighted by the free electron density distribution and likely incorporating numerous reversals of polarity, to be $\langle B_{\parallel} \rangle < 21(1 + z_{\text{mean}}) \text{ nG}$ ($>95\%$ confidence), where z_{mean} is the mean redshift of the intervening electron-density distribution (27), expected to be ~ 0.1 if the burst is at a gigaparsec distance. The combined DM and RM measurements directly constrain the gigaparsec-scale magnetization of the cosmic web along this sightline. Our results are consistent with numerous models

(27, 28) that predict that at-most nanogauss magnetic fields pervade the cosmic web. Additionally, FRB progenitor theories that propose emission from young neutron stars or other objects embedded in highly magnetized star-forming regions or galaxy centers (18–20) may be inconsistent with the low RM of FRB 150807, unless the net magnetization is externally cancelled.

The dispersion-corrected burst dynamic spectrum (Fig. 1C) shows strong modulations in both frequency and time below the instrument resolution, which are inconsistent with thermal noise associated with the telescope or the burst (supplementary text S1) (10). Instead, the intensity variations, portions of which exceed 1 kJy, have an exponential distribution. Because the burst width at each frequency is consistent with the amount of dispersion in each spectrometer channel, implying that the burst is temporally unresolved, the temporal structure in the dynamic spectrum

Fig. 1. Polarization and spectral properties of FRB 150807.

(A) Absolute position angle (ψ) of the electric field polarization vector. (B) Total intensity (black), linear polarization fraction (red), and Stokes V (blue) time-series profiles of the burst, averaged over all frequency channels. (C) Dedispersed dynamic spectrum of the burst. The intensity scale is indicated by the inset color bar. The small bars on the left of the plot show frequency channels removed because they contained radio-frequency interference. (D) The time-averaged spectrum of the burst, smoothed with a

5-MHz Gaussian filter. The time-resolution of the data in (A), (B), and (C) is 64 μs , and the frequency-resolution of the data in (C) and (D) is 390.625 kHz. The data displayed in (A) to (D) have been corrected for the frequency-dependent instrumental gain, the instrumental response to a polarized source, and the effects of the off-axis burst position. Additionally, the data displayed in (B), (C), and (D) have had the mean off-pulse levels subtracted from each channel.

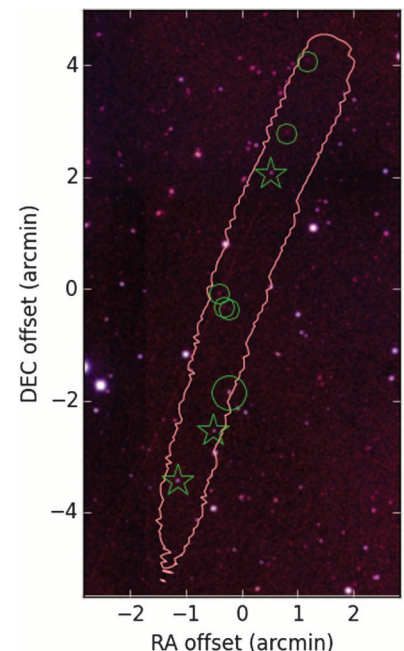
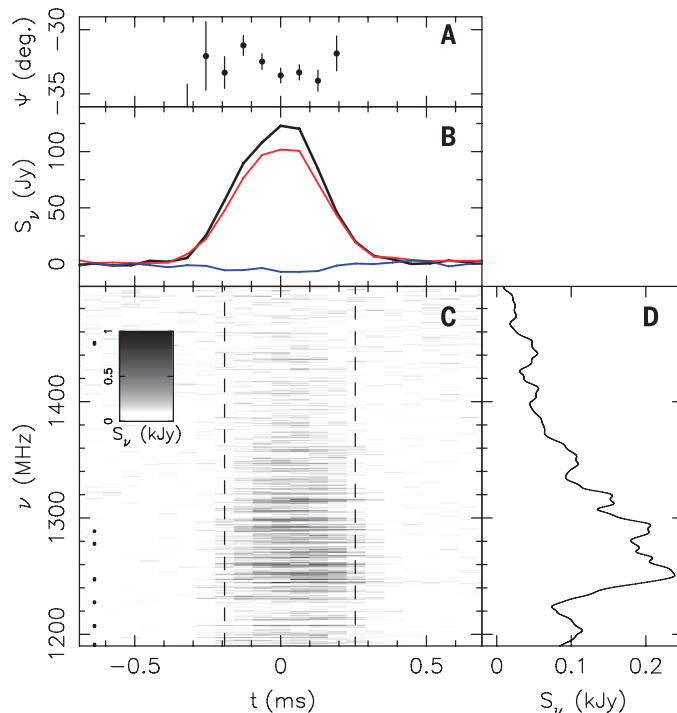


Fig. 2. Containment region and possible hosts of FRB 150807.

The pink trace shows the 95% confidence containment region from our modeling of the Parkes multibeam response pattern. Besides an 11-arc sec uncertainty in the Parkes telescope pointing, the size of the error region is dominated by the uncertainty in the multifrequency signal-to-noise ratio measurements in the weaker of the detected beams. The background is a three-color composite of images in the *J*, *H*, and *Ks* near-infrared bands from the Visible and Infrared Survey Telescope for Astronomy (VISTA) Hemisphere Survey (VHS) (21). The image is centered on right ascension 22:40:23.04 and declination $-53:16:12.4$ (J2000). The stars and circles represent sources identified as Milky Way stars and galaxies, respectively (supplementary text S2) (10). A large circle highlights the position of VHS7, the brightest galaxy inside the containment region, which has a distance of between 1 and 2 Gpc (95% confidence).

corresponds to spectral features that are narrower than the channel width, which are at random frequencies within the channels and therefore incorrectly dedispersed. We estimate the characteristic bandwidth of these spectral features to be 100 ± 50 kHz.

The spectral features with exponentially distributed intensities imply that the burst temporal profile is dominated by structure on few-microsecond scales; if the burst width was 10 μ s, the measured fluence would imply a mean flux density of 5 kJy. This structure could be intrinsic to the burst emission mechanism, in which case FRB 150807 would be similar to giant pulses from the Crab pulsar (29). In this interpretation, we would expect to observe similar spectral intensity variations in other FRBs that were detected with high significance, unless other FRBs have substantially different pulse durations. The 100-kHz structure in the spectrum of FRB 150807 may instead represent diffractive scintillation, caused by the scattering of the burst in inhomogeneous plasma along the line of sight with a characteristic time scale $\tau_d = 1/(2\pi \times 100 \text{ kHz}) = 1.6 \mu$ s (17). By analyzing the multifrequency burst

profile, we place an independent upper limit on τ_d of 27 μ s (95% confidence) at 1.3 GHz (supplementary text S1.4) (10). FRB 150807 thus exhibits weaker scattering than measured for any other FRB.

Scattering strength, quantified by the characteristic delay (τ_d) of scattered rays, is related to the line-of-sight integral of the plasma-density fluctuation power spectrum [the scattering measure (SM)], under specific assumptions about the location and geometry of the scattering medium (supplementary text S1.3) (10). Contributions to the burst DM, RM, and SM can be made by plasma within the host galaxy (if the burst originated within a galaxy), within the Milky Way, and in the IGM. The 100-kHz structure is much narrower in frequency than the expectation for Milky Way scintillations (>8 MHz) along this sightline (11). For the maximum possible redshift (0.4, $>95\%$ confidence) of FRB 150807 implied by its DM (14), intervening galaxies have only a few percent probability of being present (30) and would imply $\tau_d \gg 1$ ms (22). If $\tau_d = 1.6 \mu$ s, the low RM of the burst suggests that the scattering is unlikely to have originated in a disk-galaxy host system regardless of the host DM contri-

bution. In Fig. 3, we compare estimates for FRB scattering strengths to those for Milky Way pulsars. We applied the standard thin-screen model for the scattering geometry, which relates the SM to τ_d as

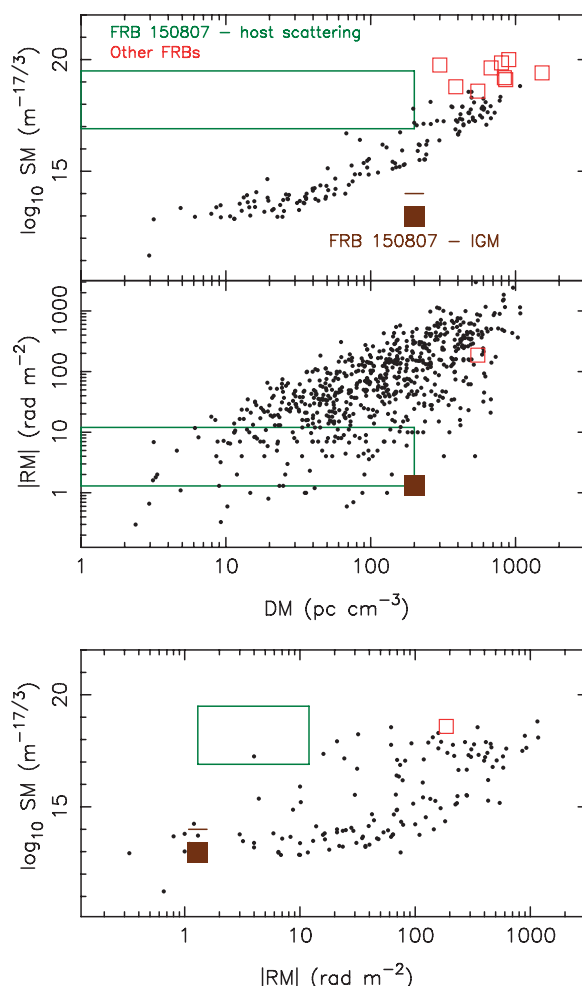
$$\text{SM} = 2.73 \times 10^{17} (1 + z_{\text{scr}})^{17/6} (\nu/1.3 \text{ GHz})^{11/3} [\tau_d (D_{\text{eff}}/1 \text{ Gpc})^{-1}]^{5/6} \text{ m}^{-17/3} \quad (1)$$

where ν is the observing frequency, z_{scr} is the redshift of the screen, and $D_{\text{eff}} = (D_{\text{scr}}/D)(D - D_{\text{scr}})$, where D_{scr} is the distance from Earth to the scattering screen and D is the Earth-source distance (31). If FRB 150807 originated in a disk galaxy like the Milky Way, the magnitude of its RM (|RM|) would be unexpectedly low for its SM if $\tau_d \geq 1.6 \mu$ s. Also, depending on whether or not the host dominated the DM, the |RM| would either be unexpectedly low for the DM, or the SM would be unexpectedly high for the DM, respectively.

As suggested for other FRBs (22), it is possible that the 100-kHz structure in FRB 150807 represents weak scattering in a host galaxy that dominated the dispersion, with lower-than-expected |RM| and SM relative to Milky Way disk sightlines. The host would be near to the Milky Way, and the localization implies that the galaxy would likely have a low mass ($\leq 10^9 M_\odot$). It is also possible that the dispersion of FRB 150807 was dominated by the IGM contribution, which would suggest a distance $D \sim 1$ Gpc (14), which is in good agreement with the localization-based constraint. If we model the IGM as a homogeneous scattering medium along the entire sightline, the SM is approximately given by setting $D_{\text{eff}} = D/2$. Setting $D = 1$ Gpc, and assuming $\tau_d = 1.6 \mu$ s, we find $\text{SM} = 9.5 \times 10^{12} \text{ m}^{-17/3}$. Although this is consistent with a prediction of $\text{SM} \approx 4 \times 10^{12} \text{ m}^{-17/3}$ in the IGM for sources at this distance (31), such a high SM may be inconsistent with the observed thermal stability of the IGM (32).

Despite its particular properties, FRB 150807 is not excluded from being drawn from the same source population as the majority of FRBs. In this case, a comparison between FRB 150807 and other FRBs provides support for the cosmological origin of a large fraction of the FRBs. The event with the second-lowest DM, FRB 010724 (1), was detected in four beams of the Parkes multibeam system, implying a fluence comparable with that of FRB 150807. Therefore, DM may correlate with source distance among FRBs, which would only be expected for a cosmological population with subdominant host-galaxy contributions. The discovery of FRB 150807 also partially resolves the lack of low-DM FRBs, which has been suggested as evidence for a nearby population with host-dominated DMs (22, 33). The weak scattering of FRB 150807 relative to other FRBs with detected scattering could indicate a relation between dispersion and scattering strength characteristic of a clumpy IGM, similar to that observed in the Milky Way interstellar medium (34). Last, an analysis of the FRB fluence distribution, including FRB 150807, finds evidence against a local-universe population (35). This analysis also predicts that events with fluences similar to that of

Fig. 3. Properties of the plasma toward FRBs and pulsars. Green boxes indicate possible ranges of DMs, RMs, and SMs contributed by a putative host galaxy of FRB 150807, assuming negligible RM and SM contributions from the IGM. The upper limit of the FRB 150807 SM range assumes a screen at 0.1 kpc from the source, the source at $D = 100$ Mpc, and the upper limit (27 μ s) on τ_d ; the lower limit assumes a screen at 10 kpc, the source at $D = 500$ Mpc, and $\tau_d = 1.6 \mu$ s. The DM range for FRB 150807 is bounded by the total estimated extragalactic component. The RM range for FRB 150807 is bounded by its total detected RM and by its extragalactic value corrected for the Milky Way contribution. Brown squares indicate the DM, RM, and SM of FRB 150807 assuming contributions predominantly from the IGM and corrected for Milky Way contributions. The brown bars were calculated assuming $\tau_d = 27 \mu$ s. Red squares indicate DMs, RMs, and SMs of other FRBs (36). We assumed extragalactic DMs contributed entirely by putative host galaxies and converted the scattering measurements into SMs assuming screens at 10 kpc from the sources and $D = 100$ Mpc. Black dots indicate DMs, RMs, and SMs of Milky Way pulsars (37). The SMs were calculated assuming intervening scattering screens equidistant from Earth and the burst source.



FRB 150807 (that is, >50 Jy ms) are not rare, with a rate at ~ 1.3 GHz of 190 ± 60 sky $^{-1}$ day $^{-1}$.

REFERENCES AND NOTES

1. D. R. Lorimer, M. Bailes, M. A. McLaughlin, D. J. Narkevic, F. Crawford, *Science* **318**, 777–780 (2007).
2. D. Thornton et al., *Science* **341**, 53–56 (2013).
3. K. W. Masui, K. Sigurdson, *Phys. Rev. Lett.* **115**, 121301 (2015).
4. M. McQuinn, *Astrophys. J.* **780**, L33 (2014).
5. Z. Zheng, E. O. Ofek, S. R. Kulkarni, J. D. Neill, M. Juric, *Astrophys. J.* **797**, 71 (2014).
6. L. Staveley-Smith et al., *Publ. Astron. Soc. Aust.* **13**, 243–248 (1996).
7. M. J. Keith et al., *Mon. Not. R. Astron. Soc.* **409**, 619–627 (2010).
8. E. Petroff et al., *Mon. Not. R. Astron. Soc.* **447**, 246–255 (2015).
9. B. Barsdell et al., Spotting Radio Transients with the Help of GPUs, *ASP Conference Series*, **461**, 37 (2012).
10. Materials and methods are available as supplementary materials on Science Online.
11. J. M. Cordes, T. J. W. Lazio, NE2001.1. A new model for the galactic distribution of free electrons and its fluctuations, <https://arxiv.org/abs/astro-ph/0207156> (2002).
12. B. M. Gaensler, G. J. Madsen, S. Chatterjee, S. A. Mao, *Publ. Astron. Soc. Aust.* **25**, 184–200 (2008).
13. D. H. F. M. Schnitzler, *Mon. Not. R. Astron. Soc.* **427**, 664–678 (2012).
14. K. Dolag, B. M. Gaensler, A. M. Beck, M. C. Beck, *Mon. Not. R. Astron. Soc.* **451**, 4277–4289 (2015).
15. Recent models suggest that the Milky Way disk is more vertically extended than previously thought (12), and different models predict DMs that vary by up to a factor of two (13).
16. L. G. Spitler et al., *Nature* **531**, 202–205 (2016).
17. B. J. Rickett, *Annu. Rev. Astron. Astrophys.* **28**, 561–605 (1990).
18. J. M. Cordes, I. Wasserman, *Mon. Not. R. Astron. Soc.* **457**, 232–257 (2016).
19. Y. Lyubarsky, *Mon. Not. R. Astron. Soc.* **442**, L9–L13 (2014).
20. L. Connor, J. Sievers, U.-L. Pen, *Mon. Not. R. Astron. Soc.* **458**, L19 (2015).
21. N. J. G. Cross et al., *Astron. Astrophys.* **548**, A119 (2012).
22. J. M. Cordes, R. S. Wharton, L. G. Spitler, S. Chatterjee, I. Wasserman, Radio wave propagation and the provenance of fast radio bursts, <https://arxiv.org/abs/1605.05890> (2016).
23. S. Dai et al., *Mon. Not. R. Astron. Soc.* **449**, 3223–3262 (2015).
24. T. Akahori, D. Ryu, J. Kim, B. M. Gaensler, *Astrophys. J.* **767**, 150 (2013).
25. S. A. Mao et al., *Astrophys. J.* **714**, 1170–1186 (2010).
26. N. Oppermann et al., *Astron. Astrophys.* **575**, A118 (2015).
27. T. Akahori, D. Ryu, B. M. Gaensler, Fast radio bursts as probes of magnetic fields in filaments of galaxies, <https://arxiv.org/abs/1602.03235> (2016).
28. F. Marinacci, M. Vogelsberger, P. Mocz, R. Pakmor, *Mon. Not. R. Astron. Soc.* **453**, 3999 (2015).
29. J. M. Cordes, N. D. R. Bhat, T. H. Hankins, M. A. McLaughlin, J. Kern, *Astrophys. J.* **612**, 375–388 (2004).
30. R. Fender, T. Oosterloo, *Mon. Not. R. Astron. Soc.* **451**, L75–L79 (2015).
31. J.-P. Macquart, J. Y. Koay, *Astrophys. J.* **776**, 125 (2013).
32. J. Luan, P. Goldreich, *Astrophys. J.* **785**, L26 (2014).
33. J. I. Katz, *Astrophys. J.* **818**, 19 (2016).
34. J. M. Cordes, J. M. Weisberg, D. A. Frail, S. R. Spangler, M. Ryan, *Nature* **354**, 121–124 (1991).
35. H. Vedantham, V. Ravi, R. M. Shannon, G. Hallinan, The fluence and distance distributions of fast radio bursts, <https://arxiv.org/abs/1606.06795> (2016).
36. More details on the MB21, including the labeling of each feed, can be found at www.atnf.csiro.au/research/multibeam.
37. R. N. Manchester et al., *Publ. Astron. Soc. Aust.* **30**, e017 (2013).

ACKNOWLEDGMENTS

We thank both D. Schnitzler and the SUPERB (Survey for Pulsars and Extragalactic Radio Bursts) collaboration for useful feedback on the manuscript. The Parkes radio telescope is part of the Australia Telescope National Facility, which is funded by the Commonwealth of Australia for operation as a National Facility managed by CSIRO. N.D.R.B. is supported by a Curtin Research Fellowship. The data for FRB 150807 reported in this paper are made available through the CSIRO data access portal at <http://doi.org/10.4225/08/580fcb0d68cc>.

SUPPLEMENTARY MATERIALS

www.sciencemag.org/content/354/6317/1249/suppl/DC1
Materials and Methods
Supplementary Text
Figs. S1 to S10
Tables S1 to S4

References (38–78)

Supplementary Computer Code Files S1 and S2

15 March 2016; accepted 27 October 2016

Published online 17 November 2016

10.1126/science.aaf6807

MICROFLUIDICS

How boundaries shape chemical delivery in microfluidics

Manuchehr Aminian, Francesca Bernardi, Roberto Camassa,*
Daniel M. Harris, Richard M. McLaughlin*

Many microfluidic systems—including chemical reaction, sample analysis, separation, chemotaxis, and drug development and injection—require control and precision of solute transport. Although concentration levels are easily specified at injection, pressure-driven transport through channels is known to spread the initial distribution, resulting in reduced concentrations downstream. Here we document an unexpected phenomenon: The channel's cross-sectional aspect ratio alone can control the shape of the concentration profile along the channel length. Thin channels (aspect ratio $\ll 1$) deliver solutes arriving with sharp fronts and tapering tails, whereas thick channels (aspect ratio ~ 1) produce the opposite effect. This occurs for rectangular and elliptical pipes, independent of initial distributions. Thus, it is possible to deliver solute with prescribed distributions, ranging from gradual buildup to sudden delivery, based only on the channel dimensions.

By exploiting the flexibility afforded by working at small scales, microfluidics and lab-on-a-chip devices have attracted interest because of their potential for simplifying and reducing costs of fluid-based laboratory processes. A key component of these devices is the pressure-driven transport of solute through channels. Recent technological advances, such as in microfluidic flow injection analysis (1, 2) and chromatographic separation (3, 4), have increased the demand for improved precision in the controlled delivery of solutes in such flows. This becomes particularly important when limited sample sizes are available, as in some applications envisioned for microfluidic laboratory analyses. We have found that the channel's aspect ratio offers a method to specify the longitudinal solute distribution, including its peak locations and asymmetries: On long time scales, thin channels deliver species with a sharp front followed by a long tapering tail (“front-loaded”), whereas thick cross sections produce the reverse result (“back-loaded”) (see Fig. 1, A and B, for schematic illustrations).

Such phenomena go beyond the enhancement over molecular diffusion that was first explained and characterized by Taylor (5) (and has since been referred to as “Taylor dispersion”), with the prediction that flowing solute spreads with an effective, boosted diffusivity inversely proportional to the molecular diffusivity. This magnification is observed beyond long, diffusive time scales once the solute has diffused across the channel.

Recent research focusing on microfluidic applications has examined how the enhanced diffusivity also depends on the cross-sectional shape of the channel (6–9). An important yet largely unexplored avenue of investigation lies in how the cross section itself induces an asymmetry in the tracer distribution. For the special case of a circular pipe, it was observed theoretically that the distribution could arrive asymmetrically (10, 11), but the precise role played by geometry in establishing the symmetry features, particularly regarding the role that the aspect ratio plays in setting front- versus back-loading, appears to be unexplored in the literature.

On the very shortest time scales, the symmetry properties of solute distributions are nonuniversal with respect to the cross-sectional geometry (12): Elliptical domains preserve initial symmetries, whereas rectangular ducts instantaneously create asymmetries. In contrast, we show here that on longer time scales, the longitudinal asymmetries are universal with respect to a broad class of geometries and are essentially set only by the aspect ratio. We are primarily interested in channels with elliptical and rectangular cross sections (“pipes” and “ducts”), whose minor and major axes (i.e., short and long sides) are $2a$ and $2b$, respectively, with the aspect ratio $\lambda = a/b$ ($0 < \lambda \leq 1$). The Péclet number, a nondimensional parameter measuring the relative importance of transport via flow versus diffusion, is defined on the basis of the shortest length scale, $Pe = Ua/\kappa$, and the diffusive time scale, $t_d = a^2/\kappa$, where U is a characteristic flow speed and κ is the molecular diffusivity of the solute. Péclet numbers for microfluidic applications are typically between 10 and 10^5 , with diffusivities ranging from 10^{-7} to 10^{-5} .

Department of Mathematics, University of North Carolina, Chapel Hill, NC 27599, USA.

*Corresponding author. Email: camassa@email.unc.edu (R.C.); rmm@email.unc.edu (R.M.M.)

cm^2/s (13). Thus, for these applications, typical length scales and flow speeds place relevant observations well beyond the nonuniversal behavior seen on the shortest time scales and onto intermediate-to-long time scales with respect to t_d .

After appropriate rescaling of variables (with physical time t normalized by t_d and denoted by τ , with longitudinal coordinate x , short transverse coordinate y , and long transverse coordinate z all normalized by a), the solute distribution T is governed by an advection-diffusion equation of the form

$$\frac{\partial T}{\partial \tau} + \text{Pe } u(y, z) \frac{\partial T}{\partial x} = \Delta T \quad (1)$$

with insulating (no-flux) boundary conditions at the wall and an initial condition depending only on the unbounded longitudinal (along channel length) variable x , which is taken to be a Dirac delta function, unless otherwise noted. The fluid flow $u(y, z)$ is a laminar, steady-state solution to the Navier-Stokes equations with no-slip (no flow at wall) boundary conditions, driven

by a negative pressure gradient. For the case of straight channels of fixed cross section, the fluid flow is expressible exactly in terms of either a polynomial or a Fourier series (see supplementary text for complete details). The partial differential equation in Eq. 1 couples the physics of fluid advection (represented by the second term) and molecular diffusion (the last term), whose solution at each time, τ , gives the spatial distribution of the concentration within the channel. Figure 1A depicts the setup and labels the various dimensions and coordinates.

A convenient tool for measuring asymmetry is statistical skewness, defined to be the centered, normalized third moment $Sk(y, z, \tau) = \int (x - \mu)^3 T dx / [\int (x - \mu)^2 T dx]^{3/2}$, where $\mu = \int x T dx$ is the mean of the distribution. This is the lowest-order integral statistic that measures asymmetry of a given distribution and whose sign typically indicates its front-loading (negative) or back-loading (positive).

Constructing this statistic requires the first three longitudinal moments of the distribution. The “partial” (pointwise) moments of the distribu-

tion $T_n(y, z, \tau) = \int x^n T(x, y, z, \tau) dx$ are longitudinal moments at a given position within the cross section. These moments obey a similar set of equations to Eq. 1, called the Aris moment equations (14). Our main results depend on calculating long time behavior of the first three moments, which we can use to construct the skewness.

Figure 1C illustrates the particle distribution T computed by a Monte Carlo simulation for a circular and thin rectangular cross section for time increasing from short, advective-dominated times to longer, diffusive time scales. Shown in each panel's inset is the cross-sectionally averaged distribution, $C(x, \tau) = |\Omega|^{-1} \int_{\Omega} T(x, y, z, \tau) dy dz$ as a function of x , where $|\Omega|$ is the area of the cross-sectional domain. Initially, the circular pipe has approximately zero cross-sectionally averaged skewness (henceforth referred to as average skewness), becoming positively skewed at intermediate times and finally symmetrizing on long times. Alternatively, the particle distributions in the thin duct develop negative average skewness on short times and remain negatively skewed for all times. The strong relationship between the mean, median,

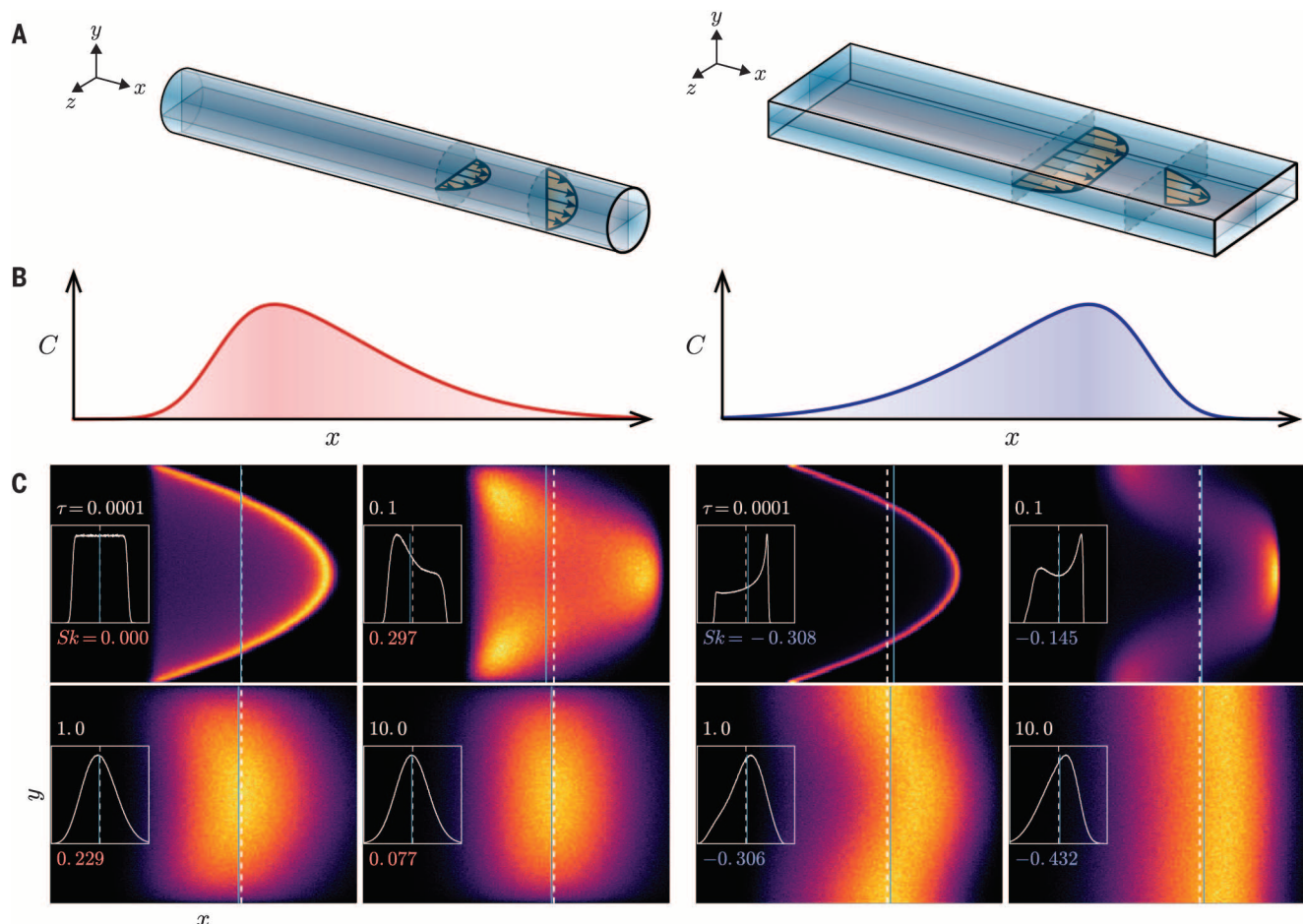


Fig. 1. Setup, schematics, and distribution evolution. (A) Flow geometry in pipes and ducts. (B) Back-loaded (left) versus front-loaded (right) distributions. (C) Snapshots of the Monte Carlo tracer distribution (T) projected through the longest cross-sectional direction (z) and (inset) the complete cross-sectionally averaged $C(x, \tau)$ for the circular pipe (left group) and rectangle $\lambda = 0.2$ (right group) with $\text{Pe} = 10^4$ at four times. Dashed lines denote the mean velocity; light

blue lines mark the median of the distribution. The horizontal axis is scaled to the leftmost and rightmost particle at each τ , and peak intensity is set by the instantaneous scalar maximum, with colors indicating concentration from zero (black) < purple < red < maximum (yellow). Skewness values (color) and time (white) are indicated at the bottom and top of the insets. We observe more mass to the left (or right) of the mean in the circle (or rectangle) at later times.

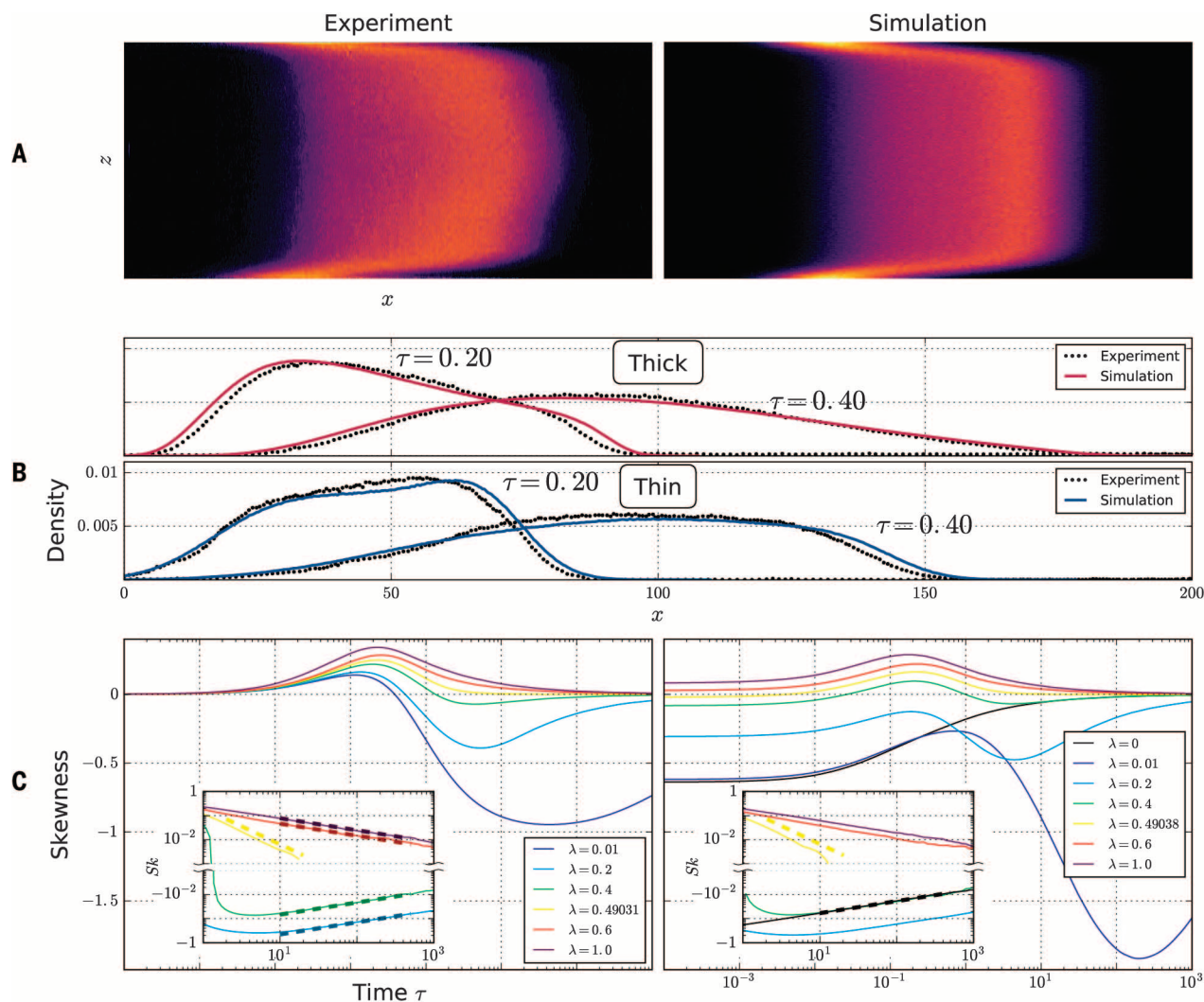


Fig. 2. Experimental, computational, and theoretical comparisons. (A) Thin-duct comparison: experiment (left) and simulation (right), projected down the short y axis (see Fig. 1A schematic), at $\tau = 0.2$. (B) Experimental and computational comparison of the cross-sectionally averaged tracer distribution along the duct (top: square duct, cross section 1 mm by 1 mm; bottom: thin rectangular duct, cross section 1 mm by 10 mm) at $\tau = 0.2$ and $\tau = 0.4$. Average flow velocities are matched (square: $Pe = 1670$; thin: $Pe = 752$).

Initial conditions were chosen to match the experiment (cross-sectionally uniform Gaussian in x , standard deviation: square, 3 mm; thin, 7.5 mm). (C) Skewness evolution: ellipses (left) and rectangles (right) in linear and log (inset) values, for varying aspect ratios. Equation 2 theoretical lines (all dashed) are shown for elliptical pipes and infinite ($\lambda = 0$) parallel plates. Special elliptical and rectangular cross sections of aspect ratio $\lambda = \lambda^*$ separate positive and negative relaxation with faster decay (dashed yellow lines).

and skewness further documents the notion that negative skewness implies front “loadedness,” as indicated by the relative position of the median and the mean. The horizontal axis is scaled by the maximum particle separation in the x direction (which roughly grows as the maximum flow speed times τ), capturing the short time spreading, whereas the distribution’s standard deviation grows slower ($\sim \sqrt{\tau}$) at long time scales (15), which appears as a narrowing of the distribution at later times. This effect proves useful to highlight the complex interplay between short and long time regimes. Lastly, we observe that on longer time scales the circular pipe has a back-loaded distribution, whereas the thin duct is front-loaded.

We next compared these observations to laboratory experiments, performed as follows: First,

we injected a small amount of fluorescein dye into a 300-mm-long square duct (1-mm-by-1-mm internal cross section) filled with distilled water, which was left to diffuse for several minutes to homogenize the initial condition. A syringe pump then pushed water through the duct, advecting the dye downstream. Side-view images were acquired with a digital still camera and post-processed to construct the cross-sectionally averaged concentration as a function of downstream position. This procedure was repeated, matching the average flow velocity of the first experiment, on a thin duct (1 mm by 10 mm) (see supplementary materials for full details).

A direct comparison between Monte Carlo simulations and our laboratory experimental results performed in square and thin rectangular

ducts is presented in Fig. 2, A and B, for intermediate time scales. Figure 2A documents the pointwise agreement between the experiment and the simulation viewed orthogonally to the long side. The near-uniform transport away from the top and bottom walls is also evident in both the experiment and the simulation; this is a consequence of flow in thin rectangles. This feature is absent for flow in elliptical cross sections and may be particularly useful in microfluidic channel design to reduce overall spreading. Figure 2B presents a comparison between the Monte Carlo simulation with the lab experiment for the cross-sectionally averaged tracer distribution at several different output times, illustrating that the thin domain is heavily front-loaded, whereas the square domain is strongly back-loaded (with variations

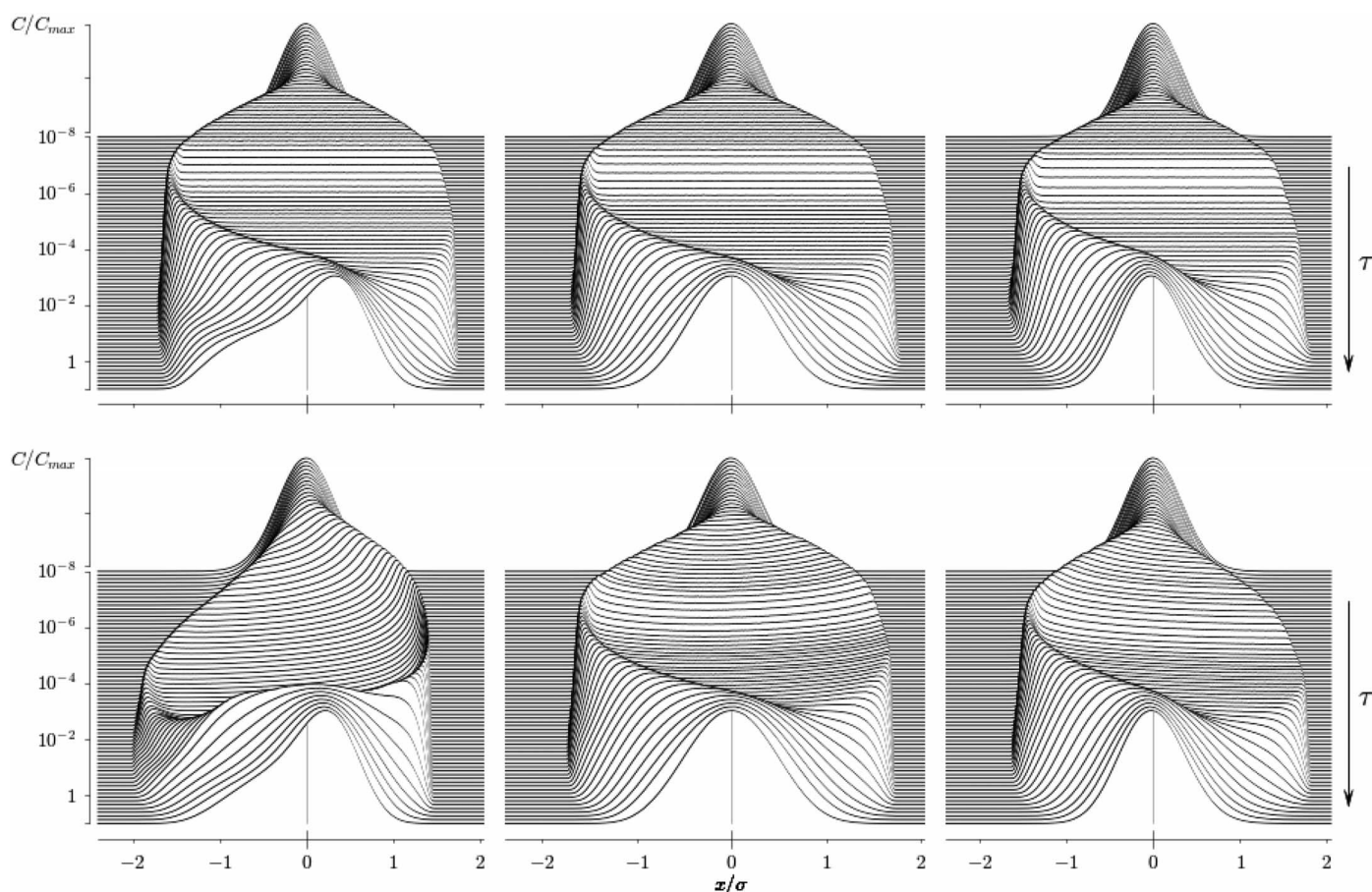


Fig. 3. Evolution of the distribution $C(x, \tau)$. Ellipses (top) and rectangles (bottom) for aspect ratios of $\lambda = 0.2$, λ^* , and 1 illustrate nontrivial asymmetry depending on geometry over many time scales (time flows from top to bottom). Distributions are scaled by their peak value and standard deviation for visualization. The mean velocity is marked by vertical lines. The front-loading evolution can be seen in the left column, whereas the back-loading persistence is apparent in the right column. The middle column (golden ratios) illustrates more rapid symmetrization.

among runs of typically less than 5%). The experimental observations quantitatively match the theory. The front- versus back-loading properties emerge as predicted by the theory in all variations of the experiment, including changes in initial data, thin-duct orientation with respect to gravity, flow rates, and concentrations.

The physical mechanism responsible for the net loading is a competition between the wall and interior. The shear flow shapes the concentration into a paraboloid, which creates an asymmetry: Away from the centerline, there is solute behind the leading front, providing a diffusive source that feeds the interior distribution and produces a left heavy tail (locally). This effect reverses at the wall. The relative influence of the wall versus the interior sets the net loading, and mathematical analysis is required to determine the precise balance.

Toward this end, we analytically assessed this dependence on the aspect ratio through the calculation of the first three moments. Each moment is an evolving function of the location within the cross section, satisfying a driven heat equation with a driver that depends on the fluid flow and lower moments. Each moment's long time behav-

ior is reduced, for its cross-sectional average, to a simple ordinary differential equation and a domain-dependent partial differential equation for its fluctuation (see supplementary text for complete details).

These calculations yield a simple formula for the long time skewness as a function of the aspect ratio and specific domain

$$Sk \sim \tau^{-1/2} \frac{3Pe^3 G_2}{(2 + 2Pe^2 G_1)^{3/2}} + \mathcal{O}(\tau^{-3/2}) \quad (2)$$

where the functions G_1 and G_2 are defined in the supplementary text and depend only on the aspect ratio and domain shape and not on location within the cross section. This surprising result predicts that the long time nonzero skewness becomes independent of y and z . The coefficient of the decay rate $\tau^{-1/2}$ can be calculated explicitly in closed form for elliptical cross sections and agrees with previous exact results for the circular pipe (10, 11).

The results of Monte Carlo simulations are shown in Fig. 2C, with varying aspect ratios in elliptical and duct domains. The majority of plots show this $\tau^{-1/2}$ decay rate at long times with a few exceptions. For the very thin do-

main ($\lambda = 0.01$), the long time regime is not yet reached, as the final diffusive time scale is $t \propto b^2/\kappa$ or $\tau = 10^4$. Notably, there are critical aspect ratios for the ellipse and duct domains that exhibit faster decay and separate positive (back-loaded, wall-dominated) from negative (front-loaded, interior-dominated) relaxation in time.

Our theory can directly predict these “golden,” cross-over aspect ratios: Because the denominator of Eq. 2 can be shown to be strictly positive, the long time sign of the skewness is determined by the numerator G_2 .

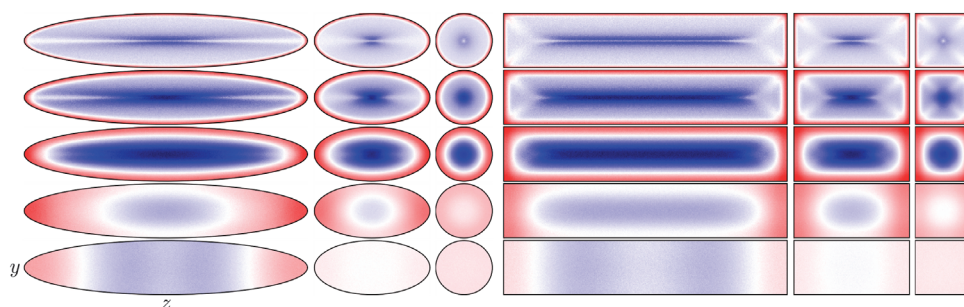
To handle the general elliptical case, working in elliptical coordinates yields exact solutions for G_1 and G_2 , in terms of a finite Fourier sum (see supplementary text for full calculations)

$$G_1 = \frac{1}{2304} \frac{(5\lambda^4 + 14\lambda^2 + 5)}{\lambda^2(\lambda^2 + 1)^3} \quad (3a)$$

$$G_2 = \frac{1}{138240} \frac{(5\lambda^4 - 22\lambda^2 + 5)}{\lambda^4(\lambda^2 + 1)^3} \quad (3b)$$

[The expression for G_1 is proportional to the coefficient for classical diffusive enhancement

Fig. 4. Pointwise skewness over cross sections. Parameters are $Pe = 10^4$ and aspect ratios (left to right) of $\lambda = 0.2, \lambda^*$, and 1.0 at times $\tau = 0.0014, 0.008, 0.046, 0.44$, and 2.5 (top to bottom). Short time skewness: positive at the walls (red) and negative in the center (blue) in all cases due to diffusive pumping. Pointwise skewness for all cross sections is approximately uniform at $\tau = 2.5$ (compare with Eq. 2), with golden ratios λ^* separating positive from negative values.



and agrees with previously calculated exact results for the ellipse (14, 16)].

The second term G_2 provides an exact prediction for the cross-over (“golden”) aspect ratio, separating front-loaded from back-loaded behavior at long times. The expression for G_2 has a simple, irrational root at aspect ratio $\lambda_{\text{ell}}^* = \sqrt{(11 - 4\sqrt{6})/5} \approx 0.49031$.

At this value, the skewness vanishes at a faster rate $\sim \tau^{-3/2}$ instead of $\sim \tau^{-1/2}$, which we observe in the numerics (Fig. 2C) with a reference $-3/2$ slope line. Further, the ratio $3G_2/(2G_1)^{3/2}$ provides the correct large Péclet prefactor to the long time decay rate as a function of aspect ratio for the skewness (defined in Eq. 2) shown by the predicted reference lines in the left inset of Fig. 2C. The agreement between the simulation and these theoretical curves can be seen from Fig. 2C to hold for time scales well before the Taylor regime is reached. In general, the long-time leading order asymptotics will be $\sim A\tau^{-1/2} + B\tau^{-3/2}$, where A is given in Eq. 2 and B is a known function of the aspect ratio and Péclet number. For aspect ratios near but different from the golden ratio, A will be very small and the scaling $\tau^{-3/2}$ will be observed for a large period of time.

As with the family of ellipses, there is a distinguished “golden” rectangle. For this, we employ a finite element scheme to solve the partial differential equations governing the moments at long times and calculate G_2 as a function of the aspect ratio. The distinguished rectangle aspect ratio is $\lambda_{\text{rect}}^* \approx 0.49038$. Again, at this value, the skewness decays as $\sim \tau^{-3/2}$, which agrees with simulations shown in Fig. 2C. Note the success of the theory in quantitatively predicting the skewness well before the final diffusion time scale. Aspect ratios below λ_{rect}^* have negative long time skewness (front-loaded), and those above λ_{rect}^* are positive (back-loaded).

Theoretical results such as these are useful in designing optimal microfluidic devices. We emphasize that our analysis gives an exact result for the elliptical domains and an accurate numerical prediction in the rectangular duct. The fact that these critical aspect ratios are so close for quite different domains further emphasizes the universality of the theory, which is particularly important in experimental applications where geometric variations are inevitable.

The role of geometry in front- and back-loading can be visualized computationally by observing the evolution of the cross-sectionally averaged distribution $C(x, \tau)$. Figure 3 shows this evolution

for varying aspect ratios (thin to thick, left to right) and geometries (top: ellipse; bottom: duct), using stacked snapshots of the distribution with time increasing from top to bottom. Again, thin domains produce front-loaded distributions, whereas thick geometries reverse this result. Also note the difference between elliptical and rectangular domains at short and intermediate times, in which the ellipse experiences symmetric spreading in contrast with the rectangular case.

Although difficult to probe in a lab experiment, we can computationally explore pointwise distributional variations within the cross section itself, as opposed to its average. Figure 4 presents the evolution of pointwise skewness as a function of aspect ratio and geometry. In agreement with our general theory, at long times, the skewness evolves to a uniform state throughout the cross section. On earlier times, there is interesting dynamics connecting the short-time positive skewness (red) at the walls and negative skewness (blue) in the interior and subsequent evolution to the long time state. This demonstrates the complex competition between the wall and the interior, and the interior ultimately prevails in the thin domains shown here.

The front- versus back-loading effects we have documented are expected to be an important factor and will ultimately influence the design of microfluidic devices by affording control of mass distribution by simple geometric means. This result may be particularly useful in flow injection analysis, where a sample bolus is injected into a carrier fluid that reacts and generates by-product gradients that are analyzed downstream (1, 2). Our new geometric control of concentration profiles allows for the tuning of gradients to optimize output response. This effect could further be used to control and generate specific chemical gradients within and at the exit of microfluidic channels (17), which may be useful for chemotaxis (18–20) and drug development (21) assays. Moreover, the additional control could improve applications such as open-channel or hydrodynamic chromatographic separation processes (3, 4), where longitudinal asymmetry presents considerable measurement challenges (22, 23). For instance, the aspect ratio phenomenon we have discovered could be exploited to minimize or actively reverse the asymmetries encountered during the separation process, sometimes referred to as “peak fronting” or “tailing” (23, 24). Among the various yet-unanswered questions are whether more complex geometries can provide additional control

and, in particular, whether more extreme asymmetries can be obtained.

REFERENCES AND NOTES

- D. Betteridge, B. Fields, *Anal. Chem.* **50**, 832A (1978).
- M. Trojanowicz, K. Kolacińska, *Analyst* **141**, 2085–2139 (2016).
- D. Dutta, D. T. Leighton Jr., *Anal. Chem.* **75**, 57–70 (2003).
- M. T. Blom, E. Chmela, R. E. Oosterbroek, R. Tjissen, A. van den Berg, *Anal. Chem.* **75**, 6761–6768 (2003).
- G. Taylor, *Proc. R. Soc. London Ser. A* **219**, 186–203 (1953).
- A. Ajdari, N. Bontoux, H. A. Stone, *Anal. Chem.* **78**, 387–392 (2006).
- D. Dutta, A. Ramachandran, D. T. Leighton Jr., *Microfluid. Nanofluidics* **2**, 275–290 (2006).
- N. Bontoux, A. Pépin, Y. Chen, A. Ajdari, H. A. Stone, *Lab Chip* **6**, 930–935 (2006).
- S. Vedel, H. Bruus, *J. Fluid Mech.* **691**, 95–122 (2012).
- P. C. Chatwin, *J. Fluid Mech.* **43**, 321–352 (1970).
- N. Barton, *J. Fluid Mech.* **126**, 205–218 (1983).
- M. Aminian, F. Bernardi, R. Camassa, R. M. McLaughlin, *Phys. Rev. Lett.* **115**, 154503 (2015).
- H. A. Stone, A. D. Stroock, A. Ajdari, *Annu. Rev. Fluid Mech.* **36**, 381–411 (2004).
- R. Aris, *Proc. R. Soc. London Ser. A* **235**, 67–77 (1956).
- R. Camassa, Z. Lin, R. M. McLaughlin, *Commun. Math. Sci.* **8**, 601–626 (2010).
- P. Chatwin, P. J. Sullivan, *J. Fluid Mech.* **120**, 347–358 (1982).
- A. G. Toh, Z. Wang, C. Yang, N.-T. Nguyen, *Microfluid. Nanofluidics* **16**, 1–18 (2014).
- J. Adler, *Science* **166**, 1588–1597 (1969).
- R. P. Futrelle, H. C. Berg, *Nature* **239**, 517–518 (1972).
- J. Adler, *J. Gen. Microbiol.* **74**, 77–91 (1973).
- S. Sugiura, K. Hattori, T. Kanamori, *Anal. Chem.* **82**, 8278–8282 (2010).
- E. Grushka, M. N. Myers, J. C. Giddings, *Anal. Chem.* **42**, 21–26 (1970).
- T. Fornstedt, G. Zhong, G. Guiochon, *J. Chromatogr. A* **741**, 1–12 (1996).
- M. Kanaotov, C. Retif, L. T. Cherney, S. N. Krylov, *Anal. Chem.* **84**, 149–154 (2012).

ACKNOWLEDGMENTS

We acknowledge funding from the Office of Naval Research (grant DURIP N00014-12-1-0749) and the NSF (grants RTG DMS-0943851, CMG ARC-1025523, DMS-1009750, and DMS-1517879). The experimental methodology and the details of the Monte Carlo simulations are documented in the materials and methods and the supplementary text.

SUPPLEMENTARY MATERIALS

www.sciencemag.org/content/354/6317/1252/suppl/DC1
Materials and Methods
Supplementary Text
Fig. S1
References (25, 26)

9 May 2016; resubmitted 22 June 2016
Accepted 20 October 2016
Published online 17 November 2016
10.1126/science.aag0532

Sensitive electromechanical sensors using viscoelastic graphene-polymer nanocomposites

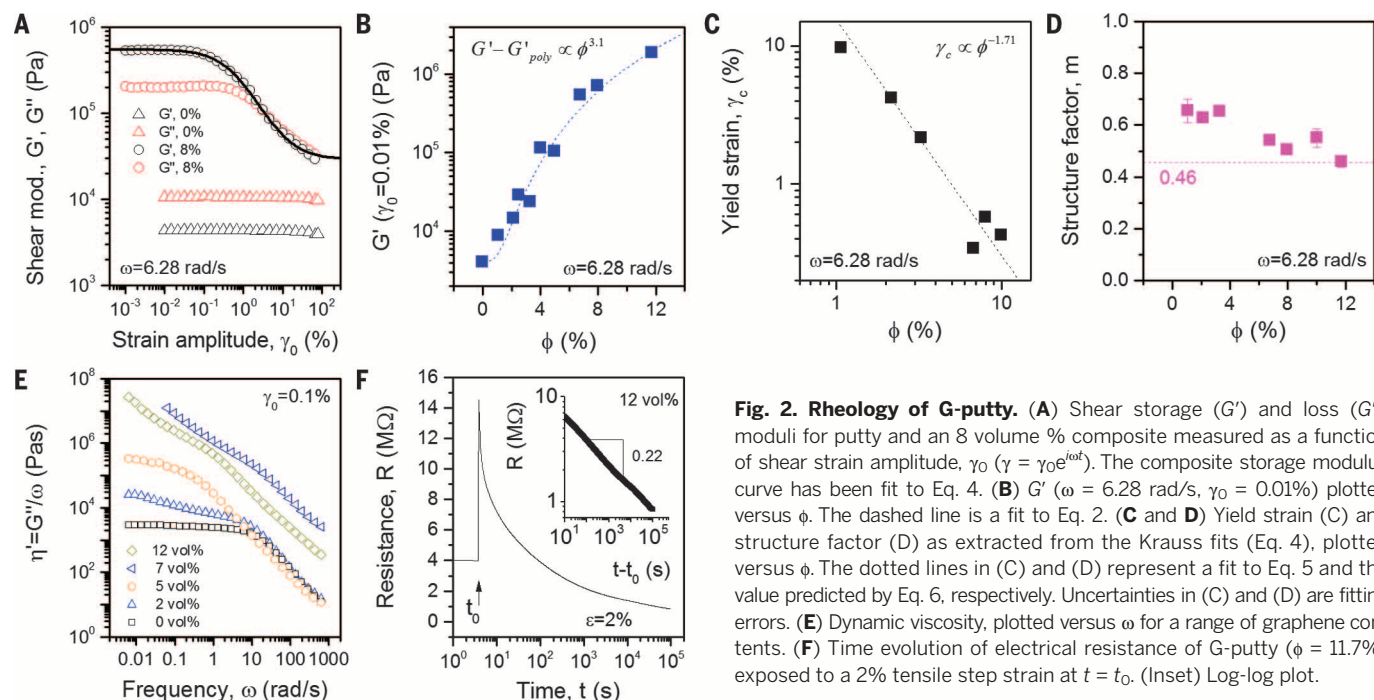
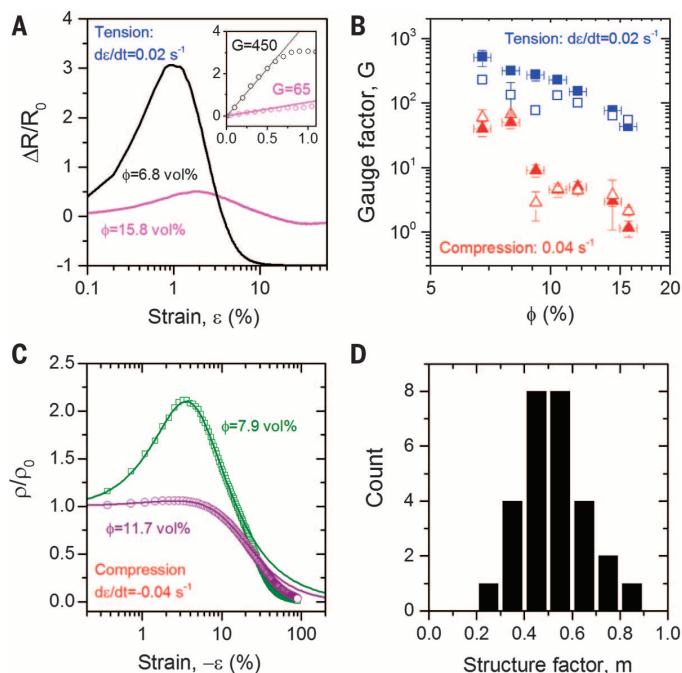


Fig. 2. Rheology of G-putty. (A) Shear storage (G') and loss (G'') moduli for putty and an 8 volume % composite measured as a function of shear strain amplitude, γ_0 ($\gamma = \gamma_0 e^{i\omega t}$). The composite storage modulus curve has been fit to Eq. 4. (B) G' ($\omega = 6.28$ rad/s, $\gamma_0 = 0.01\%$) plotted versus ϕ . The dashed line is a fit to Eq. 2. (C and D) Yield strain (C) and structure factor (D) as extracted from the Krauss fits (Eq. 4), plotted versus ϕ . The dotted lines in (C) and (D) represent a fit to Eq. 5 and the value predicted by Eq. 6, respectively. Uncertainties in (C) and (D) are fitting errors. (E) Dynamic viscosity, plotted versus ω for a range of graphene contents. (F) Time evolution of electrical resistance of G-putty ($\phi = 11.7\%$) exposed to a 2% tensile step strain at $t = t_0$. (Inset) Log-log plot.

Fig. 3. Electromechanical properties of G-putty. (A) Fractional resistance change for G-putty as a function of tensile strain. (Inset) Low-strain regime. (B) Mean (over five measurements \pm SD) gauge factor plotted versus volume fraction for both tensile (blue) and compressive (red) measurements. The solid and open symbols represent measured and predicted (Eq. 8) data, respectively. (C) Normalized resistivity as a function of strain measured in compression for two volume fractions. The lines are fits to Eq. 7. (D) Histogram showing all values of m found by fitting resistivity-strain data using Eq. 7.



the data well, giving $\phi_{c,e} = 1.75$ volume % and $n_e = 11.9$. Although the percolation threshold is roughly as expected (10), the exponent is large, which is consistent with a broad distribution of intersheet junction resistances (11). Detailed analysis of the mechanical properties of G-putty show it to display viscoelastic behavior, which is consistent with the standard linear solid model (figs. S1, S9 to S14, and S22 to S24) (5, 8). All

mechanical properties change with graphene content; for example, the stiffness increases as a power law (Fig. 1F and fig. S11).

Most relevant are the rheological properties. Shown in Fig. 2A are typical plots of storage (G') and loss (G'') modulus versus oscillatory strain amplitude, γ_0 (all rheological data are provided in figs. S15 to S21). Although both G' and G'' increase with graphene content (Fig. 2B and fig.

S15), the G' versus ϕ behavior can be analyzed via the cluster-cluster-aggregation model that treats the filler network as a fractal object, giving

$$G' - G'_{\text{poly}} \propto \phi^{(3+d_B)/(3-d_N)} \quad (2)$$

where d_N and d_B are the fractal dimensions of the network and its backbone, respectively (12, 13). As expected, the data follow a power law with exponent of 3.1 ± 0.5 .

Although both G' and G'' are invariant with strain for the putty, they both tend to fall with increasing strain amplitude for all nanocomposites. For filled elastomers, this is known as the Payne effect (14) and has been explained by Kraus (12, 15) via the strain-dependent breaking and reforming of interparticle connections in the filler network. Then, the number density of connections depends on γ_0 as

$$N = N_0 [1 + (\gamma_0/\gamma_c)^{2m}]^{-1} \quad (3)$$

where N_0 is the initial connection density, m is the network structure factor, and γ_c is the yield strain. This leads to the equation

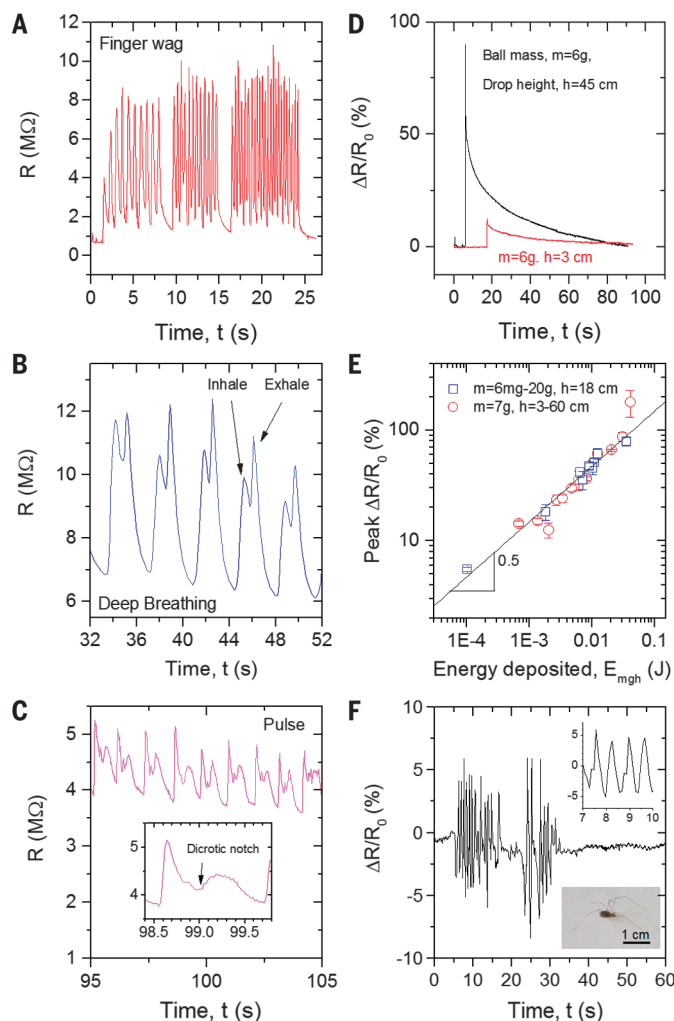
$$G'(\gamma_0) = G'_\infty + \frac{G'_0 - G'_\infty}{1 + (\gamma_0/\gamma_c)^{2m}} \quad (4)$$

where G'_0 and G'_∞ are the storage moduli in the limit of low and high frequencies, respectively (12). This model fits the data extremely well (Fig. 2A and figs. S17 and S18). Extracting γ_c and plotting versus ϕ in Fig. 2C shows a power law with exponent -1.71 ± 0.3 . Such behavior is consistent with the prediction of Shih *et al.* for fractal particulate networks (13)

$$\gamma_c \propto \phi^{-(1+d_B)/(3-d_N)} \quad (5)$$

Fig. 4. Mechanical sensing applications of G-putty. $\phi = 6.8$ volume %.

(A to C) Resistance waveforms measured while using G-putty to sense (A) finger joint motion (wagging), (B) breathing, and (C) pulse. The inset in (C) shows a single period of the pulse-waveform, with the characteristic dicotic notch indicated. (D) Fractional resistance change of flat G-putty strips (thickness $y_0 = 2$ mm) on impact from falling balls. (E) Peak $\Delta R/R_0$ plotted versus energy deposited by the falling ball (calculated from $E_{mgh} = mgh$). The line is a fit to Eq. 9. (F) Fractional resistance change associated with a spider (*Pholcus phalangioides* or cellar spider) (bottom inset) walking across a thin circular sheet of G-putty (thickness $y_0 = 2$ mm). (Top inset) Magnified response showing individual footsteps.



Combining the fits in Fig. 2, B and C, allows us to estimate $d_B = 1.4 \pm 0.2$ and $d_N = 1.6 \pm 0.2$, which is similar to carbon-black composites (12) but somewhat smaller than the values of ~ 2 found for nanoclay networks (16). In addition, the Krauss fits give structure factors close to $m = 0.5$, which is typical for filled elastomers (Fig. 2D) (12). These are consistent with the value of $m = 0.46$ predicted by the Huber-Vilgis model

$$m = (2 + d_N - d_B)^{-1} \quad (6)$$

supporting the validity of this analysis (12).

Of particular interest is the extremely low dynamic viscosity, $\eta' = G''/\omega$, of the matrix (Fig. 2E). Although the viscosity increases with ϕ as a power law (fig. S21), the zero-shear viscosity of the putty is low compared with solid polymers at ~ 3000 Pa s, which is consistent with its highly viscoelastic liquid-like nature. Such low viscosity may allow an unusual degree of nanosheet mobility. We can test this by applying a tensile step strain (2%) to the G-putty and monitoring the graphene network relaxation via its electrical resistance (Fig. 2F and fig. S25). The resistance increases sharply on application of the strain before decaying slowly as a power law (Fig. 2F,

inset). The resistance decay is very slow compared with the stress relaxation ($\tau \sim 1$ s) (figs. S22 to S24), with the power law indicating that a wide range of decay times are involved (figs. S25 and S26) (17). We interpret this behavior as the strain rapidly deforming the network and breaking nanosheet-nanosheet connections, thus increasing the resistance. However, because of the low matrix viscosity, the nanosheets are somewhat mobile and may move by diffusion or in response to the applied field via induced dipoles (figs. S27 to S33). This allows the network to slowly relax, reforming connections and giving a resistance decrease. This network relaxation can be thought of as a self-healing process. Such filler mobility is unprecedented in nanocomposites at room temperature (fig. S27). However, it also represents plasticity, meaning deformations are not fully reversible (fig. S32).

We have characterized the electrical response of the G-putty to tensile and compressive deformation (Fig. 3A). In all cases (figs. S34 to S43), the fractional resistance change, $\Delta R/R_0$, increased linearly at low strain before decreasing rapidly at higher strain, always falling below its initial value. This is considerably different to the normally observed monotonic increase of $\Delta R/R_0$ with

strain (18, 19). The initial linear increase in $\Delta R/R_0$ with ϵ means that the G-putty can be used as a strain sensor. The sensitivity, G (defined at low strain by $\Delta R/R_0 = G\epsilon$), is plotted versus ϕ in Fig. 3B. As $\phi \rightarrow \phi_{c,e}$, G increases significantly (18), reaching $\langle G \rangle = 535$ at 6.8 volume % for tensile measurements. These values surpass those of most strain sensors (nanocomposite sensors usually have $G < 40$) (fig. S58) (8, 18, 19).

To understand this unusual behavior mechanistically, we plotted resistivity ρ (calculated assuming constant volume) versus strain, observing a resistivity increase at low strain followed by a large decrease (Fig. 3C and fig. S44 to S48). Having considered other models, we propose that deformation of the nanosheet network modifies its connectivity and therefore its resistivity (figs. S2 to S5 and supplementary text S4) (8). We write the number density of internanosheet connections as the sum of a term analogous to Eq. 3 $\{N_1 = N_0[1 + (\epsilon/\epsilon_c)^{2m}]^{-1}\}$ and a term representing the reformation of connections due to diffusive or field-driven mobility of the nanosheets ($N_2 = k_2 t$). Combined with a modified percolation-type relation, $\rho \propto (N_1 + N_2)^{-n_e}$ (n_e is a scaling exponent), and using $\dot{\epsilon} = \epsilon/t$ gives

$$\frac{\rho}{\rho_0} = \left\{ \left[1 + \left(\frac{\epsilon}{\epsilon_c} \right)^{2m} \right]^{-1} + \frac{\epsilon}{\epsilon_t} \right\}^{-n_e} \quad (7)$$

where $\epsilon_t = \dot{\epsilon} N_0 / k_2$. We found that this expression fits the low-strain data extremely well in all cases (figs. S44 to S50). The fit-values of m cluster around 0.5 as expected (Fig. 3D).

Equation 7 leads to an expression for G

$$G = 2 + \frac{n_e}{\epsilon_c} - \frac{n_e}{\epsilon_t} \quad (8)$$

that we can apply, using the fit parameters associated with Eq. 7 (supplementary text S4) (8). As shown in Fig. 3B, the calculated and measured values for G match very well. We found that both n_e and G increase as the polymer molecular weight and hence viscosity decrease (fig. S51).

With these properties, G-putty is a high-performance electromechanical sensing material that can sense joint motion, breathing, and heart-beat (Fig. 4, A to C, fig. S52). When mounted on the carotid artery, the G-putty acts as a pressure sensor outputting a waveform representing the aortic pressure, allowing pulse monitoring (Fig. 4C). The unprecedented sensitivity of G-putty allows resolution of the characteristic double peak and dicotic notch. Through careful calibration, the peak-to-peak amplitude of the waveform can be converted to pulse (blood) pressure, finding the expected value of ~ 40 mmHg (figs. S53 to S57 and supplementary text S11) (8).

We also tested the G-putty as an impact sensor by dropping balls of different mass m into a thin putty sheet from different heights h . The resultant resistance waveforms show a rapid jump on impact followed by a power law decay (Fig. 4D), which is consistent with Eq. 7 (supplementary text S5) (8). The peak change in $\Delta R/R_0$ scales with impact energy ($E_{mgh} = mgh$) (Fig. 4E). We can

understand this by considering the conversion of kinetic energy to elastic energy of the network and using Eq. 7 to translate the resultant strain into a resistance change (supplementary text S5) (8), finding

$$\frac{\Delta R}{R_0} \approx \frac{n_e}{W} \left(\frac{2E_{mgh}}{\epsilon_c^2 E y_0} \right)^m \quad (9)$$

where W and y_0 are the width and thickness of the putty sensor, respectively, and E is the putty stiffness. Fitting the data in Fig. 4E to Eq. 9 gives $m = 0.5$, as expected, and $n_e/\epsilon_c \sim 5$ and so $G \sim 7$, which is in reasonable agreement with the compression data in Fig. 3B (fig. S49). To highlight the potential of G-putty as an impact sensor, we caught a small spider (mass, ~ 20 mg) (Fig. 4F, inset) and induced it to walk over a clingfilm-coated G-putty sensor. The resultant resistance plot is presented in Fig. 4F and shows individual spider footsteps, demonstrating the high sensitivity of this material.

Adding graphene to a highly viscoelastic polymer gives a composite with unprecedented electromechanical properties characterized by mobile nanosheets and nonmonotonic resistance changes as the material is strained. The nanocomposites are extremely sensitive electromechanical sensors that will find applications in a range of devices.

REFERENCES AND NOTES

1. K. S. Novoselov *et al.*, *Nature* **490**, 192–200 (2012).
2. R. J. Young, I. A. Kinloch, L. Gong, K. S. Novoselov, *Compos. Sci. Technol.* **72**, 1459–1476 (2012).
3. R. J. Young, P. A. Lovell, *Introduction to Polymers* (CRC Press, 2011).
4. S. N. Tripathi, R. S. Malik, V. Choudhary, *Polym. Adv. Technol.* **26**, 1558–1566 (2015).
5. R. Cross, *Am. J. Phys.* **80**, 870–875 (2012).
6. Y. Hernandez *et al.*, *Nat. Nanotechnol.* **3**, 563–568 (2008).
7. U. Khan *et al.*, *Langmuir* **27**, 9077–9082 (2011).
8. Materials and methods are available as supplementary materials on Science Online.
9. D. Stauffer, A. Aharony, *Introduction to Percolation Theory* (Taylor and Francis, rev. ed. 2, 1994).
10. S. Stankovich *et al.*, *Nature* **442**, 282–286 (2006).
11. P. M. Kogut, J. P. Straley, *J. Phys. Chem.* **12**, 2151–2159 (1979).
12. G. Heinrich, M. Kluppel, *Adv. Polym. Sci.* **160**, 1–44 (2002).
13. W. H. Shih, W. Y. Shih, S. I. Kim, J. Liu, I. A. Aksay, *Phys. Rev. A* **42**, 4772–4779 (1990).
14. A. R. Payne, *J. Appl. Polym. Sci.* **6**, 57–63 (1962).
15. G. Kraus, *J. Appl. Polym. Sci. Symp.* **39**, 75–92 (1984).
16. J. Vermant, S. Ceccia, M. K. Dolgopkij, P. L. Maffettone, C. W. Macosko, *J. Rheol. (N.Y.N.Y.)* **51**, 429–450 (2007).
17. H. H. Winter, M. Mours, in *Neutron Spin Echo Spectroscopy Viscoelasticity Rheology*, A. Abe *et al.*, Eds. (Springer-Verlag, 1997), pp. 165–234.
18. J. Zhao, G.-Y. Zhang, D.-X. Shi, *Chin. Phys. B* **22**, 057701 (2013).
19. C. S. Boland *et al.*, *ACS Nano* **8**, 8819–8830 (2014).

ACKNOWLEDGMENTS

We acknowledge the Science Foundation Ireland-funded AMBER research center (SFI/12/RC/2278). J.N.C. and R.J.Y. acknowledge funding from the European Union Seventh Framework Program under grant agreements 604391 and 696656, Graphene Flagship. G.R. and M.E.M. acknowledge funding from Science Foundation Ireland (G22226/RFP-1/MTR/3135) and support from COST action MP1305. “Graphene Polymer Nanocomposites” was filed at the

European Patent Organisation (EP16182749.8) on 4 August 2016; inventors, J.N.C., U.K., and C.B.; assignee, Trinity College Dublin.

SUPPLEMENTARY MATERIALS

www.sciencemag.org/content/354/6317/1257/suppl/DC1
Materials and Methods
Supplementary Text

Figs. S1 to S58
Table S1
References (20–79)
Movie S1

3 June 2016; accepted 11 November 2016
10.1126/science.aag2879

ORGANIC CHEMISTRY

Synthesis of resveratrol tetramers via a stereoconvergent radical equilibrium

Mitchell H. Keylor,^{1*} Bryan S. Matsuura,^{1*} Markus Griesser,² Jean-Philippe R. Chauvin,² Ryan A. Harding,¹ Mariia S. Kirillova,¹ Xu Zhu,¹ Oliver J. Fischer,¹ Derek A. Pratt,^{2†} Corey R. J. Stephenson^{1†}

Persistent free radicals have become indispensable in the synthesis of organic materials through living radical polymerization. However, examples of their use in the synthesis of small molecules are rare. Here, we report the application of persistent radical and quinone methide intermediates to the synthesis of the resveratrol tetramers nepalensinol B and vateriaphenol C. The spontaneous cleavage and reconstitution of exceptionally weak carbon-carbon bonds has enabled a stereoconvergent oxidative dimerization of racemic materials in a transformation that likely coincides with the biogenesis of these natural products. The efficient synthesis of higher-order oligomers of resveratrol will facilitate the biological studies necessary to elucidate their mechanism(s) of action.

Resveratrol (**1**), a naturally occurring and biologically important polyphenol (*1*), is widespread within the plant kingdom. It serves as the progenitor to an arsenal of phytoalexins—antimicrobial defense compounds that accumulate rapidly at sites of pathogenesis to neutralize invading microorganisms and promote plant survival (*2*). Several resveratrol oligomers (dimers, trimers, and tetramers) have been shown, primarily via in vitro studies, to exert biological effects that transcend this natural role, including but not limited to anti-inflammatory, immunomodulatory, and cytotoxic activities (*3*). Unfortunately, the requirement for laborious extraction and purification of resveratrol oligomers from plant matter has imposed severe limitations on the extent to which their mechanism(s) of action can be elucidated. It is therefore imperative that synthetic advances be made in order to confirm or refute the biological activities ascribed to the isolated natural products; these efforts will identify chemical frameworks that hold potential as small-molecule chemopreventives and/or chemotherapeutics and enable structural modification for both structure-activity relationship (SAR) studies and the devel-

opment of congeners with improved potency, efficacy, and bioavailability. Although the synthetic community has presented several innovative approaches to the resveratrol dimers (*4–10*), access to higher-order oligomers remains a serious challenge. In 2011, Snyder and coworkers reported a de novo synthetic approach to address this problem, accessing several higher-order oligomers through homologation of dimeric core structures (*11*). This strategy has since been used in two additional trimer syntheses (*12, 13*) and represents the only successful strategy to date for the preparation of these compounds.

Organisms that produce resveratrol (**1**) are able to harness the reactivity of delocalized phenoxyl radicals (such as **1•**) (Fig. 1) generated upon its oxidation; the resultant oligomers are typically isolated as optically active materials (*3*). Although biomimetic approaches have been reported (*14–17*), such remarkable levels of regio-, chemo-, and stereoselectivity have proven challenging to replicate in the laboratory because of the transient nature of the putative radical and quinone methide intermediates (Fig. 1, inset). We reasoned that if these intermediates could be rendered more persistent (*18*), then it would be possible to gain the advantages of efficiency offered by biomimicry without sacrificing the modularity offered by de novo synthetic approaches. Recently, we were able to recapitulate one mode of resveratrol oligomerization for the synthesis and antioxidant evaluation of two dimeric natural products, quadrangularin A

¹Department of Chemistry, University of Michigan, 930 North University Avenue, Ann Arbor, MI 48109, USA. ²Department of Chemistry and Biomolecular Sciences, University of Ottawa, 10 Marie Curie Private, Ottawa, Ontario K1N 6N5, Canada.

*These authors contributed equally to this work. †Corresponding author. Email: crjsteph@umich.edu (C.R.J.S.); dpratt@uottawa.ca (D.A.P.)

(2) and pallidol (3) (Fig. 1) (19). The synthesis featured a remarkably persistent bis(*p*-quinone methide) intermediate **4a**, similar to those (such as **5**) invoked by Niwa, Pan, and coworkers in their studies on the structural elucidation and biogenesis of resveratrol trimers and tetramers from ϵ -viniferin (**6**) (14, 17). This biosynthetic logic can similarly be applied to higher-order oligomers, in principle providing access to the gamut of 8-8' linked resveratrol tetramers (such as **7** and **8**) through a convergent oxidative coupling of ϵ -viniferin (**6**) followed by regio- and/or stereodivergent cyclizations of the resultant bis(*p*-quinone methide) **5** (Fig. 1) (3).

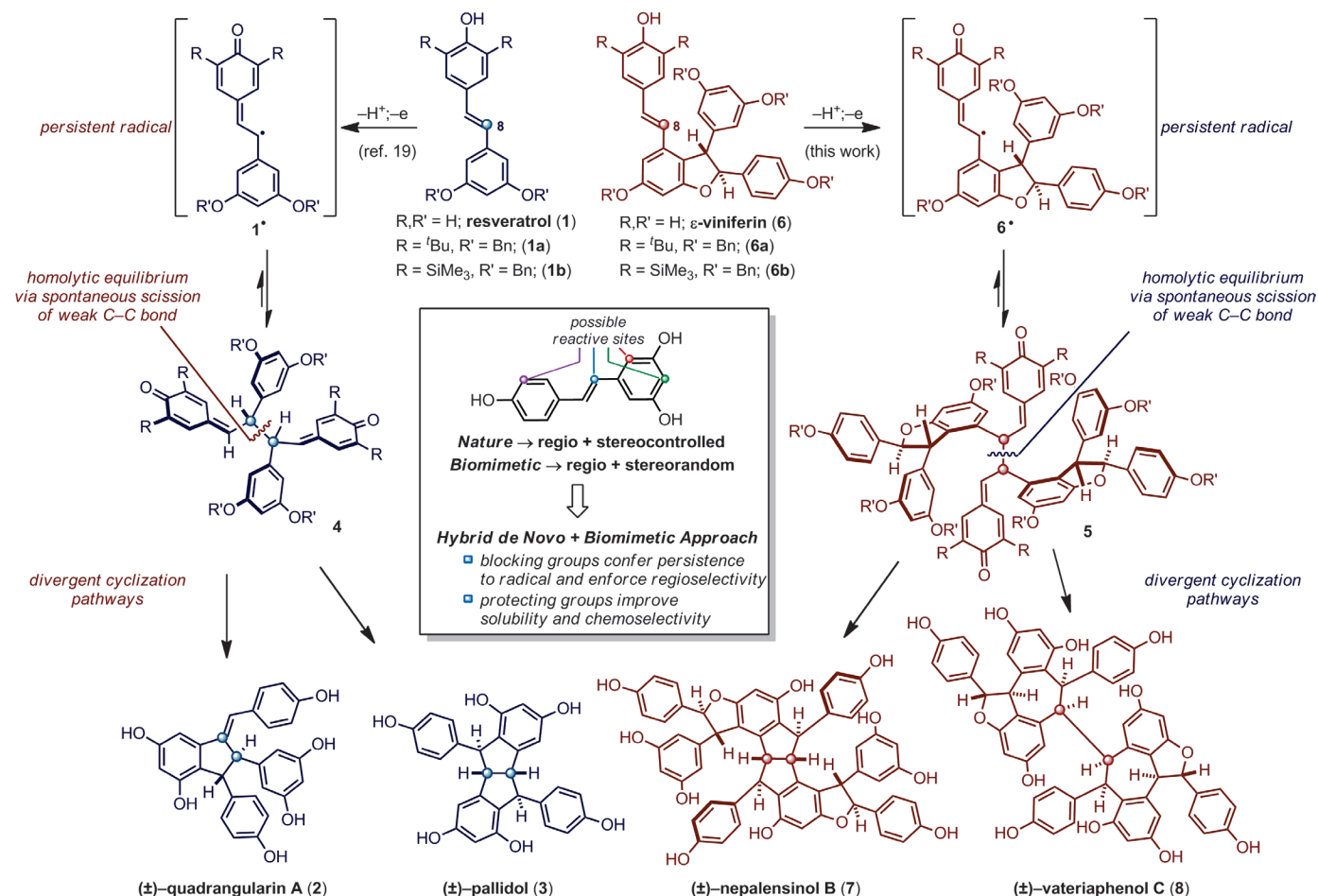
The proposed oxidative coupling presented several challenges. First, dimerization of a racemic form of **6** could, in principle, provide products derived from both homo- and heterodimerization between the (+)- and (−)-enantiomers; the (+)/(−) product is not represented in any known resveratrol oligomer. Furthermore, the dimerization reaction would generate two additional stereocenters, suggesting that the formation of six stereoisomers of product **5** is possible (fig. S9) (20). Last, it was unclear whether the intended double intramolecular cyclization of **5** would exhibit inherent preferences for specific regio- and

stereochemical outcomes. Each hemisphere of tetramer **5** possesses two resorcinol moieties that are both capable of engaging each prochiral *p*-quinone methide in Friedel–Crafts cyclizations. The possibility for both symmetrical (2×5-*exo-trig*, 2×7-*exo-trig*, and 2×8-*exo-trig*) and unsymmetrical (5-*exo-trig*/7-*exo-trig* and 5-*exo-trig*/8-*exo-trig*) cyclization modes, each capable of producing several diastereoisomers (fig. S10) (20), posed a daunting challenge.

Here, we describe the execution of this strategy for the efficient biomimetic total synthesis of the resveratrol tetramers nepalensinol B (**7**) (21, 22) and vateriaphenol C (**8**) (23). Critical to the success of these efforts was the identification and rigorous characterization of an unconventional equilibrium between isolable dimeric (**4a/b**) and tetrameric (**5a/b**) bis(*p*-quinone methide) intermediates and their phenoxyl radicals (Fig. 1) (24), a physical property initially explored as a mechanistic curiosity but which we have found to have remarkable—and potentially biogenically relevant—implications for dynamic stereocontrol in the context of resveratrol oligomer synthesis and biosynthesis. Synthetic access to these natural products and their derivatives will enable further explorations of their already promising

biological activities. For instance, nepalensinol B (**7**) is a potent inhibitor of topoisomerase II [median inhibitory concentration (IC₅₀) = 0.02 μg/mL] (22); this is 3000 times more potent than etoposide (VP-16, IC₅₀ = 70 μg/mL) (25), a clinically approved chemotherapeutic on the World Health Organization (WHO) model list of essential cytotoxic and adjuvant medicines (26).

During our studies toward resveratrol dimers (19), we discovered that intermediate **4a**, which was isolated as a 4:3 mixture of *meso:DL* diastereomers, could be quantitatively isomerized to *trans,trans*-indane **9** (Fig. 2), a product that can only derive from *meso*-**4a**. Although it was tempting to conclude that epimerization of *DL*-**4a** was proceeding via tautomerization followed by stereorandom vinyllogous protonation, independent preparation of the presumptive intermediates and their subjection to these reaction conditions did not lead to any detectable formation of **9** (fig. S7) (27). Thus, an alternate mechanism had to be responsible. In 1969, Becker reported that bis(*p*-quinone methides) similar to **4a** equilibrate in chloroform solution at room temperature with the corresponding phenoxyl radicals through a homolytic C–C bond scission process analogous to that of Gomberg's historic



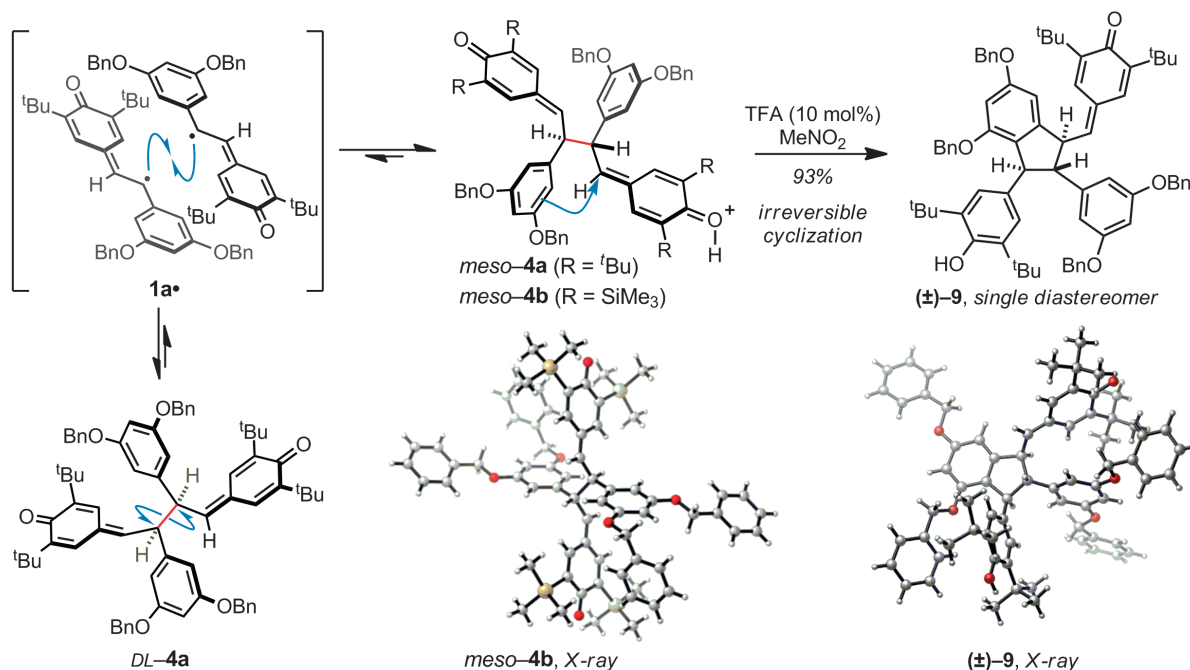


Fig. 2. Diastereoconvergent cyclization of **4a**. TFA, trifluoroacetic acid.

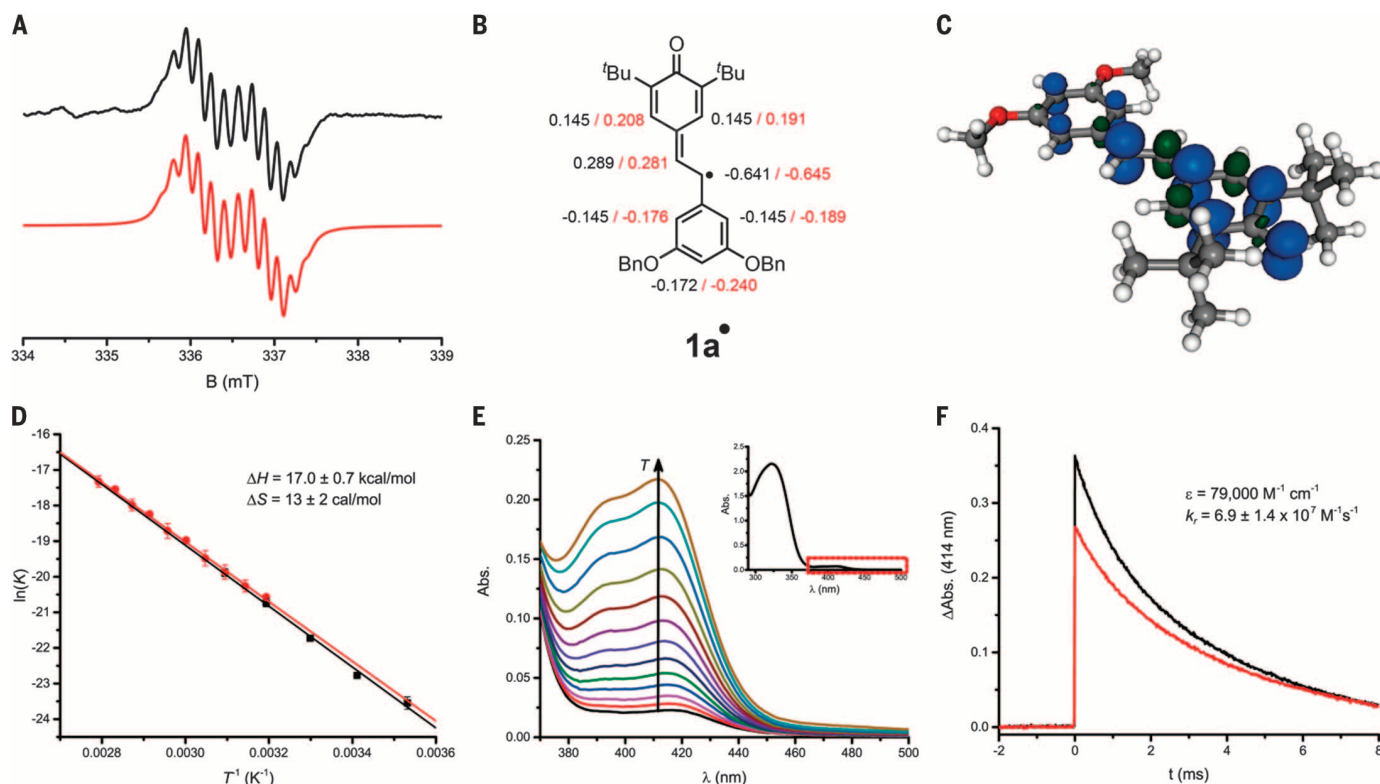


Fig. 3. Characterization of homolytic dissociation equilibrium of representative bis(*p*-quinone methide) **4a**. (A) Experimental (black) and fitted (red) EPR spectrum of **1a•** recorded at 295 K. (B) Experimental (black) and calculated (red) hyperfine coupling constants for **1a•**. (C) Spin-density distribution in **1a•** predicted with DFT (B3LYP/TZVP). (D) Temperature dependence of equilibrium constants determined with EPR (black) and UV/vis (red)

spectroscopy and corresponding calculated thermochemical parameters. The error bars represent standard deviations for three or more combined measurements. (E) Temperature dependence of absorbance corresponding to **1a•**. (Inset) Full spectrum of **4a** at 323 K. (F) Second-order decay of absorbance at 414 nm after nanosecond-pulsed irradiation of **4a** at 308 nm under an atmosphere of either nitrogen (black) or oxygen (red).

triphenylmethyl radical (24, 28). To probe whether such a mechanism could be operative for this transformation, we performed a thermal crossover experiment using differentially protected derivatives of **4**, and our observations were consistent with the formation of a statistical mixture of homo- and cross-coupled products (fig. S8) (27). Intrigued by this unusual reactivity, we undertook an extensive analysis of the homolytic dissociation equilibrium of **4a** and related derivatives.

Solutions of the bis(*p*-quinone methide) **4a** in benzene yielded prominent electron paramagnetic resonance (EPR) spectra at room temperature (Fig. 3A). The spectrum is fully consistent with what is expected for the phenoxyl radical derived from **1a** (hereafter **1a•**) (Fig. 3B); the hyperfine coupling constants derived from the simulated spectrum are in good agreement with values from related compounds in the literature (29), as well as those predicted from the spin density distribution in **1a•** calculated by using density functional theory (DFT) at the B3LYP/TZVP level of theory (Fig. 3C) (30, 31). Integration of the signals afforded $K_{eq}(\mathbf{1a}/\mathbf{4a}) = 1.8 \times 10^{-10}$ M (32). We recorded spectra at several temperatures between 10° and 50°C and used the corresponding equilibrium constants to provide an estimate of the thermodynamics of the homolysis-recombination process (Fig. 3D). Corresponding experiments were carried out by means of ultraviolet/visual (UV/vis) spectroscopy—with an expanded temperature range up to 85°C (33)—by following the increase in intensity of the low-energy absorption maximum at 414 nm (which was attributed to **1a•** with $\epsilon = 79,000$ M⁻¹ cm⁻¹, vide infra) as a function of temperature (Fig. 3E) (34). The measurements agree that the central C–C bond dissociation enthalpy (BDE) in **4a** is 17.0 ± 0.7 kcal/mol. Although this is not the weakest C–C bond reported to date (the C–C BDE in the 4,4'-dimer of 2,6-di-*t*-Bu-4-methoxyphenoxyl is reported to be a mere 6.1 ± 0.5 kcal/mol) (35), it does afford a meaningful equilibrium at room temperature.

To provide insight into the kinetics associated with this process, **4a** was subjected to laser flash photolysis (LFP) with the 308-nm emission of a nanosecond-pulsed XeCl excimer laser, and the rates of recombination of the radicals were recorded. The transient species generated by photolysis exhibited the same low-energy absorption centered at 414 nm as in the spectrum of **4a** (27). The decay of this absorbance could be fit to a second-order function by using the extinction coefficients determined from the UV/vis–EPR equilibrium experiments to afford the radical recombination rate constants, k_r (Fig. 3F). Although **1a•** features substantial spin density at C₈ (resveratrol numbering) (Fig. 1)—enabling its dimerization at that position to produce **4a**—the recombination rates were insensitive to the presence of O₂. Rate constants in the absence and presence of oxygen were found to be within error ($6.7 \pm 1.5 \times 10^7$ M⁻¹ s⁻¹ and $7.4 \pm 1.0 \times 10^7$ M⁻¹ s⁻¹, respectively), with the combined data set affording $k_r = 6.9 \pm 1.4 \times 10^7$ M⁻¹ s⁻¹. The homolysis rate constant could be estimated from the equi-

librium constant and recombination rate constant to be $k_t = 1.2 \times 10^{-2}$ s⁻¹.

The homolytic dissociation equilibrium held tremendous potential for the biomimetic preparation of higher-order resveratrol oligomers. Drawing on the similarity between the putative biogenesis of 8–8' resveratrol dimers and tetramers (Fig. 1), we sought to realize a selective dimerization of ϵ -viniferin (**6**) (or a suitably substituted derivative). In their total synthesis of the resveratrol trimer caraphenol A, Snyder and Wright reported a highly effective eight-step preparation of aldehyde **10** (12), which we have leveraged for the present synthesis. This intermediate was converted into *t*-Bu- ϵ -viniferin derivative **6a** almost exclusively as the (*E*)-isomer via Wittig olefination with phosphonium salt **11a** (27) in 85% yield (Fig. 4A). With **6a** in hand, we were poised to explore the key oxidative coupling reaction.

Despite concerns about stereo- and regioselectivity in the proposed transformations, our observations in the diastereoconvergent cyclization of **4a** (vide supra) (Fig. 2) suggested that thermodynamic differentiation of the various diastereoisomers of **5**—interconvertible via C–C homolysis-recombination—may afford some level of selectivity upon oxidative coupling, whereas the conformational requirements for productive orbital overlap may favor selected cyclization modes in the ensuing Friedel–Crafts reactions. Remarkably, subjecting of **6a** to our ferrocenium-mediated oxidative dimerization conditions afforded the desired tetrameric bis(*p*-quinone methide) **5a** as nearly a single diastereoisomer (~19:1 major isomer:all other isomers)—derived from the coupling of two monomers of the same absolute configuration (Fig. 4B). Although stereoselectivity has been observed previously in biomimetic dimerizations of racemic precursors (36–38), examples are rare and typically proceed via polar, irreversible mechanisms. Although it is possible that the stereochemical outcome of oxidative coupling of **5a** is kinetically determined during the dimerization event, it is far more likely that initial coupling produces a mixture of diastereomers that rapidly equilibrate in solution via bond homolysis-recombination.

To support this hypothesis, we subsequently carried out analogous characterization of the **5a/6a•** equilibrium as described above for **4a/1a•**. Once again, EPR spectra consistent with **6a•** were obtained from room-temperature samples of **5a** (fig. S1, A to C) (27), and the temperature dependence of the equilibrium constants (fig. S1D; also determined via UV/vis spectroscopy, fig. S1E) (27) once again enabled the determination of the key C–C BDE in **5a** to be 17.1 ± 0.4 kcal/mol—which is within error of **4a**, as were the kinetics: $k_r = 2.0 \pm 1.1 \times 10^7$ M⁻¹ s⁻¹ (fig. S1F) and $k_t = 3.6 \times 10^{-3}$ s⁻¹. Given the overall similarity of the kinetics and thermodynamics of homolysis-recombination of tetramer **5a** when compared with dimer **4a**, the equilibration of **5a** to nearly a single diastereomer was likely. Gratifyingly, exposure of **5a** to BF₃·OEt₂ at –60°C followed by warming to –30°C furnished a mixture of just two regioisomeric

cyclization products: **12a** (44%, single diastereomer) and **13/14a** (9%, 9:1 *dr*) (Fig. 4B). Each of these compounds derive from the *trans,cisoid* (*S*)/(*S*) [or (*R*)/(*R*)] diastereomer of **5a**. This does not unequivocally demonstrate that this is the lowest-energy diastereomer of **5a**, only that the cyclization of this diastereomer is favored over that from the (*R*)/(*S*) configuration. Structures **12a**, **13a**, and **14a** represent the carbon skeletons of nepalensinol B (**7**) (21, 22), vateriaphenol C (**8**) (23), and hopeaphenol (**15**) (39), respectively. The stereochemical outcome of the Friedel–Crafts cyclization leading to major product **12a** is complementary to that achieved by Snyder and coworkers through iterative homologation of the pallidol (**3**) core, which is capable of producing the stereoisomer ampelopsin H (**11**).

Global debenzoylation of **12a** and **13/14a** via Pd/C-mediated hydrogenolysis proceeded in 45 and 60% yields, respectively (27). However, attempts at removal of the four remaining *tert*-butyl groups were unsuccessful under a variety of reaction conditions, resulting in decomposition to an intractable mixture. Although extensive investigation of this transformation may have eventually revealed less destructive conditions for dealkylation of the penultimate intermediates, the use of an isosteric functional group with increased lability that could nevertheless enforce regio- and diastereoselectivity upon oxidative coupling of **6** seemed to be a more attractive solution. Our initial thoughts focused on the use of trimethylsilyl (TMS) groups in place of the *t*-Bu moieties. To our surprise, given the vast literature on the chemistry of hindered phenols and phenoxyl radicals, the persistence of 2,6-di-TMS-phenoxyl radicals had yet to be investigated. High accuracy CBS–QB3 quantum chemical calculations (40, 41) predicted that the O–H BDEs in 2,6-di-TMS-4-methylphenol (**S2**) and 2,6-di-*t*-Bu-4-methylphenol (BHT) were 80.7 and 78.6 kcal/mol, respectively [the O–H BDE in BHT has been determined experimentally to be 81.0 kcal/mol (42)]. These calculations suggest that the electronic effects of TMS and *t*-Bu groups on the thermodynamic stability of phenoxyl radicals are similar. Moreover, the reactivity of **S2** toward peroxy radicals in inhibited autoxidations of cumene was essentially indistinguishable from that of BHT ($k = 1.4 \times 10^4$ versus 2.1×10^4 M⁻¹ s⁻¹, respectively) (fig. S6) (27), suggesting that the kinetics of the reactions of the silylated phenol and phenoxyl radicals would be similar to that of their *t*-butylated counterparts.

Accordingly, **1b** (Fig. 1) could be readily oxidatively dimerized to the corresponding bis(*p*-quinone methide) dimer **4b**. Crystals of the *meso* isomer of **4b** suitable for x-ray analysis were obtained (Fig. 2) (27), confirming its identity as a bis(*p*-quinone methide) and seemingly revealing a conformational preference for antiparallel alignment of the carbonyl moieties, likely resulting from the combined influence of sterics and dipole minimization. Like its *tert*-butylated predecessor, **4b** yielded a prominent EPR spectrum at room temperature that was consistent with

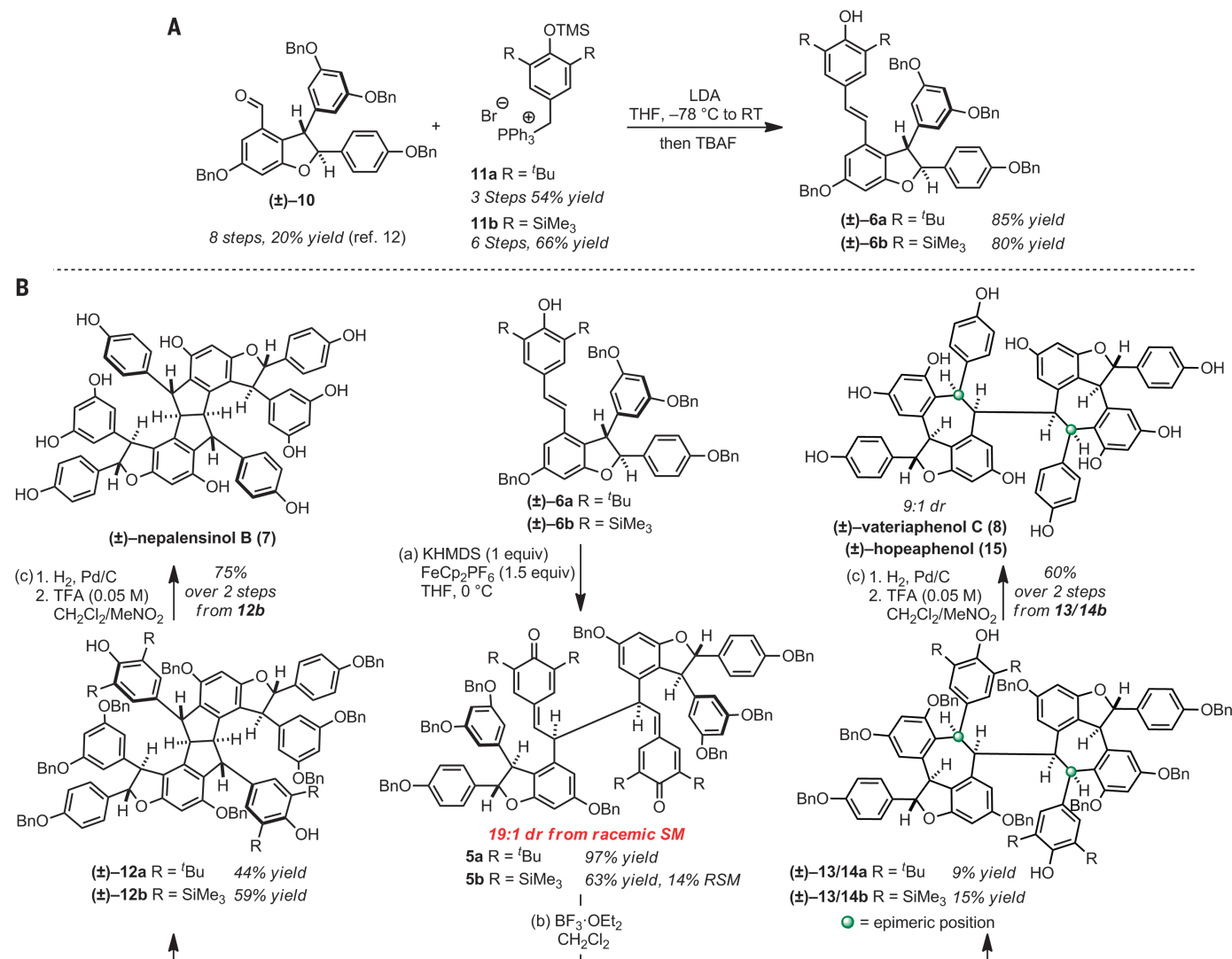


Fig. 4. 13-Step total synthesis of resveratrol tetramers. (A) Preparation of ϵ -viniferin derivatives, reagents, and conditions are as follows: ^tPr₂NH, *n*-BuLi, THF, then **11a/b**, then **10**, -78°C to room temperature, then 0°C , TBAF, 0.5 hours, 85% for **6a**, 80% for **6b**. (B) Synthesis of nepalensinol B and vateriaphenol C, reagents and conditions are as follows: (a) THF, 0°C , then KHMDS, then FeCp₂PF₆, 97% for **5a**, 63% (14% RSM) for **5b**. (b) For **5a**,

BF₃·OEt₂, CH₂Cl₂, -60° to -30°C (44% **12a** + 9% **13/14a**). For **5b**, BF₃·OEt₂, CH₂Cl₂, -78°C (59% **12b** + 15% **13/14b**). (c) 1. Pd/C (30 weight %), MeOH/EtOAc (1:1 v/v), H₂ (1 atm), filter, concentrate, then 2. TFA (0.05 M) in CH₂Cl₂/MeNO₂ (1:1 v/v), 75% for **7**, 60% for **8/15**. THF, tetrahydrofuran; TBAF, tetra-*n*-butylammonium fluoride; KHMDS, potassium hexamethyldisilazide; *dr*, diastereomeric ratio; SM, starting material; RSM, recovered starting material.

the phenoxyl radical derived from **1b** (fig. S2, A to C) (27). Efforts to determine the temperature dependence of the **4b/1b**• equilibrium were limited by the fact that **4b** was not sufficiently persistent to obtain reproducible spectra above 50°C , instead undergoing an unusual rearrangement to a derivative of the natural product δ -viniferin (27). Nevertheless, a Van't Hoff plot of the available data between 10° and 50°C afforded an estimate of the C–C BDE of 16.4 ± 0.5 kcal/mol (fig. S2, D and E) (27), which is only slightly lower (and within error) of that in **4a**. The recombination rate constant was determined with laser flash photolysis of **4b** to be $k_r = 5.3 \pm 3.0 \times 10^8 \text{ M}^{-1}\text{s}^{-1}$ (fig. S2F), which is almost one order of magnitude faster than that obtained for **4a** and explains the slightly less favorable equilibrium, given the similar values

of k_t (2.1×10^{-2} and $1.2 \times 10^{-2} \text{ s}^{-1}$ for **4b** and **4a**, respectively).

Likewise, the TMS derivative of ϵ -viniferin, **6b**, proved to be a competent substrate for FeCp₂PF₆-mediated oxidative dimerization (Fig. 4B), and the resultant bis(*p*-quinone methide) **5b** was found to undergo the same homolysis-decomposition as that of **4b** (fig. S3) (27). Cyclization with BF₃·OEt₂ at -78°C cleanly afforded **12b** (59%, single diastereomer) and **13/14b** (15%, 9:1 *dr*), respectively. The increased reactivity of the silylated derivative **5b** was evident because it was less stable to silica gel chromatography and could be cyclized at a lower temperature than could the ^tBu analog. Cyclization at slightly elevated temperatures (-60°C) afforded **12b** and **13/14b** in a 1.3:1 regioisomeric ratio, suggesting that the current level of product selec-

tivity is sensitive to conformational effects. Furthermore, allylic strain minimization before 7-*exo-trig* cyclization would predict the hopeaphenol isomer **14b** to predominate, and therefore the observed preference for formation of the vateriaphenol C core **13b** suggests a likely contribution of transannular strain and/or conformational restriction in controlling facial selectivity during attack of the prochiral *p*-quinone methides. Hydrogenolysis of **13/14b** followed by protodesilylation afforded vateriaphenol C (**8**) and hopeaphenol (**15**) in 60% yield over two steps as a 9:1 mixture of diastereoisomers. Subjecting **12b** to the same reaction sequence provided nepalensinol B (**7**) in 75% yield over two steps.

The total syntheses of resveratrol tetramers nepalensinol B (**7**, 5.1% overall yield) and vateriaphenol C (**8**, 1.1% overall yield) described

here required only 13 linear synthetic steps. Critical to our strategy was the application of thermodynamic stereocontrol in the dimerization of persistent free radicals, a process that we have extensively characterized. The efficiency of the route has enabled the preparation of sufficient quantities of material that the biological activities of these natural products can now be more thoroughly evaluated.

REFERENCES AND NOTES

- S. Quideau, D. Deffieux, C. Douat-Casassus, L. Pouységu, *Angew. Chem. Int. Ed. Engl.* **50**, 586–621 (2011).
- P. Jeandet et al., *Molecules* **19**, 18033–18056 (2014).
- M. H. Keylor, B. S. Matsuura, C. R. J. Stephenson, *Chem. Rev.* **115**, 8976–9027 (2015).
- S. A. Snyder, A. L. Zografos, Y. Lin, *Angew. Chem. Int. Ed. Engl.* **46**, 8186–8191 (2007).
- K. C. Nicolaou, T. R. Wu, Q. Kang, D. Y.-K. Chen, *Angew. Chem. Int. Ed. Engl.* **48**, 3440–3443 (2009).
- J. L. Jeffrey, R. Sarpong, *Org. Lett.* **11**, 5450–5453 (2009).
- S. A. Snyder, N. E. Wright, J. J. Pflueger, S. P. Breazzano, *Angew. Chem. Int. Ed. Engl.* **50**, 8629–8633 (2011).
- S. A. Snyder, S. B. Thomas, A. C. Mayer, S. P. Breazzano, *Angew. Chem. Int. Ed. Engl.* **51**, 4080–4084 (2012).
- C. Soldi et al., *J. Am. Chem. Soc.* **136**, 15142–15145 (2014).
- F. Klotter, A. Studer, *Angew. Chem. Int. Ed. Engl.* **53**, 2473–2476 (2014).
- S. A. Snyder, A. Gollner, M. I. Chiriac, *Nature* **474**, 461–466 (2011).
- N. E. Wright, S. A. Snyder, *Angew. Chem. Int. Ed. Engl.* **53**, 3409–3413 (2014).
- T. H. Jepsen et al., *Angew. Chem. Int. Ed. Engl.* **53**, 6747–6751 (2014).
- Y. Takaya, K.-X. Yan, K. Terashima, Y.-H. He, M. Niwa, *Tetrahedron* **58**, 9265–9271 (2002).
- M. Sako, H. Hosokawa, T. Ito, M. Iinuma, *J. Org. Chem.* **69**, 2598–2600 (2004).
- Y.-H. He, Y. Takaya, K. Terashima, M. Niwa, *Heterocycles* **68**, 93–100 (2006).
- L. Jiang, S. He, C. Sun, Y. Pan, *Phytochemistry* **77**, 294–303 (2012).
- D. Griller, K. U. Ingold, *Acc. Chem. Res.* **9**, 13–19 (1976).
- B. S. Matsuura et al., *Angew. Chem. Int. Ed. Engl.* **54**, 3754–3757 (2015).
- A side by side comparison of these structures is provided in the supplementary materials.
- M. Ohyama, T. Tanaka, M. Iinuma, C. L. Burandt, *Chem. Pharm. Bull. (Tokyo)* **46**, 663–668 (1998).
- M. Yamada et al., *Phytochemistry* **67**, 307–313 (2006).
- T. Ito, N. Abe, M. Oyama, M. Iinuma, *Helv. Chim. Acta* **91**, 1989–1998 (2008).
- H. D. Becker, *J. Org. Chem.* **34**, 1211–1215 (1969).
- K. R. Hande, *Eur. J. Cancer* **34**, 1514–1521 (1998).
- WHO, *WHO Model List of Essential Medicines* (WHO, ed. 19, 2015).
- Materials and methods are available as supplementary materials on Science Online.
- M. Gomberg, *J. Am. Chem. Soc.* **22**, 775–771 (1900).
- R. Amorati et al., *J. Org. Chem.* **69**, 7101–7107 (2004).
- A. D. Becke, *J. Chem. Phys.* **98**, 5648–5652 (1993).
- A. Schäfer, C. Huber, R. Ahlrichs, *J. Chem. Phys.* **100**, 5829–5835 (1994).
- The reduction by three orders of magnitude relative to Becker's equilibrium constant likely results from inductive withdrawal of electron-density in **1a** by the two *meta*-benzyloxy ether substituents on the resorcinol ring relative to the simple phenyl ring in Becker's example.
- Considerable decomposition was observed for experiments conducted at or above 90°C.
- The experimental extinction coefficient is in good agreement with Becker's unsubstituted radical (24) at 75,000 M⁻¹ cm⁻¹.
- J. M. Wittman, R. Hayoun, W. Kaminsky, M. K. Coggins, J. M. Mayer, *J. Am. Chem. Soc.* **135**, 12956–12959 (2013).
- J. Gagnepain, F. Castet, S. Quideau, *Angew. Chem. Int. Ed. Engl.* **46**, 1533–1535 (2007).
- R. S. Harvey et al., *Angew. Chem. Int. Ed. Engl.* **54**, 1795–1798 (2015).
- P. D. Brown, A. C. Willis, M. S. Sherburn, A. L. Lawrence, *Org. Lett.* **14**, 4537–4539 (2012).
- P. Coggon, T. J. King, S. C. Wallwork, *Chem. Commun. (Camb.)* **1966**, 439–440 (1966).
- J. A. Montgomery Jr., J. W. Ochterski, G. A. Petersson, *J. Chem. Phys.* **101**, 5900–5909 (1994).
- P. Mulder et al., *J. Phys. Chem. A* **109**, 2647–2655 (2005).
- M. Lucarini, P. Pedrielli, G. F. Pedulli, S. Cabiddu, C. Fattuoni, *J. Org. Chem.* **61**, 9259–9263 (1996).

ACKNOWLEDGMENTS

Financial support is gratefully acknowledged from the NIH–National Institute of General Medical Sciences (grant R01-GM096129), the Camille Dreyfus Teacher Scholar Award Program, and the University of Michigan to C.R.J.S., and the National Sciences and Research Council of Canada, the Canada Research Chairs program, and the University of Ottawa to D.A.P. J.-P.R.C. acknowledges the support of Ontario Graduate Scholarships. We thank J. W. Kampf for conducting x-ray diffraction experiments and solving the structures of compounds **4b** and **9**. Atomic coordinates and structure factors for the crystal structures reported are available free of charge from the Cambridge Crystallographic Database under accession nos. CCDC 1499423 and CCDC 1485815,

respectively. Additional characterization data are available in the supplementary materials. Reprints and permissions information is available at www.sciencemag.org/help/reprints-and-permissions. The authors declare no competing financial interests. Readers are welcome to comment on the online version of the paper. Correspondence and requests for materials should be addressed to C.R.J.S. (cristoph@umich.edu) or D.A.P. (dpratt@uottawa.ca).

SUPPLEMENTARY MATERIALS

www.sciencemag.org/content/354/6317/1260/suppl/DC1
Materials and Methods
Supplementary Text
Figs. S1 to S10
Tables S1 to S8
References (43–50)

5 September 2016; accepted 15 November 2016
10.1126/science.aaj1597

ASYMMETRIC CATALYSIS

A general, modular method for the catalytic asymmetric synthesis of alkylboronate esters

Jens Schmidt, Junwon Choi, Albert Tianxiang Liu, Martin Slusarczyk, Gregory C. Fu*

Alkylboron compounds are an important family of target molecules, serving as useful intermediates, as well as end points, in fields such as pharmaceutical science and organic chemistry. Facile transformation of carbon-boron bonds into a wide variety of carbon-X bonds (where X is, for example, carbon, nitrogen, oxygen, or a halogen), with stereochemical fidelity, renders the generation of enantioenriched alkylboronate esters a powerful tool in synthesis. Here we report the use of a chiral nickel catalyst to achieve stereoconvergent alkyl-alkyl couplings of readily available racemic α -haloboronates with organozinc reagents under mild conditions. We demonstrate that this method provides straightforward access to a diverse array of enantioenriched alkylboronate esters, in which boron is bound to a stereogenic carbon, and we highlight the utility of these compounds in synthesis.

Organoboron compounds play an important role in fields ranging from materials science to biochemistry to organic synthesis (1, 2); for example, in organic chemistry, they serve as products or as reaction partners in powerful transformations such as the hydroboration of olefins (3) and the Suzuki cross-coupling (4). Although impressive progress has been made in organoboron chemistry during the past decades, substantial opportunities remain, including expanding their role in enantioselective synthesis. For instance, the development of methods for the asymmetric synthesis of alkylboron compounds wherein boron is attached to a stereogenic carbon (Fig. 1A) is an important objective, given their utility both as end points (e.g., Velcade) (5, 6) and as versatile precursors to a wide range of other valuable families of molecules, including enantioenriched amines and alcohols (1, 7, 8). In particular, alkylboronate esters (Fig. 1A) simultaneously possess desirable aspects of stability (including to air and moisture, as well as configu-

rational stability) and of reactivity (stereospecific conversion of the C–B bond to C–C, C–N, C–O, C–halogen, and other C–heteroatom bonds).

Whereas early efforts to synthesize enantioenriched alkylboron compounds focused primarily on the use of stoichiometric chiral reagents to control the stereochemistry of the product (8, 9), recent investigations have increasingly focused on exploiting chiral catalysts. Virtually all methods furnish chiral alkylboronate esters that must contain a specific functional group in a specific position—for example, an aryl, an alkenyl, or a directing group (10–12).

Matteson has developed a powerful, versatile strategy for the synthesis of alkylboronate esters through the coupling of α -haloboronates with organolithium or organomagnesium reagents (Fig. 1B) (13). This reaction proceeds through initial addition of the organometallic nucleophile to the electrophilic boron, followed by a 1,2-migration (substitution with inversion) to form the desired carbon-carbon bond. The Matteson reaction serves as the foundation for a general, modular method for the synthesis of alkylboronate esters, including an enantioselective process that uses a stoichiometric chiral auxiliary (Fig. 1C); moreover, the reaction can be applied in an iterative procedure

Division of Chemistry and Chemical Engineering, California Institute of Technology, Pasadena, CA 91125, USA.

*Corresponding author. Email: gcfu@caltech.edu

that affords homologated alkylboronate esters (Fig. 1D). Aggarwal has developed an elegant related approach that uses enantioenriched α -lithiated benzoates to produce these targets, including in an iterative fashion (14).

Nevertheless, areas for improvement persist. For example, it would be attractive to exploit a chiral catalyst, rather than a stoichiometric chiral reagent, to control enantioselectivity; this is essential for the synthesis at will of any of the possible stereoisomers in the iterative strategy illustrated in Fig. 1D. Furthermore, it is desirable to use nucleophilic coupling partners other than highly reactive organolithium and organomagnesium reagents, because they limit the range of tolerated functional groups. Here we address these challenges by achieving a Matteson-like coupling in a mechanistically distinct fashion: Specifically, we use a chiral nickel catalyst to cross-couple racemic α -haloboronates with organozinc reagents, thereby generating alkylboronate esters with high enantioselectivity (Fig. 1, E to G).

We have recently established that nickel complexes catalyze the coupling of a broad range of alkyl electrophiles with a diverse array of organometallic nucleophiles, often with high levels of enantioselectivity (15–17); these cross-couplings proceed through organonickel intermediates that are generated and consumed in elementary steps such as oxidative addition, transmetalation, and reductive elimination (18). In pursuing a transition metal-catalyzed variant of the Matteson coupling, we used organozinc reagents as the nucleophilic coupling partner (Negishi-type reactions) because they can be generated under mild conditions, they do not require a stoichiometric activator (unlike, for example, the base in a Suzuki cross-coupling) (4), and they are compatible with a broad spectrum of functional groups (19).

Whereas treatment of the α -chloroboronate depicted in Fig. 2A with *n*-BuMgBr resulted in a rapid reaction (complete consumption of the electrophile within 15 min at room temperature in tetrahydrofuran and dimethylacetamide), re-

placement of *n*-BuMgBr with *n*-BuZnBr led to no coupling after 24 hours. However, through the addition of an appropriate nickel catalyst ($\text{NiBr}_2 \cdot \text{diglyme}$ and a chiral 1,2-diamine), the coupling of the previously unreactive organozinc reagent could be achieved even at 0°C (entry 1 in Fig. 2A); moreover, the reaction proceeded with very good enantioselectivity [92% enantiomeric excess (ee)] from a racemic mixture of the electrophile. This new method proved versatile: A wide array of α -haloboronates and organozinc reagents could be coupled under mild conditions with good ee (Fig. 2, A and B). Essentially no desired product was observed in the absence of the diamine, consistent with a ligand-accelerated process (20). Although we have applied chiral nickel-diamine catalysts to stereoconvergent Suzuki cross-couplings of racemic alkyl electrophiles (16), they have not previously proved to be the ligands of choice for corresponding Negishi cross-couplings.

We found that a variety of organozinc reagents could be used as the nucleophilic coupling partner,

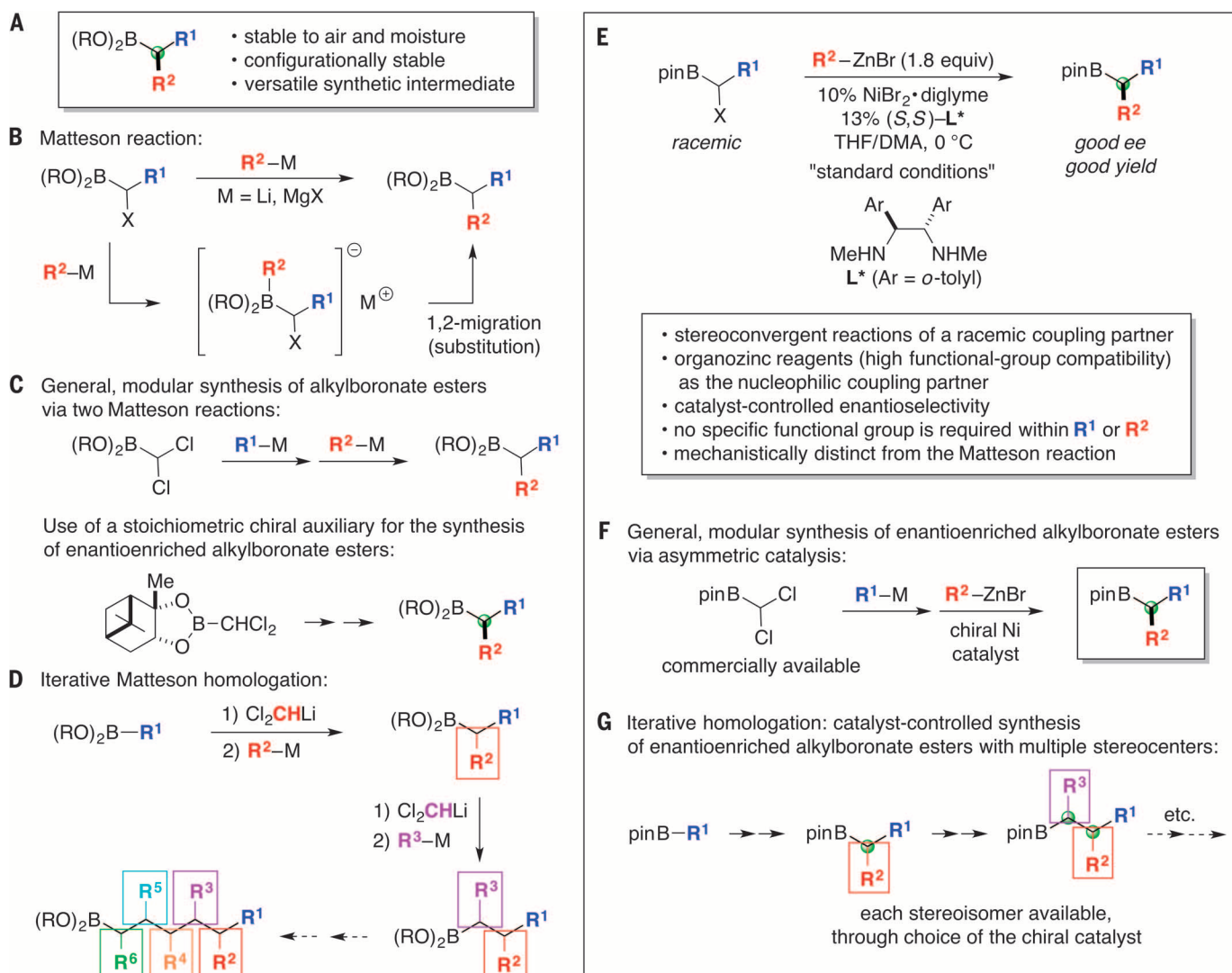
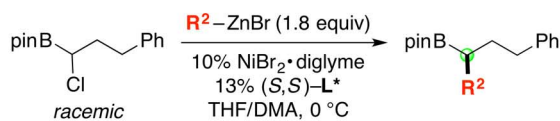


Fig. 1. Alkylboronate esters. (A to D) Background. (E to G) This study. R, alkyl group (superscripts indicate different alkyl groups); Me, methyl; pin, pinacolato; THF, tetrahydrofuran; DMA, dimethylacetamide; equiv, equivalent; ee, enantiomeric excess.

Fig. 2. Nickel-catalyzed asymmetric synthesis of alkylboronate esters. (A and B)

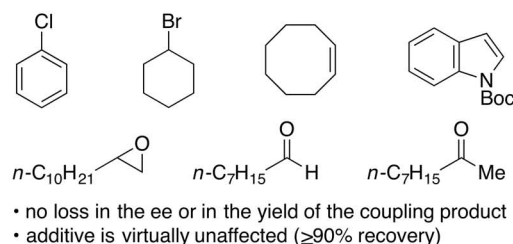
Variation in the coupling partners. The ee was determined by chiral high-performance liquid chromatography after oxidation to the alcohol. The yield was determined by isolation after chromatographic purification. **(C)** Functional-group compatibility. **(D)** Comparison of the enantioselectivity-determining step when using a chiral auxiliary versus a chiral catalyst. All data represent the average of two experiments. * α -iodoboronate was used. †Reaction temperature, 10 °C. ‡Catalyst loading, 12% $\text{NiBr}_2 \cdot \text{diglyme}$ and 16% L^* . TBS, *tert*-butyldimethylsilyl; Ac, acetyl; Ph, phenyl; Boc, *t*-butoxycarbonyl.

A Variation of the nucleophile:

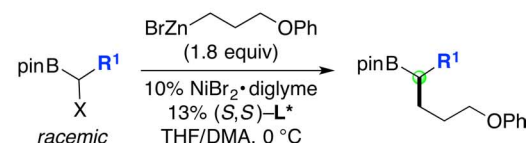


entry	R ²	ee (%)	yield (%)
1	<i>n</i> -Bu	92	72
2		90	82
3		83 (82*)	56 (95*)
4†		95	60
5‡		92	75
6		90	76

C Coupling conditions are compatible with:

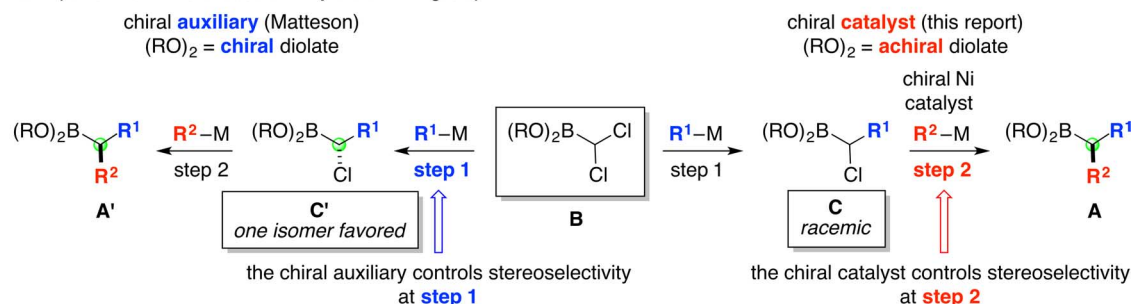


B Variation of the electrophile:



entry	R ¹	X	ee (%)	yield (%)
1	<i>n</i> -Bu	Cl	91	80
2		Cl	89	80
3		Cl	91	84
4		I	91	86
5		I	93	84
6		I	95	84
7		I	95	83
8		I	93	85
9		I	93	84

D Comparison of the stereoselectivity-determining step:



including functionalized substrates that bear a silyl ether, a cyano group, an acetal, an ester, or a primary alkyl chloride, furnishing the target alkylboronate esters with very good enantioselectivity from a racemic α -haloboronate (Fig. 2A). Yields substantially greater than 50% of highly enantioenriched product establish the stereoconvergence of both enantiomers of the electrophile into a single enantiomer of the alkylboronate ester (in contrast to a simple kinetic resolution). Under the same conditions, a secondary alkylzinc reagent furnished a low yield and moderate ee.

Similarly, an array of α -haloboronates served as suitable electrophilic coupling partners (Fig. 2B), including sterically demanding compounds (entries 4 to 9); in the latter cases, because of the sensitivity of the reaction to steric hindrance, it proved advantageous to use a more reactive α -iodoboronate, rather than an α -chloroboronate. When the coupling of the 2-phenylethyl-substituted

electrophile depicted in entry 2 was conducted on a larger scale (1.3 g of purified product), a lower catalyst loading could be used to generate the desired alkylboronate ester with comparable ee and yield (3.0% $\text{NiBr}_2 \cdot \text{diglyme}$ and 3.6% chiral ligand L^* ; 90% ee, 77% yield). To determine the compatibility of the process with various functional groups, we carried out the cross-coupling of the tetrahydropyran-substituted electrophile illustrated in entry 8 in the presence of a range of compounds (1.0 equivalent in individual experiments), and we established that the ee and yield of the product are essentially unaffected, as is the additive (Fig. 2C) (21, 22). Organolithium and organomagnesium reagents react with functional groups such as secondary alkyl bromides, epoxides, aldehydes, and ketones.

As a consequence of the mechanistic dichotomy between the Matteson reaction and this nickel-catalyzed cross-coupling, there is a divergence in

which step of the modular asymmetric synthesis leads to the stereoselective formation of product **A** (Fig. 2D). In the Matteson approach using a stoichiometric chiral auxiliary, the two chlorines of electrophile **B** are diastereotopic because of the chiral diolate ligand, and their differential reactivity in the 1,2-migration of the tetravalent boron intermediate results in the stereoselective formation of compound **C'** and then **A'** (an outline of the mechanism of the Matteson reaction is shown in Fig. 1B). In contrast, for the asymmetric nickel-catalyzed cross-coupling, racemic α -haloboronate **C** is converted by the chiral nickel-diamine catalyst into product **A** in an enantioconvergent reaction, likely through a radical generated from homolytic cleavage of the C–Cl bond (18).

We applied this nickel-catalyzed method for the stereoselective synthesis of alkylboronate esters to more complex partners. For example, under our standard conditions, a derivative of cholesterol

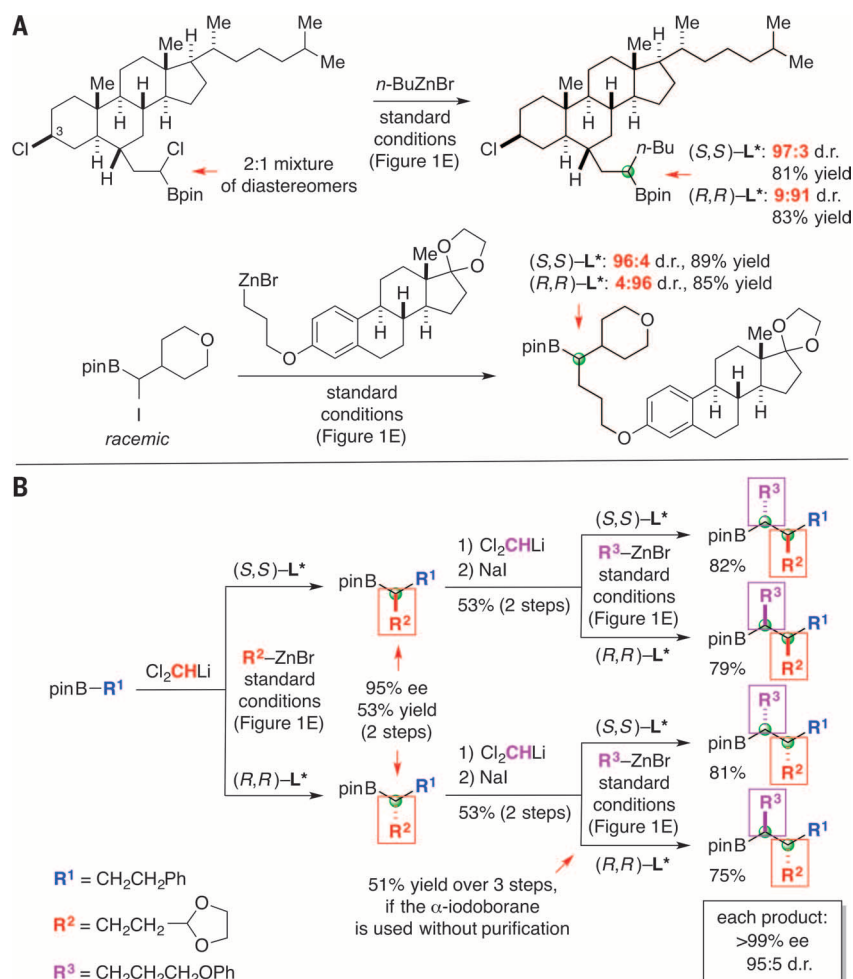
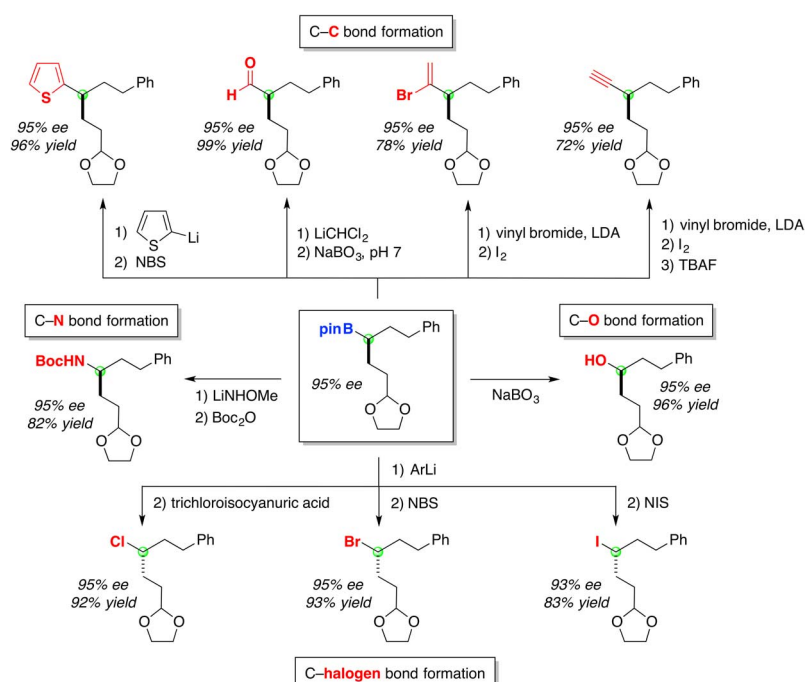


Fig. 3. Catalyst-controlled stereoselectivity in the asymmetric synthesis of alkylboronate esters.

(A) Complex coupling partners. (B) Iterative homology. d.r., diastereomeric ratio.

Fig. 4. Enantioenriched alkylboronate esters as versatile intermediates. The alkylboronate compounds are converted to diverse families of organic molecules through C–C, C–N, C–O, and C–halogen bond formation. NBS, *N*-bromosuccinimide; LDA, lithium diisopropylamide; TBAF, tetrabutylammonium fluoride; ArLi, [3,5-bis(trifluoromethyl)phenyl]lithium; NIS, *N*-iodosuccinimide.



served as a suitable electrophile (top of Fig. 3A; selective reaction of the chloride α to boron, rather than the chloride in the 3 position), and a derivative of estrone functioned as an effective nucleophile (bottom of Fig. 3A), leading to each of the desired coupling products with high stereoselectivity and in good yield. In both cases, the stereochemistry of L^* , rather than that of the substrate, is the predominant determinant of the stereochemistry α to boron.

We also demonstrated that our method can be exploited in an iterative homologation process (Fig. 3B). Thus, in contrast to a sequence of Matteson reactions using a stoichiometric chiral auxiliary, this nickel-catalyzed asymmetric coupling can provide access to any of the four possible diastereomers of the target alkylboronate ester with excellent stereoselectivity from a single starting material, simply through the choice of the appropriate enantiomer of the nickel- L^* catalyst for each key carbon-carbon bond-forming process. Once again, the configuration of the chiral catalyst, not that of the coupling partners, primarily dictates the stereochemistry of the products in Fig. 3B.

As noted at the outset, enantioenriched alkylboronate esters are extremely versatile intermediates in organic synthesis that can be converted into other important families of compounds with preservation of the ee at the boron-bound carbon (1, 7, 8, 23–26); several illustrative examples are provided in Fig. 4. Thus, C–C, C–N, C–O, and C–halogen bond formation can be achieved in good yield, affording access to a wide array of functional groups that are common in valuable synthesis targets, including bioactive molecules (e.g., heterocycles, aldehydes, amines, alcohols, and alkyl halides), all with little or no erosion in enantiomeric excess. By providing straightforward access to a broad array of alkylboronate esters, and thereby to diverse families of enantioenriched organic

compounds through subsequent functionalization (Fig. 4), our catalytic asymmetric method may have a substantial impact on the many fields that benefit from ready access to chiral molecules.

REFERENCES AND NOTES

- D. G. Hall, Ed., *Boronic Acids: Preparation and Applications in Organic Synthesis, Medicine and Materials*, vols. 1 and 2 (Wiley-VCH, 2011).
- N. Miyaura, Y. Yamamoto, in *Comprehensive Organometallic Chemistry III*, vol. 9, R. H. Crabtree, D. M. P. Mingos, Eds. (Elsevier, 2007), chap. 5.
- H. C. Brown, *Hydroboration* (Benjamin/Cummings, 1980).
- A. Suzuki, *Angew. Chem. Int. Ed.* **50**, 6722–6737 (2011).
- R. Smoun, A. Rubinstein, V. M. Dembitsky, M. Srebnik, *Chem. Rev.* **112**, 4156–4220 (2012).
- N. Ni, B. Wang, in *Boronic Acids: Preparation and Applications in Organic Synthesis, Medicine and Materials*, vol. 2, D. G. Hall, Ed. (Wiley-VCH, 2011), chap. 13.
- D. Leonori, V. K. Aggarwal, *Angew. Chem. Int. Ed.* **54**, 1082–1096 (2015).
- D. S. Matteson, *Stereodirected Synthesis with Organoboranes* (Springer, 1995).
- H. C. Brown, G. Zweifel, *J. Am. Chem. Soc.* **83**, 486–487 (1961).
- L. Zhang et al., *Science* **351**, 70–74 (2016).
- Y. Xi, J. F. Hartwig, *J. Am. Chem. Soc.* **138**, 6703–6706 (2016).
- A. Ganić, A. Pfaltz, *Chemistry* **18**, 6724–6728 (2012).
- D. S. Matteson, in *Boronic Acids: Preparation, Applications in Organic Synthesis and Medicine*, D. G. Hall, Ed. (Wiley-VCH, 2005), chap. 8.
- M. Burns et al., *Nature* **513**, 183–188 (2014).
- C. Fischer, G. C. Fu, *J. Am. Chem. Soc.* **127**, 4594–4595 (2005).
- A. Wilsily, F. Tramutola, N. A. Owston, G. C. Fu, *J. Am. Chem. Soc.* **134**, 5794–5797 (2012).
- Y. Liang, G. C. Fu, *J. Am. Chem. Soc.* **137**, 9523–9526 (2015).
- N. D. Schley, G. C. Fu, *J. Am. Chem. Soc.* **136**, 16588–16593 (2014).
- S. Xu, H. Kamada, E. H. Kim, A. Oda, E.-i. Negishi, in *Metal-Catalyzed Cross-Couplings and More*, vol. 1, A. de Meijere, S. Bräse, M. Oestreich, Eds. (Wiley-VCH, 2014), chap. 3.
- D. J. Berrisford, C. Bolm, K. B. Sharpless, *Angew. Chem. Int. Ed. Engl.* **34**, 1059–1070 (1995).
- A. C. Bissember, A. Levina, G. C. Fu, *J. Am. Chem. Soc.* **134**, 14232–14237 (2012).
- K. D. Collins, F. Glorius, *Nat. Chem.* **5**, 597–601 (2013).
- Y. Wang, A. Noble, E. L. Myers, V. K. Aggarwal, *Angew. Chem. Int. Ed.* **55**, 4270–4274 (2016).
- A. Bonet, M. Odachowski, D. Leonori, S. Essafi, V. K. Aggarwal, *Nat. Chem.* **6**, 584–589 (2014).
- S. M. Mlynarski, A. S. Karns, J. P. Morken, *J. Am. Chem. Soc.* **134**, 16449–16451 (2012).
- R. Larouche-Gauthier, T. G. Elford, V. K. Aggarwal, *J. Am. Chem. Soc.* **133**, 16794–16797 (2011).

ACKNOWLEDGMENTS

Support has been provided by the National Institutes of Health (National Institute of General Medical Sciences, R01-GM62871), the Alexander von Humboldt Foundation (fellowship for J.S.), the German National Merit Foundation (fellowship for M.S.), the David S. Koons SURF (Summer Undergraduate Research Fellowship) Endowment (fellowship for A.T.L.), and the Gordon and Betty Moore Foundation (for the Caltech Center for Catalysis and Chemical Synthesis). We thank J. M. Ahn, L. M. Henling, M. K. Takase (Caltech X-Ray Crystallography Facility), N. D. Schley, M. Shahgholi (Caltech Mass Spectrometry Facility), D. G. VanderVelde (Caltech NMR Facility), and S. C. Virgil (Caltech Center for Catalysis and Chemical Synthesis) for assistance and helpful discussions. Experimental procedures and characterization data are provided in the supplementary materials. Crystallographic data are available free of charge from the Cambridge Crystallographic Data Centre under reference CCDC-1512445.

SUPPLEMENTARY MATERIALS

www.sciencemag.org/content/354/6317/1265/suppl/DC1
Materials and Methods
Supplementary Text
Tables S1 to S7
Spectral Data
References (27–38)

23 August 2016; accepted 3 November 2016
10.1126/science.aai8611

TOPOLOGICAL MATTER

Robust spin-polarized midgap states at step edges of topological crystalline insulators

Paolo Sessi,^{1*} Domenico Di Sante,² Andrzej Szczerbakow,³ Florian Glott,¹ Stefan Wilfert,¹ Henrik Schmidt,¹ Thomas Bathon,¹ Piotr Dziawa,³ Martin Greiter,² Titus Neupert,⁴ Giorgio Sangiovanni,² Tomasz Story,³ Ronny Thomale,² Matthias Bode^{1,5}

Topological crystalline insulators are materials in which the crystalline symmetry leads to topologically protected surface states with a chiral spin texture, rendering them potential candidates for spintronics applications. Using scanning tunneling spectroscopy, we uncover the existence of one-dimensional (1D) midgap states at odd-atomic surface step edges of the three-dimensional topological crystalline insulator (Pb,Sn)Se. A minimal toy model and realistic tight-binding calculations identify them as spin-polarized flat bands connecting two Dirac points. This nontrivial origin provides the 1D midgap states with inherent stability and protects them from backscattering. We experimentally show that this stability results in a striking robustness to defects, strong magnetic fields, and elevated temperature.

The recent theoretical prediction and experimental realization of topological insulators (TIs) have considerably extended the notion of a phase of matter. Within this framework, it has been shown that—based on some topological invariants—the electronic properties of materials can be classified into distinct topological classes (*I*, *2*). In topologically nontrivial materials, unconventional boundary modes have been experimentally detected by several different techniques (*3–9*). In two-dimensional (2D) TIs, counter-propagating spin-momentum-locked 1D edge modes develop along the sample boundary; in contrast, 3D TIs (*4*) have boundary modes that are linearly dispersing chiral surface states. Although a large variety of 3D TIs have been reported, only very few 2D TIs are known [HgTe (*3*), InAs (*10*) quantum wells, and Bi bilayers (*11*)]. These 2D TIs are delicate and difficult to realize experimentally because they all require the fabrication of precisely controlled thin film heterostructures. Properties such as small band gaps (*3*, *10*), strong substrate-induced hybridization effects (*11*), or the existence of residual trivial states (*10*, *11*) make helical edge states not only challenging to study but also of limited appeal for applications. Furthermore, their topological properties are protected only as long as time-reversal symmetry is preserved.

Here, we report that 2D topological surfaces, in turn, can be the mother state for nontrivial

1D midgap states (*12*), suggesting a dimensional hierarchy of boundary states in topological insulators. Specifically, we report on the discovery of 1D topological spin-filtered channels that naturally develop at step edges of 3D topological crystalline insulators (TCIs)—i.e., materials where the existence of surface Dirac states is guaranteed by crystal symmetries.

Figure 1A displays the rock-salt structure of $\text{Pb}_{1-x}\text{Sn}_x\text{Se}$ ($x \leq 0.4$). Depending on Sn-content x , these compounds have been reported to belong to two topologically distinct phases (*13*) that can be stoichiometrically controlled. Starting from PbSe, which is topologically trivial, the substitutional solid solution $\text{Pb}_{1-x}\text{Sn}_x\text{Se}$ turns into a topologically nontrivial phase as the Sn concentration exceeds $x \approx 0.24$ (*14*, *15*). Its bulk inverted band gap cannot be adiabatically connected to a trivial state as long as some crystal symmetries are preserved. The electronic properties of high-symmetry surfaces of these TCIs are characterized by topologically protected linearly dispersing Dirac states (*13*, *14*, *16–19*). Figure 1B illustrates this scenario for the nonpolar (001) surface, which is commonly exposed after cleaving bulk crystals. It hosts four Dirac cones centered in close proximity to the \bar{X} and \bar{Y} points of the Brillouin zone. Figure 1C shows a typical image of the (001) surface acquired by scanning tunneling microscopy (STM) on a freshly cleaved $\text{Pb}_{0.67}\text{Sn}_{0.33}\text{Se}$ bulk crystal (*20*)—i.e., a material safely within the topological regime at $x \geq 0.24$. An atomically resolved image showing the Se sublattice (*21*) is displayed as an inset. The profile taken along the gray line shows that several atomically flat terraces exist, separated by step edges of different heights.

Given the equal probability of breaking the crystal bonds at every atomic layer, all steps can be mapped onto two different classes: those corresponding to an integer number n of the conventional unit cell heights a —i.e., na , from here

¹Physikalisches Institut, Experimentelle Physik II, Universität Würzburg, Am Hubland, 97074 Würzburg, Germany. ²Institut für Theoretische Physik, Universität Würzburg, Am Hubland, 97074 Würzburg, Germany. ³Institute of Physics, Polish Academy of Sciences, Aleja Lotników 32/46, 02-668 Warsaw, Poland. ⁴Physik-Institut, Universität Zürich, Winterthurerstrasse 190, CH-8057 Zürich, Switzerland. ⁵Wilhelm Conrad Röntgen-Center for Complex Material Systems (RCCM), Universität Würzburg, Am Hubland, 97074 Würzburg, Germany.
*Corresponding author. Email: sessi@physik.uni-wuerzburg.de

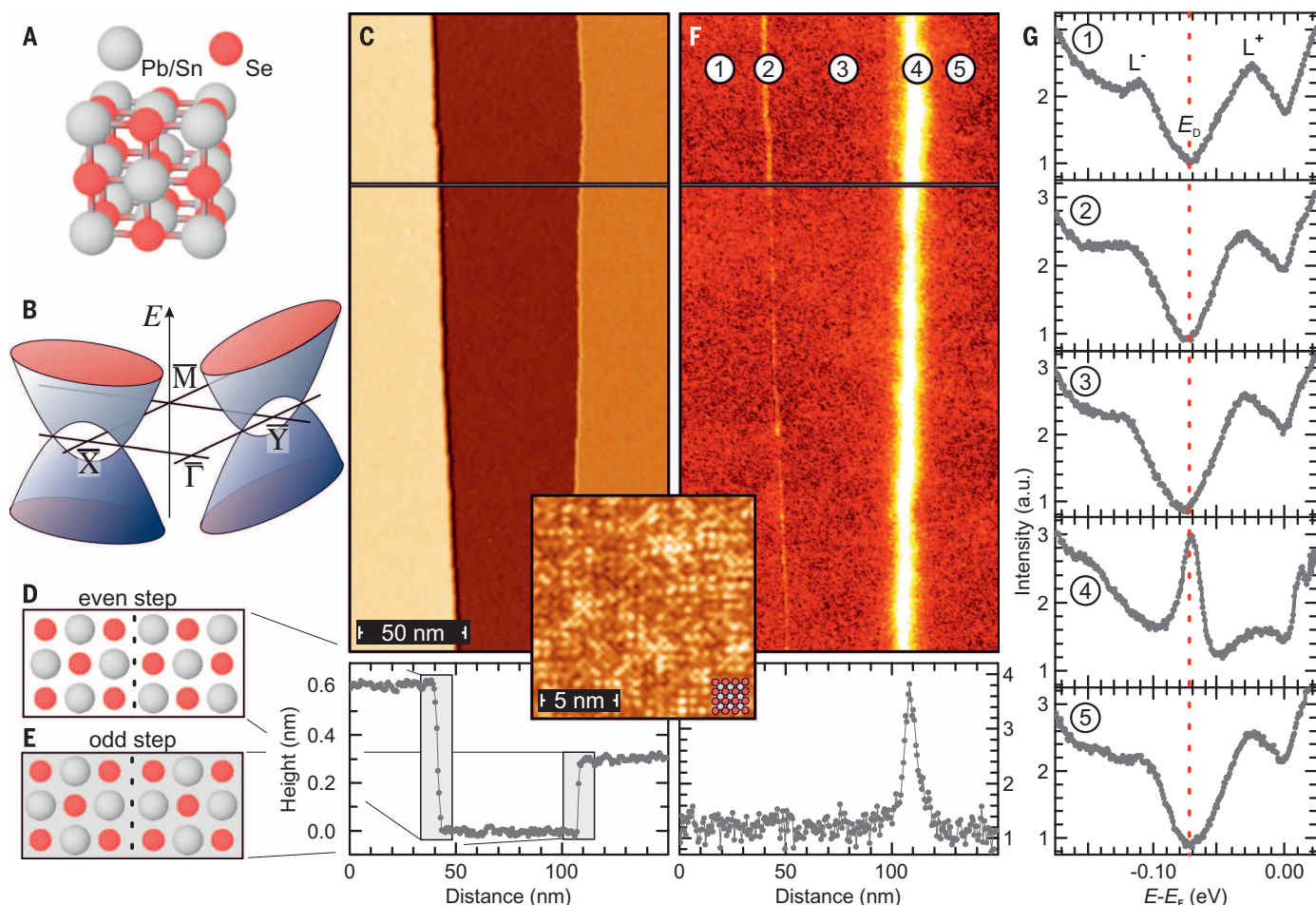
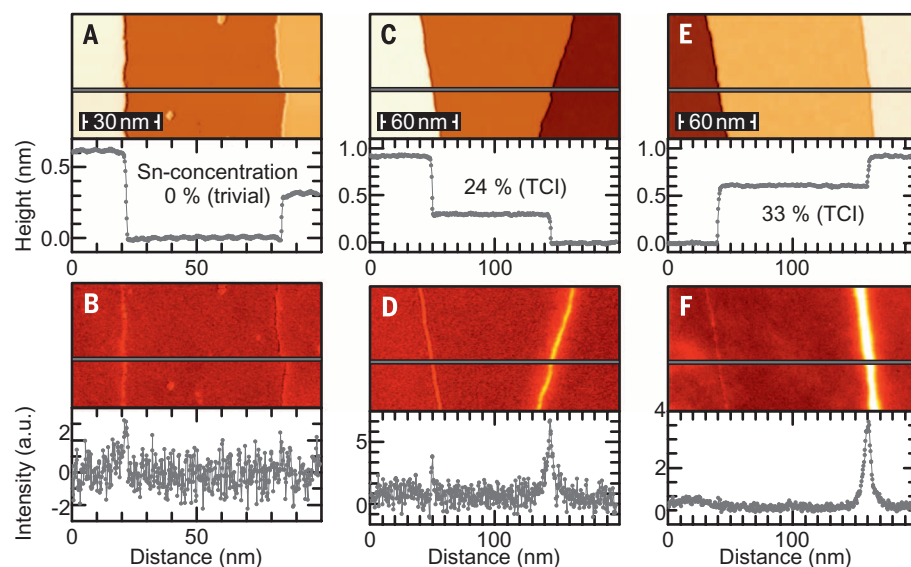


Fig. 1. Electronic properties of $\text{Pb}_{0.67}\text{Sn}_{0.33}\text{Se}$ terraces and step edges probed by STS. (A) Rock-salt crystal structure and (B) schematic band structure of $(\text{Pb,Sn})\text{Se}$. (C) Topographic STM image of a cleaved $\text{Pb}_{0.67}\text{Sn}_{0.33}\text{Se}$ surface (scan parameters: $U = -75$ mV; $I = 50$ pA). (Inset) Atomic resolution image of the Se sublattice. Two steps are visible in the main panel. The line section (bottom panel) measured along the gray line shows that their heights correspond to a single- (right) and a double-atomic step (left), respectively. Whereas the periodicity is maintained for even step edges (D), odd step edges lead to a struc-

tural π shift (E). (F) dI/dU map (top) measured at the same location as (C). The line section (bottom) reveals an enhanced conductance at the position of the single-atomic step edge. (G) Local tunneling spectra measured with the STM tip positioned at the locations indicated in (F). The spectra measured on atomically flat terraces (1, 3, and 5) and at even step edges (2) display the typical V shape with a minimum at the Dirac energy ($E_D = -75$ meV) surrounded by two maxima indicating van Hove singularities ($L^- = -110$ meV and $L^+ = -30$ meV); the spectrum measured at the position of the odd step (4) exhibits a strong peak at the Dirac energy.

Fig. 2. Sn concentration-dependent electronic properties of $(\text{Pb,Sn})\text{Se}$. Topography (top), dI/dU maps (bottom), and their corresponding profiles taken along the indicated line (bottom of each panel), measured on $\text{Pb}_{1-x}\text{Sn}_x\text{Se}$ crystals with different Sn content—i.e., (A and B) $x = 0$, (C and D) $x = 0.24$, and (E and F) $x = 0.33$ —thereby spanning the range from trivial to topological surfaces. Step edges on the trivial compound ($x = 0$) carry no particular edge feature, irrespective of their even- or oddness. In contrast, a weak and strong enhancement of the local DOS is indicated by the high dI/dU signal measured at odd step edges for $x = 0.24$ and $x = 0.33$, respectively. Scan parameters: $U = -310$ mV, $I = 30$ pA ($x = 0$); $U = -115$ mV, $I = 50$ pA ($x = 0.24$); $U = -70$ mV, $I = 100$ pA ($x = 0.33$). $T = 4.8$ K.



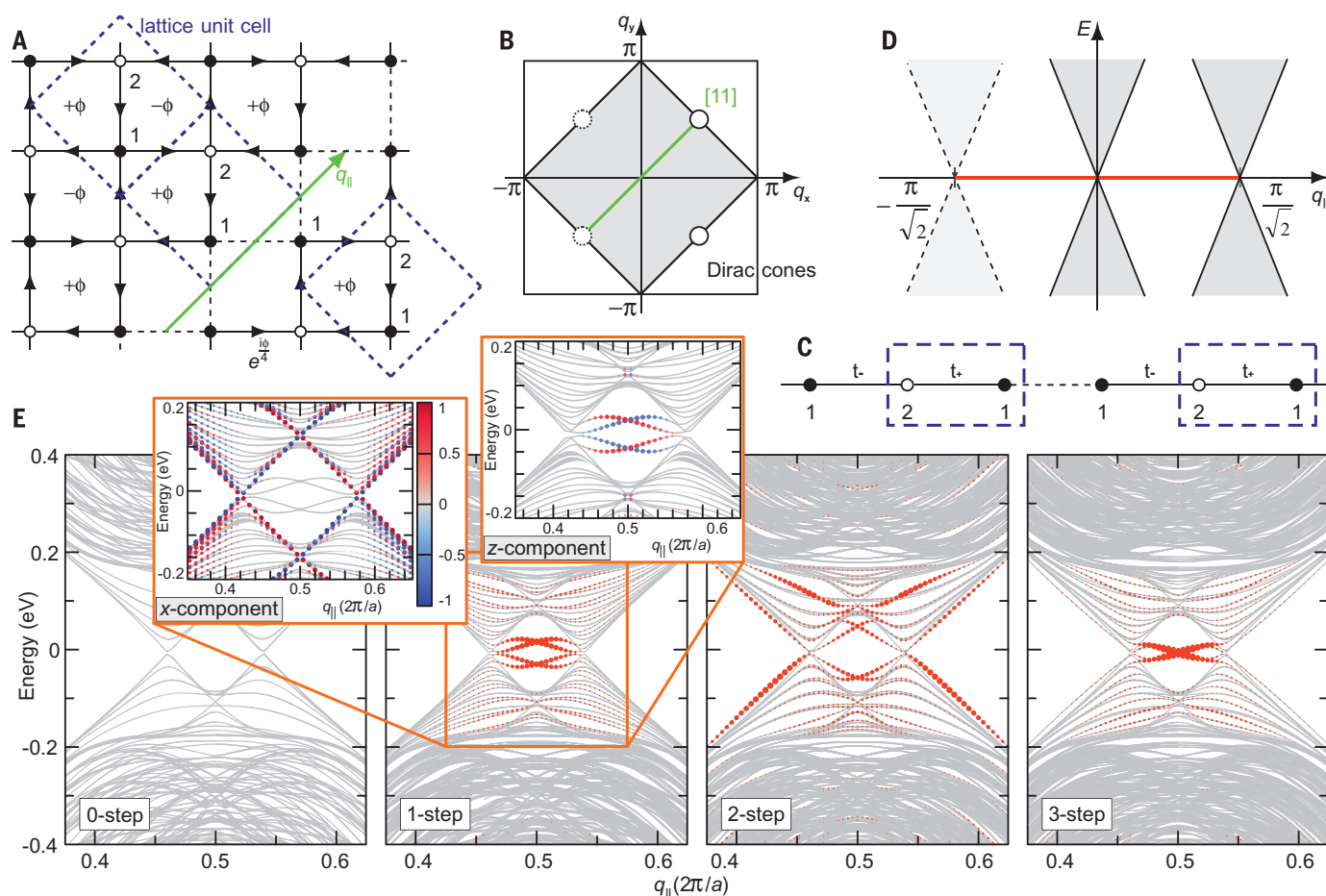


Fig. 3. Theoretical analysis of the TCI step edge electronic structure.

(A) Staggered flux lattice with a domain wall in the $[11]$ direction. (B) Brillouin zone including the projection onto the 1D domain wall. (C) Effective 1D hopping model describing the staggered flux lattice. (D) Schematic view of the resulting spectrum. (E) Tight-binding results of the electronic structure (momentum $q_{||}$ parallel to the edge) for a 3D TCI with $[110]$ -oriented step edges of different height. The continuum

of bulk states and surface contributions are shown as gray lines and red dots, respectively. Whereas strongly localized narrow bands connecting the two Dirac cones emerge at odd step edges, no such spectral weight is observed for even step edges. The two insets show the spin polarization in the presence of a single-atomic step edge: in-plane component perpendicular to the step edge (x, left) and the out-of-plane component (z, right) with the color (red and blue) indicating opposite spin directions.

on even steps—and those corresponding to half-integer multiples—i.e., $(1/2 + n)a$, called odd steps hereafter. Whereas even steps maintain the translational symmetry of the surface lattice, odd steps introduce a structural π shift (Fig. 1, D and E, shows the two situations from the top). As will be described below, this has far-reaching implications for the electronic structure of the step edges.

Figure 1F shows a differential conductance (dI/dU) map at an energy of $E - E_F = -75$ meV, which was measured simultaneously with the topographic image presented in Fig. 1C. Whereas the local density of states (DOS) is similar for all terraces and also remains essentially unchanged for the even step edge, a strong enhancement can be recognized along the odd step. Its intensity is symmetrically distributed on both sides of the step and has a width of ~ 10 nm (line profile in Fig. 1F). Remarkably, this DOS is very homogeneously distributed along the step; no evidence for scattering-induced quasiparticle interference pattern was found [for the Fourier-transformed dI/dU intensity along the step edge, see (20) and fig. S1].

To unravel the origin of this prominent electronic feature, we measured local scanning tunneling spectroscopy (STS) data on the three atomically flat terraces and the two step edges. The precise locations where the STS curves displayed in Fig. 1G have been obtained are indicated by numbers 1 to 5 in Fig. 1F. As expected, all spectra obtained on top of $\text{Pb}_{0.67}\text{Sn}_{0.33}\text{Se}(001)$ terraces (panels 1, 3, and 5) show the same features. In particular, similar to earlier observations on TCI surfaces (17, 22), the minimum visible about -75 meV marks the position of the Dirac point; the peaks L^- and L^+ identify van Hove singularities, which signal the energy position of the two saddle points below and above the Dirac point, respectively.

Whereas this local DOS profile remains essentially unperturbed at the even step edge (position 2), completely different STS curves are observed at odd step edges—e.g., at position 4. Here, the spectrum is characterized by a strong peak at the Dirac point. More generally, its emergence is associated with a strong redistribution of the spectral weight over a relatively large energy range,

as evidenced by the disappearance of the features associated with the van Hove singularities. This scenario is consistently also found for even and odd steps of higher order—i.e., triple and quadruple step edges (see fig. S2). Furthermore, the absence of scattering [similar to recent experiments on weak topological insulators (23)], the energy position locked at the Dirac point, and the association with translational symmetry breaking all point to a topological origin of these 1D channels.

To unequivocally prove that the emergence of these 1D edge states is linked to the existence of a nontrivial bulk band structure, we have performed measurements on crystals where the Sn concentration has been systematically changed, thereby spanning the entire range from trivial to topological surfaces (14) (Fig. 2). For all three concentrations—i.e., (A,B) $x = 0$, (C,D) $x = 0.24$, and (E,F) $x = 0.33$ —the topographic images displayed in Fig. 2, A, C, and E, show one even and one odd step edge (see respective line profiles at the bottom of each panel). Irrespective of the step's even- or oddness,

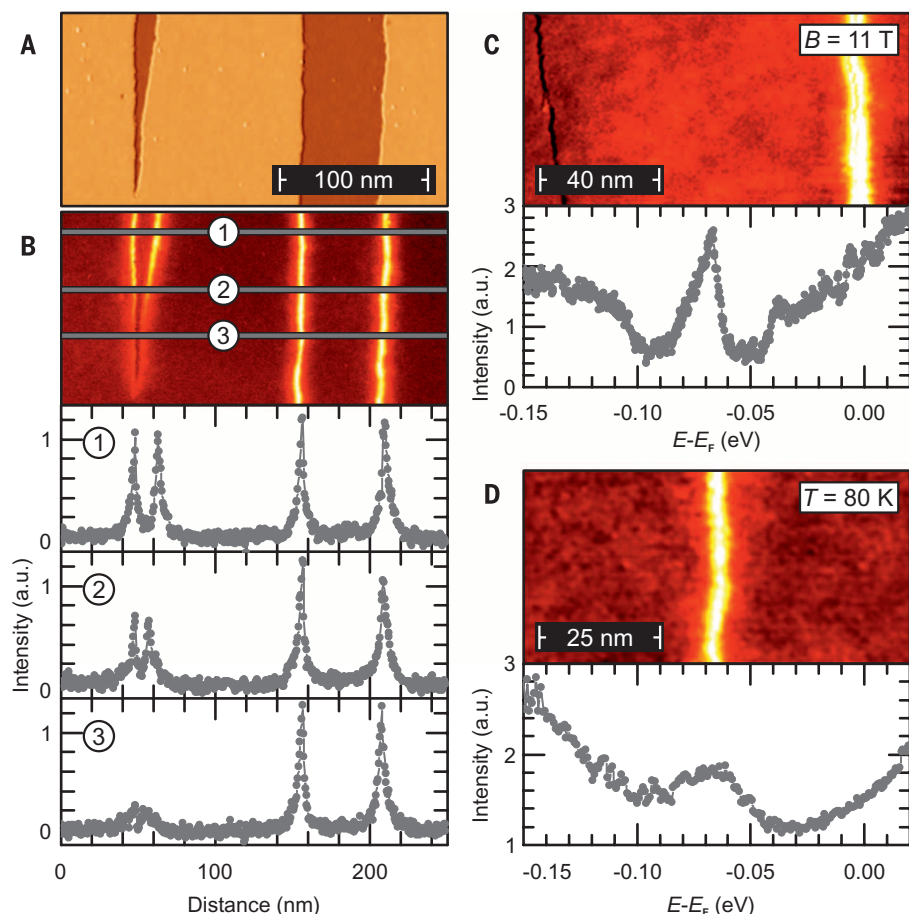


Fig. 4. Robustness of the edge state against perturbations. (A) Topographic STM image showing a $\text{Pb}_{0.67}\text{Sn}_{0.33}\text{Se}$ surface area exhibiting a total of four odd step edges. The separation between the two leftmost step edges continuously reduces from the top to the bottom of the image. (B) The dI/dU map reveals that the intensity of the edge state fades away as the edges approach below about 10 nm. Line sections along the lines indicated by numbers are plotted in the bottom panels. dI/dU maps taken around odd steps at (C) $B = 11$ T and (D) $T = 80$ K show the robustness of the 1D edge state against perturbations.

no particular edge feature is visible in the dI/dU map of the topologically trivial material—i.e., of pure PbSe without any Sn (Fig. 2B). An edge state with a slightly enhanced dI/dU intensity develops once $x = 0.24$ (Fig. 2D)—i.e., just at the critical Sn concentration required for the transition between a normal and an inverted band gap, thereby leading to a weakly protected topological nontrivial state (14). By further increasing the amount of Sn to $x = 0.33$, the $\text{Pb}_{1-x}\text{Sn}_x\text{Se}$ compound is driven deeply into the topologically nontrivial regime. Correspondingly, we observe a strong enhancement of the local dI/dU signal at the position of the odd step edge (Fig. 2F).

To understand the accumulation of midgap states at odd step edges, it is best to think of them as electronic domain walls in the surface states (24). This effective 2D electronic surface state features four Dirac cones, and domain walls are created by interchanging the two atoms in the unit cell. The simplest 2D toy model displaying an even number of Dirac cones and a two-sublattice structure is the staggered flux model—i.e., a square lattice model restricted to

nearest-neighbor hopping terms, in which neighboring plaquettes are threaded by opposite magnetic fluxes $+\phi$ and $-\phi$, with $0 < \phi < \pi$. We model a domain wall by interchanging the relative position of the two sublattices along the [11] direction (Fig. 3A). On the domain wall, the 2D Brillouin zone (BZ) of the staggered flux lattice is projected onto a 1D BZ, as indicated in green in Fig. 3B. Thereby, the two Dirac cones are not projected onto each other. We solve this system by Fourier transformation in the q_{\parallel} direction only, while keeping a real space index for the direction perpendicular to the wall. We obtain a chain model with alternating, real hopping amplitudes $t_{\pm} = 2\cos(\frac{q_{\parallel} \pm \phi}{2})$, with $-\frac{\pi}{\sqrt{2}} < q_{\parallel} \leq \frac{\pi}{\sqrt{2}}$, and a domain wall (Fig. 3C). Except for the positions of the two Dirac cones in the 1D BZ, $q_{\parallel} = 0$ and $q_{\parallel} = \frac{\pi}{\sqrt{2}}$, where $|t_{+}| = |t_{-}|$, the 1D model is gapped. Because closing the chain in the presence of the domain wall requires an odd number of sites, whereas particle-hole symmetry demands that all states with $E \neq 0$ are arranged in pairs with energies $\pm E$, we necessarily obtain a midgap state at $E = 0$ localized around the domain wall. We

obtain one such midgap state for each value of $q_{\parallel} \neq 0, \frac{\pi}{\sqrt{2}}$ —i.e., one for each real space unit cell. The spectrum will hence schematically look as depicted in Fig. 3D.

To elevate this minimal model result to an accurate description of the experimental scenario observed in Fig. 1, we have performed tight-binding calculations adapted to reproduce the band structure of a topologically nontrivial crystalline insulator (13). The model is solved for a geometry with two step edges on the topmost surface; the bottom surface is left unperturbed. Figure 3E shows the calculated band structure of an infinite terrace (left panel), a single-, a double-, and a triple-step edge (right) as a function of q_{\parallel} , the momentum along the step edge. In close analogy to the staggered flux model described above, we consider the case of step edges parallel to the [110] direction. A discussion of the step edges along the [100] direction (as those shown in the sketch of Fig. 1, D and E), as well as further details of the model and the calculation, can be found in (20). In all cases, the electronic structure obtained for the step-edge-free surface corresponds to the results expected for a TCI surface—i.e., with two Dirac cones symmetrically shifted with respect to $q_{\parallel} = \pi/a$ (gray lines). The size of the red dots is proportional to the degree of localization at the step edge.

Whereas even step edges give rise to two Dirac cones and a relatively wide open mouth-shaped feature connecting them, the odd-edge spectrum is markedly different. The states in between the Dirac cones have a narrow dispersion and therefore account for the overwhelming part of the step edge spectral weight (20). In contrast to the result of the staggered flux model presented above, these narrow states are not completely flat because the tight-binding model is not perfectly particle-hole symmetric. Furthermore, the midgap states do not extend over the whole Brillouin zone, as the Dirac cones are shifted away from high-symmetry points. For odd step edges, these states are laterally (i.e., perpendicular to the step) confined to a few nm, whereas in the z direction, they extend up to four lattice spacings. As shown in the left inset of Fig. 3E, our results for the single-atomic step edge correctly reproduce the spin-momentum locking of electronic states in the Dirac cone with an in-plane spin polarization. The right inset reveals that the two pairs of narrow, counter-propagating in-gap bands exhibit instead a high degree of out-of-plane spin polarization (maximum expectation value ≈ 0.7 for the operator $\langle \sigma_z \rangle$).

In comparison to 2D TIs, the $\text{Pb}_{1-x}\text{Sn}_x\text{Se}$ topological edge state reported here is expected to offer superior properties because it is protected by a bulk band gap that is up to 200 meV wide (14). We experimentally tested the robustness of the edge state to perturbations, such as hybridization with adjacent edge states, external magnetic field, or enhanced temperatures. For example, Fig. 4A shows a topographic STM image of a sample location with four odd step edges. Whereas the two right step edges run almost in parallel, thereby maintaining their separation, the two left step edges are inclined with respect to one another

and eventually merge close to the bottom of the image. As qualitatively evidenced by the dI/dU map of Fig. 4B and quantitatively supported by the line sections plotted at the bottom of this panel, the edge state disappears as soon as the step-step separation decreases below the spatial extent of the edge state (25)—i.e., about 10 nm. We further analyze the response of these edge states to high magnetic fields B . Figure 4C reports a dI/dU map (top) and STS data acquired on an odd step edge (bottom) at $B = 11$ T; contrary to the quantum spin Hall state found in HgTe, the 1D TCI state investigated here is robust against time-reversal symmetry breaking perturbations. Finally, Fig. 4D shows that the edge state also persists at elevated temperatures ($T = 80$ K). Despite the reduced intensity evidenced by the STS spectrum, a well-defined 1D channel is still clearly present.

The observation of a distinct type of one-dimensional states at odd step edges of topological crystalline insulators with relatively wide bulk band gaps opens up opportunities for the use of topological materials for sensing and information processing purposes well beyond existing materials (4, 10, 11). Furthermore, the absence of scattering and the high degree of spin polarization observed in tight-binding calculations indicate that the 1D midgap state might be useful for spintronics applications. By patterning the step-and-terrace structure of TCI surfaces, this may allow for the creation of well-separated conductive channels with a width of only about 10 nm. This may lead to interconnections between functional units at ultrahigh packing densities. To fully explore whether the 1D midgap state found at odd TCI step edges display quantum conductance effects, further investigations by, for example, four-probe transport measurements, will be needed.

REFERENCES AND NOTES

1. M. Z. Hasan, C. L. Kane, *Rev. Mod. Phys.* **82**, 3045–3067 (2010).
2. X.-L. Qi, S.-C. Zhang, *Rev. Mod. Phys.* **83**, 1057–1110 (2011).
3. M. König et al., *Science* **318**, 766–770 (2007).
4. D. Hsieh et al., *Nature* **452**, 970–974 (2008).
5. Y. L. Chen et al., *Science* **325**, 178–181 (2009).
6. P. Roushan et al., *Nature* **460**, 1106–1109 (2009).
7. T. Zhang et al., *Phys. Rev. Lett.* **103**, 266803 (2009).
8. B. A. Bernevig, T. L. Hughes, S.-C. Zhang, *Science* **314**, 1757–1761 (2006).
9. L. Fu, C. L. Kane, E. J. Mele, *Phys. Rev. Lett.* **98**, 106803 (2007).
10. I. Knez, R.-R. Du, G. Sullivan, *Phys. Rev. Lett.* **107**, 136603 (2011).
11. T. Hirahara et al., *Phys. Rev. Lett.* **107**, 166801 (2011).
12. J. Liu et al., *Nat. Mater.* **13**, 178–183 (2014).
13. T. H. Hsieh et al., *Nat. Commun.* **3**, 982 (2012).
14. P. Dziawa et al., *Nat. Mater.* **11**, 1023–1027 (2012).
15. B. M. Wojek et al., *Phys. Rev. B* **90**, 161202 (2014).
16. Y. Tanaka et al., *Nat. Phys.* **8**, 800–803 (2012).
17. Y. Okada et al., *Science* **341**, 1496–1499 (2013).
18. A. Gyenis et al., *Phys. Rev. B* **88**, 125414 (2013).
19. D. Zhang et al., *Phys. Rev. B* **89**, 245445 (2014).
20. See supplementary materials on Science Online.
21. I. Zeljkovic et al., *Nat. Mater.* **14**, 318–324 (2015).
22. I. Zeljkovic et al., *Nat. Phys.* **10**, 572–577 (2014).
23. C. Pauly et al., *Nat. Phys.* **11**, 338–343 (2015).
24. W. P. Su, J. R. Schrieffer, A. J. Heeger, *Phys. Rev. Lett.* **42**, 1698–1701 (1979).
25. Y. Zhang et al., *Nat. Phys.* **6**, 584–588 (2010).

ACKNOWLEDGMENTS

This research was supported by DFG (through SFB 1170 “ToCoTronics”; projects A02, B04, and C05) and by

the Polish National Science Centre NCN grants 2014/15/B/ST3/03833 and 2012/07/B/ST3/03607. We further acknowledge support by the European Research Council (ERC) through ERC-StG-TOPOLECTRICS-Thomale-336012. D.D.S. and G.S. gratefully acknowledge the Gauss Centre for Supercomputing e.V. (www.gauss-centre.eu) for funding this project by providing computing time on the GCS Supercomputer SuperMUC at Leibniz Supercomputing Centre (LRZ, www.lrz.de).

SUPPLEMENTARY MATERIALS

www.sciencemag.org/content/354/6317/1269/suppl/DC1
Materials and Methods
Supplementary Text
Figs. S1 to S7
References (26, 27)

23 July 2016; accepted 11 November 2016
10.1126/science.aah6233

BRAIN RESEARCH

Midbrain dopamine neurons control judgment of time

Sofia Soares,* Bassam V. Atallah,*† Joseph J. Paton†

Our sense of time is far from constant. For instance, time flies when we are having fun, and it slows to a trickle when we are bored. Midbrain dopamine neurons have been implicated in variable time estimation. However, a direct link between signals carried by dopamine neurons and temporal judgments is lacking. We measured and manipulated the activity of dopamine neurons as mice judged the duration of time intervals. We found that pharmacogenetic suppression of dopamine neurons decreased behavioral sensitivity to time and that dopamine neurons encoded information about trial-to-trial variability in time estimates. Last, we found that transient activation or inhibition of dopamine neurons was sufficient to slow down or speed up time estimation, respectively. Dopamine neuron activity thus reflects and can directly control the judgment of time.

Our ability to accurately estimate and reproduce time intervals is variable and depends on many factors, including motivation (1), attention (2), sensory change (3), novelty (4), and emotions (5). In addition, several neurological and neuropsychiatric disorders (6–9) are accompanied by changes in timing behavior. Midbrain dopamine (DA) neurons are implicated in many of the psychological factors (10) and disorders (6, 8, 11) associated with changes in time estimation.

Midbrain DA neurons also encode reward prediction errors (RPEs) (12–15), an important teaching signal in reinforcement learning (16). Phasic DA responses to reward-predicting cues reflect the magnitude of (17, 18), probability of (19), and expected time delay until the reward (20, 21). When expectation varies over time, DA neuron responses are smaller at times when rewards and reward-predicting cues are more expected (21, 22), indicating that DA neurons receive temporal information. Manipulations of the DAergic system by pharmacological (23) or genetic (24) approaches disrupt timing behavior, suggesting that DA neurons may directly modulate timing. However, the data from pharmacological and genetic manipulations are inconsistent: In some cases, DA seems to speed up timekeeping (23, 25), and in others, DA seems to slow down or not affect timekeeping (26, 27).

Champalimaud Research, Champalimaud Centre for the Unknown, Lisbon, Portugal.

*These authors contributed equally to this work. †Corresponding author. Email: bassam.atallah@gmail.com (B.V.A.); joe.paton@neuro.fchampalimaud.org (J.J.P.)

To determine (i) what signals are encoded by midbrain DA neurons during timing behavior and (ii) how DA neurons contribute to variability in temporal judgments, we measured and manipulated the activity of DA neurons in mice as they performed categorical decisions about duration (28). We first trained mice to perform a temporal discrimination task (Fig. 1A, left). Mice initiated trials at a central nose port, immediately triggering the delivery of two identical tones separated by a variable delay. Mice reported the delay between tones as shorter or longer than 1.5 s at one of two lateral nose ports for water reward. Incorrect choices were not rewarded. Performance was nearly perfect for the easiest intervals but more variable for intervals near 1.5 s (the boundary between the “short” and “long” categories) and was well described by a sigmoid psychometric function (Fig. 1A, middle).

We then pharmacogenetically suppressed DAergic neuronal activity and observed impaired temporal judgments on treatment days as compared with adjacent nontreatment days ($P < 0.004$, $n = 3$ mice; Fig. 1A, right). We also observed a tendency to perform fewer trials [control group, 177 ± 15 trials; clozapine N -oxide (CNO)-treated group, 115 ± 54 trials; mean \pm SD; $P = 0.05$], suggesting that the animals’ motivation was affected by DAergic suppression. To test whether fluctuations in endogenous DA neuron activity predicted systematic changes in temporal judgments, we used fiber photometry (29) to measure Ca^{2+} activity in DAergic neurons, targeting the substantia nigra pars compacta (SNc) (Fig. 1, B and C, and figs. S1 and S2).

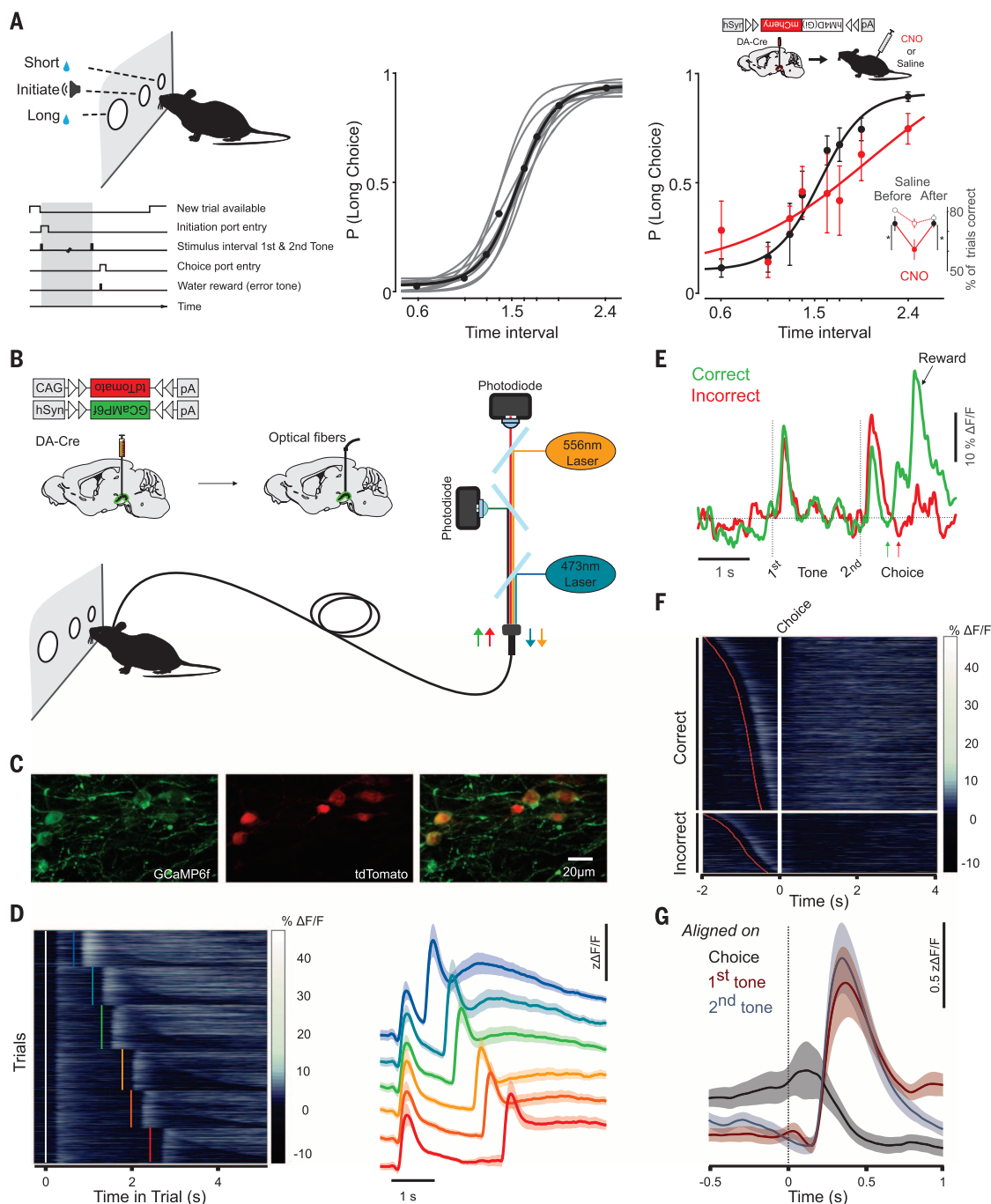


Fig. 1. Dopaminergic (DAergic) signaling is required and precisely aligned to temporal cues, not movement, during performance of a temporal categorization task. (A) Shown on the left is the task schematic and order of events (circles in the upper panel, nose-ports; gray shading in the lower panel, interval period). A logistic function fit to the daily (gray) and average (black) performance of an example mouse (10 sessions) is shown in the middle. Pharmacogenetic suppression (hM4D) was targeted to midbrain DAergic neurons, and mice were injected with either CNO or saline on adjacent days; shown on the right is mean psychometric performance on days with saline or CNO treatment (black or red, respectively; $n = 3$ mice). Error bars, SEM. The inset shows the percent of correct trials on days before and after CNO treatment in mice expressing hM4D (filled circles, $n = 3$; $*P < 0.005$) or non-hM4D-expressing controls (open circles, $n = 4$). Error bars, SEM. (B) Schematic of the photometry apparatus and viral and surgical procedure. (C) Image of the substantia nigra pars compacta (SNc) histology. (D) On the

left, all trials of DA neuronal activity recorded from a single subject are shown, split by interval duration and aligned on trial initiation (first tone delivery; white vertical line). Each row represents a trial, and within each interval, trials are sorted from fast (top) to slow (bottom) response time (RT, time from the second tone to choice; 3759 trials). Shown on the right are mean DAergic neuronal responses, split by interval duration ($n = 5$ mice; intervals are color-coded as throughout). Shading, SEM across mice. z, z-score, $\Delta F/F$, see the methods. (E) Example photometric traces recorded during a single correct and incorrect trial of the 1.74-s interval. (F) Photometric recordings of DA neuronal activity from a single subject, split by outcome (correct choices, top; incorrect choices, bottom) and aligned on choice (white). Within each outcome, trials were sorted by RTs [slow (top) to fast (bottom)]. Red dots mark the time of second-tone presentation (2426 trials). (G) Mean DAergic responses of incorrect trials aligned on the three main task events (first tone, second tone, and choice; $n = 5$ mice). Shading, SEM across mice.

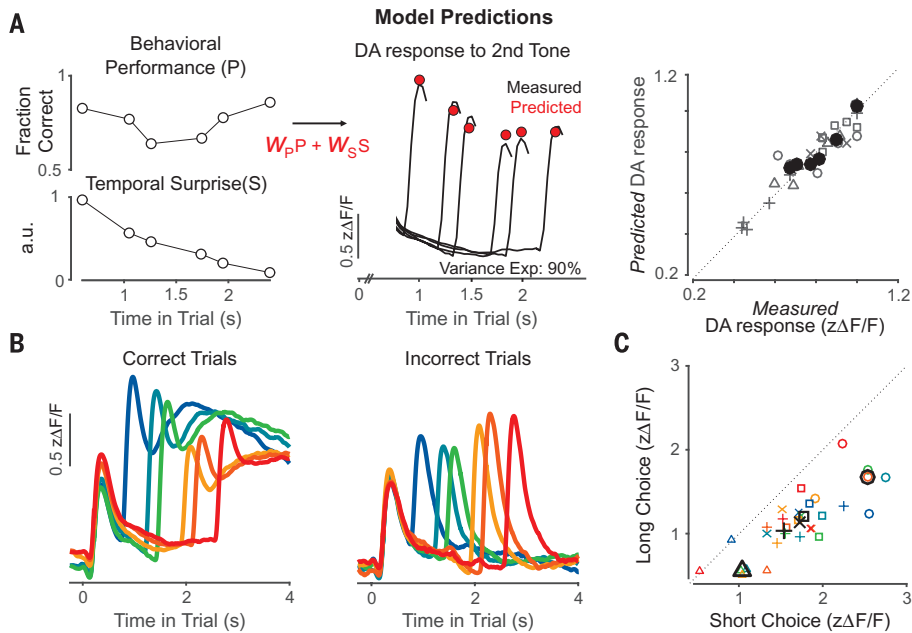
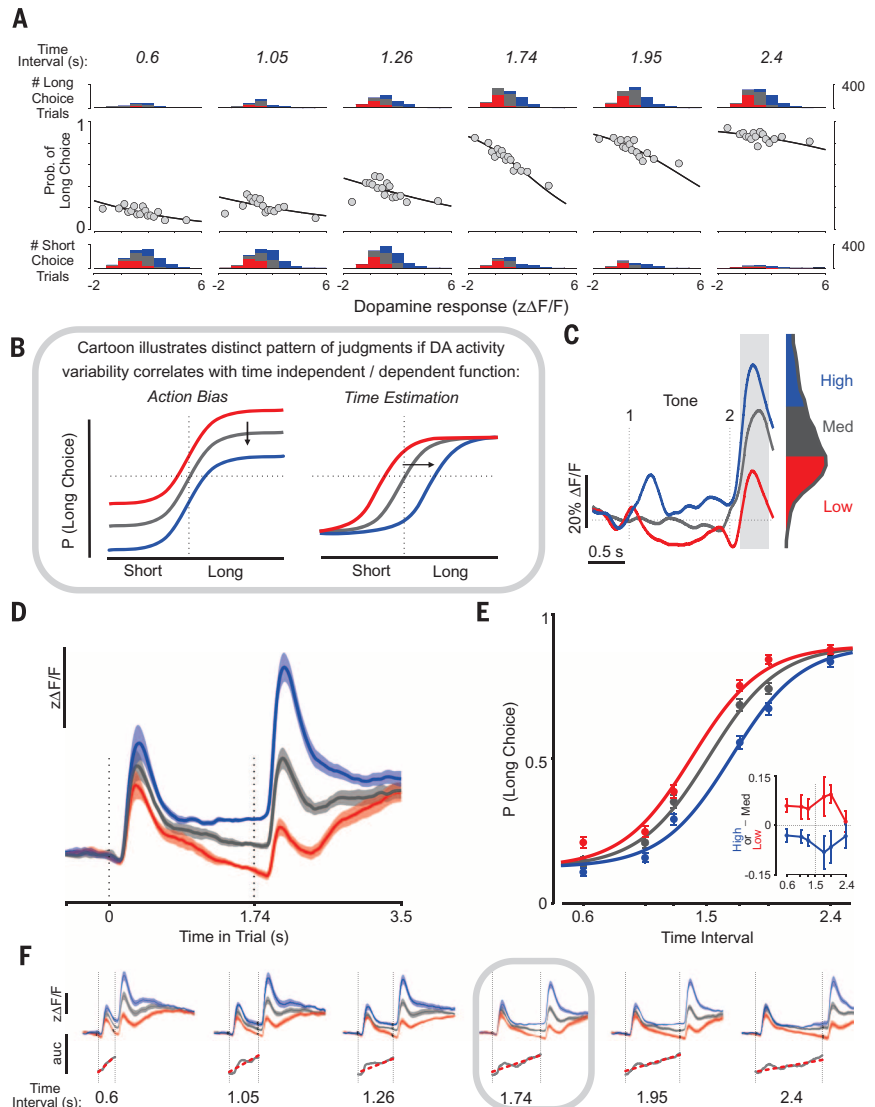


Fig. 2. DAergic responses correlate with temporal judgments and are explained by a simple model of reward prediction error (RPE). (A) Linear model (left) including RPE components: expectation of reward P (subject performance, top left) and temporal expectation S (surprise, the inverse of the subjective hazard function; bottom left). w , weight; a.u., arbitrary units. In the middle panel, measured second-tone DAergic response for six time intervals (black traces; $n = 5$ mice) are compared to predicted DA response (red dots). The graph on the right shows model predictions versus measured DAergic activity (gray symbols, individual mice; mean responses across mice, black filled circles). (B) Average measured DA response for all intervals during correct and incorrect trials. (C) Mean DA response to the second tone when an interval was judged as long versus short. Each shape represents a different mouse. Black symbols represent responses averaged across all interval stimuli.

Fig. 3. Changes in a time-dependent component of choice behavior are predicted by DAergic activity.

(A) Trial-by-trial logistic regression (black) that predicts choice from the amplitude of the second-tone DA response (gray), for each of the six time intervals (left to right). The top and bottom histograms illustrate the number of trials, as a function of DA response, in which the subject made long and short choices, respectively ($n = 8533$ trials, 5 mice). For each session and interval, DA responses are grouped into terciles—high (blue), medium (gray), and low (red)—throughout the figure. (B) Distinct patterns of temporal judgments are expected depending on the nature of the relationship between DA response and choice. (C) Three individual trials illustrating low, medium, and high second-tone DA responses (quantified as the mean response in the gray-shaded box) and grouped by tercile within the entire second-tone response distribution, depicted at right. (D) Average DA response in each tercile for the 1.74-s interval stimulus ($n = 1868$ trials, 5 mice). Shading, SEM. (E) Psychometric curves constructed using trials from each tercile of DA response. Curves are the maximum-likelihood fits of logistic functions with the lowest Bayesian information criterion scores ($n = 8533$ trials, 5 mice). Error bars, 95% confidence interval (CI). The inset shows the difference in the probability of making a long choice between medium and low or high (red or blue) DA response trials. Error bars, SEM. (F) The top row is as in (D) but for all six interval durations; data shown in (D) are outlined in gray. The bottom row shows the area under the curve (auc), distinguishing high- and low-tercile DA responses. This difference in DA response increased during the course of the trial (red linear regression; coefficient of determination r^2 ranging from 0.72 to 0.98; $P < 0.0001$).



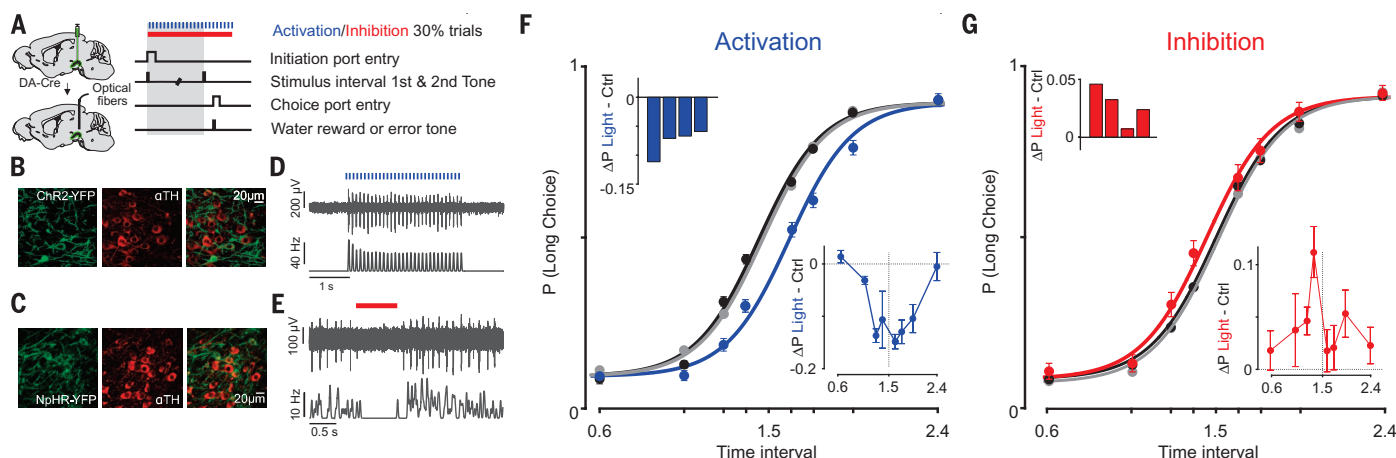


Fig. 4. Optogenetic manipulation of dopamine neurons is sufficient to change judgment of time. (A) Schematics illustrating viral strategy and subsequent fiber implantation (left) and stimulation protocol (right). (B and C) Histology confirming membrane expression of ChR2-YFP or NpHR-YFP (both green) in neurons of the SNc expressing tyrosine hydroxylase (TH, red). (D and E) Single-trial (top panels) and peri-stimulus time histogram (bottom panels) of in vivo electrophysiological measurement of two DA neurons reliably ac-

tivated and inactivated by light ($n = 53$ and 8 trials, respectively). (F) Choice behavior and psychometric curves during control trials (black), photoactivated trials (blue), and unstimulated trials immediately after photoactivation (gray) ($n = 4$ mice). Error bars, 95% CI. Insets show the mean difference in the probability of a long choice between photoactivated and control trials (top, one bar per animal; bottom, one data point per stimulus). Error bars, SEM. (G) Same as (F) but for animals whose DA neurons were inhibited ($n = 4$).

We observed DAergic responses locked to the three main task events on single trials: the first tone, the second tone, and reward delivery (or omission thereof) (Fig. 1E). Activity increased after reward delivery and decreased when the reward was omitted in the case of incorrect choices (Fig. 1F) (30). DAergic signaling has also been implicated in movement; however, DA neuron activity in this task did not reflect movement per se (Fig. 1, F and G, and fig. S3).

In this task, the second tone marks the end of the interval to be discriminated and is a sensory cue that predicts reward. The amplitude of a RPE at the time of the second tone should be modulated by two factors: the subject's expectation of reward at tone delivery and their temporal expectation of the second tone itself. First, expectation of reward varies as a function of stimulus difficulty, where the more difficult the interval to be discriminated, the lower the probability of reward (Fig. 2A). Second, because delay intervals were randomly selected from the stimulus set on each trial, occurrence of the second tone becomes less surprising with time (Fig. 2A). Indeed, animals were sensitive to changing temporal expectation, as indicated by a systematic decrease in response time (RT, the delay between second-tone delivery and choice execution) with increasing interval duration (RT for the shortest interval greater than RT for the longest interval; $P < 0.005$ in each of five mice). To test whether second-tone responses reflected a RPE that integrated information about temporal expectation and expected reward, we asked how well the pattern of average responses to all six second tones could be explained by a linear combination of temporal expectation (i.e., surprise, the inverse of the subjective hazard function; fig. S4) and performance (the probability of reward for each stimulus). On average, 90% of variance in mean

responses could be explained by a relatively equal contribution of these two factors (range, 58 to 99%; $n = 5$ mice; Fig. 2A). Reward responses were also consistent with RPE coding: Within a given choice category, they tended to be larger for intervals that animals miscategorized more often (fig. S5).

On average, DA neuron responses to the second tone contained information about elapsed time through their encoding of temporal expectation. Do these responses relate to variations in judgments of time? When animals correctly judged intervals, the response to the second tone was, on average, larger for intervals in the short category (Fig. 2B). However, on incorrect trials, the pattern was reversed: The response to the second tone was larger for intervals in the long category. Thus, DA response magnitude reflected the animals' assessment of the interval duration, not the actual interval duration. Over all intervals, the second-tone response for a given interval was significantly larger when that interval was judged as short ($P < 0.001$; Fig. 2, B and C). How do these results relate to the underlying decision and motor processes that guide choice during the task?

In principle, the trial-to-trial variations in DA neuron activity could be related to a time-dependent component of the decision, such as the speed of internal timekeeping or the location of the decision boundary in time. Alternatively, variations in DA activity might reflect a time-independent component of the behavior, such as a constant action bias. To quantitatively evaluate these two possibilities, we performed a logistic regression to assess the degree to which the magnitude of the DA neuron response to the second tone predicted animals' choices on single trials. We found that activity predicted choice to a lesser extent in the case of easy stimuli than in the case of difficult stimuli (Fig. 3A). These data sug-

gest that the DA neuron response was systematically related to the horizontal position of the psychometric curve along the time axis and not the vertical position along the choice axis (Fig. 3B). To test this, we split trials into high, medium, and low terciles of the distribution of responses to the second tone [Fig. 3, A (histograms) and C]. While the second-tone response amplitude was used to group trials, the systematic ordering of DA neuron responses emerged toward the beginning of the trial and persisted throughout an interval (Fig. 3, D and F). We next constructed psychometric curves for trials in each tercile and compared a range of models for the psychometric curve. The model that best explained the behavioral data collected from high-, medium-, and low-tercile trials consisted of three sigmoid curves that differed only in their horizontal location along the time axis (Fig. 3E). We observed a shift toward long choices when DAergic activity was low, and the opposite shift when activity was high. Specifically, as DA activity varied from the lower to the upper tercile, the psychometric threshold shifted by ~ 340 ms (i.e., $\sim 20\%$ of the 1.5-s category boundary; range, 90 to 620 ms; 6 to 42%; $n = 5$ mice). The relationship between DAergic response and psychometric shift was observed for recordings in either hemisphere (fig. S6), thus ruling out an explanation based on the laterality of short versus long choices. Instead, these results indicate that higher or lower midbrain DAergic activity is correlated with a change in a time-dependent component of the decision.

How might this correlation between DA neuron activity and the location of the psychometric curve along the time axis relate to our initial finding that temporal expectation contributed to the average second-tone response? The theory of DAergic RPE coding predicts that slower (faster)

timekeeping, by stretching (contracting) temporal surprise along the time axis, should increase (decrease) DAergic responses to the second tone (fig. S7). We observed a pattern of DAergic response to the second tone that was consistent with this (Fig. 2, B and C, and fig. S7). Furthermore, if DAergic activity reflects RPE continuously throughout a trial, differences in activity associated with slower or faster timekeeping (i.e., the separation between low- and high-activity terciles) should also grow continuously over time, and indeed, this is the case in our data (Fig. 3F and fig. S7). In contrast to the expected impact of variability in the speed of timekeeping on RPE coding, it is not apparent to us how changes in the location of the decision boundary along an animal's internal notion of time should change RPEs arising at the presentation of the second tone. The most parsimonious explanation of the data is that DA neuron activity reflects variability in the speed of internal timekeeping.

These results demonstrate a correlation between temporal judgments and DA neuron activity. However, it is unclear whether DA neuron activity simply reflects, or whether it is sufficient to cause changes in, time judgments. We mimicked the observed variability in DAergic responses by optogenetically activating or inhibiting DA neurons (Fig. 4, A to E) on a minority of randomly chosen trials. Notably, we found that increasing or decreasing DA activity resulted in a horizontal shift in the psychometric curve in the directions predicted by the photometry data, albeit more modestly in the case of photoinhibition (excitation, 140 ± 20 ms, $n = 4$ mice; inhibition, -68 ± 23 ms, $n = 4$ mice; Fig. 4, F and G, and fig. S8). These effects were transient, occurring only on stimulated trials, and thus could not be explained as resulting from learning (Fig. 4, F and G), nor were they observed in control animals (fig. S9). In addition, as was the case when sorting trials on the basis of DA response to the second tone, we observed no systematic effect on RTs, arguing against DAergic neuron activity affecting the subjects' movement toward or incentive salience of choice options during the task (fig. S10).

Here we demonstrate a direct link between signals carried by midbrain DA neurons and judgments of elapsed time. Higher or lower levels of DAergic activity not only correlated with but could directly control timekeeping. These data are in agreement with some results of pharmacological manipulations of the DAergic system during timing tasks (26), but appear at odds with some others that showed accelerated timekeeping with increased DAergic tone (23, 25). However, recent studies demonstrate that many of the pharmacological effects on timing behavior can be explained by the changes in motivation (27, 31) that accompany DAergic drug administration (32). Indeed, pharmacogenetic DAergic manipulation in our task affected motivated behavior. Variability in the effects of pharmacology on timing may result from its relatively slow time course, which allows for compensation and/or the superposition of multiple distinct behavioral effects. Our approach circumvents these issues

with genetically targeted, transient manipulations of DA neuron activity. Additionally, we focused on DA neurons in the SNc because many project to a dorsocentral region of the striatum where removal of DA input can cause a selective deficit in timing (33); however, whether DA neurons in other regions, such as the ventral tegmental area, contribute to timing variability is unknown. Last, we monitored and manipulated the activity of midbrain DA neurons, and not the levels of released DA. The relationship between tonic and phasic firing of DA neurons and DA release is not entirely clear, and it is complicated by feedback mechanisms by which released DA can affect the firing of DA neurons (34).

Although unexpected, the data presented here may explain existing behavioral data. Situations in which DAergic activity is elevated naturally, such as states of high approach motivation (35), response uncertainty (36), or cognitive engagement (37), are associated with underestimation of time (1, 2, 38). Conversely, situations that decrease DAergic activity, such as when fearful or aversive stimuli are presented (39), are associated with overestimation of time (40). These observations, together with our data, suggest that flexibility in time estimation may confer an adaptive advantage on the individual. For example, underestimating duration in better-than-expected situations may lead to longer engagement in those situations, resulting in even greater reward than if time estimation were not flexible. In other words, there may be a normative explanation for why "time flies when we are having fun" underlying our observation that DA neurons, which are so central to reward processing, exert control over time estimation.

REFERENCES AND NOTES

- P. A. Gable, B. D. Poole, *Psychol. Sci.* **23**, 879–886 (2012).
- J. T. Coull, F. Vidal, B. Nazarian, F. Macar, *Science* **303**, 1506–1508 (2004).
- M. B. Ahrens, M. Sahani, *Curr. Biol.* **21**, 200–206 (2011).
- V. Pariyadath, D. Eagleman, *PLOS ONE* **2**, e1264 (2007).
- S. Droit-Volet, W. H. Meck, *Trends Cogn. Sci.* **11**, 504–513 (2007).
- M. A. Pastor, J. Artieda, M. Jahanshahi, J. A. Obeso, *Brain* **115**, 211–225 (1992).
- M. Wittmann, D. S. Leland, J. Churan, M. P. Paulus, *Drug Alcohol Depend.* **90**, 183–192 (2007).
- V. Noreika, C. M. Falter, K. Rubia, *Neuropsychologia* **51**, 235–266 (2013).
- O. F. Wahl, D. Sieg, *Percept. Mot. Skills* **50**, 535–541 (1980).
- R. Cools, *Neuroscientist* **14**, 381–395 (2008).
- A. Lüthi, C. Lüscher, *Nat. Neurosci.* **17**, 1635–1643 (2014).
- W. Schultz, P. Dayan, P. R. Montague, *Science* **275**, 1593–1599 (1997).
- H. M. Bayer, P. W. Glimcher, *Neuron* **47**, 129–141 (2005).
- N. Eshel, J. Tian, M. Bukwich, N. Uchida, *Nat. Neurosci.* **19**, 479–486 (2016).
- E. E. Steinberg et al., *Nat. Neurosci.* **16**, 966–973 (2013).
- R. S. Sutton, A. G. Barto, *Introduction to Reinforcement Learning*, vol. 135 (MIT Press, 1998).
- P. N. Tobler, C. D. Fiorillo, W. Schultz, *Science* **307**, 1642–1645 (2005).
- J. Y. Cohen, S. Haesler, L. Vong, B. B. Lowell, N. Uchida, *Nature* **482**, 85–88 (2012).

- C. D. Fiorillo, P. N. Tobler, W. Schultz, *Science* **299**, 1898–1902 (2003).
- S. Kobayashi, W. Schultz, *J. Neurosci.* **28**, 7837–7846 (2008).
- C. D. Fiorillo, W. T. Newsome, W. Schultz, *Nat. Neurosci.* **11**, 966–973 (2008).
- B. Pasquereau, R. S. Turner, *J. Neurophysiol.* **113**, 1110–1123 (2015).
- A. V. Maricq, R. M. Church, *Psychopharmacology* **79**, 10–15 (1983).
- M. R. Drew et al., *J. Neurosci.* **27**, 7731–7739 (2007).
- C. V. Buhusi, W. H. Meck, *Behav. Neurosci.* **116**, 291–297 (2002).
- J. I. Lake, W. H. Meck, *Neuropsychologia* **51**, 284–292 (2013).
- F. Balci et al., *Brain Res.* **1325**, 89–99 (2010).
- T. S. Gouvêa et al., *eLife* **4**, e11386 (2015).
- S. P. dos Santos Matias, E. Lottem, G. P. Dugue, Z. F. Mainen, <http://biorxiv.org/content/early/2016/06/18/059758> (2016).
- W. Schultz, P. Apicella, T. Ljungberg, *J. Neurosci.* **13**, 900–913 (1993).
- A. L. Odum, L. M. Lieving, D. W. Schaa, *J. Exp. Anal. Behav.* **78**, 195–214 (2002).
- B. Panigrahi et al., *Cell* **162**, 1418–1430 (2015).
- W. H. Meck, *Brain Res.* **1109**, 93–107 (2006).
- B. S. Bunney, G. K. Aghajanian, *Naunyn Schmiedeberg's Arch. Pharmacol.* **304**, 255–261 (1978).
- E. S. Bromberg-Martin, M. Matsumoto, O. Hikosaka, *Neuron* **67**, 144–155 (2010).
- V. de Lafuente, R. Romo, *Proc. Natl. Acad. Sci. U.S.A.* **108**, 19767–19771 (2011).
- I. Fried et al., *Nat. Neurosci.* **4**, 201–206 (2001).
- R. E. Hicks, G. W. Miller, M. Kinsbourne, *Am. J. Psychol.* **89**, 719–730 (1976).
- E. B. Oleson, R. N. Gentry, V. C. Chioma, J. F. Cheer, *J. Neurosci.* **32**, 14804–14808 (2012).
- F. N. Watts, R. Sharrock, *Percept. Mot. Skills* **59**, 597–598 (1984).

ACKNOWLEDGMENTS

We thank A. Braga for assistance with behavioral training; M. Duarte for assistance with mouse colonies; G. Lopes for assistance with Bonsai; T. Monteiro, T. Gouvêa, other members of the Paton laboratory, B. Lau, E. Lottem, M. Murakami, C. Poo, A. Renart, and T. Akam for discussions and/or comments on the manuscript; Z. Mainen for support; platforms at the Champalimaud Centre for histology support and animal care; and V. Jayaraman, R. A. Kerr, D. S. Kim, L. L. Looger, and K. Svoboda from the GENIE (Genetically-Encoded Neuronal Indicator and Effector) Project at the Howard Hughes Medical Institute's Janelia Farm Research Campus for providing the AAV-GCaMP6f through the University of Pennsylvania Vector Core. Viruses for expression of NpHR3.0 and EYFP are available from the University of North Carolina Vector Core under a material transfer agreement with K. Deisseroth. Viruses for expression of GCaMP6f and TdTomato are available from the University of Pennsylvania Vector Core under a material transfer agreement with the trustees of the University of Pennsylvania on behalf of J. Wilson. The work was funded by the Bial Foundation (188/12 to J.J.P.), the Simons Foundation (Simons Collaboration on the Global Brain award 325476 to J.J.P.), Fundação para Ciência e Tecnologia (SFRH/BD/51895/2012 to S.S.), the European Molecular Biology Organization (Advanced Long Term Fellowship 983-2012 to B.V.A.), Marie Curie Actions (FP7-PEOPLE-2012-IF 326398 to B.V.A.), and the Champalimaud Foundation (internal funding to J.J.P.). Data presented in this paper can be found at www.dropbox.com/sh/ip6forddl84028j/AAAs3ry41bu4acYk1B13KDr?dl=0.

SUPPLEMENTARY MATERIALS

www.sciencemag.org/content/354/6317/1273/suppl/DC1
Materials and Methods
Figs. S1 to S10
References (41–43)

8 July 2016; accepted 4 November 2016
10.1126/science.aah5234

NEUROSCIENCE

Dopamine neurons encode performance error in singing birds

Vikram Gadagkar, Pavel A. Puzerey, Ruidong Chen, Eliza Baird-Daniel,*
Alexander R. Farhang,† Jesse H. Goldberg‡

Many behaviors are learned through trial and error by matching performance to internal goals. Yet neural mechanisms of performance evaluation remain poorly understood. We recorded basal ganglia-projecting dopamine neurons in singing zebra finches as we controlled perceived song quality with distorted auditory feedback. Dopamine activity was phasically suppressed after distorted syllables, consistent with a worse-than-predicted outcome, and was phasically activated at the precise moment of the song when a predicted distortion did not occur, consistent with a better-than-predicted outcome. Error response magnitude depended on distortion probability. Thus, dopaminergic error signals can evaluate behaviors that are not learned for reward and are instead learned by matching performance outcomes to internal goals.

When practicing piano, how do you know if you struck the right or wrong note? The problem is that there is nothing intrinsically “good” or “bad” about the sound of A-sharp. It entirely depends if that’s the note you wanted to strike at that time step of the song. Performance evaluation requires sensory feedback to be compared with internal benchmarks that change from moment to moment in a sequence. Performance errors during musical performance (1, 2) and speech production (3) are associated with a frontal error-related negativity in the electroencephalogram that may relate to activity in ventral tegmental area (VTA) dopamine neurons (4). Yet, although dopamine neurons are known to encode reward prediction error in tasks where animals seek primary rewards such as food or juice (5–7), it is not known if dopamine activity also encodes error in tasks that are not learned for primary reward and are instead learned by matching sensory feedback to internal performance benchmarks (8, 9).

Songbirds use auditory feedback to learn to sing and have a dopaminergic projection from VTA to Area X, a nucleus required for song learning (10–13). It is hypothesized that a singing bird evaluates its own song to compute an auditory-error-based reinforcement signal that guides learning—i.e., a neural signal that “tells” vocal motor circuits if the recent vocalization was “good” and should be reinforced or “bad” and be eliminated (14, 15) (Fig. 1A). The neural correlates of song evaluation remain unknown (16–18), leading to alternative models of learning that do not require online error signals (19).

To test if dopamine activity encodes performance error, we recorded songbird VTA neurons

while controlling perceived song quality with distorted auditory feedback (DAF) (18, 20–24) (Fig. 1, B to F). Beginning days before recordings, a specific song syllable was either distorted with DAF or, on randomly interleaved trials, left undistorted altogether (distortion rate $44 \pm 8\%$, $n = 26$ birds; Fig. 1, E and F). DAF was a 50-ms snippet of sound with the same amplitude and spectral content as normal zebra finch song (see supplementary text). The snippet was either a segment of one of the bird’s own syllables displaced in time (displaced-syllable DAF, $n = 10$ birds; Fig. 1E) or a synthesized sound designed to mimic broadband portions of the bird’s own song (broadband DAF, $n = 16$ birds) (20, 24). Operant broadband DAF drives dopamine and Area X-dependent reinforcement of undistorted syllable variants (13, 23). Displaced-syllable DAF, when operantly delivered contingent on the pitch of a harmonic target syllable, resulted in similar learning (Fig. 1, G and H) (20).

To test for online error responses, we compared the activity between randomly interleaved renditions of distorted and undistorted songs. We computed the z -scored difference between target onset-aligned distorted and undistorted rate histograms (Fig. 2, A to D; target onset defined as the median DAF onset time relative to distorted syllable onset, $n = 125$ neurons in 26 birds) (24). We defined the error response as the average z -scored difference in firing in a 50- to 125-ms interval following target onset (24). We plotted the distribution of error responses across the 125 VTA neurons and observed two distinct groups: one that did not exhibit significant error responses ($n = 108$ neurons, error response 0.1 ± 0.9) and a group of error-responding neurons ($n = 17$ neurons, error response 3.3 ± 0.5 ; Fig. 2, E and F) that formed a distinct cluster ($P < 0.001$, bootstrap) (24). These two groups, defined as VTAerror ($n = 17$) and VTAother ($n = 108$), were spatially intermingled (fig. S1).

All VTAerror neurons were phasically suppressed by DAF during singing (Fig. 2, A to D, G; $P < 0.05$ in 17 out of 17 VTAerror neurons, bootstrap).

Suppressions followed DAF onset with a latency of 58 ± 13 ms, lasted 86 ± 35 ms, and resulted on average in a 75% reduction in firing rate (range: 45 to 100%) (24, 25). DAF-induced suppressions during singing were highly reliable, occurring on an average of 94% of distorted trials (range: 82 to 100%). VTAerror neurons also exhibited phasic activations following the precise time-step of undistorted songs where DAF would have occurred but did not occur (Fig. 2, A to D, G, and I; $P < 0.05$ in the same 17 neurons that exhibited suppressions on distorted trials, bootstrap). Phasic activations mirrored the phasic suppressions: They followed target onsets with a latency of 51 ± 20 ms, lasted 62 ± 27 ms, and resulted on average in a 77% (range: 42 to 214%) increase in firing rate (24) (Fig. 2H).

These precisely timed phasic activations suggest that undistorted target syllables are signaled as better than predicted, as if they are evaluated against an estimate of syllable quality that is diminished by a memory of errors (i.e., a flexible performance benchmark; see supplementary text). To test if error signals are scaled by error history, we trained 10 birds in a two-target paradigm in which one syllable was distorted with a high probability (target-1, $49 \pm 4\%$) and a second syllable with low probability (target-2, $20 \pm 4\%$) (Fig. 3, A to C) (24). The magnitude and reliability of phasic suppressions did not depend on error probability (percentage of suppression: target-1: 59%, range 45 to 77%; target-2: 63%, range 20 to 100%; reliability: target-1: 90%, range 82 to 100%; target-2: 86%, range 71 to 100%, $P > 0.4$, rank sum tests; Fig. 3D), consistent with weak scaling of dopaminergic negative reward prediction error responses (6, 7). In contrast, phasic activations were significantly larger following (the more surprising) undistorted renditions of the high-probability target (increase in firing rate, target-1: 67%, range 42 to 159%; target-2: 22%, range -3 to 48%, $P < 0.001$, rank sum test; Fig. 3E). Error responses to target-2 did not depend on whether or not the preceding target-1 was distorted and vice versa, indicating that song time steps are independently evaluated against temporally aligned performance benchmarks ($P > 0.05$, rank sum tests and fig. S2).

More than 95% of Area X-projecting VTA neurons are dopaminergic (11). Fourteen of 125 VTA neurons were antidromically identified as projecting to Area X (Fig. 1, B to D), and 13 out of 14 VTAX neurons encoded performance error (Fig. 2, E and F). Firing patterns of VTAerror neurons were like those of mammalian dopamine neurons (see supplementary text and figs. S3 to S5).

Dopamine activity correlates with movement (26, 27). We quantified movement with microdrive-mounted accelerometers (fig. S6 and movie S1). The activity of many VTA neurons was modulated by movement, which was in turn correlated with singing. But movement patterns during singing were not affected by DAF, and error responses were not affected by movement ($n = 26$ out of 26 birds, $P > 0.05$, bootstrapped d' analysis, see supplementary text, tables S1 and S2, and figs. S6 to S10).

Department of Neurobiology and Behavior, Cornell University, Ithaca, NY 14853, USA.

*Present address: Department of Neurological Surgery, Weill Cornell Medical College, New York, NY 10065, USA. †Present address: Department of Anatomy, University of California, San Francisco, CA 94143, USA. ‡Corresponding author. Email: jessehgoldberg@gmail.com

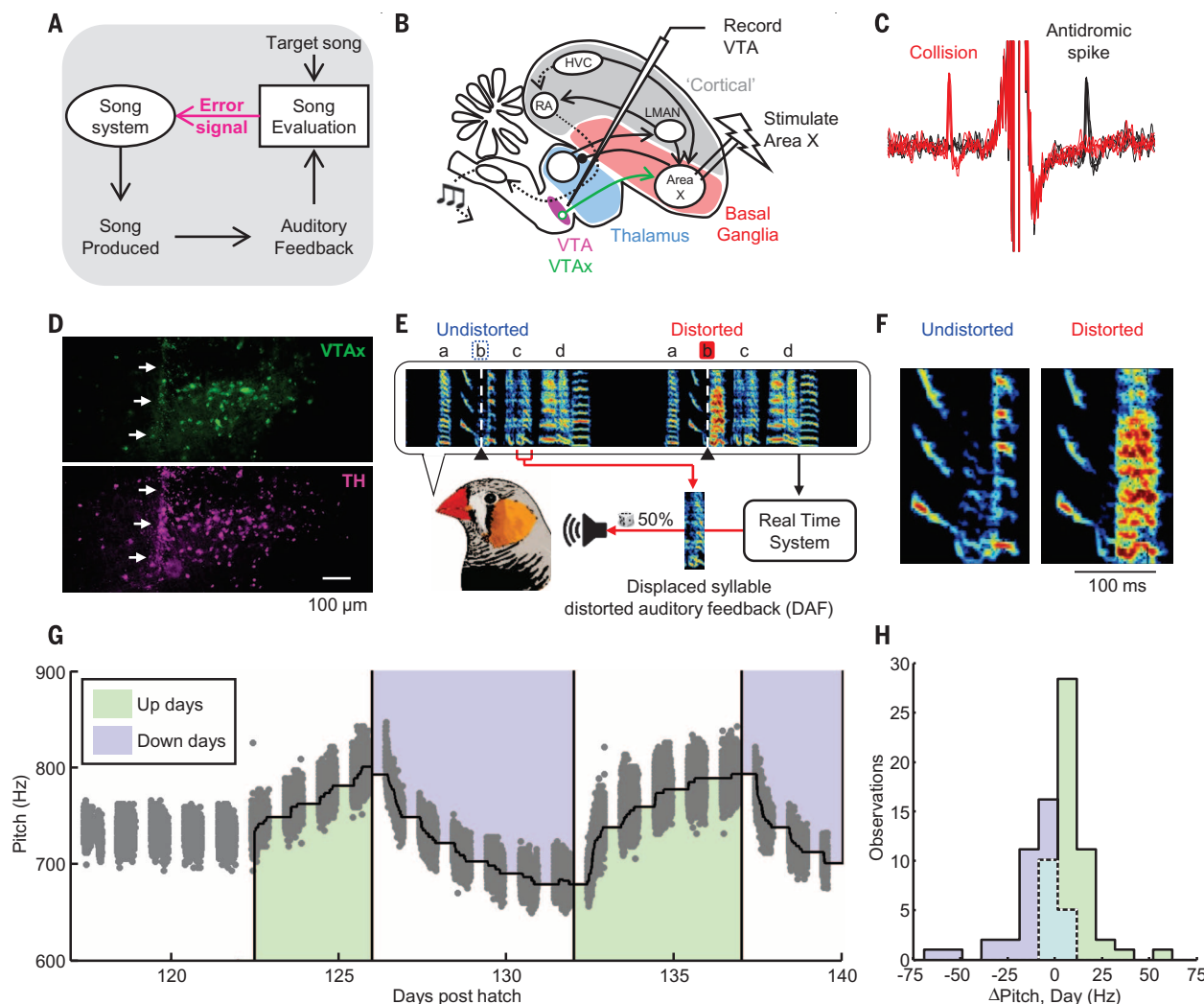


Fig. 1. Experimental test of performance error signals in birdsong. (A) Evaluation of auditory feedback during singing is hypothesized to result in “error” signals that reach the song system. (B) Strategy for antidromic identification of VTAx dopamine neurons. (C) Antidromic spikes (black) and spike collisions (red) of a VTAx neuron. (D) VTAx neurons labeled by injection of retrograde tracer into Area X (green, top) and colabeled dopamine neurons stained with antibody against tyrosine hydroxylase (TH) (purple, bottom). White arrows point to the visible path of the electrode that recorded the VTAx unit shown in Fig. 2A (scale bar, 100 μ m; anterior-right, dorsal-top). (E) Example of displaced-

syllable DAF. A snippet of syllable “c” was played back during production of the target syllable “b” (target time, black triangles and white dashed lines). Randomly interleaved target renditions were left undistorted (undistorted trials, blue dashed line). (F) Expanded view of the target syllable. (G) Pitch-contingent displaced-syllable DAF drives learning. Gray dots denote mean pitch of 49,716 target syllable renditions sung over 23 days for one bird. Shading demarcates distorted renditions; green, low-pitch variants distorted (up days); blue, high-pitch variants distorted (down days). (H) Histogram of pitch changes learned during each day ($n = 4$ birds).

VTAerror neurons might encode not performance error but simply the presence or absence of DAF as if it were an aversive stimulus (see supplementary text). An aversive response should persist in birds during nonsinging periods, whereas performance error should be restricted to singing. During nonsinging periods, VTAerror neurons did not differentially respond to playback of distorted and undistorted renditions of the bird’s own song (normalized firing rate, distorted: 1.0 ± 0.2 ; undistorted: 1.1 ± 0.1 ; $P > 0.3$, unpaired t test) (Fig. 4) and did not exhibit pauses in response to DAF (fig. S11). Confinement of VTAerror responses to singing is consistent with performance error.

Performance error signals during singing are similar to prediction error signals during reward seeking (5). Suppression of VTAerror activity after distorted syllables resembles the dopamine response to worse-than-predicted reward outcomes. Activation of VTAerror neurons after undistorted syllables resembles the dopamine response to better-than-predicted reward outcomes. The scaling of positive VTAerror responses according to error history suggests that song is evaluated against flexible performance benchmarks. Positive reward prediction error signals are also scaled by reward prediction (6, 7). Finally, performance and reward prediction error signals could underlie similar learning mecha-

nisms. Dopamine-modulated corticostriatal plasticity links external stimuli to reward-maximizing responses (14). Dopamine-modulated corticostriatal plasticity also exists inside Area X (28) and could similarly link each time step in the song to the specific vocalization that produces a favorable outcome when produced at that time step (supplementary text and fig. S12). Such a mechanism would explain the reinforcement of undistorted syllable variants in operant DAF paradigms (Fig. 1, G and H) (18, 20, 21, 23) and could contribute to natural song learning (14).

Yet, unlike reward prediction error, performance error during singing is not derived from sensory feedback of intrinsic reward or reward-predicting

value. The absence of error responses in birds passively hearing distorted or undistorted syllables suggests that there is nothing intrinsically

“good” or “bad” about these sounds according to the performance-monitoring system. Performance error might instead derive from evaluation of

auditory feedback against internal performance benchmarks that require, at each time step of the song sequence, information about the desired

Fig. 2. VTA neurons encode performance error during singing.

(A) Spectrogram, voltage trace, and the instantaneous firing rate of a VTAx neuron (DAF, red shading; undistorted targets, blue lines).

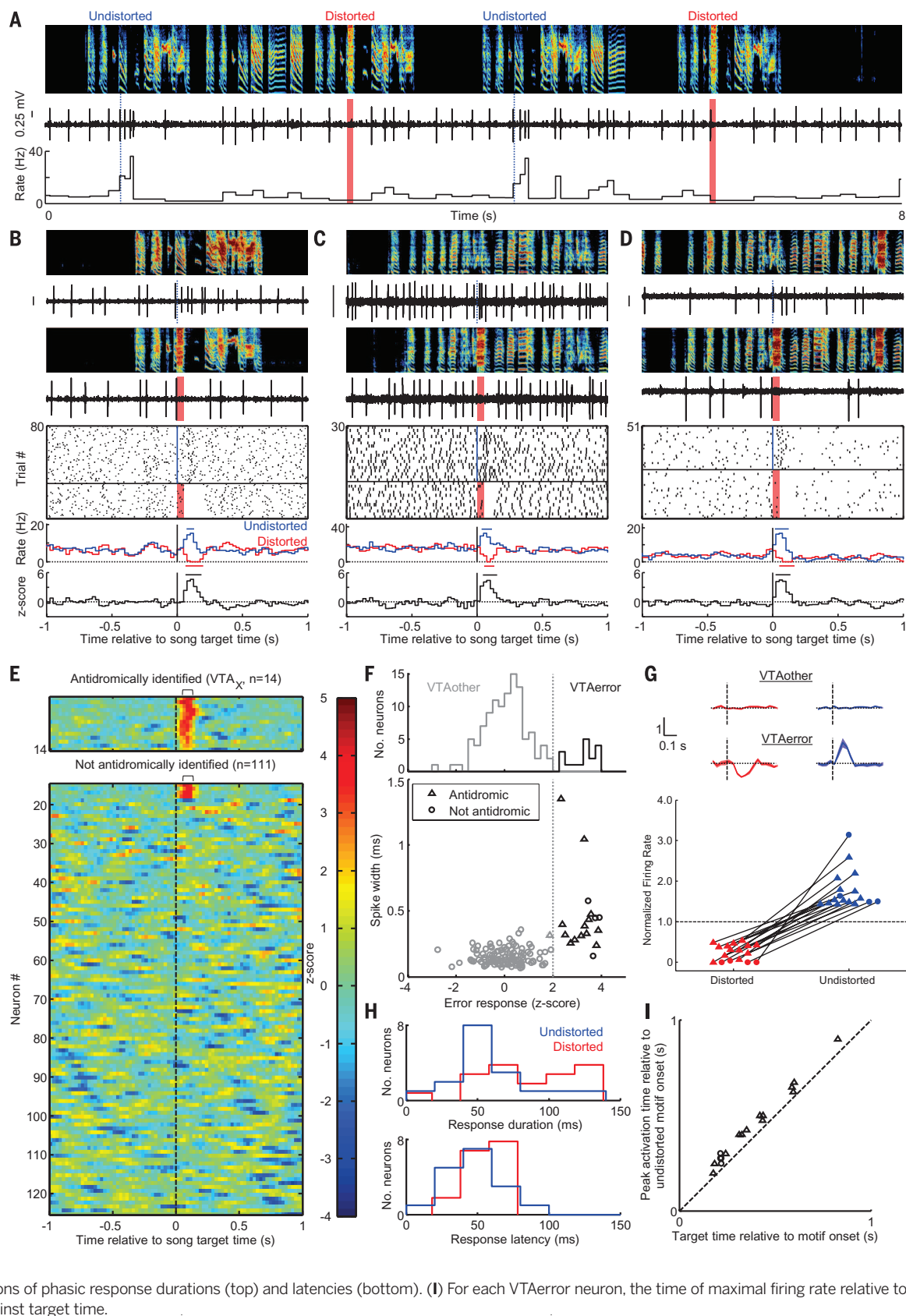
(B) Top to bottom: spectrograms, spiking activity during undistorted and distorted trials, corresponding spike raster plots and rate histograms, and z-scored difference between undistorted and distorted rate histograms (plots aligned to target onset). Horizontal bars in histograms indicate significant deviations from baseline ($P < 0.05$, z test) (24).

(C and D) Two additional VTAerror neurons as in (B). (E) Each row plots the z-scored difference between undistorted and distorted target-aligned rate histograms. VTAx neurons (top, $n = 14$) and non-antidromic neurons (bottom, $n = 111$) are independently sorted by maximal z score.

(F) Top, distribution of error responses (24). Bottom, spike width versus error response (triangles: antidromic; circles: nonantidromic neurons).

(G) Normalized response to distorted and undistorted targets (mean \pm SEM) for VTAother (top) and VTAerror neurons (middle). Bottom, scatterplot of normalized rate in the 50 to 125 ms following distorted and undistorted trials (solid fills indicate $P < 0.05$, bootstrap).

(H) Distributions of phasic response durations (top) and latencies (bottom). (I) For each VTAerror neuron, the time of maximal firing rate relative to motif onset is plotted against target time.



outcome, the actual outcome, and also the predicted probability of achieving the desired outcome. It remains unknown how upstream

circuits construct the VTAerror signal. Multiple auditory cortical areas, including one that projects to VTA, respond to DAF specifically during

singing (22, 25), providing a candidate pathway for auditory mismatch signals to reach VTA. A newly identified Area X-basal forebrain-VTA pathway (29) might additionally provide a temporally precise and syllable-specific memory of errors required to compute a benchmark against which mismatch error signals are scaled.

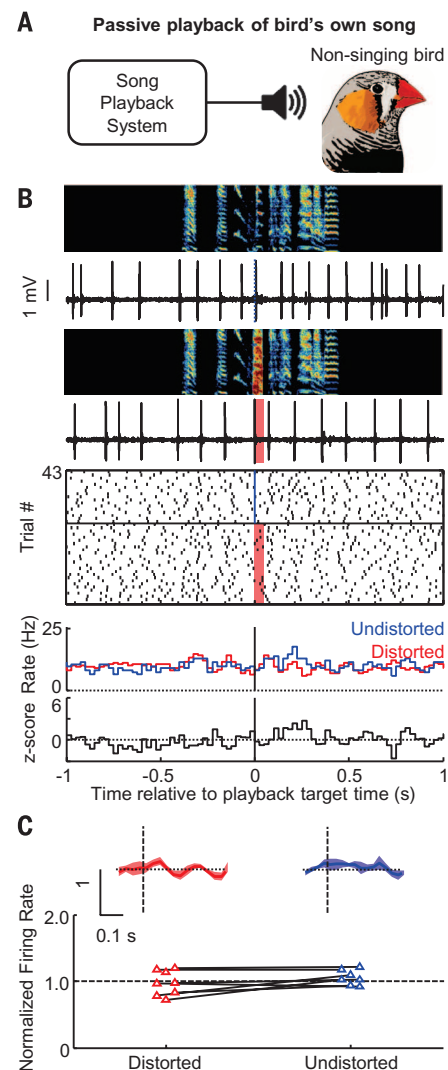


Fig. 4. Response of VTAerror neurons to bird-song during nonsinging. (A) Distorted and undistorted renditions of the bird's own song was played back during nonsinging periods. (B) Top to bottom: spectrograms, spiking activity of the VTAx neuron shown in Fig. 3 during playback of undistorted and distorted songs, corresponding spike raster plots and rate histograms, and z-scored difference between undistorted and distorted rate histograms (all plots aligned to target onset). (C) Normalized responses to distorted and undistorted targets (mean \pm SEM) for VTAerror neurons during passive playback (top). Bottom, scatterplot of normalized rate in the 50 to 125 ms following target time (empty fills indicate no significant response, $P > 0.05$, bootstrap) (24).

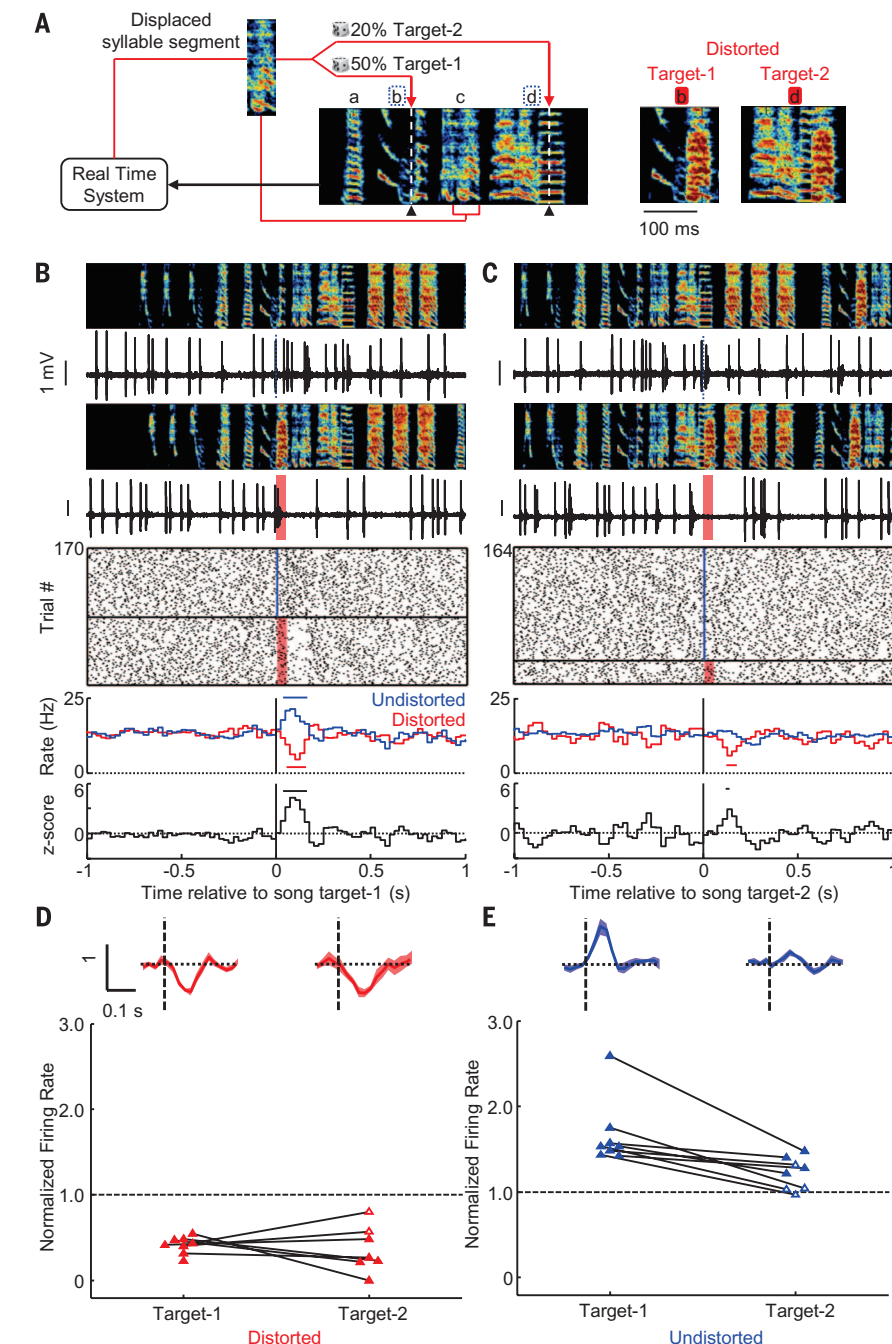


Fig. 3. VTAerror responses depend on error probability. (A) Displaced-syllable DAF scheme with two targets per motif (syllable b: target-1, distortion rate 50%; syllable d: target-2, distortion rate 20%; target times marked with dashed white line and black triangle). The distorted versions of the two target syllables are shown at right (color scheme as in Fig. 1E). (B) Target-1 and (C) target-2 error responses for the same neuron. Top to bottom: spectrograms, spiking activity during undistorted and distorted trials, corresponding spike raster plots and rate histograms, and z-scored difference between undistorted and distorted rate histograms (all plots aligned to target onset). Horizontal bars in histograms indicate significant deviations from baseline ($P < 0.05$, z test) (24). (D) Top, normalized responses to distorted targets (mean \pm SEM) for VTAerror neurons. Bottom, scatterplot of normalized rate in the 50 to 125 ms following target time (solid fills indicate $P < 0.05$, bootstrap). (E) Same as (D) but for undistorted targets.

REFERENCES AND NOTES

1. C. Maidhof, N. Vavatzanidis, W. Prinz, M. Rieger, S. Koelsch, *J. Cogn. Neurosci.* **22**, 2401–2413 (2010).
2. K. Katahira, D. Abia, S. Masuda, K. Okanoya, *Neurosci. Res.* **61**, 120–128 (2008).
3. K. M. Trewartha, N. A. Phillips, *Front. Hum. Neurosci.* **7**, 763 (2013).
4. C. B. Holroyd, M. G. Coles, *Psychol. Rev.* **109**, 679–709 (2002).
5. W. Schultz, P. Dayan, P. R. Montague, *Science* **275**, 1593–1599 (1997).
6. C. D. Fiorillo, P. N. Tobler, W. Schultz, *Science* **299**, 1898–1902 (2003).
7. H. M. Bayer, P. W. Glimcher, *Neuron* **47**, 129–141 (2005).
8. D. M. Wolpert, J. Diedrichsen, J. R. Flanagan, *Nat. Rev. Neurosci.* **12**, 739–751 (2011).
9. S. Singh, R. Lewis, A. Barto, J. Sorg, *IEEE Trans. Auton. Ment. Dev.* **2**, 70–82 (2010).
10. M. Konishi, *Z. Tierpsychol.* **22**, 770–783 (1965).
11. A. L. Person, S. D. Gale, M. A. Farries, D. J. Perkel, *J. Comp. Neurol.* **508**, 840–866 (2008).
12. C. Scharff, F. Nottebohm, *J. Neurosci.* **11**, 2896–2913 (1991).
13. L. A. Hoffmann, V. Saravanan, A. N. Wood, L. He, S. J. Sober, *J. Neurosci.* **36**, 2176–2189 (2016).
14. M. S. Fee, J. H. Goldberg, *Neuroscience* **198**, 152–170 (2011).
15. K. Doya, T. Sejnowski, *Adv. Neural Inf. Process. Syst.* **7**, 101–108 (1995).
16. A. Leonardo, *Proc. Natl. Acad. Sci. U.S.A.* **101**, 16935–16940 (2004).
17. A. A. Kozhevnikov, M. S. Fee, *J. Neurophysiol.* **97**, 4271–4283 (2007).
18. K. Hamaguchi, K. A. Tschida, I. Yoon, B. R. Donald, R. Mooney, *eLife* **3**, e01833 (2014).
19. R. Hahnloser, S. Ganguli, in *Principles of Neural Coding*, S. Panzeri, P. Quiroga, Eds. (CRC Taylor and Francis, Boca Raton, FL, 2013), pp. 547–564.
20. A. S. Andalman, M. S. Fee, *Proc. Natl. Acad. Sci. U.S.A.* **106**, 12518–12523 (2009).
21. E. C. Turner, M. S. Brainard, *Nature* **450**, 1240–1244 (2007).
22. G. B. Keller, R. H. Hahnloser, *Nature* **457**, 187–190 (2009).
23. F. Ali *et al.*, *Neuron* **80**, 494–506 (2013).
24. Materials and methods are available as supplementary materials on Science Online.
25. Y. Mandelblat-Cerf, L. Las, N. Denisenko, M. S. Fee, *eLife* **3**, e02152 (2014).

ACKNOWLEDGMENTS

We thank J. Fetcho, M. Warden, M. Long, A. Andalman, and D. Aronov for comments on the manuscript; J. Cohen for mouse VTA recording data; T. Bollu and D. Murdoch for technical support; J. Wu and K. Maher for histology; and A. Treska for art. Funding support was provided to J.H.G. by NIH (grant ROINS094667), Pew Charitable Trusts, and Klingenstein Neuroscience Foundation and to V.G. by Simons Foundation. V.G. and J.H.G. designed the research, analyzed the data, and wrote the paper. V.G., P.A.P., R.C., A.R.F., E.B.-D., and J.H.G. performed experiments. The authors declare no competing financial interests. Data can be accessed at www.nbb.cornell.edu/goldberg/.

SUPPLEMENTARY MATERIALS

www.sciencemag.org/content/354/6317/1278/suppl/DC1
Materials and Methods
Supplementary Text
Figs. S1 to S12
Tables S1 to S2
Movie S1
References (30–68)

1 August 2016; accepted 24 October 2016
10.1126/science.aah6837

NEUROSCIENCE

Mind the gap: Neural coding of species identity in birdsong prosody

Makoto Araki,¹ M. M. Bandi,² Yoko Yazaki-Sugiyama^{1*}

Juvenile songbirds learn vocal communication from adult tutors of the same species but not from adults of other species. How species-specific learning emerges from the basic features of song prosody remains unknown. In the zebra finch auditory cortex, we discovered a class of neurons that register the silent temporal gaps between song syllables and are distinct from neurons encoding syllable morphology. Behavioral learning and neuronal coding of temporal gap structure resisted song tutoring from other species: Zebra finches fostered by Bengalese finch parents learned Bengalese finch song morphology transposed onto zebra finch temporal gaps. During the vocal learning period, temporal gap neurons fired selectively to zebra finch song. The innate temporal coding of intersyllable silent gaps suggests a neuronal barcode for conspecific vocal learning and social communication in acoustically diverse environments.

There are more than 5000 species of songbirds, each with unique species-selective acoustic features in their songs (1–3) after accounting for individual variance. The vocal characteristics of birdsongs are learned from early auditory experience with adult tutors within species-specific constraints (4). Juvenile birds learning to sing must simultaneously balance competing criteria: keeping their individual song distinct from conspecifics (5) while avoiding divergence beyond their own species' song identity (6, 7). Both experience-dependent and innate mechanisms contribute to species-selective song learning (8). The observed behavioral discrimination of conspecific and heterospecific vocalizations suggests innate contributions to song learning (9–12). In the zebra finch, one song unique to each individual is learned during development. The songs comprise stereotyped repeats of a few syllables, called “song motifs,” in which syllables are separated by silent gaps. The brain circuits that are necessary for song learning and production are well identified (13). However, the brain mechanisms for the detection of conspecific vocalization, while also accommodating individual differences in song learning, remain unknown.

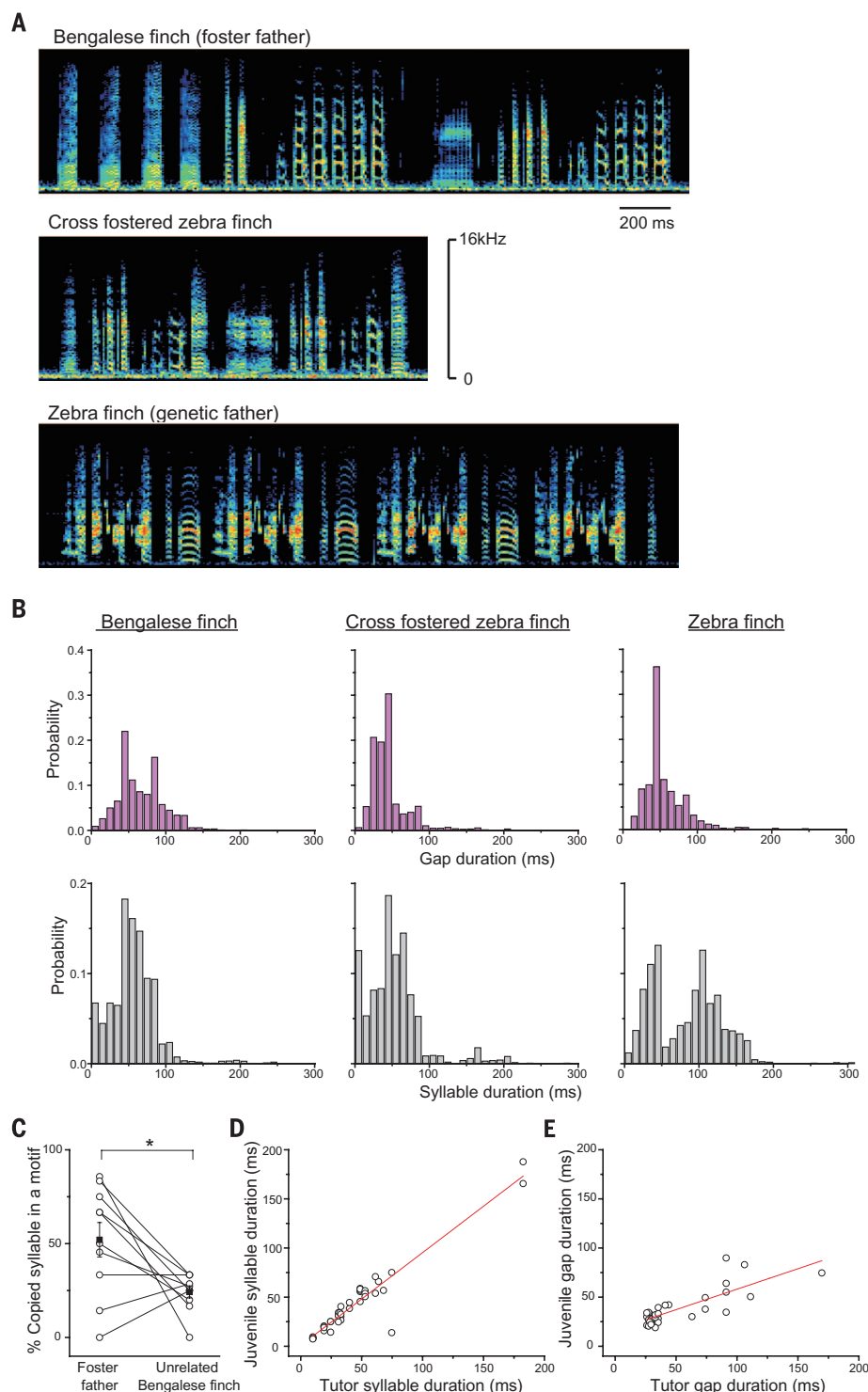
We performed a cross-fostering experiment in which zebra finches were raised by Bengalese finch foster parents (X-fostered zebra finches) (14). Zebra finch song syllables, excluding introductory notes, showed bimodal distributions in length and were separated by silent gaps with durations of 20 to 100 ms (Fig. 1B and fig. S1A). Gaps longer than 200 ms are recognized as gaps between song bouts (15). In contrast, Bengalese finch songs included a larger number of syllables sung in variable sequence, and the distribution of syllable durations was shorter than in zebra finch songs (Fig. 1, A and B, and fig. S1, B and C). The probability distributions of the silent gap

durations in Bengalese and zebra finch songs overlapped; however, Bengalese finch songs included a larger number of longer gaps (Fig. 1B and fig. S1C). X-fostered zebra finch juveniles learned Bengalese finch syllable morphologies (Fig. 1C; rate of copied syllables from tutor song was greater than rate of random matching with unrelated Bengalese finch songs; $P < 0.029$, paired t test) as well as syllable durations (Fig. 1D). The durations of tutor and copied juvenile syllables showed a linear correlation (slope = 0.94, $r^2 = 0.907$) and no significant difference ($P > 0.5$, paired t test, 44 ± 6 ms versus 43 ± 6 ms, mean \pm SD). Even the difference in syllable duration histograms (Fig. 1B, bottom), measured by Kullback-Leibler distance, between X-fostered and normal zebra finch songs was similar to that between Bengalese finch and zebra finch songs, whereas the difference between X-fostered zebra finch and Bengalese finch songs was much smaller than that between zebra finch and Bengalese finch songs (fig. S1C; note that the Kullback-Leibler distance is order-sensitive). Furthermore, X-fostered zebra finch songs included more syllables than normal zebra finch songs (fig. S1B) but consisted of a clear motif, not a variable sequence.

Despite learning the syllable morphology of Bengalese finches, X-fostered zebra finches did not learn their temporal silent gaps. When they copied syllable chunks from Bengalese finch tutors, they truncated gaps that were longer than normal zebra finch gaps (>50 ms) but copied gaps that were similar to those of normal zebra finches (<50 ms) (Fig. 1E). Tutor gaps were significantly longer than copied juvenile gaps ($P = 0.002$, paired t test, 51 ± 6 ms versus 38 ± 3 ms, mean \pm SD). The slope of the correlation between tutor and copied juvenile gap duration was shallower than for syllable duration (Fig. 1E; slope = 0.42, $r^2 = 0.640$). The distribution of gap duration in X-fostered zebra finch songs also remained closer to that of zebra finch songs, which typically do not involve gaps greater than 80 ms (Fig. 1B and fig. S1C). The difference in the histograms of gap duration probability between X-fostered and normal zebra finch songs was much

¹Neuronal Mechanism of Critical Period Unit, Okinawa Institute of Science and Technology (OIST) Graduate University, Okinawa, Japan. ²Collective Interactions Unit, OIST Graduate University, Okinawa, Japan.

*Corresponding author. Email: yazaki-sugiyama@oist.jp



smaller than that between Bengalese finch and zebra finch songs, and the difference between X-fostered zebra finch and Bengalese finch songs was larger than that between zebra finch and Bengalese finch songs (fig. S1C). Despite no conspecific auditory exposure, X-fostered zebra finches developed a normal zebra finch gap range while learning Bengalese finch syllable morphology. Innate gap duration coding was also observed in

adult zebra finches reared without adult tutor song experience (isolated zebra finches), as they developed normal silent gap duration ranges while syllable durations were rather abnormal (fig. S1, C and D).

In the zebra finch ascending auditory pathway, neurons in field L (L3) preferentially respond to natural sounds, such as birdsong, and are unresponsive to artificial sounds, such as white noise

Fig. 1. Temporal gap coding is innate, whereas syllable morphology coding is experience-dependent. Juvenile zebra finches fostered by Bengalese finch learned Bengalese finch syllable morphology but not temporal gap timing. **(A)** Sound spectrographs of a Bengalese finch, a cross-fostered zebra finch (raised by Bengalese finches), and a zebra finch song (genetic father of the same cross-fostered zebra finch). **(B)** Normalized probability of gap and syllable durations in songs from 10 each of zebra finches in the colony, cross-fostered zebra finches, and Bengalese finches in the colony. **(C)** Percentage of copied syllables from foster father songs and randomly matched syllable with unrelated zebra finch songs in each cross-fostered zebra finch song, and their average ($n = 10$ birds). $*P < 0.05$. **(D)** Duration of copied syllables in cross-fostered zebra finches plotted against syllable durations of Bengalese finch foster fathers (linear regression: $y = 0.94x + 0.00084$). **(E)** Duration of gaps separating two adjacently copied syllables in cross-fostered zebra finch songs plotted against the original Bengalese finch foster father gap durations (linear regression: $y = 0.42x + 0.016$).

(16). In single-unit extracellular recordings, we identified two neuronal subtypes in zebra finch field L3: lower-firing neurons (LFs; <1.5 Hz) and higher-firing neurons (HFs) (Fig. 2B). Both LFs and HFs responded to the playback of zebra finch songs [conspecific song (CON)] but not to continuous white noise (WHN) (16). Both neuron types were also tested with (i) artificial songs in which syllables were replaced with white noise [white noise song (WNS)] to see whether their response was related to the temporal patterns of zebra finch songs and not to the acoustic features, and (ii) another artificial song in which the syllabic frequency and amplitude properties were retained but their phases were scrambled [phase-scrambled song (PSS)]. LFs responded strongly to PSS but not to WNS (Fig. 2, A to C). Given that response strengths for PSS did not vary by altering the time window over which phases were scrambled (fig. S2, A and B), LFs appeared to encode syllable-wide acoustic morphology. In contrast, HFs responded to WNS as well as PSS, suggesting the encoding of the temporal alignment of syllables in zebra finch song (Fig. 2, A to C).

We then investigated whether HFs encode temporal silent gaps of zebra finch song by recording their responses to trains of the same syllable or short epochs of white noise. Train stimulations were made with each syllable of the CON to which HFs responded most robustly within the test stimulation (fig. S3 and supplementary materials). HFs responded well to varieties of syllable trains, depending on the duration of silent gaps (Fig. 3B) and syllable durations (Fig. 3C) in the train. HFs responded to syllable trains when each syllable was separated by silent gaps of 20 to 100 ms in the trains. However, they

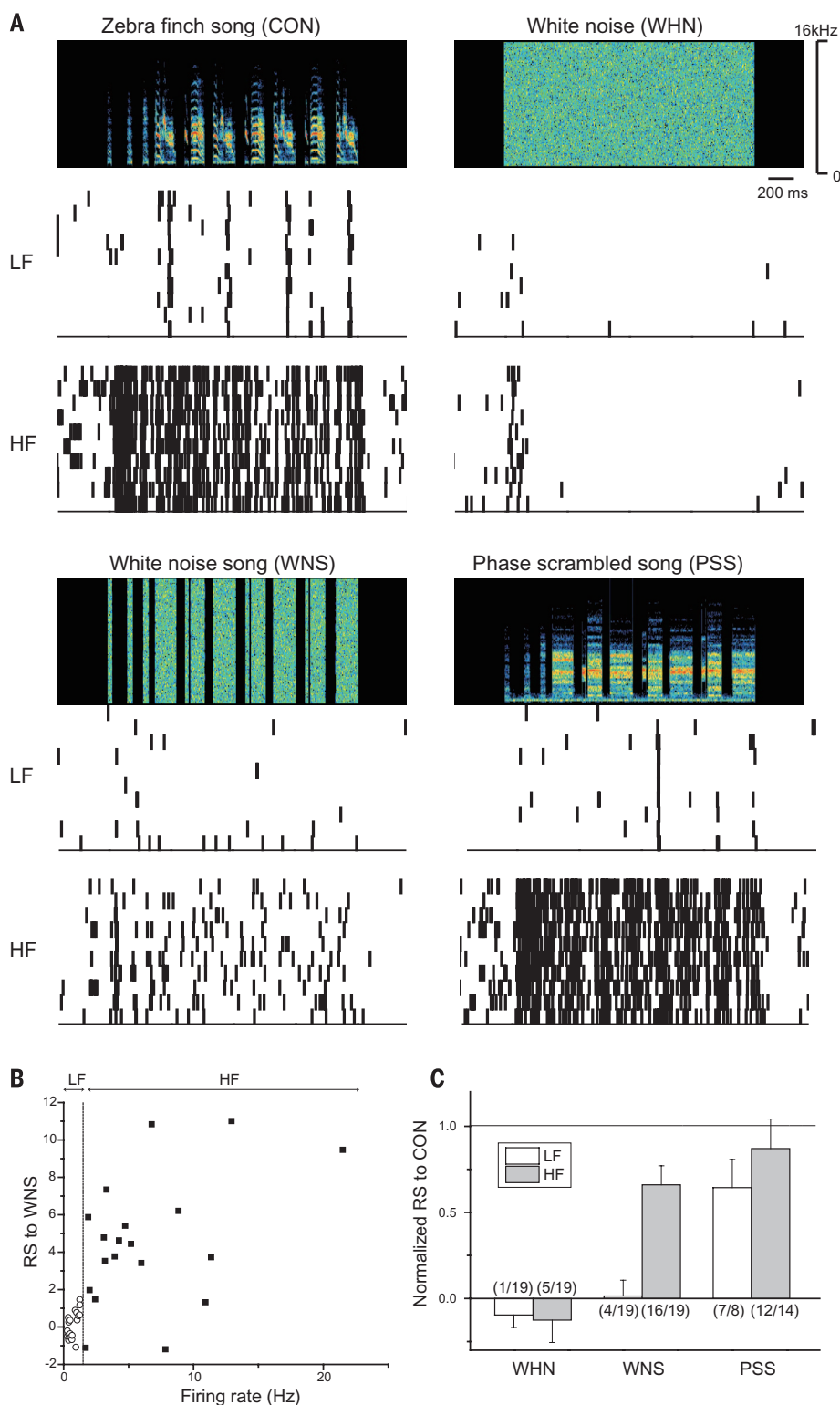


Fig. 2. Two neuron types dissociate the encoding of temporal gaps and morphology of acoustic elements. (A) Sound spectrographs of song stimulation (top) and raster plots of lower-firing (LF; middle) and higher-firing (HF; bottom) neuronal responses to the songs, shown for zebra finch song (CON), continuous white noise (WHN), artificial song with white-noise syllables (WNS), and artificial song with phase-scrambled syllables (PSS). (B) Response strength (RS) to WNS for each neuronal unit as a function of firing rate. LFs and HFs exhibit distinctive response strength to WNS. (C) Response strength to WHN, WNS, and PSS, normalized by CON in LF and HF neurons (mean ± SE). Numbers in parentheses indicate the number of units that showed significant response out of total unit included.

did not respond to trains with gaps of only 5 ms, nor to trains with longer gaps (200 and 400 ms) (Fig. 3B). The range of gap durations to which HFs responded (20 to 100 ms) matched well with that in natural zebra finch songs (Fig. 1B). Moreover, HFs did not respond to syllable trains if the durations of each syllable were too short (27 ms) or too long (>1 s). They responded equally well to trains of syllables with durations in the range of 36 to 167 ms (Fig. 3C), which were within the range of natural zebra finch songs (Fig. 1B). HFs also responded to syllable trains, in which each syllable was replaced with white noise of the same duration, similarly depending on the durations of white-noise syllables and silent gaps (Fig. 3, B and C, bottom).

In rodents, cats, and primates, A1 neurons respond to trains of short tones repeated with intertone intervals of 10 to 40 Hz through stimulus-synchronous firing or rate coding (17–20). We calculated the vector strength, which represents the level of periodicity of spike occurrence, to see whether zebra finch HFs respond in a stimulus-synchronous manner, as reported in mammals (17–20). HFs responded to syllable or white-noise trains in a stimulus-synchronous manner (showing spike responses to each syllable in the trains) as long as gaps were longer than 20 ms (Fig. 3D and fig. S4C), but this response was not dependent on interelement intervals (fig. S4, A and B). Even when syllable durations and thus interelement intervals were longer, HFs did not respond to trains in which the gaps were too short (5 ms). We did identify a small number of HFs (2/19) that responded to the offset of a sound (Off cell and On-Off cell; fig. S4D).

HFs responded to trains of syllables with durations in the range of 36 to 167 ms in a stimulus-synchronous manner. With stimulus-synchronous spike responses, HFs encoded information about the duration of each syllable in trains with durations of increased HF spike activity in response to each syllable in a train. The bin number of the spike histogram, which continuously went beyond the baseline after syllable onset, showed a linear correlation with the duration of sound elements (Fig. 3E). HFs also encoded information about groups of syllables, in particular the number of syllables in a train, by decreasing their firing responses to each syllable along with repeats in a train (Fig. 3F)—a pattern also observed with the white-noise repeats. However, when gap durations were 400 ms, HFs decreased their firing rates by only a small amount. Thus, HFs filtered the repeats of short acoustic events with a specific duration range that were separated by gaps also with a specific duration range, which were similar to a natural song. However, HFs did not capture the sequence of syllables within a train. We compared the response strength to a given syllable in a song and that to the same syllable in the same order in a train to see whether HFs detect syllable sequence in a song (fig. S3). The response strength for a given syllable in a song was not different from that for the same syllable at the same location in a train with 20- to 100-ms gaps. This response

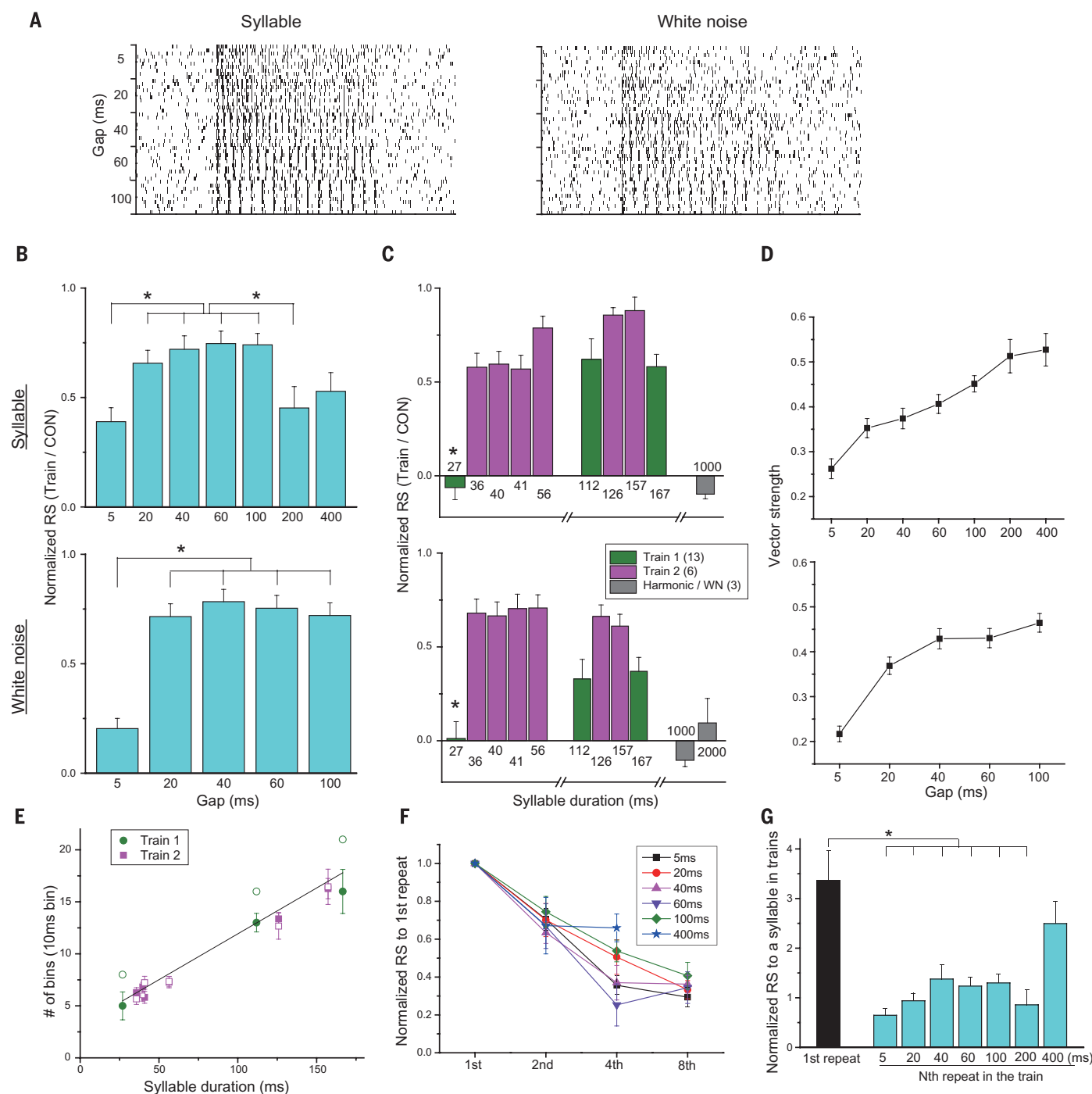


Fig. 3. Properties of temporal information coding in HF neurons. (A) Raster plots of HF responses to syllable trains (left) or to white-noise trains (right) with gaps of 5, 20, 40, 60, and 100 ms (10 trials per gap). (B) Normalized response strength to the train stimulation, averaged for the syllable trains (top) or white-noise trains (bottom) that had the same gap duration (5 to 100 ms, 19 HF; 200 to 400 ms, 6 HF). (C) Normalized response strength to the train stimulation, averaged for the syllable trains (top) or white-noise trains (bottom) that had the same syllable duration or white-noise duration. Different colors denote responses of different HF groups tested with different train sets (13 and 6 HF for train sets 1 and 2, respectively). (D) Vector strength of the response to the syllable train (top) or the white-noise train (bottom) for each gap duration in HF neurons. (E) Average number of bins that went beyond twice the standard deviation of baseline in the histogram, where spike number binned between onset and 50 ms after the first four syllables,

in trains with gaps of 60 to 100 ms, as a function of syllable duration or white-noise duration. There is a linear correlation between syllable duration and spike bin numbers in the response ($r = 0.956$). The color code is the same as (C). (F) Response strength to the second, fourth, and eighth syllables in the train, normalized by the first syllable and averaged within syllable trains with the same gap, in synchronized HF neurons (mean \pm SE). Data are averages of 41, 46, 47, 49, or 41 trains with gaps of 5, 20, 40, 60, or 100 ms from 18 synchronized HF, and of 7 trains with 400-ms gaps from 5 HF. (G) Response strength to a given syllable in the train, normalized by the response strength for the same syllable in the same location in songs and averaged within the syllable trains with the same gap duration in HF-synchronized neurons (mean \pm SE). Data are averages of 51 trains with gaps of 5, 20, 40, 60, and 100 ms from 17 synchronized HF, and of 2 trains with a 400-ms gap from 2 HF. All data in (B) to (G) are shown as means \pm SE. All asterisks in this figure are derived from analysis of variance (ANOVA) with post hoc Tukey test, $P < 0.05$.

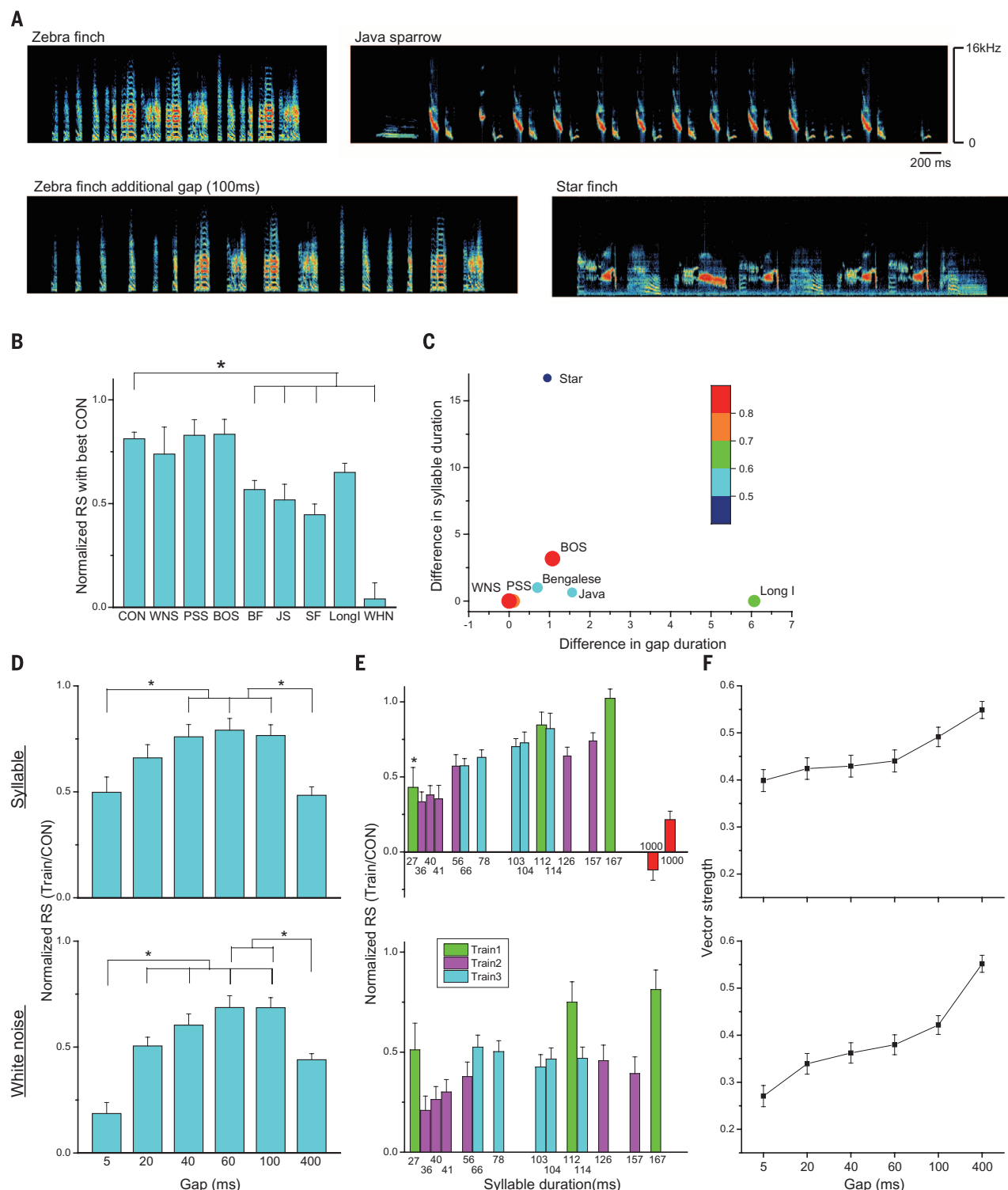


Fig. 4. Temporal information coding in HF neurons for recognition of conspecific songs in juveniles. (A) Sound spectrographs of zebra finch song (CON), Java sparrow, artificial CON in which silent gaps were elongated (LongI), and star finch songs. (B) Average response strength to CON and artificial CONs that have the same temporal structure (WNS and PSS), bird's own song (BOS), heterospecific songs (BF, JS, and SF), LongI, and WHN, normalized to CON in juvenile HF neurons (mean \pm SE). (CON and BF were averaged for three songs, and JS and SF were averaged for two songs; $n = 21$ HF). (C) Heat bubble map of response strength to each song stimulation in the function of Kullback-Leibler distance for the probability distribution of syllable and gap durations from

zebra finch songs (calculated from histogram in Fig. 1B and fig. S7A). (D) Normalized response strength to train stimulation, averaged for syllable trains (top) or white-noise trains (bottom) that had the same gap duration. (E) Normalized response strength to train stimulation, averaged for syllable trains (top) or white-noise trains (bottom) that had the same syllable duration. Different colors denote response of different units tested with different train sets (nine, four, and eight HF for train sets 1, 2, and 3, respectively). (F) Vector strength of the response to the syllable train (top) or the white-noise train (bottom) in HF neurons. All data in (B) to (G) are shown as means \pm SE. All asterisks in this figure are derived from ANOVA with post hoc Tukey test, $P < 0.05$.

strength was significantly smaller than the first repeat in the same train. However, when the gap duration was 400 ms, the response strength to a given syllable at any order was not different from that to the first repeat (Fig. 3G). HF conveyed information regarding the number of repeats and chunks of syllables by decreasing their firing rates with repeats. The syllable counts were reset to 1 when the gap was greater than 400 ms, which would match the counting of syllable number in a motif of zebra finch songs and detection of the start of a new song or motif. Here we found that HFs detected temporal gaps in zebra finch songs; moreover, we observed that these temporal information-coding properties were maintained even after learning songs from Bengalese finch foster fathers (fig. S5). Although we cannot exclude the possibility of recently suggested embryonic song learning in other species (21), these findings suggest that HFs' neuronal properties are innately coded.

Finally, we tested whether HFs in the juvenile zebra finch brain encode species-specific silent gaps and operate as a barcode reader to detect conspecific songs during learning. We recorded HF neuronal responsiveness during the vocal learning period, 50 to 60 DPH (days post hatch), using both normally raised and X-fostered zebra finch juveniles. In addition, we recorded from juvenile birds, which were isolated from their fathers starting at 10 to 12 DPH, thereby extending the sensory learning period (22), to test whether HFs detect conspecific songs without forming a tutor song memory. To see whether HFs in juvenile birds discriminate conspecific songs from other species songs, we recorded their response to a variety of birdsongs. Because there was no difference in conspecific song discrimination of HF response among normal, X-fostered, and isolated juveniles (fig. S6B), we pooled all data. HFs responded significantly less to all Java sparrow, star finch, and Bengalese finch songs. HFs also responded less to artificial CONs that preserved syllable morphology and duration but introduced additional 100-ms gaps for each intersyllable interval, although this did not reach significance. In contrast, HFs responded similarly well to artificially modified zebra finch songs in which temporal patterns were unchanged but morphology was disrupted (PSS and WNS) (Fig. 4, A and B). The response strength to a song declined if the distance from zebra finch songs was large enough (Fig. 4C and fig. S6A). Despite juvenile songs [bird's own song (BOS)] being immature, and despite differences in syllable and gap duration distributions between adult zebra finch songs, HFs still responded relatively well to BOS. Juvenile HFs showed gap and duration selectivity similar to adult zebra finch HFs. Both detected trains of short sounds, the durations of which varied from a few tens to hundreds of milliseconds that were separated by silent gaps of 20 to 100 ms (Fig. 4, D and E). As in adults, juvenile HFs also showed stimulus-synchronized responses (Fig. 4F) and encoded the durations of each sound epoch, as well as

groups of syllables using response attenuation (fig. S6, C to E).

Our findings show that in response to prosodic melodies of adult zebra finch tutors, a subset of neurons in the juvenile zebra finch primary auditory forebrain innately encode silent temporal gap patterns, while a different subset of neurons encode the morphology of song elements. Temporal gap patterns indexed the species specificity of songs and could not be altered by early auditory experience. In contrast, the learning of morphology or acoustic structure of syllables was experience-dependent. These two discrete features of song were processed in parallel by dissociable neural circuits. Parallel information processing of sensory signals is reported in various systems, such as time and intensity differences in barn owl sound localization (23) or phase and amplitude analysis in the electric fish jamming avoidance response (24). In the song system, parallel information processing is consistent with the need to detect and learn two competing criteria embedded in one acoustic signal: species-specific song identity encoded in fixed temporal gaps versus individual song diversity reflected in variable morphology within a species. The selective neural processing of silent gaps between syllables suggests a possible means of extracting parameters for learning from processed sensory information, based on the match between the temporal dynamics of the song stimulus and an innate species-specific template (25) resident in the cortical neural network.

The properties of silent gap durations combined with other temporal parameters may enable phonological complexity. In rodent, cat, and primate species that largely use single-note repetitions, A1 neurons are sensitive to on and off temporal patterns of repeated sounds (26, 27) termed "acoustic flutter" (17, 19). In contrast, birds and humans have more complex vocalizations where the variance in syllabic durations is larger than that of intrasyllabic temporal gaps. Our findings from zebra finch A1 neurons suggest that animals with complex vocalizations that live in biodiverse acoustic environments may have evolved neural mechanisms that use silent temporal gap patterns as barcodes for conspecific identification and communication. Considering the large-scale neural information processing required to learn vocal patterns, we hypothesize that complex phonological systems may use temporal gap patterns and other features of acoustic structure to reduce the dimensionality of information processing for a given acoustic signal. In the zebra finch, our results using artificial white noise with innate temporal gaps indicate that morphological information is dispensable during temporal gap coding, supporting metabolic efficiency in vocal learning (28, 29).

REFERENCES AND NOTES

- M. Konishi, *Annu. Rev. Neurosci.* **8**, 125–170 (1985).
- R. J. Brooks, J. B. Falls, *Can. J. Zool.* **53**, 879–888 (1975).
- P. H. Becker, in *Acoustic Communication in Birds*, D. E. Kroodsma, E. H. Miller, Eds. (Academic Press, 1982), pp. 297–319.
- A. J. Doupe, P. K. Kuhl, *Annu. Rev. Neurosci.* **22**, 567–631 (1999).
- O. Tchernichovski, F. Nottebohm, *Proc. Natl. Acad. Sci. U.S.A.* **95**, 8951–8956 (1998).
- O. Fehér, H. Wang, S. Saar, P. P. Mitra, O. Tchernichovski, *Nature* **459**, 564–568 (2009).
- T. J. Gardner, F. Naef, F. Nottebohm, *Science* **308**, 1046–1049 (2005).
- J. A. Soha, P. Marler, *Anim. Behav.* **60**, 297–306 (2000).
- P. Marler, S. Peters, *Science* **198**, 519–521 (1977).
- R. Dooling, M. Searcy, *Dev. Psychobiol.* **13**, 499–506 (1980).
- D. A. Nelson, P. Marler, *Anim. Behav.* **46**, 806–808 (1993).
- C. S. Whaling, M. M. Solis, A. J. Doupe, J. A. Soha, P. Marler, *Proc. Natl. Acad. Sci. U.S.A.* **94**, 12694–12698 (1997).
- F. Nottebohm, J. A. Paton, D. B. Kelley, *J. Comp. Neurol.* **207**, 344–357 (1982).
- Y. Yazaki-Sugiyama, R. Mooney, *J. Neurophysiol.* **92**, 2771–2788 (2004).
- C. Scharff, F. Nottebohm, *J. Neurosci.* **11**, 2896–2913 (1991).
- N. Amin, A. Doupe, F. E. Theunissen, *J. Neurophysiol.* **97**, 3517–3531 (2007).
- T. Lu, L. Liang, X. Wang, *Nat. Neurosci.* **4**, 1131–1138 (2001).
- X. Gao, M. Wehr, *Neuron* **86**, 292–303 (2015).
- D. Bendor, X. Wang, *Nat. Neurosci.* **10**, 763–771 (2007).
- T. Lu, X. Wang, *J. Neurophysiol.* **84**, 236–246 (2000).
- D. Colombelli-Négrel et al., *Curr. Biol.* **22**, 2155–2160 (2012).
- A. Roper, R. Zann, *Ethology* **112**, 458–470 (2006).
- M. Konishi, *Harvey Lect.* **86**, 47–64 (1992).
- W. Heiligenberg, *Neural Nets in Electric Fish* (MIT Press, 1991).
- P. Marler, in *Simpler Networks and Behavior*, J. C. Fentress, Ed. (Sinauer Associates, Sunderland, MA, 1976), pp. 314–329.
- X. Wang, M. M. Merzenich, R. Beitel, C. E. Schreiner, *J. Neurophysiol.* **74**, 2685–2706 (1995).
- J. A. Grace, N. Amin, N. C. Singh, F. E. Theunissen, *J. Neurophysiol.* **89**, 472–487 (2003).
- H. Barlow, in *Sensory Communication*, W. A. Rosenblith, Ed. (MIT Press, 1961), pp. 217–234.
- M. S. Lewicki, *Nat. Neurosci.* **5**, 356–363 (2002).

ACKNOWLEDGMENTS

We thank C. Yokoyama for continuous thoughtful discussions on this project and valuable help in preparing the manuscript; C. P. Connaughton for valuable discussions and for providing Matlab code for phase scrambling; R. Mooney, M. J. Coleman, and N. Shannon for critical reading of the manuscript; Y. Morohashi for maintenance of the experimental animals and help with behavioral experiments; and K. Wada and M. Soma for providing star finch and Java sparrow songs, respectively. Supported by OIST Graduate University and a JSPS KAKENHI Grant-in-Aid for Scientific Research (C) (24500403) (Y.Y.-S.). All relevant data are stored at OIST Graduate University and are available from the authors on request and/or are included in the manuscript and supplementary materials. Author contributions: Y.Y.-S., M.M.B., and M.A. designed the experiments; Y.Y.-S. performed the behavioral experiments; M.A. performed all other experiments; M.A., Y.Y.-S., and M.M.B. analyzed the data; and Y.Y.-S. and M.M.B. wrote the paper.

SUPPLEMENTARY MATERIALS

www.sciencemag.org/content/354/6317/1282/suppl/DC1
Materials and Methods
Figs. S1 to S6
Reference (30)

30 July 2016; accepted 24 October 2016
10.1126/science.aah6799

DEVELOPMENT ECONOMICS

The long-run poverty and gender impacts of mobile money

Tavneet Suri^{1,2,3,4,5*} and William Jack⁶

Mobile money, a service that allows monetary value to be stored on a mobile phone and sent to other users via text messages, has been adopted by the vast majority of Kenyan households. We estimate that access to the Kenyan mobile money system M-PESA increased per capita consumption levels and lifted 194,000 households, or 2% of Kenyan households, out of poverty. The impacts, which are more pronounced for female-headed households, appear to be driven by changes in financial behavior—in particular, increased financial resilience and saving—and labor market outcomes, such as occupational choice, especially for women, who moved out of agriculture and into business. Mobile money has therefore increased the efficiency of the allocation of consumption over time while allowing a more efficient allocation of labor, resulting in a meaningful reduction of poverty in Kenya.

Mobile money was first introduced in South Africa and the Philippines about 10 years ago (*1*). In March 2007, these services were followed in Kenya by “M-PESA” (M is for mobile, “pesa” is Swahili for “money”), which was to become that country’s dominant (although not only) mobile money service. M-PESA has been celebrated internationally as an innovation that could bring the unbanked population into the formal financial system, with associated impacts on economic well-being and welfare (*2*).

Nearly 10 years after its launch, mobile money is ubiquitous in Kenya. It is used by at least one individual in 96% of Kenyan households (with a total of 5 million households in the country, 96% of which have a mobile phone). These individuals have access to 110,000 agents (*3*) who provide deposit and withdrawal services. In a country with only 2700 automatic teller machines (ATMs) (*4*), the agent network has been an essential factor in the success of M-PESA (*5*). Recently, additional financial services have been deployed over the M-PESA network, including M-Shwari (in collaboration with the Commercial Bank of Africa), a bank account offering savings and credit services accessed entirely through the M-PESA platform, and Lipa na M-PESA, a retail payment facility (see supplementary text).

By the end of 2015, a total of 271 mobile money services were being offered in 93 countries around the world, from Argentina to Zambia, and a further 110 services were planned. At that time, there were 411 million registered accounts,

of which 134 million were active on a 90-day basis, and an average of 33 million transactions were being executed per day. In 19 markets, there were more mobile money accounts than bank accounts, and 37 markets had at least 10 times as many mobile money agents as bank branches (*6*).

We report the results of a study of the long-run impact that M-PESA has had on the economic lives of Kenyans. In earlier work (*7–10*) (see supplementary text), we showed that access to mobile money allowed individuals to protect themselves against income and health risks. Individuals could draw on a wider network of social support, and they received more remittances more quickly from more different types of people in response to negative shocks. We documented a greater number of transactions and larger transactions, both in response to unexpected adverse events (*9*) and overall (*10*). However, notwithstanding the short-term economic benefits of consumption smoothing, whether such a transformative financial innovation could also help to raise the level of consumption and lift people out of poverty over the longer term remained unresolved.

Between 2008 and 2014, we conducted five rounds of a household panel survey, initially representative at the national level (excluding the sparsely populated far north). The first survey was administered to 3000 households across 118 administrative units known as locations (*11*). Attrition was nontrivial in subsequent rounds in 2009, 2010, 2011, and 2014, but higher in Nairobi than elsewhere. The 2011 survey was targeted specifically toward the attrited households from earlier rounds, and Nairobi was dropped from the sample after 2011 (480 households) (*12*). Outside of Nairobi, attrition was still 35% over the 6-year period, and by 2014 we were able to collect data on 1608 households. We discuss attrition in more detail below.

To identify the causal effects of M-PESA on the economic well-being of households, we used changes in access to mobile money—not adoption itself. We measured access to the service by the geographic proximity of households to M-PESA agents. Agent density, quantified by the number of agents within 1 km of the household, exhibited large variation across our sample in 2014 (mean = 8.75, SD = 17.03).

Changes in these measures of access can be used to assess the impact of M-PESA because, as we showed in our earlier work, the geographic rollout of agents up to 2010 was not systematically correlated with the initial level of, or changes in, individual and household characteristics that might have been associated with future outcomes [see table 6C in (*9*), replicated as table S2]. Figures S1 and S2 illustrate the variation we are using. We do not use the change in density from 2010 to 2014, because further expansion of mobile banking outlets after 2010 (including by competitors and facilitated by new regulations from the Central Bank of Kenya) may have been more strategically deployed, and thus correlated with underlying demand.

In further support of the assumption that the agent rollout between 2008 and 2010 was exogenous to household characteristics, we conducted a falsification test [table 7A in (*9*), replicated as table S3]. Using data on consumption and unexpected shocks from another survey of rural Kenyan households, we showed that households living in areas that were later to see large increases in agent access experienced the same levels of risk sharing before the launch of M-PESA as those in areas that would later exhibit less agent growth. A similar exercise shows that earlier levels of household per capita consumption were not correlated with the level or future growth in access to agents. This holds both for (i) socioeconomic variables that we collected in 2008 (although we do not include consumption, which could have been affected in the short run by M-PESA, which was launched more than a year before our first survey) as reported in table S2, and (ii) measures of food consumption in 2007 from the same data set that we used for the falsification tests in (*9*), reported in table S3.

We thus estimate the long-term impact of M-PESA by comparing outcomes, as measured in the 2014 survey, of households that saw relatively large increases in agent access between 2008 and 2010, with outcomes of households that experienced relatively small increases in agent access over the same period. In particular, we estimate regressions with the following specification:

$$y_{ij} = \alpha + \beta \Delta A_{ij} + \phi X_{ij} + \gamma_j + \varepsilon_{ij} \quad (1)$$

where y_{ij} is the relevant outcome for household (or individual) i in location j (*13*), ΔA_{ij} is the change in agent density (i.e., the number of agents within 1 km of the household) between 2008 and 2010, X_{ij} are additional controls (gender, age, and age squared of the household head), and γ_j are location fixed effects. Standard errors are clustered at the location level.

¹Sloan School of Management, Massachusetts Institute of Technology, Cambridge, MA, USA. ²Abdul Latif Jameel Poverty Action Lab (J-PAL), Massachusetts Institute of Technology, Cambridge, MA, USA. ³Kenya Lead Academic, International Growth Center, London, UK. ⁴National Bureau of Economic Research, Cambridge, MA, USA. ⁵Innovations for Poverty Action, New Haven, CT, USA. ⁶Department of Economics, Georgetown University, Washington, DC, USA.

*Corresponding author. Email: tavneet@mit.edu

To investigate differences in impacts by gender, we estimate regressions of the form

$$y_{ij} = \alpha + \beta \Delta A_{ij} + \mu \text{Female}_{ij} + \delta \Delta A_{ij} \times \text{Female}_{ij} + \phi X_{ij} + \gamma_j + \varepsilon_{ij} \quad (2)$$

where *Female* is a dummy indicating the gender of the household head (in household level regressions) or of the individual (in the case of individual level outcomes). With this specification, the marginal effect of an increase in agent density for females is simply $(\beta + \delta)$.

Because gender could be correlated with other characteristics Z_{ij} that allowed individuals and households to benefit from access to mobile money, we include additional interaction terms of the form $\Delta A_{ij} \times Z_{ij}$ in the regression above. For the individual-level regressions, we include education, and for household level regressions, we add education, wealth, and bank account ownership (education and wealth are dummy variables for whether the household is below the median value in the sample and we use a dummy for the household being unbanked, all measured in 2008). If, as a result of including these interactions, the coefficient δ were no longer significant, we would infer that the gender effect was driven by these other characteristics. From this specification, we report the effect of changes in agent density for females, over and above the effects associated with Z_{ij} (i.e., the sum of the main effect of agents and the female interaction).

We report results for three categories of outcome variables: (i) average consumption per person in a household and household poverty rates, (ii) physical and financial wealth, and (iii) occupational choices and migration. In all our regressions, we report the Šidák-Holm P value, which accounts for the testing of multiple hypotheses.

Summary statistics of interest are reported in table S1. Mean daily per capita consumption was 208 Kenyan shillings ($SD = 301$), or a little over \$2.50 at the prevailing nominal exchange rate at the time of the 2014 survey. We estimate that 43.3% of our sample had per capita consumption less than \$1.25 per day (a common measure of extreme poverty), and that for 66.0% it was less than \$2 per day. Among household heads in the sample, 24.6% reported “farming” as their primary occupation, and 17.5% said they ran a business. On average, in 41.2% of households, at least one person in the household had migrated either temporarily or permanently since 2008.

The impacts of the exogenous change in access to agents on consumption and poverty are summarized in Table 1, which reports the average effect across both men and women, as well as the interaction between change in agent density and a female dummy. The reported net “effect for female headed” households is simply the sum of the direct effect and the interaction term. To interpret this statistic, the entry “effect for female headed, 25th–75th percentile” calculates the difference in the dependent variable between female-

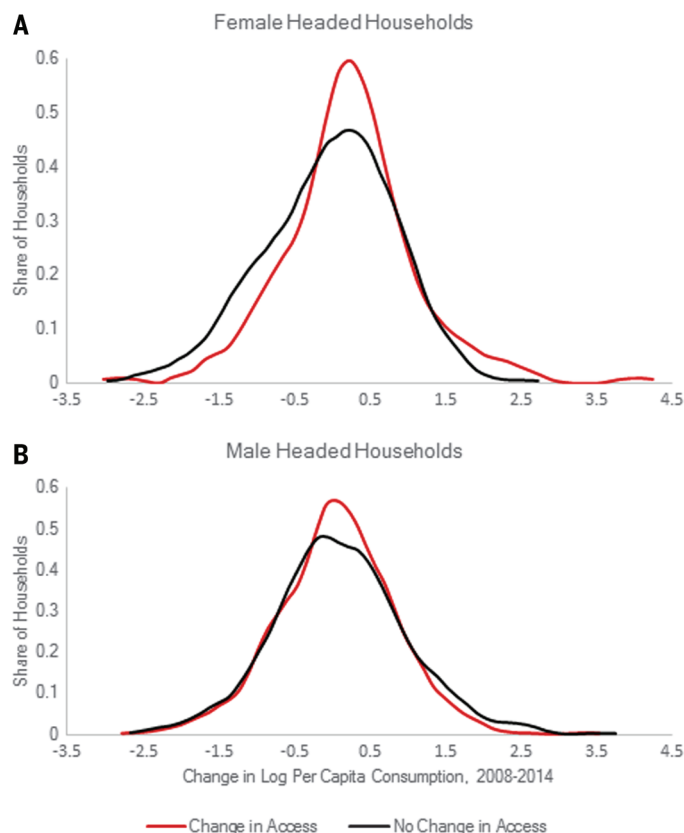


Fig. 1. Change in log(per capita consumption) by gender, for households with and without improvements in agent access. (A) Data for female-headed households; (B) data for male-headed households. The horizontal axis in each graph measures the change in log(per capita consumption) over the period 2008 to 2014. Red lines show the distribution of these changes for households that showed a growth in agent density; black lines show the distributions for households with no growth in agent density. Overall, 55% of households in the sample had no growth in agent density.

headed households that experienced a change in agent access at the third quartile of the distribution, versus those at the first quartile. In terms of agent density, this is a move from zero agents within 1 km of the household to six agents. We refer to this measure as the interquartile impact.

Column 1 of Table 1 indicates that log(per capita consumption) increased significantly in areas in which agent access increased, but that the effect for female-headed households was more than twice that average. Female-headed households at the third quartile of the change in agent density experienced per capita consumption that was some 18.5% higher than those at the first quartile (Šidák-Holm $P = 0.00$). To control for potential unobserved baseline differences, column 2 reports results for changes in log(per capita consumption), including location fixed effects, which in effect is a control for location-specific trends in consumption levels. If anything, consumption growth for male-headed households was negative, while that of female-headed households was positive and statistically significant (Šidák-Holm $P = 0.04$). Increased agent access also reduced both extreme poverty (the share of the population living on less than \$1.25) and general poverty (\$2 per day) significantly. The interquartile impact on extreme poverty among female-headed households was 9.2 percentage points off a base of 43.3%, or by 22%. The interquartile impact on \$2-per-day poverty

of female-headed households was 8.6 percentage points.

To further interpret our regression results, we apply the estimated coefficients at the mean changes in agent density for the sample, scaled by the number of relevant households in the country (see supplementary text). On the basis of this kind of calculation, we estimate that the spread of mobile money helped raise at least 194,000 households out of extreme poverty, and induced 185,000 women to switch into business or retail as their main occupation.

Finally, allowing for interactions between changes in agent density and other observable household characteristics has no impact on our results (see tables S4 to S6 for complete results). Exactly what it might be about female headedness that yields these large impacts on consumption and poverty is discussed below.

Figure 1 illustrates the results in column 2 of Table 1, comparing the distributions of the change in per capita consumption for households that experienced no growth in agent density (55% of households) to those that did. There was little difference between these distributions for male-headed households, but we found a shift to the right for the female-headed households that saw agent growth. This shift was particularly noticeable in the bottom half of the distribution, where per capita consumption growth was largely negative. We infer that the primary impact on female-headed households

Table 1. Consumption and poverty. Standard errors (in parentheses) are clustered at the location level. * $P < 0.1$, ** $P < 0.05$, *** $P < 0.01$. All specifications include location fixed effects and controls for gender, age, and age squared of the household head. All measurements are from 2008; complete estimates are shown in tables S4 to S6.

	(1)	(2)	(3)	(4)
	log(Per capita consumption)	Change in log(per capita consumption)	Extreme poverty (US \$1.25)	Poverty (US \$2)
Overall effect				
Change in agent density	0.012** (0.005)	−0.003 (0.003)	−0.007*** (0.002)	−0.007** (0.003)
Šidák-Holm P value	0.04	0.35	0.00	0.05
Effect disaggregated by gender of household head				
Change in agent density	0.009** (0.004)	−0.005* (0.003)	−0.006*** (0.002)	−0.005* (0.003)
Female head × change in agent density	0.022*** (0.008)	0.020*** (0.007)	−0.010*** (0.004)	−0.009 (0.006)
Female head	−0.080 (0.077)	−0.117* (0.068)	0.032 (0.042)	0.028 (0.036)
Effect of agent density for female headed	0.031*** (0.008)	0.014** (0.007)	−0.015*** (0.004)	−0.014*** (0.005)
Šidák-Holm P value	0.00	0.04	0.00	0.02
Effect for female headed, 25th–75th percentile	0.185	0.085	−0.092	−0.086
Observations	1593	1593	1593	1593
Overall effect of gender when controlling for interactions with education of household head, wealth, and bank account				
Effect of agent density for female headed	0.030*** (0.006)	0.015** (0.006)	−0.015*** (0.003)	−0.015*** (0.004)
Šidák-Holm P value	0.00	0.02	0.00	0.00

Table 2. Effects on assets. Standard errors (in parentheses) are clustered at the location level. * $P < 0.1$, ** $P < 0.05$, *** $P < 0.01$. All specifications include location fixed effects and controls for gender, age, and age squared of the household head. Safety and convenience refer to the safety and convenience scores of the financial instruments a household uses (see supplementary text for the full definitions).

	(1)	(2)	(3)	(4)	(5)	(6)	(7)	(8)
	log(Assets)	log(Savings)	Safety	Convenience	Bank account	SACCO	ROSCA	M-PESA
Overall effect								
Change in agent density	0.009 (0.010)	0.022*** (0.009)	0.002 (0.001)	−0.002 (0.001)	0.006*** (0.002)	0.002 (0.001)	−0.001 (0.002)	−0.000 (0.002)
Šidák-Holm P value	0.90	0.17	0.83	0.69	0.01	0.84	0.93	0.93
Effect disaggregated by gender of household head								
Change in agent density	0.008 (0.010)	0.021** (0.009)	0.002 (0.001)	−0.001 (0.001)	0.007*** (0.002)	0.001 (0.002)	−0.001 (0.002)	−0.000 (0.002)
Female head × change in agent density	0.010 (0.014)	0.011 (0.017)	−0.003 (0.003)	−0.003 (0.003)	−0.002 (0.005)	0.002 (0.004)	0.001 (0.005)	−0.001 (0.006)
Female head	−0.716*** (0.165)	−0.509*** (0.156)	−0.002 (0.027)	0.070** (0.033)	−0.118*** (0.041)	−0.061* (0.037)	0.022 (0.043)	−0.044 (0.044)
Effect of density for female headed	0.018 (0.013)	0.032* (0.017)	−0.001 (0.003)	−0.004 (0.003)	0.005 (0.005)	0.003 (0.004)	−0.000 (0.005)	−0.001 (0.006)
Šidák-Holm P value	0.85	0.53	0.99	0.85	0.96	0.96	0.99	0.99
Effect for female headed, 25th–75th percentile	0.110	0.223	−0.006	−0.026	0.027	0.020	−0.001	−0.006
Observations	1580	1484	1518	1518	1593	1593	1593	1593
Overall effect of gender when controlling for interactions with education of household head, wealth, and bank account								
Effect of density for female headed	0.012 (0.012)	0.035** (0.015)	−0.002 (0.003)	−0.003 (0.003)	0.004 (0.004)	0.002 (0.003)	−0.001 (0.005)	−0.000 (0.005)
Šidák-Holm P value	0.95	0.20	0.95	0.95	0.95	0.95	0.98	0.98

Table 3. Effects on occupational choice, migration and household composition. Standard errors (in parentheses) are clustered at the location level. * $P < 0.1$, ** $P < 0.05$, *** $P < 0.01$. All specifications include location fixed effects and controls for gender, age, and age squared of the household head. Business/sales refers to individuals who report their main occupation to be a business, sales, or retail. Semiskilled refers to individuals reporting being one of: carpenter, mason, conductor, waiter, cook, driver, electrician, mechanic, watchman, secretary, tailor. Secondary refers to a dummy for the individual holding more than one occupation.

	(1)	(2)	(3)	(4)	(5)	(6)	(7)
	Business/sales	Semiskilled	Farming	Secondary	Migration	No. of migrants	Household size
Overall effect							
Change in agent density	0.002*	0.000	−0.004***	−0.001	0.000	0.009	−0.017*
	(0.001)	(0.001)	(0.001)	(0.001)	(0.002)	(0.008)	(0.009)
Šidák-Holm P value	0.27	0.96	0.00	0.77	1.00	0.77	0.27
Effect by gender of household head							
Change in agent density	0.001	0.000	−0.003***	0.000	0.000	0.008	−0.014
	(0.001)	(0.001)	(0.001)	(0.001)	(0.002)	(0.009)	(0.010)
Female head × change in agent density	0.002	−0.000	−0.002***	−0.002**	−0.001	0.002	−0.020
	(0.001)	(0.001)	(0.001)	(0.001)	(0.005)	(0.024)	(0.019)
Female head	0.094***	−0.147***	0.089***	−0.020	0.052	−0.071	−0.537**
	(0.014)	(0.011)	(0.012)	(0.014)	(0.039)	(0.113)	(0.223)
Effect of agent density for female headed	0.003**	0.000	−0.005***	−0.002**	−0.001	0.011	−0.035**
	(0.001)	(0.001)	(0.001)	(0.001)	(0.005)	(0.023)	(0.017)
Šidák-Holm P value	0.15	0.96	0.00	0.11	0.96	0.95	0.15
Effect for female headed, 25th–75th percentile	0.018	0.000	−0.031	−0.011	−0.007	0.064	−0.207
Observations	4772	4772	4772	4772	1593	1593	1593
Overall effect of gender when controlling for interactions with education of household head, wealth, and bank account							
Effect of agent density for female headed	0.003*	0.000	−0.005***	−0.002**	−0.002	0.010	−0.028
	(0.001)	(0.001)	(0.001)	(0.001)	(0.005)	(0.022)	(0.018)
Šidák-Holm P value	0.25	0.96	0.00	0.10	0.96	0.96	0.38

was therefore to protect them from falls in consumption in the longer term, or to boost it marginally, consistent with our earlier results on risk sharing (9).

The higher consumption levels we observed could be driven by increased labor or capital income, or simply by transfers between individuals with different propensities to consume. In turn, mobile money could have facilitated these changes through a number of channels: as a secure means of storing value, it could increase the return to savings and hence future consumption; it has allowed greater access to credit, both formally (through services such as M-Shwari) and informally, potentially increasing investment in productive assets; it has facilitated informal risk sharing, which, as well as smoothing consumption, could lead households to adopt higher-risk but higher-return income-earning strategies or occupations; by reducing the cost of long-distance remittances, it could allow internal migration of breadwinners to higher-return labor markets; and by making payments easier and safer (including via Lipa na M-PESA), it could have boosted small-scale trade and induced changes in occupational choices. Although we lack definitive evidence on all possible mechanisms, there is some support for the savings and occupational choice channels identified above.

To empirically test for these potential mechanisms, we first explored how the observed changes

in agent access are associated with changes in household assets (Table 2). Although there is no impact on physical asset holdings, we do measure a change in the log of total financial savings (including self-reported cash plus balances in bank accounts, savings clubs [savings and credit cooperatives (SACCOs) or rotating savings and credit associations (ROSCAs)], and mobile money accounts, as reported in column 2. The inter-quartile impact on financial savings of female-headed households is 22.3%.

However, as shown in columns 3 to 6, we were unable to detect a differential gender effect of the change in M-PESA access on the likelihood of using various financial products to save. That said, the change in access to mobile money does predict the adoption of a bank account (although not other financial products) in the sample as a whole (column 3), but this may be driven by the supply-side response as banks began either competing with mobile money or collaborating with M-PESA to create bank accounts like M-Shwari. Columns 3 and 4 show little evidence of impacts of agent access on self-reported safety and convenience of the household's financial instruments (see supplementary text) (14).

Table 3 presents evidence on the potential roles of occupational choice at the individual level, as well as household level migration and demographic composition, in driving the large observed changes in economic well-being. Indi-

viduals who saw larger increases in agent access were more likely to be working in “business or sales,” and less likely to be working in farming or to have a secondary occupation. These results are consistent with, although stronger than, some weak evidence of the impact of microcredit on occupational choices, primarily on business ownership (15–17). The last two effects were concentrated primarily among women, which suggests that financial inclusion helped them to graduate from subsistence agriculture and to reduce their reliance on multiple part-time occupations. This could be because mobile money allows women to directly access remittances and/or have more agency. It could also be that because women tend not to be the primary earner in the household, they may have been more constrained before the advent of mobile money. The results on women switching into business are the same for women in male-headed households, so the effects in Table 3 are not driven only by female-headed households.

By facilitating internal remittances, mobile money could have led to a more efficient allocation of labor over space and time, and indeed of human capital investment in the form of schooling choices. Column 5, which measures whether anyone in the household migrated since 2007, and column 6, which measures the number of migrants between 2007 and 2014, of Table 3 show insignificant increases in migration in response

to expanded M-PESA access. On the other hand, columns 7 and 8 provide suggestive evidence that the expansion led to a reduction in average household size. The effects were concentrated on children and could have been associated with lower fertility or children going to boarding school, although the magnitude of the effects is very small (see table S14). In table S13, we also report impacts on a range of remaining outcomes in the data, illustrating improvements in some household characteristics, such as what the house is made of, and what fuel and power the household uses.

Overall, attrition from our original non-Nairobi sample between 2008 and 2014 was 35% (18). To establish the robustness of our conclusions, we report two additional tests in tables S7 to S12 that show our results are not materially affected (see supplementary text). First, we restricted our analysis to the subsample of 50.4% of households in villages in which attrition was less than 35%, a subsample in which the attrition rate was only 17% after 6 years. Tables S7, S9, and S11 show these results, which are consistent with those in Tables 1 to 3. Second, we reweighted the data for attrition using the methods of (19). These results are reported in tables S8, S10, and S12, again consistent with our main findings. Looking across all these attrition checks, the results for consumption and poverty are robust, especially for female-headed households. The results for the overall sample on savings and bank accounts are also robust, as are the results on occupational choice. However, the results for household size are not robust to these checks. Finally, we find that attrition is largely uncorrelated with the independent variable of interest, changes in agent density, especially in locations with low attrition (see supplementary text).

In 2010, Kenya passed agent banking regulations that let banks compete directly with the existing M-PESA network. This was followed in 2011 by the launch of M-Shwari, a popular mobile phone-based bank account operating entirely through M-PESA (see supplementary text) and in 2014 by the opening of the M-PESA agent network to other telecommunications companies and banks. At the same time, the number of M-PESA agents continued to grow exponentially, from 23,000 agents in 2010 to 110,000 in 2014, and in a way that was now potentially correlated with underlying demand. Our estimates of the long-term causal impact of the initial deployment of agents thus include the effect of the subsequent competitive deepening. We argue that this is the correct measure of the impact of M-PESA, because this competitive deepening—especially for mobile phone banking products such as M-Shwari, and given the open M-PESA agent network—was a consequence of M-PESA itself.

Our evidence is in contrast to results reported in a number of recent studies of the impact of increasing access to credit for women. For example, a series of experimental studies (15–17, 20–23) on the impact of microcredit, typically targeted to female clients, found very limited

impacts on economic outcomes. Karlan and Zinman (24) reported results of a randomized trial in the Philippines that showed high demand for credit at market interest rates. But the credit itself had limited and in some cases negative impacts on business activities and subjective well-being, and did not affect women and men differentially. Similarly, the economic returns to capital grants (not loans) to small businesses have been found in a number of settings to be limited for female-operated entities, but positive for those run by men (25–27).

In contrast, more basic financial services such as the ability to safely store, send, and transact money—taken for granted in most advanced economies, and which in the form of mobile money have reached millions of Kenyans at unprecedented speed over the past decade—appear to have the potential to directly boost economic well-being. We have shown that access to mobile money has lifted as many as 194,000 households out of poverty, and has been effective in improving the economic lives of poor women and of members of female-headed households. Our evidence, and earlier work, suggests that these impacts derive from a more efficient allocation of labor, savings, and risk. On the other hand, we do not find any evidence that mobile money increased the overall safety and convenience of households' store of value. Although providing external sources of capital to such populations could, of course, have even larger impacts, our results suggest that having a private, low-cost means of managing financial resources is also necessary and can itself meaningfully reduce poverty rates among vulnerable groups. For women, the route out of poverty might not be more capital, but rather financial inclusion at a more basic level, which enhances their ability to manage those financial resources that are already accessible. Thus, although mobile phone use correlates well with economic development (28–31), mobile money causes it.

REFERENCES AND NOTES

- Two large mobile network operators, Vodacom and MTN, recently shut down their mobile money services in South Africa because of high operating costs and a high prevalence of bank accounts. See the relevant press articles at www.fin24.com/Tech/Companies/why-vodacom-m-pesa-has-flopped-in-sa-20160509 and www.businessdailyafrica.com/Corporate-News/MTN-scraps-mobile-money-business-in-South-Africa/539550-3382710-13vftp7z/.
- See supplementary text for more background and detail on mobile money in Kenya.
- Communications Commission of Kenya, Annual Report for the Financial Year 2014–2015; www.ca.go.ke/index.php/annual-reports.
- The number of ATMs was 2698 in June 2015. In June 2014 it was 2618, and in June 2010 it was 1943. These data come from the Central Bank of Kenya Statistics. www.centralbank.go.ke/national-payments-system/payment-cards/number-of-atms-atm-cards-pos-machines/.
- I. Mas, A. Ng'weno, *J. Payments Strategy Systems* **4**, 352–370 (2010).
- GSMA, "State of the Industry Report: Mobile Money" (2015); www.gsma.com/mobilefordevelopment/wp-content/uploads/2016/04/SOTIR_2015.pdf.
- W. Jack, T. Suri, "Mobile money: The economics of M-PESA" (2011); www.mit.edu/~tavnnet/M-PESA-Final2.pdf.
- T. Suri, W. Jack, T. Stoker, *Proc. Natl. Acad. Sci. U.S.A.* **109**, 10257–10262 (2012).

- W. Jack, T. Suri, *Am. Econ. Rev.* **104**, 183–223 (2014).
- W. Jack, A. Ray, T. Suri, *Am. Econ. Rev.* **103**, 356–361 (2013).
- See supplementary text and (9) for more detail on the survey data collected.
- About 1027 households are covered in all five rounds, but (excluding 2011) 1299 households are covered in the four rounds.
- One level of local administrative units in Kenya are referred to as "locations," each with a population of 3000 households on average.
- We focus on safety and convenience as these are the most commonly cited reasons for using one financial instrument over any other (cost is only mentioned in 3.6% of cases).
- A. Banerjee, D. Karlan, J. Zinman, *Am. Econ. J. Appl. Econ.* **7**, 1–21 (2015).
- O. Attanasio, B. Augsburg, R. de Haas, E. Fitzsimons, H. Harmgart, *Am. Econ. J. Appl. Econ.* **7**, 90–122 (2015).
- B. Augsburg, R. de Haas, H. Harmgart, C. Meghir, *Am. Econ. J. Appl. Econ.* **7**, 183–203 (2015).
- Over such a long panel in this kind of environment, this rate of attrition is not unusually high. For example, see footnote 19 in (9), which provides a list of studies that have comparable attrition rates.
- J. Fitzgerald, P. Gottschalk, R. Moffitt, *J. Hum. Resources* **33**, 251–299 (1998).
- A. Banerjee, E. Duflo, R. Glennerster, C. Kinnan, *Am. Econ. J. Appl. Econ.* **7**, 22–53 (2015).
- A. Tarozzi, J. Desai, K. Johnson, *Am. Econ. J. Appl. Econ.* **7**, 54–89 (2015).
- B. Crépon, F. Devoto, E. Duflo, W. Parienté, *Am. Econ. J. Appl. Econ.* **7**, 123–150 (2015).
- M. Angelucci, D. Karlan, J. Zinman, *Am. Econ. J. Appl. Econ.* **7**, 151–182 (2015).
- D. Karlan, J. Zinman, *Science* **332**, 1278–1284 (2011).
- S. de Mel, D. McKenzie, C. Woodruff, *Q. J. Econ.* **123**, 1329–1372 (2008).
- S. de Mel, D. McKenzie, C. Woodruff, *Am. Econ. J. Appl. Econ.* **1**, 1–32 (2009).
- S. de Mel, D. McKenzie, C. Woodruff, *Science* **335**, 962–966 (2012).
- J. Blumenstock, G. Cadamuro, R. On, *Science* **350**, 1073–1076 (2015).
- J. Aker, I. Mbiti, *J. Econ. Perspect.* **24**, 207–232 (2010).
- J. Aker, C. Ksoll, T. Lybbert, *Am. Econ. J. Appl. Econ.* **4**, 94–120 (2012).
- Mobile phones do not necessarily dominate other forms of communication. Aker *et al.* (32) found that distribution of free newspapers improves electoral accountability more than randomized text messages.
- J. C. Aker, P. Collier, P. C. Vicente, *Rev. Econ. Stat.* **10.1162/REST_a_00611** (2016).

ACKNOWLEDGMENTS

We thank S. Asman and G. Ramani for management of the 2014 data collection, and Financial Sector Deepening Kenya and the Gates Foundation for financial support for the data collection. The study received institutional review board approval from the MIT Committee on Use of Humans as Experimental Subjects, IRB 1403006291. T.S. is on the board of directors of Innovations for Poverty Action, which participated in some of the rounds of data collection. The DOI for round 5 of the data is 10.7910/DVN/LIDVIH (<https://dataverse.harvard.edu/dataverse/mobilemoney>).

SUPPLEMENTARY MATERIALS

www.sciencemag.org/content/354/6317/1288/suppl/DC1
Supplementary Text
Figs. S1 to S4
Tables S1 to S14
Reference (33)

13 July 2016; accepted 9 November 2016
10.1126/science.aah5309

ORIGIN OF LIFE

Transient compartmentalization of RNA replicators prevents extinction due to parasites

Shigeyoshi Matsumura,^{1,2,3*} Ádám Kun,^{4,5*} Michael Ryckelynck,^{2,6} Faith Coldren,² András Szilágyi,^{4,7} Fabrice Jossinet,⁶ Christian Rick,^{2,6} Philippe Nghe,¹ Eörs Szathmáry,^{4,5,8,9†} Andrew D. Griffiths^{1,2†}

The appearance of molecular replicators (molecules that can be copied) was probably a critical step in the origin of life. However, parasitic replicators would take over and would have prevented life from taking off unless the replicators were compartmentalized in reproducing protocells. Paradoxically, control of protocell reproduction would seem to require evolved replicators. We show here that a simpler population structure, based on cycles of transient compartmentalization (TC) and mixing of RNA replicators, is sufficient to prevent takeover by parasitic mutants. TC tends to select for ensembles of replicators that replicate at a similar rate, including a diversity of parasites that could serve as a source of opportunistic functionality. Thus, TC in natural, abiological compartments could have allowed life to take hold.

The earliest molecular replicators (1, 2) must have been plagued by freeloading parasitic replicators (3–6). For example, when the RNA genome of the Q β virus was replicated in vitro using the viral replicase, 83% of the genome was deleted due to selection for RNAs with the fastest replication rate (7). Eventually, reproducing compartments (protocells) must have arisen, taming parasites by spatially limiting their propagation and allowing group selection at the compartment level, preventing functional collapse (5, 8–10). Indeed, serial fusion-division cycles of water-in-oil emulsion droplets, which function as artificial cell-like compartments (11), allows prop-

agation of a compartmentalized replicative cycle catalyzed by Q β replicase (12, 13).

However, a more rudimentary type of population structure (14), in which replicators underwent repeated cycles of mixing and interaction in local groups, similar to Wilson's trait group model (15), may have existed before the evolution of reproducing protocells (9, 16, 17).

Here, we demonstrate that repeated cycles of mixing and transient compartmentalization (TC) in abiological compartments—for example, atmospheric aerosol droplets (18), microcompartments in hydrothermal vents (19), ice eutectic phases (20), clusters on mineral surfaces (21, 22), or lipid

vesicles (23)—is sufficient to maintain functional replicators and provides a simple solution to allow the evolution of molecular complexity before the appearance of the first protocells.

We used a droplet-based microfluidic system (24) to investigate TC (Fig. 1 and fig. S1). The functional replicator (MDV-VS RNA) comprises the trans Varkud satellite (trans VS) ribozyme (25), inserted into the midvariant (MDV-1) of Q β genomic RNA (26), which is replicated by Q β replicase (fig. S2). Replication was studied under three conditions, in duplicate: (i) uncompartimentalized (bulk), (ii) with TC in ~1 million 12-pL (28- μ m diameter) droplets (unselected, compartmentalized), and (iii) with TC in ~1 million 12-pL droplets and selection of the droplets based on ribozyme activity (selected, compartmentalized). In each case, 50 μ L of aqueous phase, containing 1.5×10^6 molecules (290 fg) of MDV-VS RNA (corresponding to a Poisson distribution with a mean, λ , of ~0.4 RNA

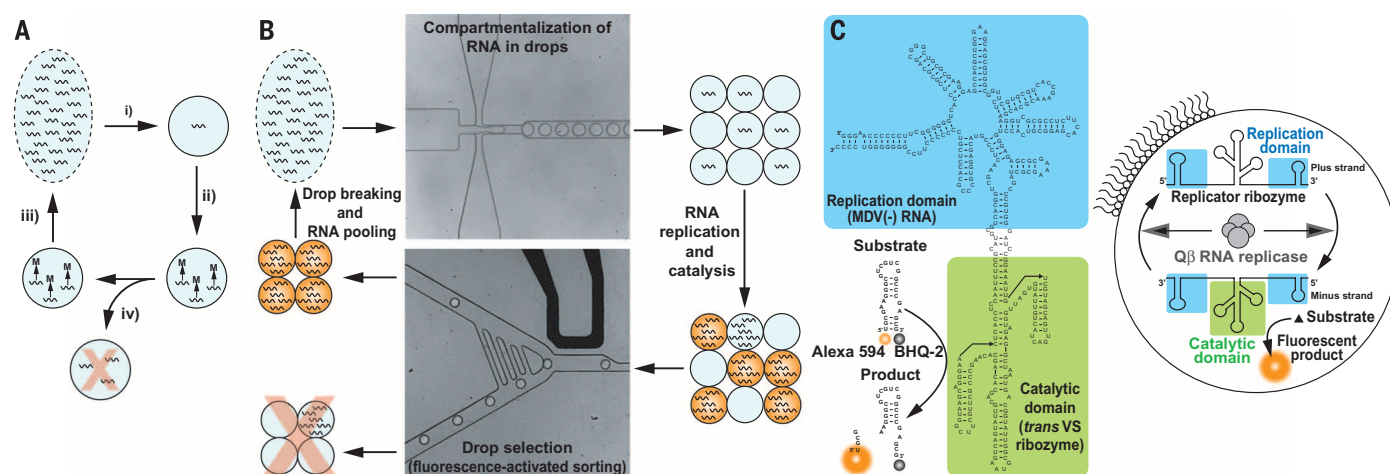


Fig. 1. Primordial TC and its experimental embodiment. (A) Primordial RNA molecules are compartmentalized (i), replicate in the compartments and ribozyme activity contributes to the “metabolism” (M) of the compartments (ii), and compartments containing ribozymes that contribute to the “metabolism” pass on more RNAs to the pool (iii) than compartments containing parasites (iv). (B) In the microfluidic system, RNA molecules are compartmentalized in aqueous droplets in an inert carrier oil, replicate in the

droplets, and catalyze a fluorogenic reaction. Fluorescence-activated droplet sorting (FADS) (30) is used to sort droplets containing active ribozymes, and the RNA from the sorted droplets is pooled before the next round of selection. (C) The trans VS ribozyme (25), inserted into the minus strand of the midvariant (MDV-1) RNA (26), is replicated in droplets using Q β RNA replicase (7). The ribozyme cleaves a nonfluorescent RNA substrate to generate a fluorescent product.

¹École Supérieure de Physique et de Chimie Industrielles de la Ville de Paris (ESPCI Paris), CNRS UMR 8231, 10 Rue Vauquelin, 75231 Paris Cedex 05, France. ²Institut de Science et d'Ingénierie Supramoléculaires (ISIS), CNRS UMR 7006, Université de Strasbourg, 8 Allée Gaspard Monge, BP 70028, 67083 Strasbourg Cedex, France. ³Graduate School of Science and Engineering, University of Toyama, 3190 Gofuku, Toyama, 930-8555, Japan. ⁴Parmenides Center for the Conceptual Foundations of Science, Munich/Pullach, Germany. ⁵MTA-ELTE-MTM Ecology Research Group, Budapest, Hungary. ⁶Architecture et Réactivité de l'ARN, CNRS UPR 9002, Université de Strasbourg, 67084 Strasbourg, France. ⁷MTA-ELTE Theoretical Biology and Evolutionary Ecology Research Group, Department of Plant Systematics, Ecology and Theoretical Biology, Budapest, Hungary. ⁸Department of Plant Systematics, Ecology and Theoretical Biology, Institute of Biology, Eötvös University, Budapest, Hungary. ⁹Conflict and Cooperation in Evolutionary Systems Program, Institute of Advanced Studies, Kőszeg, Hungary.

*These authors contributed equally to this work.

†Corresponding author. Email: szathmari.eors@gmail.com (E.S.); andrew.griffiths@espci.fr (A.D.G.)

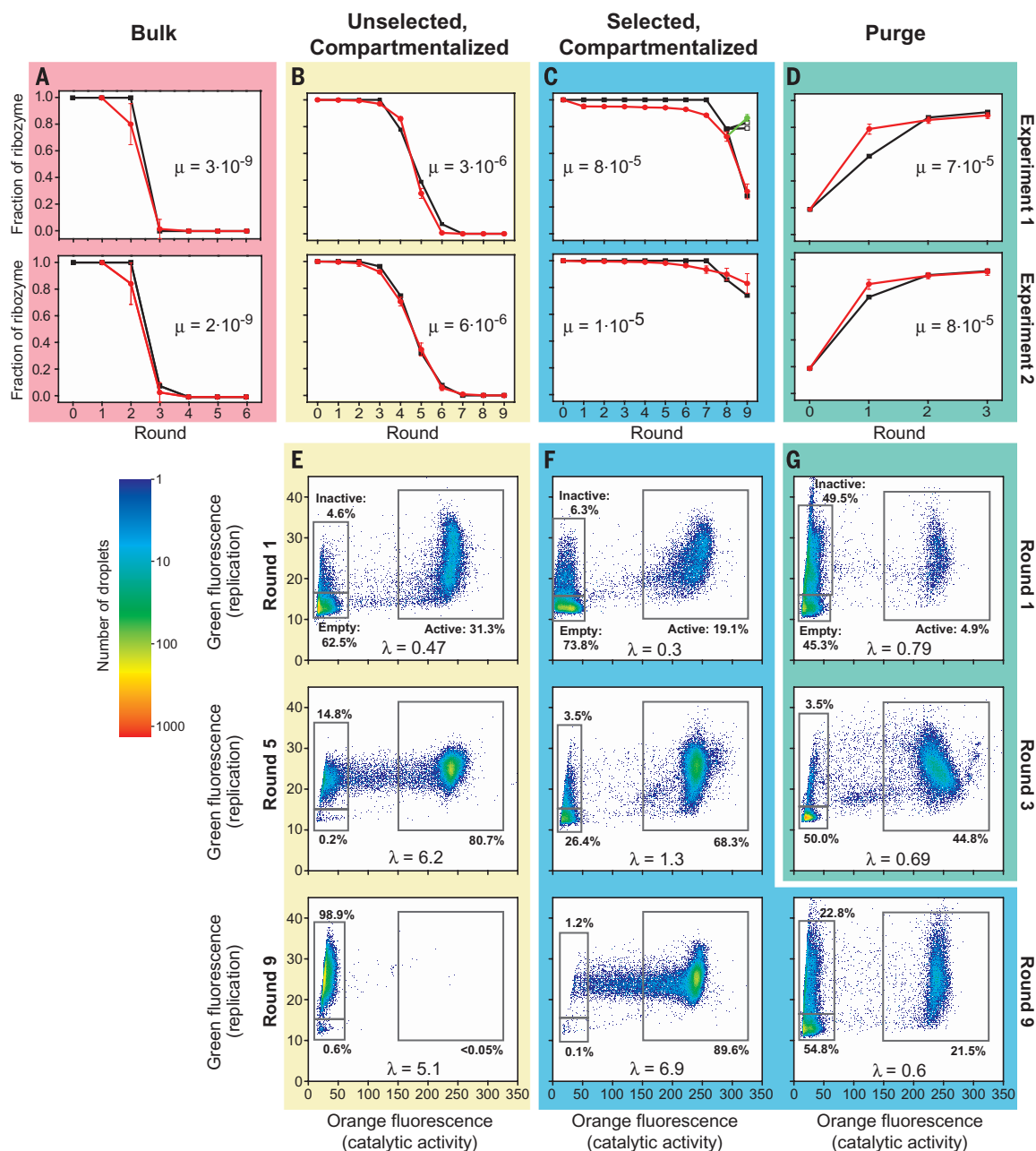


Fig. 2. Survival of functional ribozymes in bulk and with TC in the presence and absence of selection. (A to D) Fraction of MDV-VS ribozymes versus round of selection. Experimental results (black squares) are shown for two independent experiments (experiments 1 and 2) for each condition together with SFA modeling results using experimental λ values (red circles) and mutation rate, μ , used to fit the data. Error bars, mean \pm 1 SD. (A) Bulk. (B) Unselected, compartmentalized. (C) Selected, compartmentalized. Round 9 of experiment 1 was performed at both λ of 6.9 (black squares, experimental results; red circles,

SFA modeling) and 0.6 (in duplicate) (white squares, experimental results; green circles, SFA modeling). (D) Purge (ability to purge parasites and reach equilibrium). (E to G), Droplet fluorescence (in relative fluorescence units) for experiment 1. Boxes define droplet populations that contain no RNA replicators (empty), parasitic RNA replicators (inactive), and catalytically active RNA replicators (active). The percentage of droplets in each population and λ is indicated. (E) Unselected, compartmentalized. (F) Selected, compartmentalized. (G) Purge. Green and orange fluorescence values are relative fluorescence units.

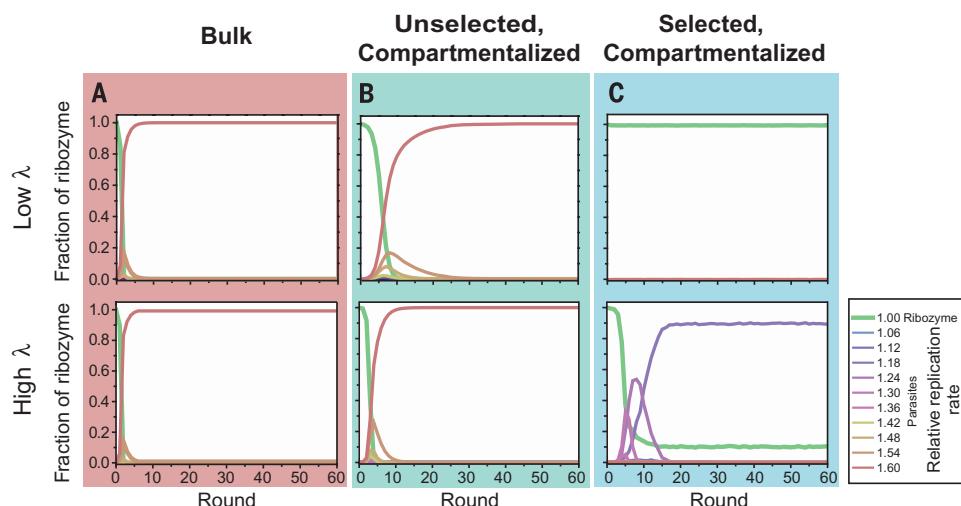
molecules per droplet), was used to start the experiment. Replication was followed using a green fluorescent RNA intercalating dye, and hydrolysis of the substrate RNA by the ribozyme was measured simultaneously by the increase in orange fluorescence (fig. S2, C and E). After a 3-hour replication, for bulk and unselected compartmentalized experiments, RNA was simply pooled.

However, for the selected compartmentalized experiments, all droplets with orange fluorescence >150 relative fluorescence units (containing functional ribozymes) were sorted, and RNA from the sorted droplets was pooled. To initiate the next round, 290 fg of purified RNA was inoculated into 50 μ L of fresh reagents. This process was repeated for a total of 4 to 9 rounds.

In bulk, MDV-VS RNA disappeared by round 4 (Fig. 2A), as did the corresponding catalytic activity, due to the appearance of parasitic RNAs that are shorter than MDV-VS RNA (figs. S3 to S5), replicate faster (fig. S2, C and G), and are limited in diversity (fig. S6A).

Without selection for ribozyme activity, compartmentalization slowed down, but did not

Fig. 3. Modeling of ribozyme and parasites dynamics. Fraction of MDV-VS ribozyme and 10 different parasitic RNA replicators, with different relative replication rates compared with the MDV-VS ribozyme, calculated using the SFA model versus round of selection at $\lambda = 0.6$ (Low λ) and $\lambda = 7$ (High λ). This corresponds to 0.6 million and 7 million replicators, respectively, either in bulk or distributed into 1 million compartments (droplets). (A) Bulk. (B) Unselected, compartmentalized. (C) Selected, compartmentalized.



prevent, the extinction of MDV-VS RNA, which had essentially disappeared by round 7 (Fig. 2B), out-competed by parasitic RNAs (figs. S3 to S5). The fraction of droplets containing replicated RNA (high green fluorescence, in the “active” and “inactive” gates) that contained active ribozymes (high orange fluorescence, in the “active” gate) fell from >87% in round 1 to <0.05% by round 9 (Fig. 2E and fig. S7, A and B), indicating that by round 9 almost all occupied droplets contained parasitic RNAs with no catalytic activity.

However, selecting the compartments based on ribozyme activity prevented extinction of the MDV-VS RNA. By round 9, full-length MDV-VS RNA was still readily observed (Fig. 2C), and >86% of high green fluorescent droplets also showed high orange fluorescence and therefore contained functional replicating ribozymes (Fig. 2F and fig. S7, C and D), but a high diversity (fig. S6A) of shorter parasitic RNAs was also present (figs. S3 to S5). The fraction of MDV-VS RNA was dependent on the mean initial number of RNA molecules per droplet, λ : When round 9 (experiment 1) was performed at λ of 6.9, the fraction of MDV-VS RNA was 0.28 but increased to 0.83 at λ of 0.60 (Fig. 2C), slightly higher than in the previous round (where the fraction of MDV-VS RNA was 0.78 at λ of 4.4).

The ability to purge parasites was confirmed by performing an experiment at $\lambda \approx 0.6$, starting with a 1:4 mixture of MDV-VS RNA and a parasite, cloned from the bulk selection, that replicates 1.46 times as fast as MDV-VS RNA (fig. S2, C and G). The fraction of MDV-VS RNA rose quickly from 0.19 to reach a plateau of 0.92 by round 3 (Fig. 2D). The fraction of droplets containing replicated RNA (high green fluorescence) that contained active ribozymes (high orange fluorescence) also increased from $\leq 10.3\%$ in round 1 to $\geq 90.6\%$ by round 3 (Fig. 2G and fig. S8, A and B). Thus, MDV-VS RNA and parasites converge to equilibrium from above or below the equilibrium position, provided the droplets are selected for catalytic activity.

We can surmise that if catalytically active replicators provide a selective advantage at the

compartment level, TC can prevent takeover by parasites and functional collapse. However, despite selection of the compartments, parasitic replicators were not fully purged, and the fraction of parasite is a function of λ .

To better understand the system dynamics and the nature of the parasites, we developed a model that takes into account the stochastic first appearance (SFA) of parasites by mutation (see supplementary materials). There is a close fit between the experimental and SFA modeling results using experimental λ values (Fig. 2, A to D, and fig. S6). The model shows that, in bulk (Fig. 3A) and with unselected compartments (Fig. 3B), the parasite with the highest replication rate (1.60 times as fast as MDV-VS RNA) takes over, driving MDV-VS RNA to extinction. However, when the compartments are selected, MDV-VS RNA reaches an equilibrium with parasites. The fraction of MDV-VS RNA at equilibrium is a function of λ , and it is a parasite with a replication rate only slightly faster than MDV-VS RNA (1.18 times faster) that is most abundant (Fig. 3C; see also fig. S9). The low replication rate of these “soft” parasites allows them to coexist with cocompartmentalized MDV-VS RNA, which catalyzes enough product formation to allow droplet sorting. Indeed, the enzymatic activity of MDV-VS RNA becomes vital for survival of the “soft” parasites, which function as bona fide parasites, not simply RNAs that replicate quickly. However, “hard” parasites, with higher replication rates, are not sorted because the final fraction of cocompartmentalized MDV-VS RNA (and thus product) is too low. The higher frequency of “soft” parasites in the selected, compartmentalized experiment than in bulk was confirmed experimentally (supplementary materials and fig. S8C). Similar results were obtained using a deterministic minimum model (supplementary materials and fig. S10), indicating that stochastic compartmentalization effects (27) are not required to alleviate parasite spread.

The results indicate that, before reproducing protocells, trait group selection based on repeated cycles of TC and mixing could have allowed life on

earth to take off. Here, compartments that did not reach the selection threshold were eliminated, but trait group selection would operate whenever transiently arising groups containing a larger number of functional replicators contribute more replicators to the pool seeding the next “generation” of compartments than those containing a larger number of parasites (9, 16, 17). This would be the case, for example, if an RNA replicase ribozyme was replicating both itself and parasites. “Soft” parasites that do not “kill” the functionality of the compartments are like well-adapted contemporary parasites that do not kill their host. The persistence of a diversity of “soft” parasites (fig. S6), which have lost their original activity, could be an important source of genetic diversity because long-term selection could turn some parasites into replicators with novel (even surprising) functionality for the group (28) in the same way that novel function evolves from gene duplication (29). Our results are relevant whether one adheres strongly or weakly to the RNA world (2) or not at all, provided that there were macromolecular replicators with the possibility of heterocatalytic function.

REFERENCES AND NOTES

1. L. E. Orgel, *Nature* **358**, 203–209 (1992).
2. W. Gilbert, *Nature* **319**, 618 (1986).
3. J. Maynard Smith, *Nature* **280**, 445–446 (1979).
4. C. Bresch, U. Niesert, D. Harnasch, *J. Theor. Biol.* **85**, 399–405 (1980).
5. E. Szathmáry, L. Demeter, *J. Theor. Biol.* **128**, 463–486 (1987).
6. M. Eigen, *Naturwissenschaften* **58**, 465–523 (1971).
7. D. R. Mills, R. L. Peterson, S. Spiegelman, *Proc. Natl. Acad. Sci. U.S.A.* **58**, 217–224 (1967).
8. E. Szathmáry, J. Maynard Smith, *Nature* **374**, 227–232 (1995).
9. J. Maynard Smith, E. Szathmáry, *The Major Transitions in Evolution* (Freeman, Oxford, 1995).
10. Á. Kun et al., *Ann. N. Y. Acad. Sci.* **1341**, 75–95 (2015).
11. D. S. Tawfik, A. D. Griffiths, *Nat. Biotechnol.* **16**, 652–656 (1998).
12. N. Ichihashi et al., *Nat. Commun.* **4**, 2494 (2013).
13. Y. Bansho, T. Furubayashi, N. Ichihashi, T. Yomo, *Proc. Natl. Acad. Sci. U.S.A.* **113**, 4045–4050 (2016).
14. R. Michod, *Am. Zool.* **23**, 5–14 (1983).
15. D. S. Wilson, *Proc. Natl. Acad. Sci. U.S.A.* **72**, 143–146 (1975).

16. E. Szathmáry, *J. Theor. Biol.* **159**, 99–109 (1992).
17. E. Szathmáry, J. Maynard Smith, *J. Theor. Biol.* **187**, 555–571 (1997).
18. C. M. Dobson, G. B. Ellison, A. F. Tuck, V. Vaida, *Proc. Natl. Acad. Sci. U.S.A.* **97**, 11864–11868 (2000).
19. E. V. Koonin, W. Martin, *Trends Genet.* **21**, 647–654 (2005).
20. A. Kanavarioti, P. A. Monnard, D. W. Deamer, *Astrobiology* **1**, 271–281 (2001).
21. T. Czárán, E. Szathmáry, in *The Geometry of Ecological Interactions: Simplifying Spatial Complexity*, U. Dieckmann, R. Law, J. A. J. Metz, Eds. (IASA and Cambridge University Press, Cambridge, 2000), pp. 116–134.
22. P. Szabó, I. Scheuring, T. Czárán, E. Szathmáry, *Nature* **420**, 340–343 (2002).
23. P. L. Luisi, P. Walde, T. Oberholzer, *Curr. Op. Coll. Int. Sci.* **4**, 33–39 (1999).
24. M. T. Guo, A. Rotem, J. A. Heyman, D. A. Weitz, *Lab Chip* **12**, 2146–2155 (2012).
25. H. C. Guo, R. A. Collins, *EMBO J.* **14**, 368–376 (1995).
26. D. R. Mills, F. R. Kramer, S. Spiegelman, *Science* **180**, 916–927 (1973).
27. A. Traulsen, A. M. Sengupta, M. A. Nowak, *J. Theor. Biol.* **235**, 393–401 (2005).
28. B. Könnny, T. Czárán, E. Szathmáry, *BMC Evol. Biol.* **8**, 267 (2008).
29. S. Ohno, *Evolution by Gene Duplication*. (Springer, New York, 1970).
30. J.-C. Baret et al., *Lab Chip* **9**, 1850–1858 (2009).

ACKNOWLEDGMENTS

Comments by M. Santos and H. de Vladar are gratefully acknowledged. This work was supported by the European Union Seventh Framework Program (FP7/2007–2013) under grant agreements 225167 (eFlux) and 294332 (EvoEvo).

SUPPLEMENTARY MATERIALS

www.sciencemag.org/content/354/6317/1293/suppl/DC1
Materials and Methods
Supplementary Text
Figs. S1 to S12
Database S1
References (31–42)

17 May 2016; accepted 9 November 2016
10.1126/science.aag1582

SYNTHETIC BIOLOGY

β-cell-mimetic designer cells provide closed-loop glycemic control

Mingqi Xie,¹ Haifeng Ye,² Hui Wang,¹ Ghislaine Charpin-El Hamri,³
Claude Lormeau,^{1,4} Pratik Saxena,¹ Jörg Stelling,^{1,4*} Martin Fussenegger^{1,5*}

Chronically deregulated blood-glucose concentrations in diabetes mellitus result from a loss of pancreatic insulin-producing β cells (type 1 diabetes, T1D) or from impaired insulin sensitivity of body cells and glucose-stimulated insulin release (type 2 diabetes, T2D). Here, we show that therapeutically applicable β-cell-mimetic designer cells can be established by minimal engineering of human cells. We achieved glucose responsiveness by a synthetic circuit that couples glycolysis-mediated calcium entry to an excitation-transcription system controlling therapeutic transgene expression. Implanted circuit-carrying cells corrected insulin deficiency and self-sufficiently abolished persistent hyperglycemia in T1D mice. Similarly, glucose-inducible glucagon-like peptide 1 transcription improved endogenous glucose-stimulated insulin release and glucose tolerance in T2D mice. These systems may enable a combination of diagnosis and treatment for diabetes mellitus therapy.

Diabetes mellitus is a complex and progressive disease with a pathophysiology involving metabolic impairments that can lead to many clinical complications and currently affects more than 415 million people worldwide (1, 2). Diabetic patients have a chronically elevated blood-glucose concentration, called hyperglycemia, that results from either a selective autoimmune destruction of pancreatic insulin-producing β cells (type 1 diabetes, T1D) or a progressive exhaustion of active β cells due to environmental factors that include a sedentary lifestyle, malnutrition, or obesity (type 2 diabetes, T2D) (2, 3). Unless treated in time, sustained hyperglycemia can initiate pathologic cascades that result in more severe disorders such as cardiovascular

diseases, renal failures, the metabolic syndrome, or hormone dysfunctions (4–7). Therefore, improved glycemic control by a therapeutic intervention that either enables tightly controlled insulin delivery or restores a patient's β-cell function will be important in diabetes treatment (8).

Because T1D patients suffer from complete insulin deficiency (3, 9), treatment options focus on a disciplined or automated supply of exogenous insulin (10). For T2D therapy, there are more treatment options, owing to the progressive and multifactorial nature of this disease type (1, 2). For example, incretin hormones [e.g., glucagon-like peptide 1 (GLP-1) analogs] improve glucose-stimulated insulin secretion of exhausting β cells (11). Recent studies capitalizing on engineered mammalian cells to produce insulinogenic proteins within a patient are gathering momentum because they promise effective drug production, delivery, and dosage (12). For example, the regeneration of glucose-responsive insulin-secreting β cells from stem cells (9, 13) represents a breakthrough as transplantation of these ex vivo programmed cells into T1D patients would restore their glucose-stimulated insulin expression. Alternatively, engineering of glucose-responsive insulin expression elements into extrapancreatic mammalian cell types (14) can protect against

diabetic vulnerabilities such as autoimmune (re)targeting in T1D (15) and metabolic stress-induced β-cell apoptosis in T2D (16). Recently, synthetic biology-inspired rational circuit design has led to the engineering of immunoprotective implants, providing trigger-inducible insulin (17) or GLP-1 expression (18) with traceless and non-invasive signals. However, neither of these approaches provided closed-loop control of therapeutic dosage based on glucose sensing.

We engineered a glucose-inducible transcriptional system in an extrapancreatic human cell line that directly senses glycemia-relevant extracellular glucose concentrations and coordinates dose-dependent transcription of insulin and GLP-1. Glucose sensing was achieved by coupling a β-cell-mimetic cascade of glycolysis-mediated calcium entry (19) to a synthetic excitation-transcription coupling system (20) in human embryonic kidney 293 (HEK-293) cells. HEK-293 is widely used to study ion-channel activities and enables high-level production of antidiabetic proteins (17, 18, 21, 22). We designed a HEK-293-based assay to evaluate the stimulus strength of membrane depolarization (Fig. 1A). When exposing different calcium-responsive promoters to 75 mM potassium chloride (KCl), the synthetic promoter P_{NFAT2}, containing nuclear factor of activated T cells (NFAT) repeats from the murine interleukin-4 (IL-4) promoter (23), was most responsive to chemically induced membrane depolarization (Fig. 1B). Cotransfection of a voltage-gated calcium channel such as Ca_v1.2 showed amplified excitation-transcription coupling and higher sensitivity (Fig. 1C). Five tandem NFAT_{IL4}-repeats 5' of a minimal promoter [pMX57, P_{NFAT3}-SEAP; P_{NFAT3} (NFAT_{IL4})₅-P_{min}] showed optimal induction ratios between resting and depolarized membrane potentials (Fig. 1D) and could distinguish between signals generated by voltage-gated calcium channels of different activation thresholds (Fig. 1E).

To evaluate the effects of each β-cell-derived component for sensing glucose [the glucose transporter 2 (GLUT2), glucokinase (GCK), ATP-sensitive potassium channel (K_{ATP}), and voltage-gated calcium channel (Ca_v1.3)] with the pMX57-based depolarization assay, we used a combinatorial screening approach (Fig. 2, A and B). Expression of K_{ATP} did not improve glucose sensing; overexpression of GLUT2 increased glucose-induced

¹Department of Biosystems Science and Engineering, ETH Zurich, Mattenstrasse 26, CH-4058 Basel, Switzerland.

²Shanghai Key Laboratory of Regulatory Biology, Institute of Biomedical Sciences and School of Life Sciences, East China Normal University, Dongchuan Road 500, 200241 Shanghai, China. ³Institut Universitaire de Technologie, IUT, Département Génie Biologique, F-69622 Villeurbanne Cedex, France. ⁴SIB-Swiss Institute of Bioinformatics, ETH Zurich, Mattenstrasse 26, CH-4058 Basel, Switzerland. ⁵University of Basel, Faculty of Science, Mattenstrasse 26, CH-4058 Basel, Switzerland.

*Corresponding author. Email: fussenegger@bsse.ethz.ch (M.F.); joerg.stelling@bsse.ethz.ch (J.S.)

calcium-dependent transcription; and GCK overexpression appeared to cause toxic effects at higher extracellular glucose concentrations (Fig. 2B). Indeed, semiquantitative transcriptional profiling confirmed that GLUT1 (24) as well as K_{ATP} are endogenously expressed in HEK-293 cells (fig. S1A), and most mammalian cells express at least one hexokinase isoform (25). Therefore, ectopic expression of the $Ca_v1.3$ channel was sufficient to confer glucose sensitivity to HEK-293 cells (Fig. 2B). In contrast, putative glucose sensors such as the T1R2/T1R3 sweet taste receptors (26) failed to respond to glucose concentrations relevant for glycemic control (fig. S1B). Therefore, $Ca_v1.3$ represents the missing component needed to reconstitute an intact, physiologically relevant glucose-sensing cascade in HEK-293 cells (Fig. 2A) and to establish mimetic β -cell function in nonpancreatic human cells.

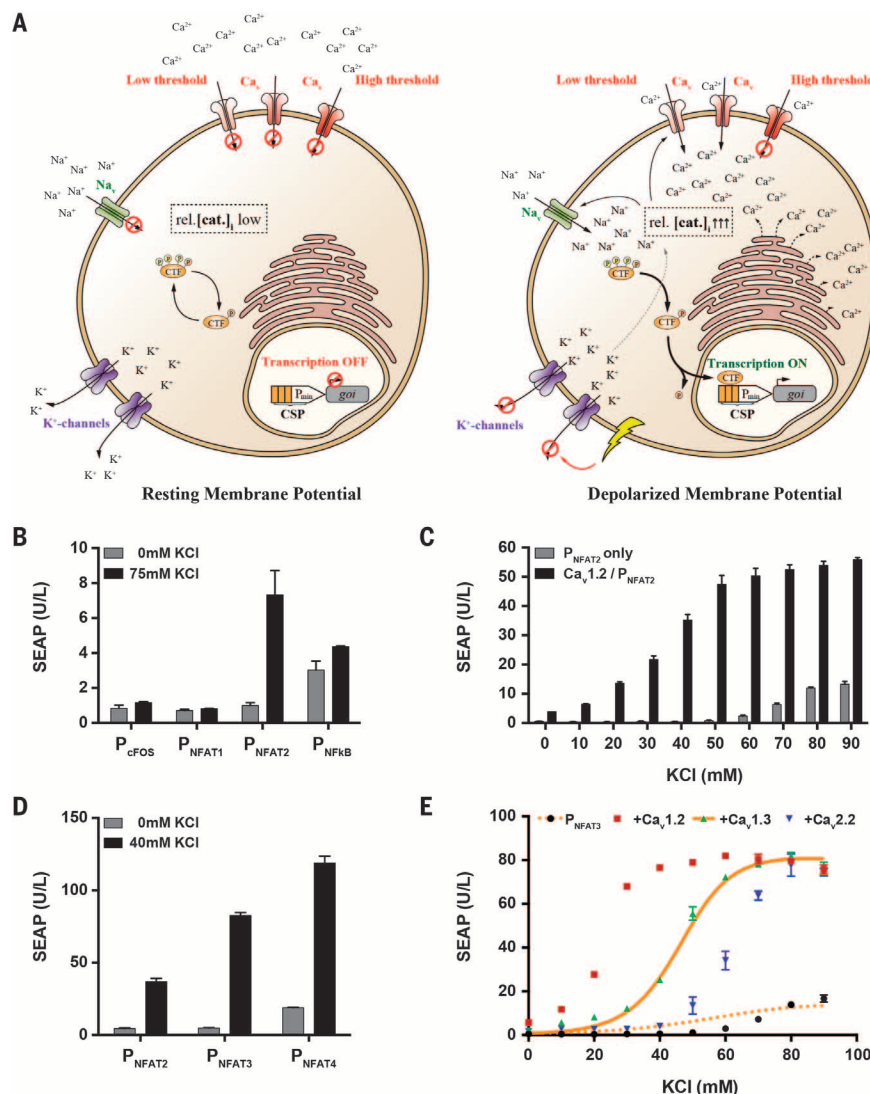
To quantitatively analyze the β -cell-derived glucose-sensing cascade, ensure consistency in the design steps, and predict circuit operation in vivo, we developed a dynamic mathematical model

(fig. S6 and supplementary methods). This ordinary differential equation (ODE) model covers the components shown in Fig. 2, a detailed representation of the cell's electrophysiology (fig. S7), and a previously developed representation of in vivo glucose-insulin regulation (21). We parametrized the model with experimental data across conditions and experimental assays (supplementary methods) to establish a single, quantitative representation of the system. The model reproduced, among others, the potassium (Fig. 1E) and glucose (Fig. 2B) dose-response curves; it was used for quantitative circuit characterization and essential predictions of in vivo behaviors.

To test the substrate specificity of the $Ca_v1.3$ / P_{NFAT3} -constituted glucose-sensing system, we cultured $Ca_v1.3$ /pMX57-transgenic HEK-293 cells in media containing osmotic controls (fig. S2A), common dietary sugars (fig. S2B), or other nutrients (fig. S2C). D-Glucose was the only substrate that activated human placental secreted alkaline phosphatase (SEAP) expression from the synthetic excitation-transcription coupling system at phys-

ologically relevant concentrations. Additionally, the glucose-sensing system was insensitive to inflammatory cytokines inducing NFAT signaling pathways (27) (fig. S2, D and E). Capitalizing on the tight induction kinetics of the P_{NFAT3} -regulated gene expression system (fig. S3) and on the system's strict $Ca_v1.3$ -dependent activation (fig. S4), we constructed a stable human HEK-293^{NFAT3-SEAP1} cell line transgenic for P_{NFAT3} -driven SEAP expression (fig. S5). Ectopic expression of the $Ca_v1.3$ channel in HEK-293^{NFAT3-SEAP1} resulted in improved induction ratios between low and high extracellular glucose concentrations (Fig. 2C; ~4.6 fold-induction from 5 to 25 mM glucose) compared to the transient configuration (Fig. 2B; ~2.6 fold-induction). Glucose-stimulated induction of $Ca_v1.3$ -transgenic HEK-293^{NFAT3-SEAP1} cells was significant within 24 hours and reached maximal SEAP levels after cultivation in high-glucose medium for 48 hours (Fig. 2D). Additionally, SEAP expression could be switched to dose-dependent regulation even after maintaining the $Ca_v1.3$ -transgenic HEK-293^{NFAT3-SEAP1} cells in low-glucose conditions (2 mM) for different

Fig. 1. Engineering of an excitation-transcription coupling system. (A) Diagram of the synthetic excitation-transcription coupling system. At resting membrane potentials, basal ion currents keep the relative concentration of intracellular cations (rel.[cat.]) low, the plasma membrane hyperpolarized, and calcium-specific promoters (CSPs) repressed. Blocking of K^+ channels or triggered cation entry increases rel.[cat.]; depolarizes the membrane potential, which is amplified by the opening of threshold-dependent voltage-gated sodium (Na_v) or calcium (Ca_v) channels; and promotes nuclear translocation of calcium-responsive transcription factors to induce CSP-driven gene expression. (B to E) Functional tests: cells were depolarized with KCl, and SEAP levels were profiled after 48 hours. (B) CSPs activated by chemically induced membrane depolarization: HEK-293 transfected with pMX53 (P_{cFOS} -SEAP-pA), pHY30 (P_{NFAT1} -SEAP-pA), pMX56 (P_{NFAT2} -SEAP-pA), or pKR32 (P_{NFkB} -SEAP-pA). (C) $Ca_v1.2$ -amplified excitation-transcription coupling: HEK-293 (co)transfected with pMX56 (P_{NFAT2} -SEAP-pA) and $Ca_v1.2$. (D) CSP optimization: HEK-293 cotransfected with $Ca_v1.2$ and CSP-driven SEAP expression vectors (pMX56, P_{NFAT2} -SEAP-pA; pMX57, P_{NFAT3} -SEAP-pA; pMX58, P_{NFAT4} -SEAP-pA). (E) Activation threshold-dependent excitation-transcription coupling: HEK-293 cotransfected with pMX57 and either $Ca_v1.2$, $Ca_v1.3$, or $Ca_v2.2$. Experimental (symbols) and simulation data (lines) are combined. All experimental data presented are mean \pm SD, $n \geq 5$ independent experiments.



periods of time (fig. S8A), and an independent time-course experiment showing glucose-mediated sensitization, as well as starvation-mediated desensitization, confirmed the reversibility of the synthetic excitation-transcription coupling system (fig. S8B). The mathematical model reproduced this behavior quantitatively (Fig. 2, C and D, and figs. S8B and S9), and independent predictions for varying $\text{Ca}_v1.3$ dosages agreed well with experiments (Fig. 2), emphasizing the model's consistency across constructs and conditions.

To test the potential of the glucose-induced excitation-transcription coupling system for diabetes treatment, we implanted $\text{Ca}_v1.3$ -transgenic HEK-293_{NFAT-SEAP1} cells microencapsulated in clinically validated alginate beads (28) intraperitoneally into mice. In vivo, our implanted transcriptional regulation system operated in a dose- and $\text{Ca}_v1.3$ -dependent manner, as recapitulated by the same in vitro dynamic model coupled to a mathematical representation of mouse physiology (fig. S10). Notably, the system translated the characteristic average fasting glycemia values of wild-type as well as T1D- and T2D-diabetic mouse models into correspondingly expressed SEAP levels in the serum (Fig. 3A and fig. S11).

State-of-the-art treatment options for diabetes mellitus are either long-acting drugs, such as stabilized GLP-1 variants that allow a decrease in

the administration frequency to weekly periods (T2D) (1, 29), or portable electronic pump systems that self-sufficiently inject rapid-acting insulin analogs according to the patient's instantaneous glycemia (T1D) (10, 30). To test whether the GLP-1 expression levels achieved by the glucose-inducible excitation-transcription coupling system were compatible with T2D treatment, we cotransfected HEK-293 cells with $\text{Ca}_v1.3$ and the short human GLP-1 (shGLP1) variant (18) (pMX115; P_{NFAT5}-shGLP1-pA), which enabled exclusive GLP-1 expression under hyperglycemic conditions (fig. S12A). Implanting 5×10^6 microencapsulated $\text{Ca}_v1.3$ /pMX115-transgenic HEK-293 cells into T2D mice resulted in self-sufficient GLP-1 expression (Fig. 3B) and substantially improved glucose-stimulated insulin secretion (Fig. 3C) and glucose tolerance (Fig. 3D). Similarly, cotransfection of $\text{Ca}_v1.3$ with an insulin expression vector (pMX100; P_{NFAT5}-mINS-pA) (21) provided hyperglycemia-triggered insulin expression (fig. S12B). In agreement between experiments and model, self-sufficient insulin expression from $\text{Ca}_v1.3$ /pMX100-transgenic implants not only restored the typical insulin deficiency in a T1D mouse model (fig. S13A) but also corrected the animals' persistent hyperglycemia within 2 to 3 days (fig. S13B). Notably, hypoglycemic side effects resulting from basal or excessive insulin expression at normoglycemic levels that

are often observed in classical insulin monotherapies (10) or with immature β cells (31) were not detected (fig. S13, A and B).

We conducted extensive simulation studies to systematically assess potential side effects associated with the robustness of hyperglycemia-triggered insulin expression when the patient's physiological state is unknown or changing. The model predicted that an implant would improve glucose tolerance (fig. S13, C and D) and might provide self-sufficient inactivation during parallel insulin therapies (fig. S13E) and/or reactivation in cases of recurrent β -cell loss (fig. S13F). Indeed, implantation of microencapsulated HEK- β cells (Fig. 4A) stably transgenic for reversible glucose-stimulated insulin secretion (figs. S14 and S15) restored glucose (Fig. 4B) and blood insulin homeostasis (Fig. 4C) in T1D mice as predicted by the mathematical model (fig. S13). Glucose homeostasis of treated T1D mice was robust during the entire 3-week study (Fig. 4B), and treated animals challenged by glucose tolerance tests (Fig. 4D) to simulate meal responses did not suffer from glycemic excursions during the HEK- β -mediated restoration of normoglycemia (Fig. 4B). In contrast, T1D mice receiving negative-control implants ($\text{Ca}_v1.3$ /pMX115-transgenic HEK-293 cells) remained hyperglycemic and did not survive the first glucose tolerance test at day 7 (Fig. 4, B and D).

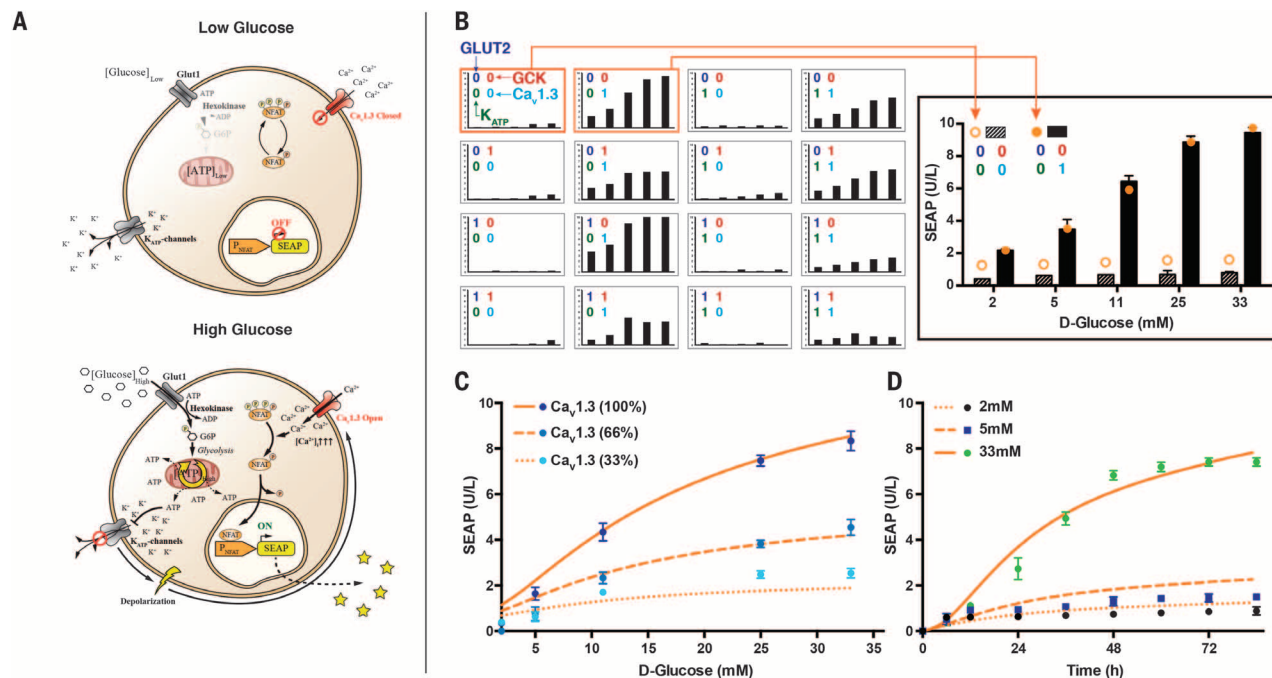


Fig. 2. Glucose sensing by extrapancreatic human cells. (A) Diagram of glucose sensing in engineered HEK-293 cells. Low extracellular glucose does not lead to membrane depolarization-based activation of voltage-gated $\text{Ca}_v1.3$ channels. High extracellular glucose results in glucose uptake, increased adenosine 5'-triphosphate (ATP) production, closure of ATP-sensitive potassium channels (K_{ATP}), $\text{Ca}_v1.3$ -mediated Ca^{2+} influx, and calcineurin-dependent SEAP induction by synthetic P_{NFAT} promoters. (B) Combinatorial analysis of glucose-sensing components in extrapancreatic human cells. HEK-293 cotransfected with pMX57 (P_{NFAT3}-SEAP-pA) and either constitutive hGLUT2,

GSK, K_{ATP} , $\text{Ca}_v1.3$ expression vectors (1), or pcDNA3.1(+) (0) were cultivated at the indicated glucose concentrations, and SEAP levels were profiled after 48 hours. (C) $\text{Ca}_v1.3$ -dependent glucose sensing. HEK-293_{NFAT-SEAP1} transfected with different amounts of $\text{Ca}_v1.3$ (100%: 2000 ng) were cultivated at different glucose concentrations and SEAP levels were profiled after 48 hours. (D) SEAP expression kinetics. $\text{Ca}_v1.3$ -transgenic HEK-293_{NFAT-SEAP1} were cultivated at the indicated glucose concentrations, and SEAP levels were profiled at 12-hour intervals. Orange lines and dots show corresponding simulations. Data presented are mean \pm SD, $n \geq 5$ independent experiments.

β cells modulate insulin release not only in response to glucose but also by the action of glucorecretins such as GLP-1 (29). We therefore engineered HEK-293 for HEK- β componentry, as well as for constitutive expression of the GLP-1 receptor (GLPIR) and P_{CRE} -driven insulin expression (Fig. 4E). The resulting HEK- β_{GLP} showed insulin secretion dynamics (fig. S16) similar to that of HEK- β , but was also sensitive to the animals' food intake (Fig. 4F). Although HEK- β_{GLP} was similar to HEK- β in attenuating glycemic excursions in oral glucose tolerance tests (Fig. 4G), glucose homeostasis was less efficiently restored in T1D mice compared to HEK- β (Fig. 4H). This finding was confirmed by model simulations (fig. S17) and established HEK- β as the prime β -cell-mimetic design.

In a comparative analysis of reversible glucose-stimulated insulin secretion by HEK- β , the pancreatic β -cell line 1.1E7 (32), and human islets over 3 weeks, HEK- β showed higher insulin secretion capacity than 1.1E7 and human islets in vitro (fig. S15C). In T1D mice, microencapsulated HEK- β and 1.1E7 were equally efficient in establishing postprandial glucose metabolism (Fig. 4G), but HEK- β restored glucose homeostasis more efficiently than 1.1E7 after 2 weeks and reached fasting glycemia levels of wild-type mice over the 3-week period (Fig. 4B). With human islets, postprandial glucose metabolism could only be restored in two out of four T1D mice (fig. S18), which confirms performance variations of encapsulated human islets (28). However, in these two T1D mice, the human islets provided glucose tolerance similar to that of HEK- β (Fig. 4D).

State-of-the-art strategies for cell-based treatment of diabetes include a variety of approaches

such as islet transplantation (33), differentiation of β -like cells from pluripotent precursor cells using culture additives (9, 13) or genetic lineage-control networks (34), and designer cells engineered for trigger-controlled insulin or GLP-1 secretion (17, 18). β -cell mimetics coordinate precise sensing of blood-glucose concentrations and insulin production in a dose-dependent, reversible, and closed-loop manner. The quest for biological glucose sensors has resulted in the design of several biosensors, but they were either not sufficiently sensitive (26) or quantified glucose indirectly (27). By contrast, our strategy to evaluate the components managing glucose sensing in native β cells has revealed $Ca_v1.3$ as the single most important component that programs extrapancreatic human cells such as HEK-293 to profile physiological blood-glucose concentrations in a precise, reversible, and dynamic fashion. Coupling of $Ca_v1.3$ -based glucose sensing to insulin production and secretion resulted in the β -cell-mimetic HEK- β that provided increased 3-week insulin secretion profiles compared to the pancreatic cell line 1.1E7 and human islets in vitro. Control of postprandial glucose metabolism was similar between HEK- β and 1.1E7, but only HEK- β reached the blood glucose concentrations of healthy mice. Because the different insulin-release dynamics of HEK- β , 1.1E7, and human islets in vitro had no substantial impact on postprandial glucose metabolism, the differences in the secretion modality—constitutive for HEK- β , vesicular for 1.1E7 and human islets—may not be as relevant in response to meals as generally thought. This is supported by our model simulations and by the latest generation of basal insulin analogs such as insulin degludec (Tresiba, Novo Nordisk), which provides autonomous glucose control for up to 42 hours

without the need to synchronize its administration with meals (35).

Human islets seem to be the optimal choice for cell-based diabetes therapies because the β cells are embedded in an organ structure, providing optimal support for glycemic control (31). However, human islets are in chronically short supply (34) and difficult to maintain in culture, and as a result of quality variations of available donor batches, treatment success remains unpredictable (37). Although immortalized β -cell lines have been developed to overcome the cultivation and quality issues of human islets, none of the available β -cell lines shows the performance level of glucose-induced insulin release required for successful diabetes therapy (32). Therefore, recent strategies for cell-based diabetes treatment focus on differentiation of (induced pluripotent) stem cells into β -like cells using mixtures of chemicals and growth factors (9, 13) or rational programming by synthetic lineage-control networks (34). Although β -like cells produced from in vitro-differentiated pancreatic progenitor cells may have a promising future (clinical trial NCT02239354), available differentiation protocols are complex, expensive, and likely incompatible with large-scale bioprocessing. Additionally, in vitro-differentiated β -like cells require considerable time to mature into β cells after implantation, which may limit the life span of the implant before inactivation by fibrosis (36). β -cell-mimetic designer cells such as HEK- β could provide an attractive alternative: (i) They use glucose-sensor components evolved in native β cells (19), (ii) take advantage of robust parental cell lines with a track record in biopharmaceutical manufacturing (37), and (iii) show glucose-induced insulin release performance comparable to that of β -cell lines and

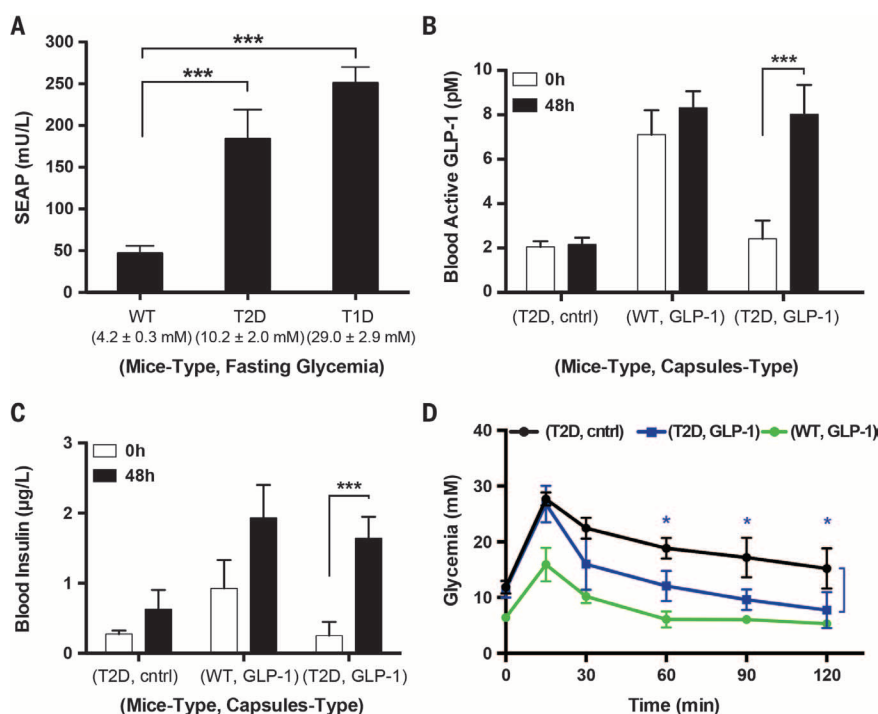
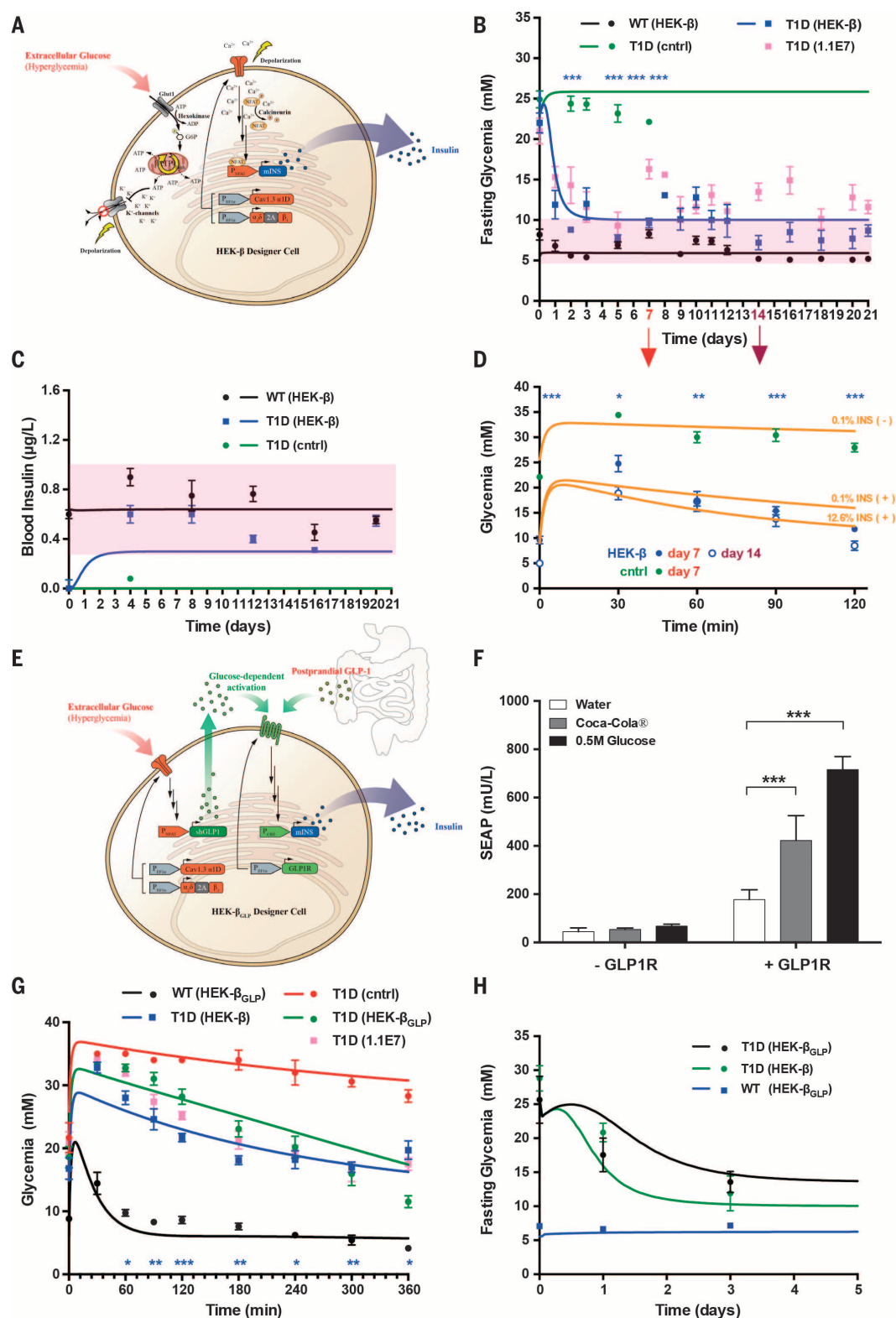


Fig. 3. $Ca_v1.3$ -dependent glucose sensing and anti-diabetic treatment potential in diabetic mice. (A) Dose-dependent glycemia-induced SEAP expression in diabetic mice. Microencapsulated $Ca_v1.3$ -transfected HEK-293_{NFAT-SEAP1} (1×10^4 ; 500 cells per capsule) were implanted into mice suffering from type 1 (T1D) or type 2 (T2D) diabetes, and blood SEAP levels were quantified after 48 hours. (B and C) Self-sufficient GLP-1 expression in wild-type (WT) and T2D mice. Microencapsulated HEK-293 cells cotransfected with $Ca_v1.3$ and pMX115 (P_{NFAT} -shGLP1-pA) (1×10^4 ; 500 cells per capsule) were implanted into WT or T2D mice, and blood GLP-1 (B) as well as insulin (C) concentrations were quantified after 48 hours. Microencapsulated $Ca_v1.3$ -transgenic HEK-293_{NFAT-SEAP1} cells were used as a negative control (cntrl). (D) Intraperitoneal glucose tolerance test of WT and T2D mice. Treatment groups shown in (B) and (C) received intraperitoneal glucose injections (2 g per kilogram of body weight) 48 hours after implantation, and glycemic profiles of each animal were tracked every 30 min. Data are mean \pm SEM; analysis was by two-tailed *t* test ($n = 8$ mice). **P* < 0.05, ****P* < 0.001 versus control.

Fig. 4. Treatment potential of β -cell-mimetic designer cells in T1D mice.

(A) Diagram of HEK- β . Extracellular D-glucose triggers glycolysis-dependent membrane depolarization, which activates the voltage-gated calcium channel $\text{Ca}_v1.3$, resulting in Ca^{2+} influx, induction of the calmodulin-calcineurin signaling cascade, and P_{NFAT} -mediated induction of insulin secretion. **(B)** Self-sufficient glyce-mic control in WT and T1D mice. Microencapsulated HEK- β or 1.1E7 cells (500 cells per capsule) were implanted into WT and T1D mice (1×10^4 capsules per mouse), and fasting glycemia was recorded for 3 weeks. T1D mice treated with negative-control implants ($\text{Ca}_v1.3/\text{pMX115}$ -transgenic HEK-293; cntrl) did not survive the first glucose tolerance test on day 7 (D). **(C)** Self-sufficient insulin expression in WT and T1D mice. Postprandial blood insulin concentrations of treatment groups shown in (B) were profiled for up to 3 weeks. Curves of matching colors [(B) and (C)] represent corresponding model-based predictions. Physiological blood glucose and insulin concentrations are indicated by a red background. **(D)** Intra-peritoneal glucose tolerance tests in T1D mice. On days 7 and 14 (arrows), treatment groups shown in (B) and (C) received intraperitoneal glucose injections (2 g/kg), and glycemic profiles of each animal were tracked every 30 min. Orange lines represent model-based predictions with 0.1 to 12.6% residual insulin production treated with (+) or without (-) HEK- β implants (-, S13C). **(E)** Diagram of HEK- β_{GLP} . Glucose triggers dose-dependent P_{NFAT} -driven expression of glucagon-like peptide 1 (shGLP1) for autocrine activation of ectopically expressed GLP-1 receptor (GLP1R), leading to P_{CRE} -driven insulin secretion. In vivo, insulin expression by HEK- β_{GLP} cells may also be triggered following postprandial GLP-1 release by intestinal cells. **(F)** Response of β -cell-mimetic implants to meals. WT mice were implanted with 5×10^6 micro-encapsulated $\text{Ca}_v1.3/\text{pMX57}$ -transgenic HEK-293 cells (-GLP1R) or $\text{Ca}_v1.3/\text{pMX61}/\text{pMX258}$ -transgenic HEK- β_{GLP1R} cells (+GLP1R) and received oral doses of 200 μl of H₂O, Coca-Cola, or sugared water (0.5 M glucose). Resulting blood SEAP levels were quantified after 48 hours. **(G)** Oral glucose tolerance test of WT and T1D mice. Mice received 5×10^6 microencapsulated HEK- β , 1.1E7 or HEK- β_{GLP} or negative-control implants (cntrl; $\text{Ca}_v1.3/\text{pMX115}$ -transgenic HEK-293). After oral administration of sugared water (2 g/kg glucose in H₂O), glycemic excursions were recorded for 6 hours. Curves of matching colors represent corresponding model simulations. **(H)** Self-sufficient glyce-mic control by implanted HEK- β and HEK- β_{GLP} . Microencapsulated HEK- β or HEK- β_{GLP} cells (5×10^6) were implanted into WT or T1D mice (1×10^4 capsules per mouse), and fasting glycemia was recorded for 3 days. Curves of matching colors represent corresponding model simulations. Data are mean \pm SEM, statistics by two-tailed t test ($n = 8$ mice). * $P < 0.05$, ** $P < 0.01$, *** $P < 0.001$ HEK- β versus control.



human islets. Additionally, rational programming of designer cells enables (iv) straightforward fine-tuning of performance parameters and provides (v) flexibility to couple glucose sensing to the production of other therapeutic proteins such as GLP-1 required for T2D therapy (1, 29).

REFERENCES AND NOTES

1. S. Cornell, *Ther. Clin. Risk Manag.* **11**, 621–632 (2015).
2. J. Tuomilehto, S. Bahjri, *Nat. Rev. Endocrinol.* **12**, 127–128 (2016).
3. K. S. Polonsky, *N. Engl. J. Med.* **367**, 1332–1340 (2012).
4. S. J. Cleland, *Nat. Rev. Endocrinol.* **8**, 476–485 (2012).
5. G. I. Shulman, *N. Engl. J. Med.* **371**, 1131–1141 (2014).
6. S. M. Grundy, *Nat. Rev. Drug Discov.* **5**, 295–309 (2006).
7. P. M. Rao, D. M. Kelly, T. H. Jones, *Nat. Rev. Endocrinol.* **9**, 479–493 (2013).
8. J. E. Bruin et al., *Stem Cell Rep.* **4**, 605–620 (2015).
9. A. Rezaei et al., *Nat. Biotechnol.* **32**, 1121–1133 (2014).
10. J. C. Pickup, *N. Engl. J. Med.* **366**, 1616–1624 (2012).
11. D. J. Drucker, M. A. Nauck, *Lancet* **368**, 1696–1705 (2006).
12. G. M. Church, M. B. Elowitz, C. D. Smolke, C. A. Voigt, R. Weiss, *Nat. Rev. Mol. Cell Biol.* **15**, 289–294 (2014).
13. F. W. Pagliuca et al., *Cell* **159**, 428–439 (2014).
14. B. E. Tuch et al., *Gene Ther.* **10**, 490–503 (2003).
15. C. Aguayo-Mazzucato, S. Bonner-Weir, *Nat. Rev. Endocrinol.* **6**, 139–148 (2010).
16. L. Marzban et al., *Diabetes* **55**, 2192–2201 (2006).
17. S. A. Stanley et al., *Science* **336**, 604–608 (2012).
18. H. Ye, M. Daoud-El Baba, R. W. Peng, M. Fusseneberger, *Science* **332**, 1565–1568 (2011).
19. F. M. Ashcroft, P. Rorsman, *Nat. Rev. Endocrinol.* **9**, 660–669 (2013).
20. M. D'Arco, A. C. Dolphin, *Sci. Signal.* **5**, pe34 (2012).
21. D. Ausländer et al., *Mol. Cell* **55**, 397–408 (2014).
22. H. Ye et al., *Proc. Natl. Acad. Sci. U.S.A.* **110**, 141–146 (2013).
23. J. W. Rooney, M. R. Hodge, P. G. McCaffrey, A. Rao, L. H. Glimcher, *EMBO J.* **13**, 625–633 (1994).
24. M. Elsner, M. Tiedge, B. Guldakke, R. Munday, S. Lenzen, *Diabetologia* **45**, 1542–1549 (2002).
25. R. B. Robey, N. Hay, *Oncogene* **25**, 4683–4696 (2006).
26. H. J. Jang et al., *Proc. Natl. Acad. Sci. U.S.A.* **104**, 15069–15074 (2007).
27. F. Macian, *Nat. Rev. Immunol.* **5**, 472–484 (2005).
28. A. J. Vegas et al., *Nat. Med.* **22**, 306–311 (2016).
29. G. G. Holz 4th, W. M. Kühtreiber, J. F. Habener, *Nature* **361**, 362–365 (1993).
30. S. J. Russell et al., *N. Engl. J. Med.* **371**, 313–325 (2014).
31. T. J. Kieffer, *Cell Stem Cell* **18**, 699–702 (2016).
32. J. T. McCluskey et al., *J. Biol. Chem.* **286**, 21982–21992 (2011).
33. D. W. Scharp, P. Marchetti, *Adv. Drug Deliv. Rev.* **67**, 68, 35–73 (2014).
34. P. Saxena et al., *Nat. Commun.* **7**, 11247 (2016).
35. A. N. Zaykov, J. P. Mayer, R. D. DiMarchi, *Nat. Rev. Drug Discov.* **15**, 425–439 (2016).
36. M. Kastellorizios, N. Tzipnis, D. J. Burgess, *Adv. Exp. Med. Biol.* **865**, 93–108 (2015).
37. F. M. Wurm, *Nat. Biotechnol.* **22**, 1393–1398 (2004).

ACKNOWLEDGMENTS

We thank V. Haellman and H. Zulewski for critical comments on the manuscript. This work was supported by a European Research Council advanced grant (ProNet no. 321381) and in part by the Natural Science Foundation of China (no. 31522017) and the National Centre of Competence in Research Molecular Systems Engineering. All data supporting the findings of this study are presented in the main paper and supplementary materials. Plasmids are available from M.F. on request. M.X. and M.F. are inventors on a patent application filed by the ETH Zurich on the β -cell mimetic designer cells (application nos. EP16180000.8 and EP16200258.8). M.X., H.Y., H.W., P.S. and G.C. conducted the experiments; C.L., M.X., and J.S. developed the mathematical model; M.X., C.L., J.S., and M.F. designed the experiments and wrote the manuscript.

SUPPLEMENTARY MATERIALS

www.sciencemag.org/content/354/6317/1296/suppl/DC1
Materials and Methods
Supplementary Text
Figs. S1 to S18
Tables S1 to S12
References (38–62)

4 February 2016; accepted 10 November 2016
10.1126/science.aaf4006

VIRAL EVOLUTION

Ecological speciation of bacteriophage lambda in allopatry and sympatry

Justin R. Meyer,^{1,*} Devin T. Dobias,^{2,3} Sarah J. Medina,¹ Lisa Servilio,¹ Animesh Gupta,⁴ Richard E. Lenski⁵

Understanding the conditions that allow speciation to occur is difficult because most research has focused on either long-lived organisms or asexual microorganisms. We propagated bacteriophage λ , a virus with rapid generations and frequent recombination, on two *Escherichia coli* host genotypes that expressed either the LamB or OmpF receptor. When supplied with either single host (allopatry), phage λ improved its binding to the available receptor while losing its ability to use the alternative. When evolving on both hosts together (sympatry), the viruses split into two lineages with divergent receptor preferences. Although the level of divergence varied among replicates, some lineages evolved reproductive isolation via genetic incompatibilities. This outcome indicates that, under suitable conditions, allopatric and sympatric speciation can occur with similar ease.

Studies of extant and extinct species provide evidence that biological evolution can promote diversification rather than mere replacement of one form by another (1). Moreover, asexual microbes frequently diversify when cultured in the laboratory (2), even in simple conditions that would seem to favor homogeneity (3). Sympatric diversification in sexual populations has long been thought to be difficult because constant recombination prevents an interbreeding population from splitting into genetically distinct lineages that occupy different ecological niches (4, 5). However, putative examples of sympatric speciation have advanced the argument that speciation in a recombining population may occur under certain circumstances (6, 7), although other studies have disputed these claims (8). This debate is important because the process of speciation is fundamental to biological evolution.

To shed light on this question, we conducted evolution experiments with viruses to examine the effect of recombination on their divergence into distinct ecological niches. We studied a virulent (i.e., strictly lytic) derivative of phage λ , which infects *Escherichia coli*. Most λ can use only a single outer-membrane protein, LamB, as a receptor, but the strain we studied, EvoC, can also exploit a second receptor, OmpF (9). The ability

to use OmpF arose via five point mutations in the host-recognition gene, *J*. To examine λ diversification, we propagated virus populations on one or both of two strains of *E. coli* that differ only in whether they possess the *lamB* or *ompF* genes, which encode LamB and OmpF, respectively (10). Phages tend to exploit specific receptors (11), leading us to predict that populations of the generalist phage EvoC would evolve toward increased receptor specificity. Whether or not two receptor specialists evolved, however, would likely also depend on the effects of recombination. When two or more λ viruses infect the same cell, their genomes can recombine (12).

We use λ as a model for analyzing the mechanisms of speciation. Viruses are diverse (13), and their rates and mechanisms of speciation will depend on their life histories, just as the rates and mechanisms vary in plants and animals. However, some salient features of speciation are shared, even across such distant taxa. For example, viruses that infect the same species and cell types are thought to have evolved mechanisms to limit recombination, including divergences in nucleotide composition and RNA structure that are analogous to prezygotic barriers in plants and animals (14–16). One feature of our system that might promote sympatric speciation is the connection between the viruses' ecological niches (i.e., host cells) and where genetic exchange occurs. Specialists that use the same receptor will naturally tend to recombine because they are more likely to infect the same host. Therefore, reproductive isolation can evolve as a by-product of ecological divergence, without requiring other mutations that govern recombination. Such dual-effect mutations have been described in other systems and are important because their simultaneous effects on ecological niches and mating

¹Division of Biology, University of California San Diego (UCSD), La Jolla, CA 92093, USA. ²Department of Biology, Washington University, St. Louis, MO 63130, USA.

³Department of Biology, Loyola University Chicago, 1032 West Sheridan Road, Chicago, IL 60660, USA. ⁴Department of Physics, UCSD, La Jolla, CA 92093, USA. ⁵Department of Microbiology and Molecular Genetics and BEACON Center for the Study of Evolution in Action, Michigan State University, East Lansing, MI 48824, USA.

*Corresponding author. Email: justin.raymond.meyer@gmail.com

Fig. 1. Specialization in allopatry and sympatry.

Phage λ populations 1 to 6 evolved with OmpF-only host cells, populations 7 to 12 with LamB-only cells, and populations 13 to 18 with both types.

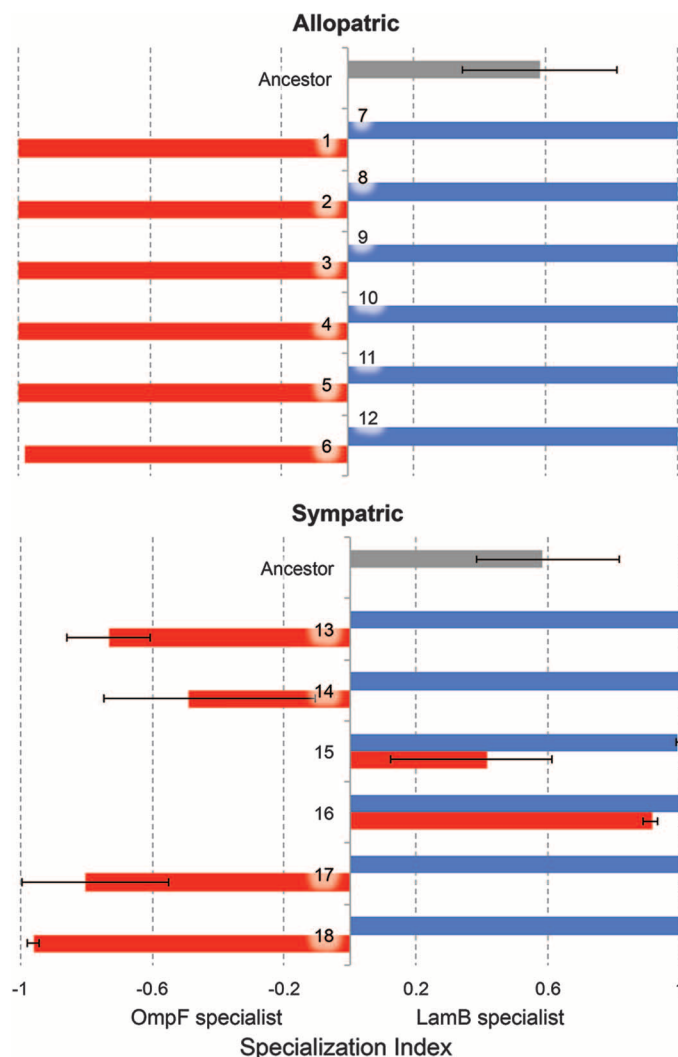
Specialization index =

$$\frac{(\text{plaques}_{\text{LamB}} - \text{plaques}_{\text{OmpF}})}{(\text{plaques}_{\text{LamB}} + \text{plaques}_{\text{OmpF}})}$$

Index values of 1 and -1 indicate complete LamB and OmpF specialization, respectively.

Values for populations 1 to 12 were measured using samples of the entire λ population.

Using whole-population samples for populations 13 to 18 would hide the underlying diversity of specialists, so each bar shows the mean of six phages isolated on either OmpF-only (red bars) or LamB-only (blue bars) hosts. Error bars denote 95% confidence intervals.



propensities promote speciation when resources are patchily distributed (17–19).

We propagated six initially homogeneous and identical populations of λ strain EvoC for 35 cycles of dilution into host populations containing an equal mix of genotypes expressing either the LamB or OmpF receptor (20). The high initial ratio of viruses ($\sim 10^8$) to bacteria ($\sim 2 \times 10^6$) increases the opportunity for co-infection and recombination. After 8 hours, surviving bacteria were killed to stop the host population from evolving resistance, and a new cycle of viral reproduction was initiated by transferring 1% of the phage into a fresh population of naive bacteria. Twelve other phage populations were also cultured with a single host type (half expressing only LamB and half expressing only OmpF). We describe these single-host populations as allopatric because the separate flasks prevent viruses that use different hosts from recombining at any point in time. We call the mixed-host treatments sympatric because viruses that infect the different host types in one generation may infect the same host and recombine in the next generation. One caveat to this

terminology is that viral recombination can only occur within host cells, thereby introducing a subtle fine-scale spatial element to the sympatric treatment.

Strong receptor specialization evolved in all 12 single-host populations (Fig. 1). All six phage populations (7 to 12) that evolved with only the LamB-expressing hosts could no longer produce plaques on OmpF cell lawns (20). Five of six populations (1 to 5) propagated on only the OmpF-expressing cells evolved similar specialization; one population (6) continued to produce plaques on LamB hosts but at lower levels than on OmpF hosts. The ancestral phage EvoC produced plaques on both hosts, although more on the type expressing the LamB receptor (Fig. 1).

To determine whether phage performance on the two hosts also diverged when phages evolved on mixed hosts, we isolated six phages that produced plaques on LamB hosts and six on OmpF hosts from each sympatric-treatment population. We performed the same assay on these 72 isolates as on the single-host populations (Fig. 1). Four populations (13, 14, 17, and 18) evolved both OmpF

and LamB specialists, although most were not as specialized as those that evolved in allopatry. Two populations (15 and 16) contained a mixture of LamB specialists and generalists that, like the ancestral phage, could infect both LamB and OmpF hosts. Therefore, diversification occurred in sympatry as well as in allopatry.

Models of adaptive radiations indicate that ecological speciation requires a trade-off in the ability to use different resources (21). Moreover, the relation must be convex, such that a diminished ability to use one resource is outweighed by an improvement on the alternative. We measured the adsorption rates for the ancestor and two isolates from each sympatric population, one isolated on OmpF-only cells and the second on LamB-only cells (Fig. 2). In all six cases, the ancestral values fell below the line connecting the evolved isolates (sign test, one-tailed $P = 0.0156$). This pattern indicates that mutations that increase specialization provide greater gains in adsorption rate on the focal receptor than losses on the alternative one. With all else being equal, natural selection should favor specialization and drive diversification. Adsorption rate is an important component of phage fitness, but not every adsorption event necessarily leads to a productive infection. Nonetheless, the correlation in receptor specialization based on adsorption rates and plaque formation is highly significant (20) (fig. S1).

We sequenced the host-recognition gene, *J*, from one phage isolated on each host from the mixed-host populations, one from each OmpF-only population, and one from five of the six LamB-only populations (20). (Population 8 was not represented because the sample failed to preserve.) In total, we found 67 substitutions at 28 different positions. All were nonsynonymous and in the reactive region of the host-recognition J protein (22), indicating that they were likely adaptive (Fig. 3A). The LamB specialists had fewer mutations than the OmpF specialists (means of 1.41 and 4.54, respectively; $t = 9.93$, $df = 21$, two-tailed $P < 0.0001$). It is not surprising that the LamB specialists had fewer mutations, given that the most recent ancestor (EvoC) favored LamB and that the ancestor of EvoC (λ strain cI26) only used LamB. In general, the evolved LamB specialists did not reacquire that preference via reversion; only 1 of the 12 sequenced alleles reverted at a single site of the five that distinguish EvoC from cI26 (a2988c in population 17). Only two sites had mutations in both LamB and OmpF specialists, whereas 10 sites had parallel substitutions across independently evolved specialists of the same type.

A cluster analysis performed on the basis of the genetic distance among *J* alleles shows the different pattern of substitutions between the LamB and OmpF specialists (20) [analysis of similarities (ANOSIM) $R = 0.659$, $P = 0.0001$ (Fig. 3B)]. Phages isolated on the same host genotype but from different flasks had more similar *J* alleles than phages isolated from the same flask but specialized on different hosts. By contrast, there are no compelling differences between phages specialized on the same host type but

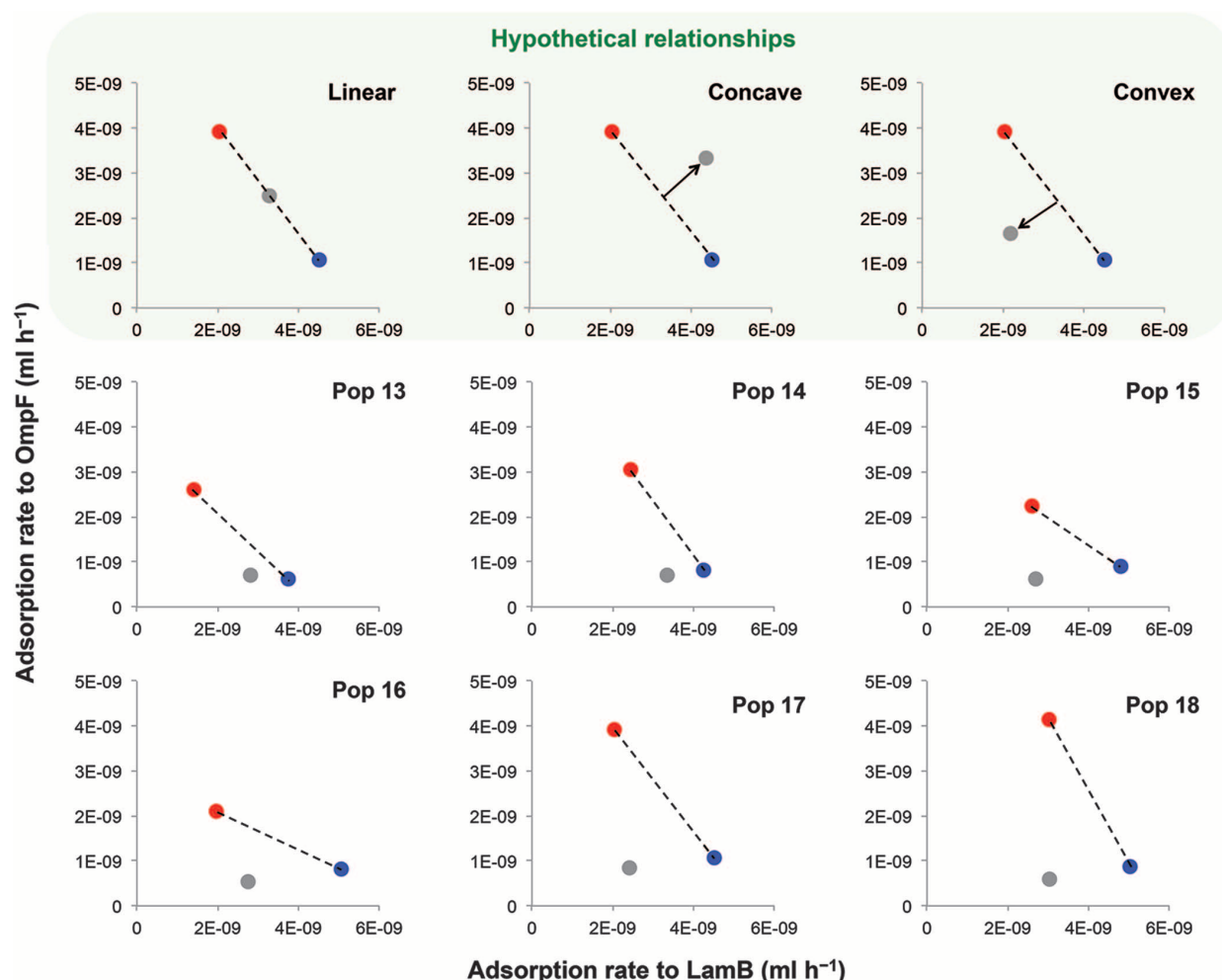


Fig. 2. Adsorption rates for two isolates from each sympatric population and the ancestor. The three top panels show hypothetical locations of the ancestor relative to evolved isolates. The six panels below show the data for each population that evolved on mixed hosts. Red symbols indicate phages isolated on OmpF-only hosts, blue symbols indicate phages isolated on LamB-only hosts, and gray symbols show the ancestor (EvoC). The ancestral rates were separately measured for each panel to ensure independence. See text for statistical analysis.

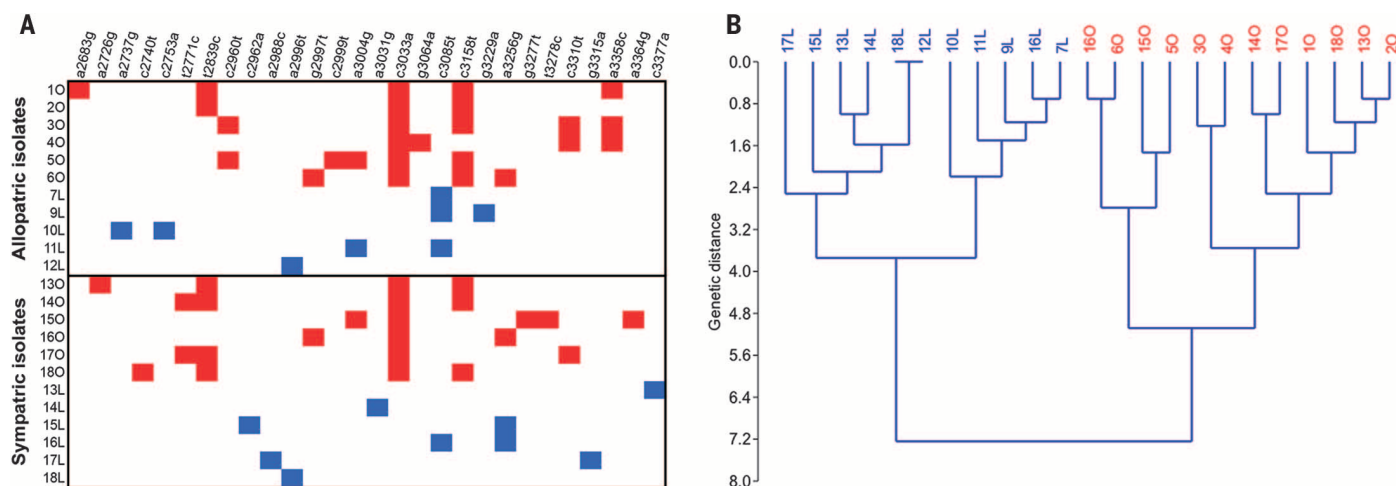
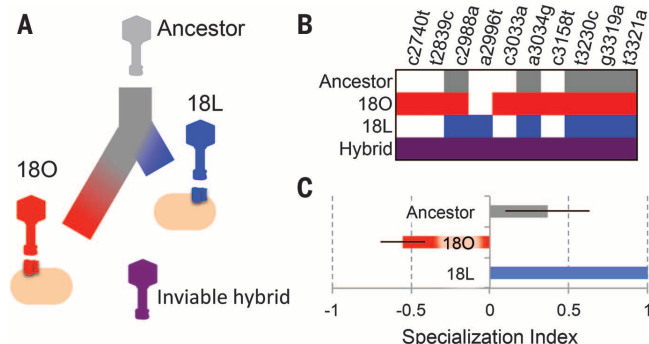


Fig. 3. Genetic signatures of ecological diversification. (A) Substitutions in the *J* gene from λ isolated from allopatric and sympatric treatments. Rows are λ isolates; columns are mutations. Red and blue fill shows mutations in phages isolated on OmpF-only and LamB-only hosts, respectively. (B) Cluster analysis using Ward's method separates alleles from independently evolved phages isolated on OmpF-only and LamB-only hosts, regardless of allopatric or sympatric treatment.

Fig. 4. Phage genotypes engineered to test interaction of mutations from *OmpF* and *LamB* specialists.

(A) Schematic of phage diversification in population 18 and the engineered hybrid of the two specialists. (B) Engineered *J* alleles. Colored fill shows mutations in engineered phages relative to the lysogenic phage background, c1857, used to engineer the four alleles shown. (C) Specialization index from plaque assays for the ancestor and two engineered specialists. The engineered hybrid with one *LamB*- and four *OmpF*-specific mutations did not produce plaques on either host. Error bars indicate 95% confidence intervals.



evolved in allopatry versus sympatry (20) (ANOSIM $R = 0.075$, $P = 0.1336$). These patterns indicate that selection in the two-host sympatry treatment drove the generalist phage populations to diverge into two subpopulations with distinctive genomes and preferences for the different receptors.

Another layer of reproductive isolation may arise along with host preference, if the mutations for *LamB* and *OmpF* specialization are incompatible. The Dobzhansky-Muller model predicts that speciation will occur if hybrids have lower fitness than their parents, reducing effective gene flow (23). To examine this possibility, we focused on population 18, where the *LamB* and *OmpF* specialists had one and four mutations, respectively, in the *J* gene (Fig. 3A). Using multiplexed automated genome engineering (MAGE) (20, 24) to edit a lysogenic strain of phage, c1857, we constructed alleles corresponding to the ancestral EvoC strain, the *LamB* specialist, the *OmpF* specialist, and a hybrid with all five mutations from the two specialists (Fig. 4, A and B). As expected, the constructed strains with the evolved alleles were specialists, and the one with the EvoC allele was a generalist (Fig. 4C). These observations indicate that the mutations in *J* are responsible for most, if not all, of the divergence in receptor preferences. Whole-genome sequencing of the specialists 18O and 18L revealed four additional mutations, but they occur in genes unlikely to affect interactions with the host receptor (20). Sympatric speciation is more feasible when a single gene has a large effect on ecological differentiation because it reduces the extent to which recombination could prevent divergence. Other studies of newly formed species have also found that variation in one or a few genomic regions accounts for most reproductive isolation (25).

Our first attempt to construct a hybrid between the *LamB* and *OmpF* specialists produced no viable phage, which suggests that the hybrid might not be viable. Our second attempt, however, produced a few infectious phages. Given this discrepancy, we hypothesized that the viable phages may have resulted from reversion or compensatory mutations that occurred during the

MAGE procedure. To test this, we sequenced the reactive region of *J* for five randomly chosen hybrids. All five had reverted the a2996t mutation to the ancestral state, removing the single *LamB*-specialization mutation and thereby recreating the *OmpF*-specialized allele. Thus, we found no viable true hybrids, providing evidence that the mutations that encode *OmpF* and *LamB* specialization are incompatible.

Our results show that λ likely evolved two mechanisms of reproductive isolation: (i) divergent host use leading to positive assortative recombination and (ii) genetic incompatibilities. These barriers satisfy the criteria for the biological species concept (5, 26). The distinctive ecological niches and genomic changes in the specialist phages also fulfill some other species definitions (27, 28). However, the specialists fall far short of a widely used criterion in phage taxonomy, namely <70% sequence similarity (28). We take this discrepancy to mean that we have observed the essential processes that can lead to speciation, but they have not operated long enough for the specialists to be classified as distinct species.

Four features of the experimental system contributed to the success of sympatric speciation and the speed with which it occurred. First, the convex trade-off between exploiting the two hosts set the stage for specialists to evolve. Second, the homogenizing effect of recombination was limited because a few mutations in a single gene accomplished this specialization. Third, the connection between host use and reproduction generated a barrier to gene flow as a by-product of natural selection. Fourth, the mutations that improved use of the alternative receptors were incompatible, preventing gene flow between the lineages. Determining how widespread these features are in nature remains an important empirical challenge. Understanding which features, if any, can be relaxed without disrupting speciation is both a theoretical and an empirical challenge.

REFERENCES AND NOTES

1. D. Schluter, *The Ecology of Adaptive Radiation* (Oxford Univ. Press, 2000).

2. R. Kassen, *Experimental Evolution and the Nature of Biodiversity* (Roberts, 2014).
3. P. B. Rainey, M. Travisano, *Nature* **394**, 69–72 (1998).
4. S. Gavrilits, *J. Hered.* **105** (suppl. 1), 743–755 (2014).
5. E. Mayr, *Animal Species and Evolution* (Belknap Press, 1963).
6. M. Barluenga, K. N. Stölting, W. Salzburger, M. Muschick, A. Meyer, *Nature* **439**, 719–723 (2006).
7. J. L. Feder, C. A. Chilcote, G. L. Bush, *Nature* **336**, 61–64 (1988).
8. C. H. Martin et al., *Evolution* **69**, 1406–1422 (2015).
9. J. R. Meyer et al., *Science* **335**, 428–432 (2012).
10. T. Baba et al., *Mol. Syst. Biol.* **2**, 2006.0008 (2006).
11. A. A. Lindberg, *Annu. Rev. Microbiol.* **27**, 205–241 (1973).
12. A. R. Poteete, *FEMS Microbiol. Lett.* **201**, 9–14 (2001).
13. A. T. Peterson, *Virology* **11**, 131 (2014).
14. G. A. Schachtel, P. Bucher, E. S. Mocarski, B. E. Blaisdell, S. Karlin, *J. Mol. Evol.* **33**, 483–494 (1991).
15. E. C. Bronson, J. N. Anderson, *J. Mol. Evol.* **38**, 506–532 (1994).
16. D. R. Forsdyke, *Microbes Infect.* **16**, 96–103 (2014).
17. S. Duffy, C. L. Burch, P. E. Turner, *Evolution* **61**, 2614–2622 (2007).
18. M. R. Servadio, G. S. Van Doorn, M. Kopp, A. M. Frame, P. Nosil, *Trends Ecol. Evol.* **26**, 389–397 (2011).
19. K. E. Filchak, J. B. Roethele, J. L. Feder, *Nature* **407**, 739–742 (2000).
20. Materials and methods and supplementary text are available as supplementary materials on Science Online.
21. M. Doebeli, *Adaptive Diversification* (Princeton Univ. Press, 2011).
22. S. Chatterjee, E. Rothenberg, *Viruses* **4**, 3162–3178 (2012).
23. D. R. Matute, I. A. Butler, D. A. Turissini, J. A. Coyne, *Science* **329**, 1518–1521 (2010).
24. H. H. Wang et al., *Nature* **460**, 894–898 (2009).
25. H. D. Bradshaw Jr., S. M. Wilbert, K. G. Otto, D. W. Schemske, *Nature* **376**, 762–765 (1995).
26. Q. Wheeler, R. Meier, *Species Concepts and Phylogenetic Theory: A Debate* (Columbia Univ. Press, 2000).
27. D. J. Howard, S. H. Berlocher, *Endless Forms: Species and Speciation* (Oxford Univ. Press, 1998).
28. M. Achtman, M. Wagner, *Nat. Rev. Microbiol.* **6**, 431–440 (2008).

ACKNOWLEDGMENTS

This work was supported in part by the BEACON Center for the Study of Evolution in Action (NSF Cooperative Agreement DBI-0939454). We thank N. Hajela for help in the lab, I.-N. Wang and H. Wang for materials, and the UCSD Institute for Genomic Medicine Genomics Center for genome sequencing. Sequence reads are available at the National Center for Biotechnology Information (accession number SRP093504) and other data at the Dryad Digital Repository (doi: 10.5061/dryad.4qb79). Correspondence and requests for materials should be addressed to J.R.M. Sharing of biological material requires a material transfer agreement, described at <http://blink.ucsd.edu/research/conducting-research/mta/index.html>.

SUPPLEMENTARY MATERIALS

www.sciencemag.org/content/354/6317/1301/suppl/DC1
Materials and Methods
Supplementary Text
Fig. S1
Tables S1 and S2
References (29–39)

19 August 2016; accepted 9 November 2016
Published online 24 November 2016
10.1126/science.1244466

ECOLOGICAL GENOMICS

The genomic landscape of rapid repeated evolutionary adaptation to toxic pollution in wild fish

Noah M. Reid,¹ Dina A. Proestou,² Bryan W. Clark,³ Wesley C. Warren,⁴ John K. Colbourne,⁵ Joseph R. Shaw,^{5,6} Sibel I. Karchner,^{7,8} Mark E. Hahn,^{7,8} Diane Nacci,⁹ Marjorie F. Oleksiak,¹⁰ Douglas L. Crawford,¹⁰ Andrew Whitehead^{1*}

Atlantic killifish populations have rapidly adapted to normally lethal levels of pollution in four urban estuaries. Through analysis of 384 whole killifish genome sequences and comparative transcriptomics in four pairs of sensitive and tolerant populations, we identify the aryl hydrocarbon receptor–based signaling pathway as a shared target of selection. This suggests evolutionary constraint on adaptive solutions to complex toxicant mixtures at each site. However, distinct molecular variants apparently contribute to adaptive pathway modification among tolerant populations. Selection also targets other toxicity-mediating genes and genes of connected signaling pathways; this indicates complex tolerance phenotypes and potentially compensatory adaptations. Molecular changes are consistent with selection on standing genetic variation. In killifish, high nucleotide diversity has likely been a crucial substrate for selective sweeps to propel rapid adaptation.

The current pace of environmental change may exceed the maximum rate of evolutionary change for many species (1), yet little is known of the circumstances and mechanisms through which evolution might rescue species at risk of decline (2). The Atlantic killifish, *Fundulus heteroclitus*, is nonmigratory and abundant in U.S. Atlantic coast salt-marsh estuaries (3), including sites contaminated with complex mixtures of persistent industrial pollutants (Fig. 1A) that have reached lethal levels in recent decades (4). Some killifish populations resident in polluted sites exhibit inherited tolerance to normally lethal levels of these highly toxic pollutants (5) (Fig. 1B). To understand the genetics of rapid adaptation to radical environmental change in wild populations, we sequenced complete genomes from 43 to 50 individuals from each of eight populations (Fig. 1A and table S1): four tolerant (T) populations from highly polluted sites, each paired with a nearby reference [sensitive (S)] population. We combined these data with RNA sequencing (RNA-seq) to uncover unique

and shared functional pathways and adaptive signatures of selection across populations.

Genomes from T1 and S1 populations were sequenced to 7-fold coverage per individual and the remaining populations, to 0.6-fold coverage (6). Genetic variation is strongly partitioned by geography (Fig. 1C); northern populations (T1, S1, T2, S2, T3, and S3) form a cluster distinct from southern populations (T4 and S4), consistent with their known phylogeography (7). In tolerant populations, nucleotide diversity is reduced genome-wide, and Tajima's D is shifted positive, relative to sensitive population counterparts (fig. S1); these indicate reduced effective population

size in polluted sites. Tolerant-sensitive (T-S) population pairs share the most similar genetic backgrounds, and the fixation index (F_{ST}) is low between them (0.01 to 0.08) (fig. S2). We conclude that tolerant populations are recently and independently derived from local gene pools.

We identified genomic regions that are candidates for pollution tolerance (table S2 and fig. S3) by defining outlier regions as 5-kb windows that fell in the extreme 0.1% tails (for π and Tajima's D) and 99.9% tails (for F_{ST}) of null distributions simulated from demographic models estimated from the data (6). Most outlier regions are small (52 to 69 kb), although a few are up to ~1.8 Mb (fig. S4). For each T-S population pair, signatures of selection are skewed in prevalence toward the tolerant population (fig. S5). Most outliers are specific to a tolerant population (0.5% of 5-kb outlier windows are shared) (fig. S6). However, loci showing the strongest signals of recent selection [highly ranked outliers (6)] are shared (Fig. 2A), suggesting convergent evolution for pollution tolerance. Within these shared outliers are key genes involved in the aryl hydrocarbon receptor (AHR) signaling pathway (*AHR2a*, *AHR1a*, *AIP*, and *CYP1A*) (Fig. 2B).

The importance of these outliers is supported by transcriptomics. When sensitive and tolerant populations were raised in a common clean environment for two generations and embryos were challenged with a model toxic pollutant, the polychlorinated biphenyl (PCB) 3,3',4,4',5-pentachlorobiphenyl (PCB 126)–tolerant populations exhibit reduced inducibility of AHR-regulated genes (Fig. 2C). The 70 genes up-regulated in response to pollutant challenge in sensitive populations, but not in tolerant populations (table S3), are enriched for those regulated by the AHR signaling pathway ($P < 0.0001$). Impaired AHR signaling is most apparent with the canonical transcriptional targets of AHR (Fig. 2C and table

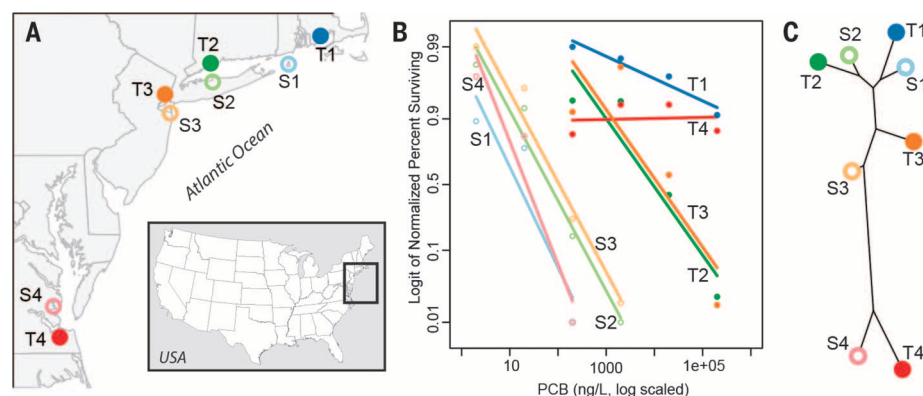


Fig. 1. Focal *F. heteroclitus* populations. (A) Locations of pollution-tolerant (“T”; bold tone, filled circles) and sensitive (“S”; pastel tone, open circles) population pairs numbered from north to south. (B) Population variation in larval survival (linear regression of logit survival to 7 days post hatch) after two generations reared in a common environment, when challenged with increasing log exposure concentrations of PCB 126. Populations from polluted sites exhibit tolerance to pollutants at concentrations hundreds to thousands of times normally lethal levels. (C) Phylogenetic tree, estimated from genome-wide biallelic single-nucleotide polymorphism (SNP) frequencies, showing that genetic differentiation is lowest between T-S population pairs [Phylogeny Inference Package (PHYLIP) Gene Frequencies and Continuous Characters Maximum Likelihood (CONTML) module, bootstrap supports are 100 for all branches].

¹Department of Environmental Toxicology, University of California, Davis, CA 95616, USA. ²Agricultural Research Service, U.S. Department of Agriculture, Kingston, RI 02881, USA. ³Oak Ridge Institute for Science and Education, Office of Research and Development, U.S. Environmental Protection Agency, Narragansett, RI 02882, USA. ⁴McDonnell Genome Institute, Washington University School of Medicine, St. Louis, MO 63108, USA. ⁵School of Biosciences, University of Birmingham, Edgbaston B15 2TT, UK. ⁶School of Public and Environmental Affairs, Indiana University, Bloomington, IN 47405, USA. ⁷Biology Department, Woods Hole Oceanographic Institution, Woods Hole, MA 02543, USA. ⁸Boston University Superfund Research Program, Boston University, Boston, MA 02218, USA. ⁹Office of Research and Development, U.S. Environmental Protection Agency, Narragansett, RI 02882, USA. ¹⁰Department of Marine Biology and Ecology, Rosenstiel School of Marine and Atmospheric Science, University of Miami, Miami, FL 33149, USA.

*Corresponding author. Email: awhitehead@ucdavis.edu

S4). Dominant pollutants at T sites include halogenated aromatic hydrocarbons (HAHs) and polycyclic aromatic hydrocarbons (PAHs) that bind AHR and initiate aberrant signaling that causes malformations during development and subsequent embryo and larval lethality, as well as toxicity in adults (8). Given that the AHR pathway is repeatedly desensitized in tolerant populations (Fig. 2C) (9) and top-ranked outliers contain AHR pathway genes, we conclude that the AHR signaling pathway is likely a key and repeated target of natural selection in tolerant populations. This convergence suggests that adaptive options are constrained to modifications of this signaling pathway that mediates the toxicity of many HAHs and PAHs.

AHR deletions are found in tolerant populations. Four paralogs of *AHR* exist in the *F. heteroclitus* genome (10). Knockdown of *AHR2a* is protective of toxicity from many HAHs and PAHs [e.g., (11)]. Tandem paralogs *AHR2a* and *AHR1a* are within a highly ranked outlier region in all tolerant populations (Fig. 2A). Note that three tolerant populations have deletions (fig. S7) spanning *AHR2a* and *AHR1a* (Fig. 3A). In T4, a deletion is found in a single haplotypic background (fig. S8) that segregates at high frequency (81%) but is absent in S4 (Fig. 3B). In T4 individuals, RNA-seq data reveal expression of a chimeric transcript (joining exon

10 of *AHR2a* and exon 7 of *AHR1a*). In T1 and T3, different deletions spanning *AHR2a* and *AHR1a* (Fig. 3, A and B) occur in two and one haplotypic backgrounds, respectively (fig. S9). A deletion is present in at least one sensitive population (Fig. 3B), but no deletion was found in T2. Variation in this region is also associated with sensitivity to PCB toxicity in T1 (12) and in PCB-adapted tomcod (13). We thus conclude that *AHR* genes are likely common loci of selection for multiple genetic variants, including deletions, where a single deletion-associated haplotype has swept in the southern tolerant population.

The strongest signal of selection we observed is in a window that is a shared outlier in all tolerant populations [aryl hydrocarbon receptor-interacting protein (AIP) in Fig. 2A]. In northern tolerant populations, a single large (650-kb) haplotype has swept to high frequency, accompanied by reduced pi. In T4, a different haplotype has swept to high frequency (Fig. 3C). In T1 (sequenced to higher coverage), we detect recombination breakpoints, allowing identification of a core haplotype region (~100 kb) that coincides with peak differentiation (fig. S10), within which we find AIP. Variation near this locus also associates with sensitivity to PCB toxicity in T1 (12). AIP regulates cytoplasmic stability and cytoplasmic-

nuclear shuttling of the AHR protein and thereby influences AHR signaling and regulates toxicity (14).

A key transcriptional target of AHR, the biotransformation gene *CYP1A*, is within a top-ranking outlier region shared by all tolerant populations (Fig. 2A). Genotypes from tolerant populations are highly differentiated from sensitive populations (Fig. 3D) and *CYP1A* single-nucleotide polymorphism (SNP) variants are linked with tolerance (15). In northern tolerant populations, *CYP1A* duplications have swept to high frequency, where individuals have up to eight copies of the *CYP1A* gene (Fig. 3E and figs. S7 and S11), and duplicates are present in some sensitive populations. *CYP1A* expression is not increased in northern tolerant populations (embryos) (table S4), as one might expect after duplication. However, because *AHR* knockout in rodents decreases basal *CYP1A* expression (16) and AHR signaling is impaired in tolerant killifish, we hypothesize that *CYP1A* duplication has been favored as a compensatory, dosage-compensating adaptation for impaired AHR signaling in northern tolerant fish. In contrast, we find no evidence of duplication in T4 (Fig. 3E), although this region retains a strong signature of selection (Fig. 2A) and is highly differentiated from S4 (Fig. 3D). PAHs primarily contaminate T4, and these chemicals interact

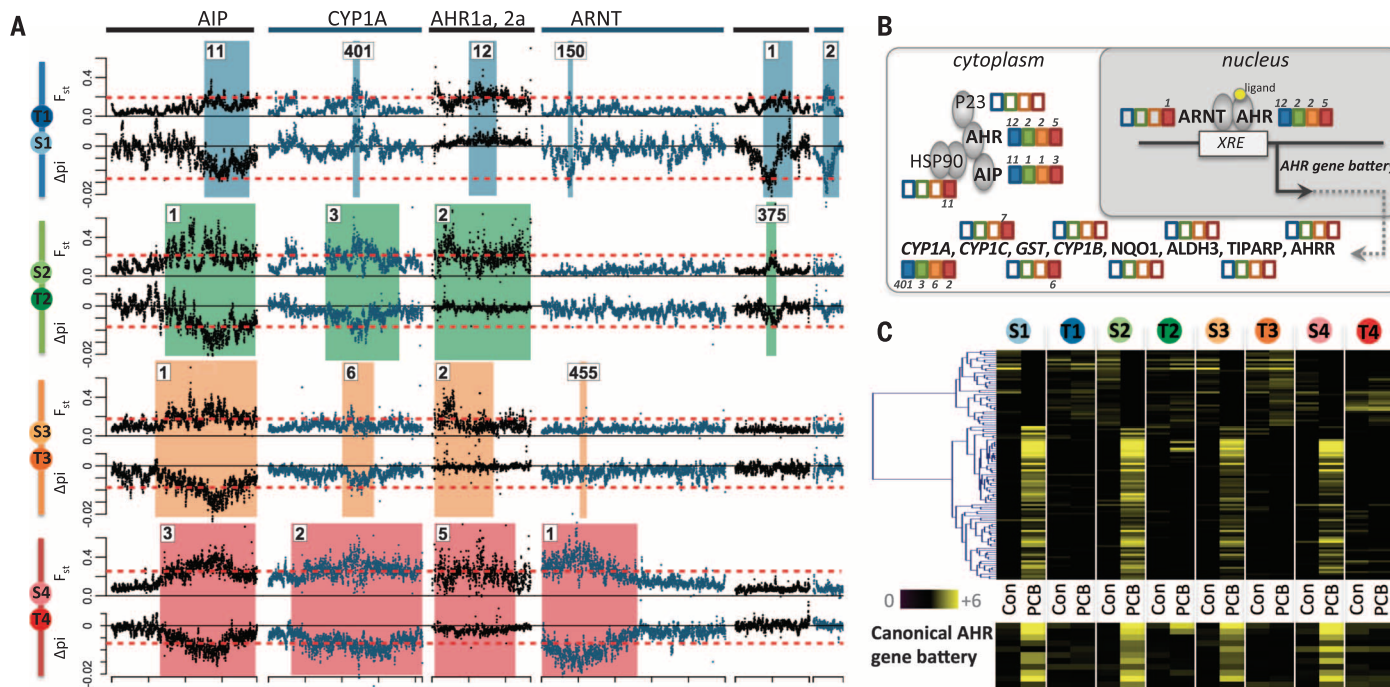


Fig. 2. Patterns of structural and functional genomic divergence. (A) Allele frequency differentiation (F_{ST} , top) and nucleotide diversity (π , bottom) difference (tolerant π – sensitive π) for each population pair studied for top-ranking outlier regions (including the top two per pair). Colored panels span the outlier region of each respective population comparison where number indicates outlier rank for each tolerant-sensitive pair. Red dashed lines indicate outlier thresholds. Each tick on x axis is at the 500-kb position on the scaffold, and each candidate gene name is indicated (top) for each outlier region. Top outlier regions are not colocalized in the genome (fig. S3). (B) Model of key molecules in the AHR signaling pathway, including regulatory genes and

transcriptional targets (*AHR* gene battery). Boxes next to genes are color-coded by population pair; filled boxes indicate the gene is within a top-ranking outlier region for that pair, and number indicates ranking of the outlier region as in (A). Top-ranking outlier regions contain AHR pathway genes and tend to be outliers in all population pairs, although some significant outliers are population-specific. (C) Gene-expression (of developing embryos) heat map shows up-regulated genes in response to PCB 126 exposure ("PCB"; 200 ng/liter) compared with control exposure ("Con") for sensitive populations, most of which are unresponsive in tolerant populations. The bottom panel highlights genes characterized as transcriptionally activated by ligand-bound AHR (table S4).

differently with *AHR*-induced *CYP1A* than with HAHs, which dominate northern sites (17). We propose that different chemical pollutants acting as selective agents may govern the fate of different *CYP1A* variants between HAH- and PAH-polluted sites.

Although AHR pathway genes are among shared outliers, they are also within population-specific outlier regions. Tandem paralogs *AHR1b* and *AHR2b* are within an outlier region in T3 and T4 (fig. S12) so that all four *AHR* paralogs are within outlier regions for one or more tolerant populations. Five additional AHR pathway genes are significant outliers for only T4. Two of these (*ARNT1c* and *HSP90*) (figs. S13 and S14) directly interact with AHR protein, whereas the remaining three (*CYP1C1/IC2*, *GFRP*, and *GSTT1*) (figs. S15 and S16) are PAH biotransformation genes that are also key transcriptional targets of *AHR* (Fig. 2C). The inclusion of PAH biotransformation genes among outliers specific to T4 (primarily polluted with PAHs) likely reflects differences between cellular effects of PAHs and HAHs (17).

Other selective targets include genes outside of AHR signaling. Some PAHs, particularly those that are abundant only at T4, cause cardiotoxicity independent of AHR (18) through disruption

of voltage-gated potassium channels and regulation of intracellular calcium (19). Note that two genes whose products form the conductance pore of the voltage-gated potassium channel (*KCNB2* and *KCNC3*) are within top-ranking outlier windows in T4 (figs. S17 and S18). Similarly, ryanodine receptor (RYP) regulates intracellular calcium, and RYP3 is within an outlier window in T4 (fig. S19). We conclude that components of the adaptive phenotype are underpinned by genes that are both related and unrelated to AHR signaling, consistent with complex adaptations to complex chemical mixtures.

Our results also suggest compensatory adaptation associated with the (potential) costs of evolved pollution tolerance. AHR signaling has diverse functions and interacts with multiple pathways, including estrogen and hypoxia signaling, regulation of cell cycle, and immune system function (20). Estrogen receptor 2b is within an outlier region in T2 (fig. S20), and estrogen receptor-regulated genes are enriched within outlier gene sets for all tolerant populations ($P < 0.001$) (fig. S21). Estrogen receptor is also inferred as a significant upstream regulator for genes differentially expressed between tolerant and sensitive populations ($P < 0.05$) (e.g., genes in Fig.

2C). Hypoxia-inducible factor 2 α is within an outlier window in T3 (fig. S22). Interleukin and cytokine receptors are in outlier windows in T4 (fig. S23). We conclude that some components of the adaptive phenotype in polluted sites may be due to compensation for the altered AHR signaling that underlies the primary pollutant-tolerance phenotype. Selection for compensatory changes may be common following rapid adaptive evolution.

In animal models, single gene (*AHR*) knockout can protect from toxicity of some HAH or PAH compounds [e.g., (21)]. However, in wild killifish populations, adaptive genotypes appear complex, including multiple AHR signaling pathway elements and other genes. We suggest that this complexity arises from two primary factors. First, tolerant sites are contaminated with complex mixtures of hydrocarbons. Mixture components may interact in subtly different ways with AHR (17), and some exert toxicity through pathways other than AHR (18), such that adaptations in multiple pathways are required. Second, because many of the AHR signaling pathway genes identified here as targets of selection interact with multiple regulatory pathways (20), changes to their function may have deleterious consequences

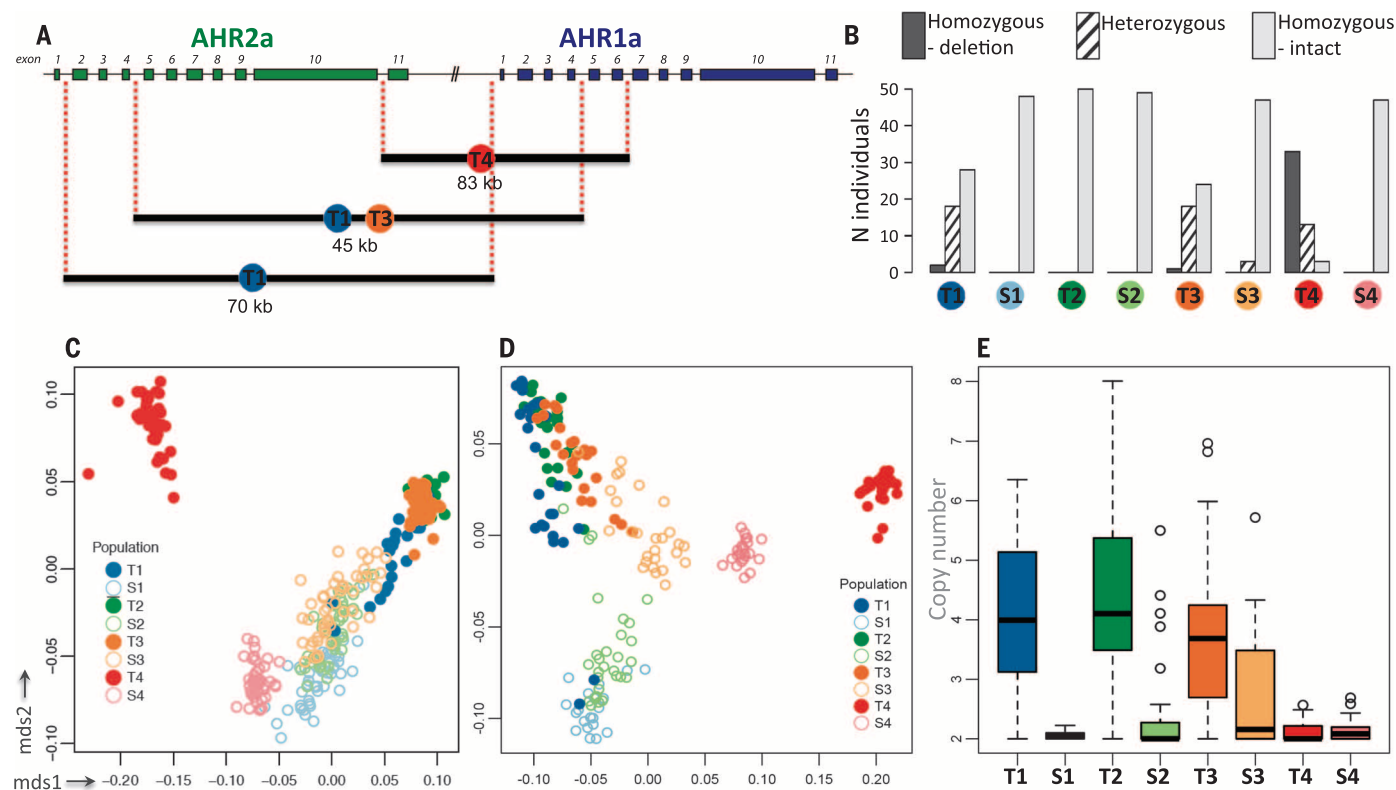


Fig. 3. Patterns of adaptive genetic variation for top-ranking and shared outliers. (A) Gene model of *AHR2a* and *AHR1a* (green or blue squares represent exons). Black bars indicate deleted regions present within tolerant populations. (B) The number of individuals homozygous for specific deletions (gray bar), heterozygous (hatched gray bar), or homozygous wild type (light bar) within each population. (C) Multidimensional scaling (MDS) plot of genotypic variation on the scaffold containing the *AIP* gene. (D) MDS

plot of genotypic variation on the scaffold containing the *CYP1A* gene. (E) Bar plot of copy number of the duplications around *CYP1A*, where boxes, whiskers, and dots represent interquartile range, 1.5 \times interquartile range, and the remainder, respectively (the background diploid state includes two copies). Although the *CYP1A* region is highly differentiated in all tolerant populations (D), *CYP1A* duplications are found only in northern tolerant populations (E).

that may result in selection for compensatory change. Other changes in these highly altered estuaries may also exert selection pressures [e.g., estrogenic pollutants (22), hypoxia, or altered species diversity].

A fundamental question in evolutionary biology pertains to the nature and number of variants recruited by natural selection. The relative contributions of de novo variants, standing variation, and the number of competing beneficial variants depend in part on the strength of selection, its spatial patterning, existing genetic diversity and the beneficial mutation rate. Although modes of evolution can be difficult to distinguish (23), our data are revealing. We observe signals of convergence and divergence. Genes in the AHR pathway are repeated targets of selection, even in populations exposed to distinct chemical mixtures and separated by substantial genetic distance. This suggests adaptive constraint. Yet, different variants are often favored in different tolerant populations (e.g., *AHR* and *CYP1A*), some of which are present in sensitive populations, and common variants (e.g., large *AIP* haplotype) have rapidly swept in multiple populations of this low-dispersal fish. This suggests that selection on preexisting variants was important for rapid adaptation in killifish and that multiple molecular targets were available for selective targeting of a common pathway. The prevalence of soft sweeps is predicted to be high during rapid adaptation (24).

Evolutionary change relies on genetic variation that may preexist, or arise through new mutation, at a rate that scales by population size. *F. heteroclitus* at present has large population

sizes (3) and a range of standing genetic variation (nucleotide diversity up to 0.016 for T3 and T4) that places them as one of the most diverse vertebrates (25). These factors suggest that Atlantic killifish have been unusually well positioned to evolve the necessary adaptations to survive in radically altered habitats.

REFERENCES AND NOTES

1. A. P. Hendry, T. J. Farrugia, M. T. Kinnison, *Mol. Ecol.* **17**, 20–29 (2008).
2. G. Bell, *Philos. Trans. R. Soc. Lond. B Biol. Sci.* **368**, 20120080 (2012).
3. I. Valiela, J. E. Wright, J. M. Teal, S. B. Volkman, *Mar. Biol.* **40**, 135–144 (1977).
4. D. Nacci *et al.*, *Mar. Biol.* **134**, 9–17 (1999).
5. D. Nacci, D. Champlin, S. Jayaraman, *Estuaries Coasts* **33**, 853–864 (2010).
6. Materials and methods are available as supplementary materials on Science Online.
7. D. D. Duvernell, J. B. Lindmeier, K. E. Faust, A. Whitehead, *Mol. Ecol.* **17**, 1344–1360 (2008).
8. R. Pohjanvirta, *The AH Receptor in Biology and Toxicology* (Wiley, Hoboken, NJ, 2012).
9. A. Whitehead, W. Pilcher, D. Champlin, D. Nacci, *Proc. Biol. Sci.* **279**, 427–433 (2012).
10. A. M. Reitzel *et al.*, *BMC Evol. Biol.* **14**, 6 (2014).
11. B. W. Clark, C. W. Matson, D. Jung, R. T. Di Giulio, *Aquat. Toxicol.* **99**, 232–240 (2010).
12. D. Nacci, D. Proestou, D. Champlin, J. Martinson, E. R. Waits, *Mol. Ecol.* **25**, 5467–5482 (2016).
13. I. Wirgin *et al.*, *Science* **331**, 1322–1325 (2011).
14. M. Nukaya *et al.*, *J. Biol. Chem.* **285**, 35599–35605 (2010).
15. D. A. Proestou, P. Flight, D. Champlin, D. Nacci, *BMC Evol. Biol.* **14**, 7 (2014).
16. J. V. Schmidt, G. H. T. Su, J. K. Reddy, M. C. Simon, C. A. Bradfield, *Proc. Natl. Acad. Sci. U.S.A.* **93**, 6731–6736 (1996).
17. M. S. Denison, A. A. Soshilov, G. He, D. E. DeGroot, B. Zhao, *Toxicol. Sci.* **124**, 1–22 (2011).
18. J. P. Incardona *et al.*, *Environ. Health Perspect.* **113**, 1755–1762 (2005).
19. F. Brette *et al.*, *Science* **343**, 772–776 (2014).
20. T. V. Beischlag, J. Luis Morales, B. D. Hollingshead, G. H. Perdew, *Crit. Rev. Eukaryot. Gene Expr.* **18**, 207–250 (2008).
21. P. M. Fernandez-Salguero, D. M. Hilbert, S. Rudikoff, J. M. Ward, F. J. Gonzalez, *Toxicol. Appl. Pharmacol.* **140**, 173–179 (1996).
22. S. R. Greytak, A. M. Tarrant, D. Nacci, M. E. Hahn, G. V. Callard, *Aquat. Toxicol.* **99**, 291–299 (2010).
23. J. J. Berg, G. Coop, *Genetics* **201**, 707–725 (2015).
24. B. Wilson, P. Pennings, D. Petrov, *bioRxiv* 10.1101/052993 (2016).
25. E. M. Leffler *et al.*, *PLOS Biol.* **10**, e1001388 (2012).

ACKNOWLEDGMENTS

Sequence data are archived at the National Center for Biotechnology Information (BioProject PRJNA323589). Phylogenetic tree data are archived at Dryad (doi: 10.5061/dryad.68n87). We thank G. Coop, B. Counterman, D. Champlin, I. Kirby, and A. Bertrand for their valuable input. Primary support was from the NSF (collaborative research grants DEB-1265282, DEB-1120512, DEB-1120013, DEB-1120263, DEB-1120333, DEB-1120398 to J.K.C., D.L.C., M.E.H., S.I.K., M.F.O., J.R.S., W.C.W., and A.W.). Further support was provided by the National Institutes of Environmental Health Sciences (1R01ES021934-01 to A.W.; P42ES007381 to M.E.H.; R01ES019324 to J.R.S.), and the National Science Foundation (OCE-1314567 to A.W.). B.W.C. was supported by the Postdoctoral Research Program at the U.S. Environmental Protection Agency (EPA) administered by the Oak Ridge Institute for Science and Education (agreement DW92429801). The views expressed in this article are those of the authors and do not necessarily represent the views or policies of the EPA.

SUPPLEMENTARY MATERIALS

www.sciencemag.org/content/354/6317/1305/suppl/DC1
Materials and Methods
Figs. S1 to S26
Tables S1 to S4
References (26–45)

6 July 2016; accepted 31 October 2016
10.1126/science.aah4993

Migrate to Monarch[®].

Environmentally-friendly Nucleic Acid Purification Kits from New England Biolabs

Want to feel good about your choice in DNA purification? With our fast and reliable Monarch Nucleic Acid Purification Kits, you can achieve optimal purification while creating less waste. Available for plasmid minipreps, DNA gel extraction and enzymatic cleanup (including PCR), our products use up to 44% less plastic and are packaged using responsibly-sourced, recyclable materials. Make the change and migrate to Monarch today.



“ *These kits might be the best I have used for the price. The best part is that it uses less plastic for production!! Thank you for caring about our environmental impacts, NEB!!!* ”

— NEB customer

Request your free sample at www.NEBMonarch.com

A man in a black tuxedo with a red bow tie is conducting with a white baton. His eyes are closed, and he has a serene expression. Surrounding him are various 3D molecular models: purple and blue structures on the left, red and orange structures on the right, and several colorful (green, blue, pink, orange) ribbon diagrams of protein structures floating around his chest and arms. The background is dark with some glowing blue spots.

invitrogen

One conductor, a symphony of enzymes

Finally, a complete, one-buffer system—for beautifully simple cloning

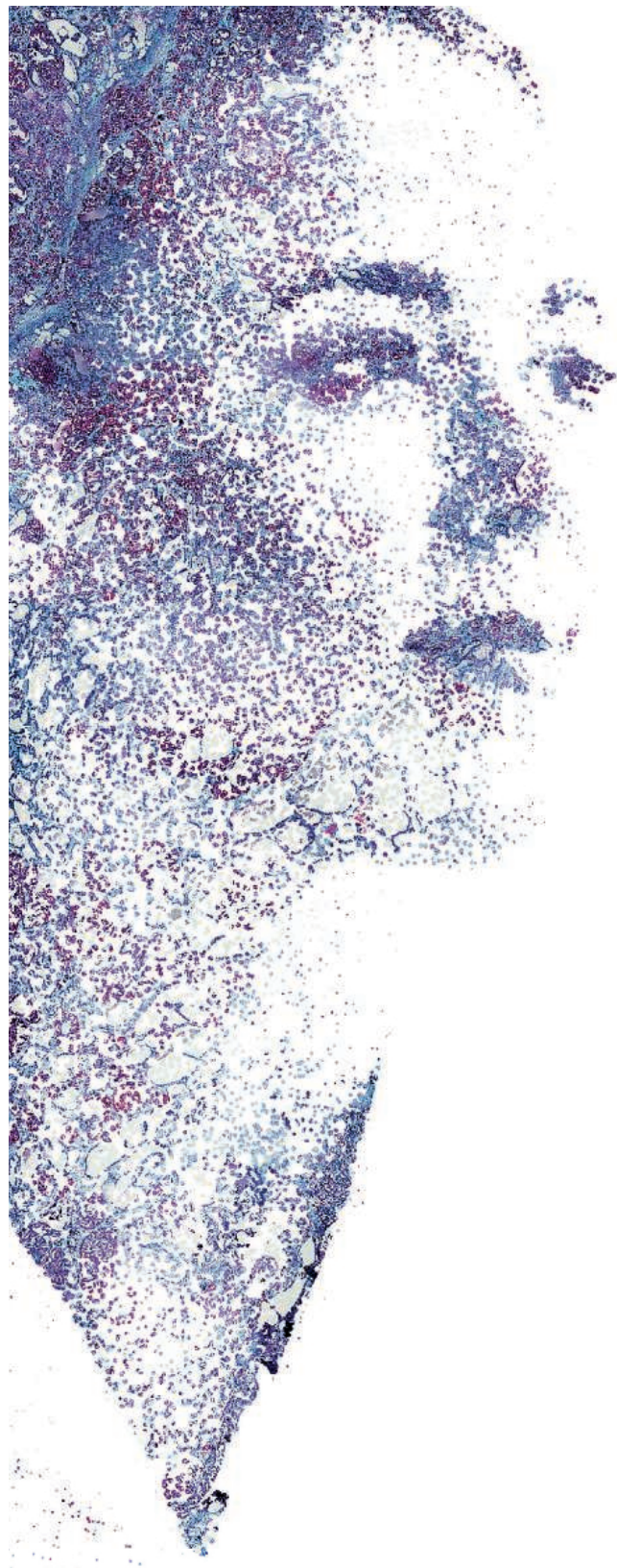
Introducing the Invitrogen™ Anza™ Restriction Enzyme Cloning System:

- One buffer for all restriction enzymes
- One digestion protocol for all DNA types
- Complete digestion in 15 minutes
- Overnight digestion without star activity

Choose simplicity at thermofisher.com/Anza

ThermoFisher
SCIENTIFIC

For Research Use Only. Not for use in diagnostic procedures. © 2015 Thermo Fisher Scientific Inc. All rights reserved. All trademarks are the property of Thermo Fisher Scientific and its subsidiaries unless otherwise specified. CO126010 0815



Looking to add more to your transcriptome analysis?

Complete the picture with RNAscope® *in situ* hybridization.

**Visualize expression for virtually any gene
in any tissue from any species**

Elevate your genome and transcriptome analysis by adding morphological context with gene expression data. RNAscope® *in situ* hybridization technology delivers unrivaled single-molecule sensitivity and specificity—with the flexibility to analyze virtually ANY gene target in ANY tissue. Same-day results and automated assays mean you can validate or add your NGS data quickly, easily, and all backed by our performance guarantee.

Learn more at acdbio.com/applications



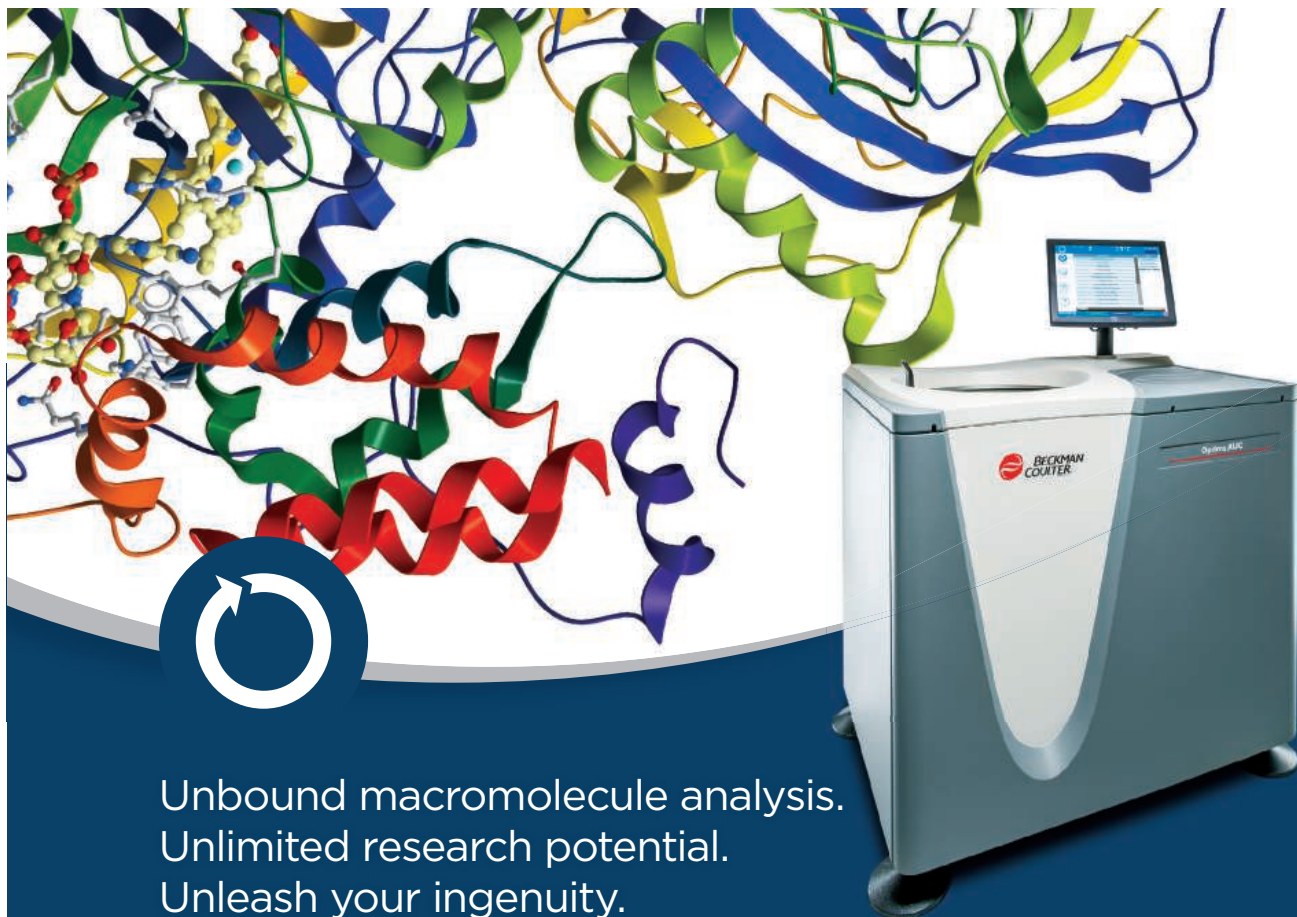
Enabling Research, Drug Development & Diagnostics

For Research Use Only. Not for diagnostic use. RNAscope is a registered trademark of Advanced Cell Diagnostics, Inc. in the United States or other countries. All rights reserved.
©2016 Advanced Cell Diagnostics, Inc. Doc #: MK 51-087/112916

RNAscope ISH
GET HYBRIDIZED
GIVEAWAY

Win a BMW 330e iPerformance Hybrid
or research grant of US \$40,000
Visit rna.acdbio.com/gethybridized to enter today





Unbound macromolecule analysis.
Unlimited research potential.
Unleash your ingenuity.

Unsurprisingly, it's all possible with the Optima AUC.

The new Optima AUC is a faster, more sophisticated, and easy-to-use analytical research tool for your macromolecule research. With precise absorbance scans in <7 seconds/sector,* and interference scans in <5 seconds/scan, the Optima AUC gives you the fastest data acquisition rate yet. Remote data export provides unmatched convenience for analyzing your data.

By analyzing proteins as interacting elements instead of in isolation, AUC more closely approximates true physiological conditions by considering:

- The protein's conformation (folded or unfolded)
- Assembly reversibility (interacting systems)
- Stoichiometry (associative state)
- Heterogeneity (aggregation)

Undecided? Visit info.beckmancoulter.com/optimaauc to learn more.

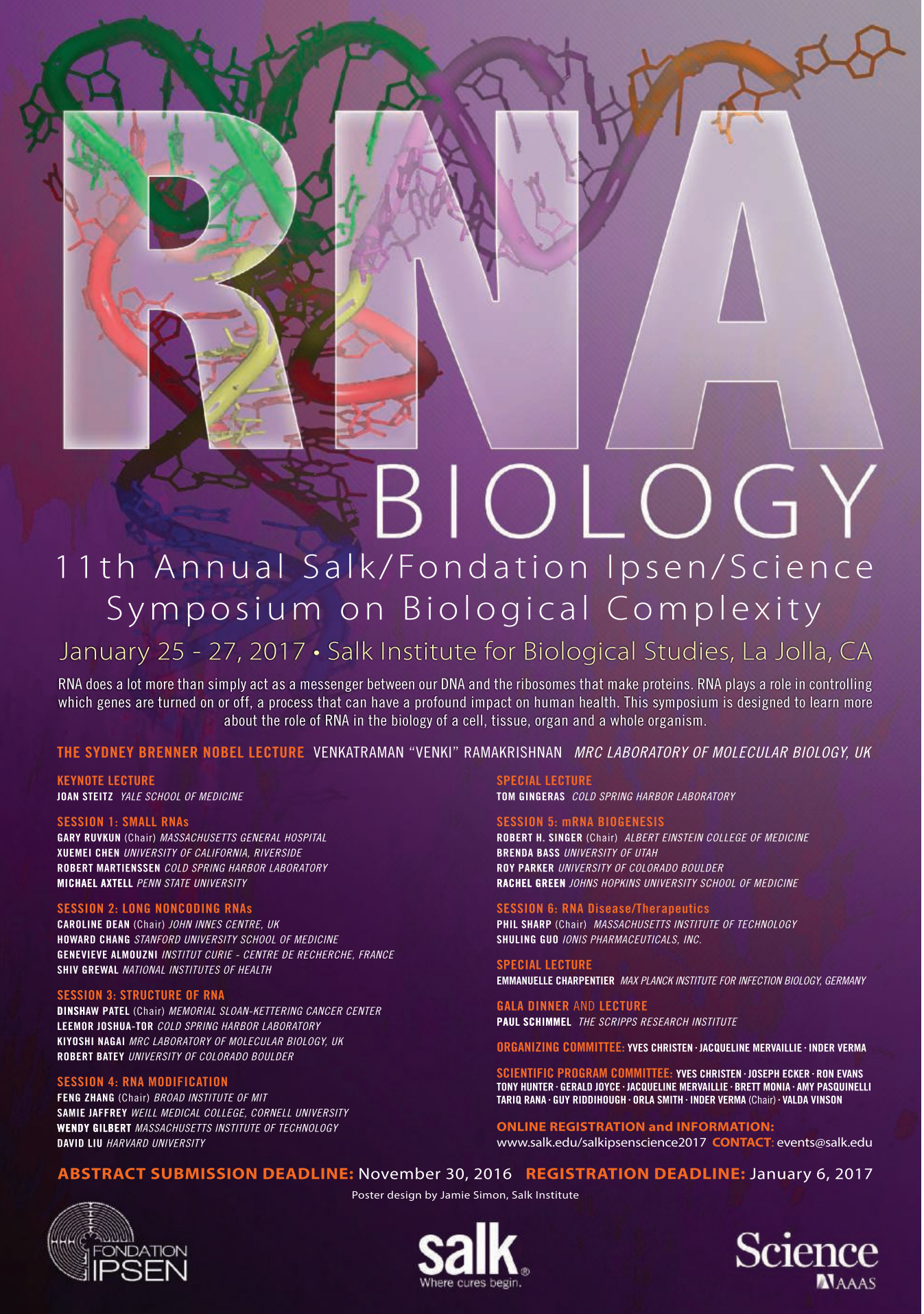
* At Optimal rotor speeds, at 10 μm radial resolution

© 2016 Beckman Coulter, Inc. All rights reserved. Beckman Coulter, the stylized logo, and the Beckman Coulter product and service marks mentioned herein are trademarks or registered trademarks of Beckman Coulter, Inc. in the United States and other countries.

For Beckman Coulter's worldwide office locations and phone numbers, please visit "Contact Us" at beckman.com

CENT-1576ADV03.16-A





RNA BIOLOGY

11th Annual Salk/Fondation Ipsen/Science Symposium on Biological Complexity

January 25 - 27, 2017 • Salk Institute for Biological Studies, La Jolla, CA

RNA does a lot more than simply act as a messenger between our DNA and the ribosomes that make proteins. RNA plays a role in controlling which genes are turned on or off, a process that can have a profound impact on human health. This symposium is designed to learn more about the role of RNA in the biology of a cell, tissue, organ and a whole organism.

THE SYDNEY BRENNER NOBEL LECTURE VENKATRAMAN “VENKI” RAMAKRISHNAN *MRC LABORATORY OF MOLECULAR BIOLOGY, UK*

KEYNOTE LECTURE

JOAN STEITZ *YALE SCHOOL OF MEDICINE*

SESSION 1: SMALL RNAs

GARY RUVKUN (Chair) *MASSACHUSETTS GENERAL HOSPITAL*

XUEMEI CHEN *UNIVERSITY OF CALIFORNIA, RIVERSIDE*

ROBERT MARTIENSSEN *COLD SPRING HARBOR LABORATORY*

MICHAEL AXTELL *PENN STATE UNIVERSITY*

SESSION 2: LONG NONCODING RNAs

CAROLINE DEAN (Chair) *JOHN INNES CENTRE, UK*

HOWARD CHANG *STANFORD UNIVERSITY SCHOOL OF MEDICINE*

GENEVIEVE ALMOUZNI *INSTITUT CURIE - CENTRE DE RECHERCHE, FRANCE*

SHIV GREWAL *NATIONAL INSTITUTES OF HEALTH*

SESSION 3: STRUCTURE OF RNA

DINSHAW PATEL (Chair) *MEMORIAL SLOAN-KETTERING CANCER CENTER*

LEEMOR JOSHUA-TOR *COLD SPRING HARBOR LABORATORY*

KIYOSHI NAGAI *MRC LABORATORY OF MOLECULAR BIOLOGY, UK*

ROBERT BATEY *UNIVERSITY OF COLORADO BOULDER*

SESSION 4: RNA MODIFICATION

FENG ZHANG (Chair) *BROAD INSTITUTE OF MIT*

SAMIE JAFFREY *WEILL MEDICAL COLLEGE, CORNELL UNIVERSITY*

WENDY GILBERT *MASSACHUSETTS INSTITUTE OF TECHNOLOGY*

DAVID LIU *HARVARD UNIVERSITY*

SPECIAL LECTURE

TOM GINGERAS *COLD SPRING HARBOR LABORATORY*

SESSION 5: mRNA BIOGENESIS

ROBERT H. SINGER (Chair) *ALBERT EINSTEIN COLLEGE OF MEDICINE*

BRENDA BASS *UNIVERSITY OF UTAH*

ROY PARKER *UNIVERSITY OF COLORADO BOULDER*

RACHEL GREEN *JOHNS HOPKINS UNIVERSITY SCHOOL OF MEDICINE*

SESSION 6: RNA Disease/Therapeutics

PHIL SHARP (Chair) *MASSACHUSETTS INSTITUTE OF TECHNOLOGY*

SHULING GUO *IONIS PHARMACEUTICALS, INC.*

SPECIAL LECTURE

EMMANUELLE CHARPENTIER *MAX PLANCK INSTITUTE FOR INFECTION BIOLOGY, GERMANY*

GALA DINNER AND LECTURE

PAUL SCHIMMEL *THE SCRIPPS RESEARCH INSTITUTE*

ORGANIZING COMMITTEE: YVES CHRISTEN · JACQUELINE MERVAILLIE · INDER VERMA

SCIENTIFIC PROGRAM COMMITTEE: YVES CHRISTEN · JOSEPH ECKER · RON EVANS · TONY HUNTER · GERALD JOYCE · JACQUELINE MERVAILLIE · BRETT MONIA · AMY PASQUINELLI · TARIQ RANA · GUY RIDDIHOUGH · ORLA SMITH · INDER VERMA (Chair) · VALDA VINSON

ONLINE REGISTRATION and INFORMATION:

www.salk.edu/salkipsenscience2017 **CONTACT:** events@salk.edu

ABSTRACT SUBMISSION DEADLINE: November 30, 2016 **REGISTRATION DEADLINE:** January 6, 2017

Poster design by Jamie Simon, Salk Institute





Genome Fragment Analyzer

High-throughput genomic techniques require high-throughput instruments to measure the quality of input materials like DNA, genomic DNA (gDNA), and RNA. Advanced Analytical Technologies (AATI) designed the Fragment Analyzer INFINITY Capillary Electrophoresis System to meet this need in the workflow of automated laboratories. INFINITY is compatible with virtually any robotic arm, can run over 2,400 samples a day without intervention, and interfaces with laboratory information management systems to label samples automatically. It is also compatible with all of the original Fragment Analyzer qualitative and quantitative kits, which cover a wide range of nucleic acid sample types. To assess sample quality, AATI uses two kinds of metrics, or quality numbers: A fixed RNA quality number evaluates samples with consistent features like total RNA and correlates to the commonly used industry metric, while adaptive DNA and gDNA quality numbers have adjustable thresholds to appraise fragmented DNA and gDNA, which often vary widely between samples due to purification or shearing.

Advanced Analytical Technologies

For info: 515-964-8500
www.aati-us.com/product

Profiling Panels

NanoString Technologies offers nCounter Vantage 3D Panels, a portfolio of products that power our 3D Biology products for simultaneous analysis of DNA, RNA, and proteins.

Up to 800 targets can be detected and quantified from the same sample, which opens the opportunity for multianalyte signature discovery and validation on a single platform, even for challenging FFPE samples. nCounter Vantage 3D products can be mixed and matched to customize panels for specific applications and research questions. Comprehensive data collection and uniform data output from nCounter Analysis Systems, including the new SPRINT Profiler, can help scientists identify novel biomarkers for translational and diagnostics research.

NanoString Technologies

For info: 888-358-6266
<http://3d.nanostring.com>



ddPCR Multiplex Mutation Screening Kits

Droplet Digital PCR (ddPCR) Multiplex Mutation Screening Kits detect several key actionable cancer mutations and the wild-type allele in a single reaction. The combination of ddPCR and multiplexing technologies increases the throughput of genetic analysis to give clinical researchers more information per patient sample. Bio-Rad's ddPCR Multiplex Mutation Screening portfolio comprises *KRAS G12/G13*, *KRAS Q61*, *NRAS G12*, *NRAS G12/G13*, *NRAS Q61*, *BRAF V600*, and *EGFR* exon 19 deletion screening kits. This collection represents common actionable mutations found in numerous cancers and screened for during clinical research to connect specific genetic alterations with diagnosis, treatment efficacy, and disease recurrence. Sample partitioning in ddPCR enables detection of rare nucleic acid sequences in a complex background of competing sequences while minimizing the effect of inhibitory substances. The kits identify mutations present at allelic frequencies at or below 0.5%, making them ideal for use with FFPE and liquid biopsy samples.

Bio-Rad

For info: 800-424-6723
www.bio-rad.com/MultiplexKits

Sequencing and Epigenetic Services

With its comprehensive repertoire of services, Zymo Research makes genome-wide epigenetic analysis available to every researcher. All next-generation epigenetic sequencing is competitively priced and features state-of-the-art sample prep technologies and workflows as well as cutting-edge bioinformatics. We offer the most comprehensive services for 16S ribosomal RNA and shotgun sequencing from any sample type. Using the most advanced pipelines for sample collection, nucleic acid isolation, and library preparation, ZymoBIOMICS allows for superior sequencing and analysis. The entire workflow is validated using the ZymoBIOMICS Microbial Community Standards, and provides non-biased community profile analysis. Tasks are customizable and can be combined to suit your needs, and include low-bioburden processing and accurate DNA/RNA isolation using the ZymoBIOMICS product line for the most accurate taxonomic profiling. Just send us your samples, and we will return the genome-wide analyses as customizable, publication-ready graphs and figures.

Zymo Research

For info: 888-882-9682
www.zymoresearch.com

Transcriptome Profiling Assay

Molecular characterization of patient-derived xenografts used in cancer research provides valuable information on oncogenic mechanisms, candidate drug targets, and pathway status. Driver-Map offers a novel, comprehensive end-to-end service portfolio for identifying differential gene expression, mapping clinically actionable mutations in RNA, detecting cellular composition (immune/stromal components),

and profiling immunotherapy targets. The Driver-Map transcriptome profiling assay has the unique advantage of selectively profiling human genes in a background of mouse cells, as well as providing pathway status. Researchers can profile and characterize with Driver-Map to determine if xenograft/patient-derived xenograft models have captured and retained the molecular and biological heterogeneity of the disease. Driver-Map offers superior sensitivity to detect low-to-medium abundant genes, and provides reproducible and reliable data even from low amounts (10 ng) of RNA. No cross-reactivity of real-time PCR primers with mouse transcripts occurs, making this assay highly specific to human cells.

Cellecta

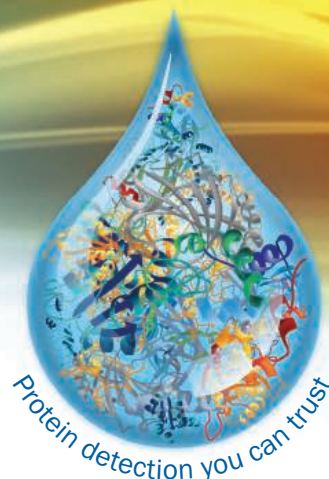
For info: 877-938-3910
www.cellecta.com

Electronically submit your new product description or product literature information! Go to www.sciencemag.org/about/new-products-section for more information.

Newly offered instrumentation, apparatus, and laboratory materials of interest to researchers in all disciplines in academic, industrial, and governmental organizations are featured in this space. Emphasis is given to purpose, chief characteristics, and availability of products and materials. Endorsement by *Science* or AAAS of any products or materials mentioned is not implied. Additional information may be obtained from the manufacturer or supplier.

R&D SYSTEMS
a **bio-technē** brand

Luminex



R&D Systems is Your New Trusted Source for Luminex® Instrumentation!

Direct access to Luminex staff for world-class on-site and 24x7x365 remote support

Unlimited emergency equipment repair

Discounts and special acquisition programs tailored to any lab's budget

Learn more about Luminex® instruments | rndsystems.com/luminexinstruments

bio-technē

Global info@bio-technē.com bio-technē.com/find-us/distributors TEL +1 612 379 2956
North America TEL 800 343 7475 Europe | Middle East | Africa TEL +44 (0)1235 529449
China info.cn@bio-technē.com TEL +86 (21) 52380373





There's only one **Science**

Science Careers Advertising

For full advertising details, go to ScienceCareers.org and click For Employers, or call one of our representatives.

Tracy Holmes

Worldwide Associate Director
Science Careers
Phone: +44 (0) 1223 326525

THE AMERICAS

E-mail: advertise@sciencecareers.org
Fax: +1 (202) 289 6742

Tina Burks

Phone: +1 (202) 326 6577

Nancy Toema

Phone: +1 (202) 326 6578

Online Job Posting Questions

Phone: +1 (202) 312 6375

EUROPE / INDIA / AUSTRALIA / NEW ZEALAND / REST OF WORLD

E-mail: ads@science-int.co.uk
Fax: +44 (0) 1223 326532

Sarah Lelarge

Phone: +44 (0) 1223 326527

Kelly Grace

Phone: +44 (0) 1223 326528

Online Job Posting Questions

Phone: +44 (0) 1223 326528

JAPAN

Katsuyoshi Fukamizu (Tokyo)

E-mail: kfukamizu@aaaas.org
Phone: +81 3 3219 5777

Hiroyuki Mashiki (Kyoto)

E-mail: hmashiki@aaaas.org
Phone: +81 75 823 1109

CHINA / KOREA / SINGAPORE / TAIWAN / THAILAND

Danny Zhao

E-mail: dzhao@aaaas.org
Phone: +86 131 4114 0012

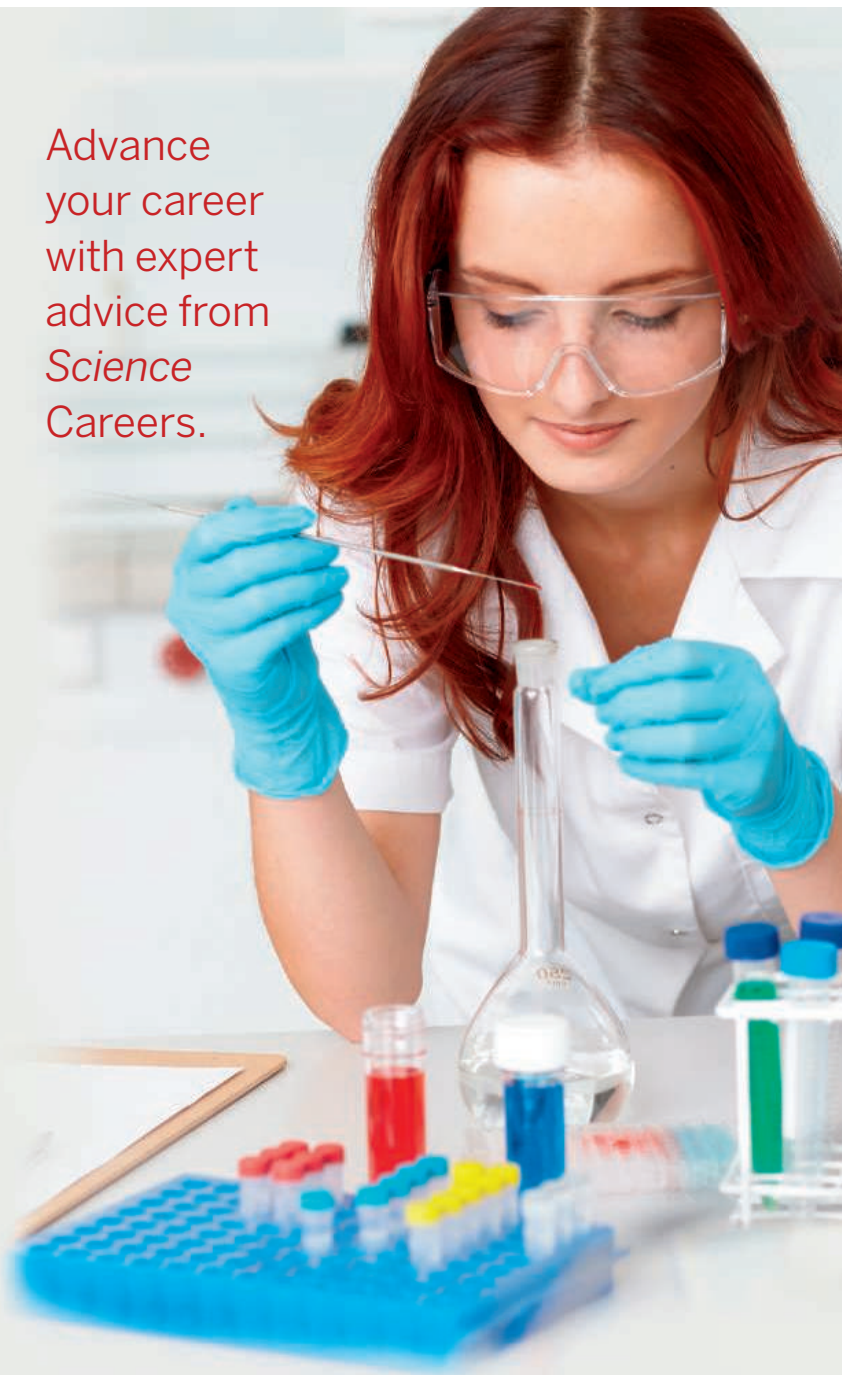
All ads submitted for publication must comply with applicable U.S. and non-U.S. laws. Science reserves the right to refuse any advertisement at its sole discretion for any reason, including without limitation for offensive language or inappropriate content, and all advertising is subject to publisher approval. Science encourages our readers to alert us to any ads that they feel may be discriminatory or offensive.

Science Careers

FROM THE JOURNAL SCIENCE **AAAAA**

ScienceCareers.org

Advance
your career
with expert
advice from
**Science
Careers.**



Download Free Career Advice Booklets!

ScienceCareers.org/booklets

Featured Topics:

- Networking
- Industry or Academia
- Job Searching
- Non-Bench Careers
- And More



Science Careers

FROM THE JOURNAL SCIENCE **AAAAA**

In 2017, CNRS is recruiting permanent researchers



Disabled candidates can also be recruited by contractual agreement.

in all scientific fields

life sciences, chemistry, environmental sciences and sustainable development, humanities and social sciences, computer sciences, engineering, mathematics, physics, nuclear and particle physics, Earth sciences and astronomy.



Online registration at www.cnrs.fr
from **December 1, 2016**
to **January 6, 2017**



ÉCOLE POLYTECHNIQUE
FÉDÉRALE DE LAUSANNE

Faculty Position in Environmental Science and Engineering at the Ecole polytechnique fédérale de Lausanne (EPFL)

EPFL's School of Architecture, Civil and Environmental Engineering (ENAC) invites applications for a Faculty position in the Institute of Environmental Engineering. Appointment at all levels (i.e. Tenure Track-, Associate-, and Full Professor) will be considered.

The Institute of Environmental Engineering currently covers a diverse portfolio of research and teaching in (non-exhaustive list): climate change adaptation, biogeochemical cycles, cryosphere, hydrology, hydrodynamics, limnology, precipitation, water quality, bioremediation, ecotoxicology, air quality, renewable energy, city and landscape monitoring/sustainability, ecology, and ecosystem dynamics. These research themes are underpinned by technical innovations and developments in, for example: remote and in situ sensing, field robotics (water, land, air), numerical modelling, as well as cutting-edge chemical, genomic, proteomic, and isotope analysis facilities. Our institute also hosts the newly established Swiss Polar Institute, which coordinates and supports research in Polar and other extreme environments, including the Alps.

In this context, we seek a candidate who can develop and lead an internationally recognized research program and strengthen our curriculum within the broadly defined area of Environmental Science and Engineering, complementing and integrating with existing groups. The successful candidate will be committed to excellence in undergraduate/graduate level teaching as well as supervision of PhD students and postdocs.

EPFL offers internationally competitive start-up resources, salaries, and benefits.

With its main campus located in Lausanne, Switzerland, EPFL is a dynamically growing and wellfunded institution fostering excellence and diversity. It has a highly international campus at an exceptionally attractive location boasting first-class experimental and computational infrastructure. As a technical university

covering essentially the entire palette of engineering and science, EPFL offers a fertile environment for research collaboration between different disciplines. The EPFL environment is multi-lingual and multi-cultural, with English serving as a common interface.

To apply, please follow the application procedure on

<https://academicjobsonline.org/ajo/jobs/8558>

The following documents are requested in PDF format: cover letter including a statement of motivation, curriculum vitae, publications list, statement of research and teaching interests as well as the names and addresses, including emails, of at least three references (may be contacted at a later stage).

Screening will start on **February 1st, 2017** and the search will continue until the position is filled.

Further enquiries should be made to the Chair of the Search Committee:

Professor Anders Meibom

Director of the Environmental Engineering Institute
School of Architecture, Civil and Environmental
Engineering, EPFL-ENAC
E-mail: searchenvironmental@epfl.ch

For additional information on EPFL, please consult:
<http://www.epfl.ch> or <http://enac.epfl.ch>

EPFL aims to increase the presence of women amongst its faculty, and qualified female candidates are strongly encouraged to apply.

Science Careers Job Fair at the AAAS Annual Meeting

February 17, 2017

11:00 AM - 4:00 PM EST



A Day of Recruiting Opportunities and Career Workshops

Science Careers and **AAAS** offer an exciting career event at the 2017 AAAS Annual Meeting in Boston, Massachusetts.

- **JOB SEEKERS:** Join us for a chance to meet with recruiters from top scientific organizations and to get valuable advice from career experts. The combination of valuable career development content and exciting career opportunities makes this a free “must-attend” event for scientists.

*For more details and to register, visit
sciencemag.org/careers/jobfair*

- **EMPLOYERS:** Save time and money by meeting hundreds of scientists in person.

For information and to reserve your exhibit space package please contact us today.

Space is limited.

[202 326-6577](tel:2023266577)

advertise@sciencecareers.org



Hynes Convention Center

Room 210
Boston, MA

To book your booth, contact:

US: 202-326-6577

Europe: +44 (0) 1223 326528

advertise@sciencecareers.org

ScienceCareers

FROM THE JOURNAL SCIENCE  AAAS

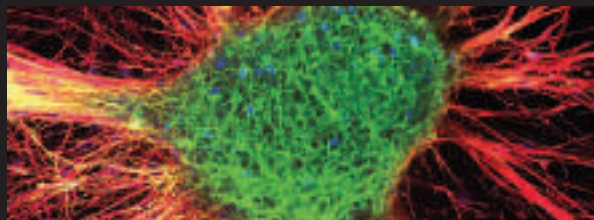
SCIENCECAREERS.ORG

Group Leader in Cancer Biology

The Wellcome Trust/Cancer Research UK Gurdon Institute
University of Cambridge

Closing date: 9th January 2017

Salary: £48,327 to £66,835 + start up package



The Gurdon Institute is a world-renowned centre in the fields of developmental, cell, and cancer biology, located in the heart of the historic city of Cambridge, and part of the University's School of Biological Sciences. Its aim is to provide the best possible environment for research, and to foster interactions and collaborations between scientists with diverse but complementary interests. It is generously supported by core funding from the Wellcome Trust and Cancer Research UK, and benefits from state-of-the-art facilities in a friendly, modern environment.

We are now seeking to recruit one or more new Group Leaders at junior or midcareer level in any area of cancer biology whose research complements our existing strengths in human organoid systems, mouse genetics, in vivo imaging, epigenetics and DNA replication and repair. This would be an ideal position for a scientist wishing to take up his or her first position as an independent researcher, and offers a world class platform for career development with a generous start up package. Informal enquiries are invited and can be directed to any of the Institute's Group Leaders or to glsearch@gurdon.cam.ac.uk.

To apply online, please click on the 'Apply' button at <http://www.jobs.cam.ac.uk/job/12056/>. This will route you to the University's Web Recruitment System, where you will need to register an account to complete the online application form. Please upload your CV, covering letter, publications list, a brief outline of your future research plans and the details of three referees. Applicants are strongly advised to check that the referees can provide references within two weeks of the closing date.

www.gurdon.cam.ac.uk (About the Institute)



IHU-Méditerranée Infection –Marseille, France Full Professor Chair in Electron Microscopy

In the context of AMIDEX, the IHU-Méditerranée Infection – Directors Pr D. Raoult (Marseille, Fr). Recruit a Full professor in electron microscopy for 3 years (+2), salary 3000 to 4500 euro (depending of experience). The aims is 1-to develop new technology related to electron microscopy to investigate microbes and giant viruses. 2-investigate the biology of microbes and giants viruses through a full research program, 3-teach to students the electron microscopy and application to biology. The chair holder will lead his/her own research team to be built and to be integrated in an existing large institute IHU-Méditerranée Infection at Aix-Marseille University. He/she is expected to assume responsibility for all managerial tasks that are usual to this full professor level position. He/she will benefit from an endowed package including a team start-up budget (post-doctoral and doctoral contracts, operating and equipment costs, missions...).

Application: CV, Summary of the Past experiences, List of publications, Recommendation letters

Contact: Didier.Raoult@gmail.com

ETH zürich

Assistant Professor (Tenure Track) of Pharmacoepidemiology

→ The Department of Chemistry and Applied Biosciences of ETH Zurich (www.chab.ethz.ch) invites applications for the above-mentioned position at the Institute of Pharmaceutical Sciences (www.pharma.ethz.ch) in cooperation with the Department of Clinical Pharmacology and Toxicology at the University Hospital Zurich (www.usz.ch). The assistant professorship is located at ETH Zurich (campus Hoenggerberg) and the University Hospital Zurich.

→ The new assistant professor has a strong scientific profile in the field of epidemiological studies, e.g. in population pharmacokinetics. The research area should be broad and include new approaches such as molecular pharmacoepidemiology, the development of new statistical tools and methodological approaches to study drug use and its effect and efficacy. Successful applicants provide an internationally recognised research portfolio, and demonstration of acquisition of competitive third-party funding is desirable. The future assistant professor will develop an independent research programme, shows a team-oriented attitude and commitment to interdisciplinary and interinstitutional cooperation. She or he will participate in both undergraduate and graduate teaching.

→ Assistant professorships have been established to promote the careers of younger scientists. ETH Zurich implements a tenure track system equivalent to other top international universities.

→ Please apply online at www.facultyaffairs.ethz.ch

→ Applications include a curriculum vitae, a list of publications, a statement of future research and teaching interests, a description of the three most important achievements as well as the contact details of three referees. The letter of application should be addressed to the President of ETH Zurich, Prof. Dr. Lino Guzzella. The closing date for applications is 28 February 2017. ETH Zurich is an equal opportunity and family friendly employer and is further responsive to the needs of dual career couples. We specifically encourage women to apply.

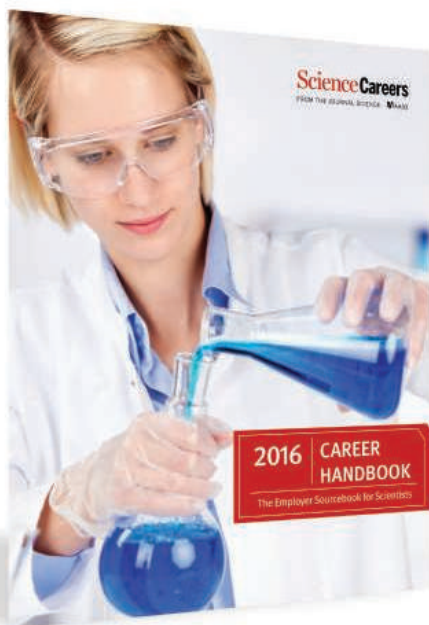
2017 Career Handbook

RECRUIT AND PROMOTE YOUR BRAND



Science Careers will publish the 2017 issue of its annual Career Handbook, which is promoted and distributed all year long.

A combination of career development content alongside your branding ads makes this the perfect place to promote your organization's opportunities. With bonus distribution to events throughout the year and push marketing including banner ads and e-mail blasts to potential candidates, your company will gain valuable exposure to scientists eager to learn about career opportunities.



BENEFITS TO YOUR COMPANY

- Opportunity to brand your organization to scientists beyond your normal reach.
- Print bonus distribution of 2,500 copies to career fairs and meetings around the globe.
- Booklet PDF e-mailed to 100,000 scientists including all *Science Careers* registrants.
- Your logo included in two Career Path newsletters and online on the booklet landing page.
- The booklet PDF will also be posted on *Science Careers* for one year with marketing to drive readers to the booklet and your company. Marketing includes banners, e-mail blasts, and promotion across AAAS/*Science* newsletters.

Book early to secure a cover spot.

Ad materials due by December 30.

SCIENCECAREERS.ORG

Science Careers

FROM THE JOURNAL SCIENCE  AAAS

Call your *Science* representative to book your space or for more information.

The Americas

202-326-6577

Europe/RoW

+44 (0) 1223-326500

China/Korea/

Singapore/Taiwan

+86-10-6871-1722



Announcing a 4-week Intensive Summer Course at Princeton

Neurotechnologies for Analysis of Neural Dynamics

Directors: David W. Tank and Michael Berry, Princeton University, Dates: June 11 – July 8, 2017

Online Application Form and Course Schedule: NAND.princeton.edu

Application Deadline: Rolling admissions starting February 1, 2017.

This course is designed to emphasize the major ways that scientists trained in the physical and information sciences contribute to the advance of neuroscience. It will introduce students with quantitative training in the physical sciences, mathematics or engineering to the concepts and research methodologies of modern neuroscience. Topics covered will range from cellular biophysics to systems neuroscience, including particularly imaging methods for the study of single neurons, networks of neurons and human brain dynamics during execution of behavioral computations. The course will be unique in its focus on neural dynamics at several scales of complexity – cells, circuits, intact brains – and the combination of didactic lectures and laboratory exercises, including cellular biophysics, synaptic interactions and plasticity in neuronal networks, and fMRI imaging of targeted brain regions in human subjects. The course includes substantive instruction in neurotechnologies, ranging from large-scale multi-electrode and optical recording, optogenetic stimulation and mathematical analysis of neural dynamics within the datasets produced by these methods. The capstone of this course will be one-week student-designed research projects integrating concepts and methodologies encountered during the initial formal lectures and laboratory exercises.

Women and under-represented minorities are encouraged to apply.

WAYNE STATE UNIVERSITY

Tenure/Tenure Track Faculty Position in Geology

The Department of Geology at Wayne State University invites applications for a tenure-track position in **Hydrogeology** or **Geophysics** at the rank of assistant or associate professor beginning in August 2017. Preference will be given to candidates who use innovative approaches to study complex problems in fields such as: groundwater flow and contaminant transport, surface-groundwater exchange, environmental geophysics, and solid earth geophysics. Applicants must have a Ph.D., postdoctoral experience, and an outstanding record of research achievement. Successful applicants are expected to establish and maintain vigorous, externally funded research programs and to participate in graduate and undergraduate education in geology and environmental science.

Wayne State University is a large, comprehensive, nationally ranked research institution that offers state-of-the-art research facilities and highly competitive start-up packages. WSU is located in midtown Detroit, which enjoys vibrant cultural and educational amenities amidst the rich natural environment of the Great Lakes. Wayne State is also ideally situated to explore the multifaceted legacy of environmental concerns common to post-industrial urban regions.

Please apply on-line at jobs.wayne.edu (posting #042344) by **January 3, 2017** for full consideration. In addition to an online application that includes cover letter and curriculum vitae, applicants must submit a 2-page statement of their research plans and have three letters of reference sent to: **Faculty Search Committee, Department of Geology, Wayne State University, Detroit, MI 48202** or to Dr. David Njus, Chair at (ad5348@wayne.edu). Applications will be considered only when all materials have been received.

Wayne State University is an Affirmative Action/Equal Opportunity Employer. Women and members of minority groups are especially encouraged to apply.

2017

**AAAS MARTIN AND
ROSE WACHTEL
CANCER RESEARCH**

AWARD

Recognize the work of an early career scientist who has performed outstanding work in the field of cancer research. Award nominees must have received their Ph.D. or M.D. within the last 10 years. The winner will deliver a public lecture on his or her research, receive a cash award of **\$25,000**, and publish a Focus article in *Science Translational Medicine*.

For more information visit
www.aaas.org/aboutaaas/awards/wachtel
or e-mail wachtelprize@aaas.org.
Deadline for submission: March 1, 2017.

Science Translational Medicine | AAAS

10 ways that *Science* Careers can help advance your career

1. Register for a free online account on ScienceCareers.org.
2. Search thousands of job postings and find your perfect job.
3. Sign up to receive e-mail alerts about job postings that match your criteria.
4. Upload your resume into our database and connect with employers.
5. Watch one of our many webinars on different career topics such as job searching, networking, and more.
6. Download our career booklets, including Career Basics, Careers Beyond the Bench, and Developing Your Skills.
7. Complete an interactive, personalized career plan at “my IDP.”
8. Visit our Career Forum and get advice from career experts and your peers.
9. Research graduate program information and find a program right for you.
10. Read relevant career advice articles from our library of thousands.

Visit ScienceCareers.org today — all resources are free



Science Careers

FROM THE JOURNAL SCIENCE  AAAS

SCIENCECAREERS.ORG

By Nancy Grace Roman

Following my lucky star

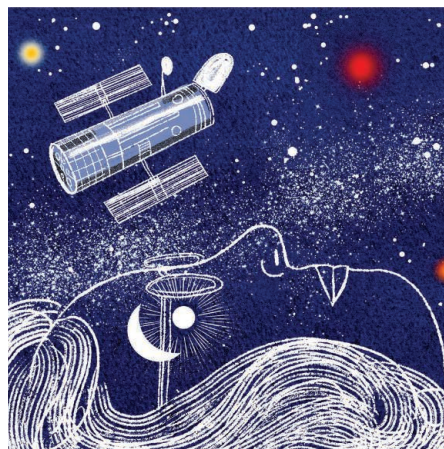
About 30 years ago, while lunching with science faculty members during a campus visit, I was asked to what I attributed my success. My spur of the moment reply, “The ability to write and speak easily and well,” surprised them. But I answered this way because many of the activities I engaged in during my 21-year career running NASA’s astronomy program—justifying projects to my supervisors, Congress, and the Bureau of the Budget; meeting with the research community to spark interest in the possibilities of observations from space; speaking to lay audiences to excite them about basic science—required that I present my case clearly and concisely. I still believe that communication is important. But now that I’ve had more time to reflect, I realize that perseverance—or stubbornness—and a certain amount of luck were equally important.

When I was a girl, women were not supposed to be scientists. When I asked my high school guidance counselor for permission to take a second year of algebra, she sneered, “What lady would take mathematics instead of Latin?” The college environment was similar. If the dean of women could not dissuade a girl from majoring in science or engineering, she had nothing more to do with her.

My first bit of encouragement came in my third year of college, when the physics department chairman said to me, “I usually try to talk women out of majoring in physics, but I think *maybe* you *might* make it.” In graduate school, it was clear that the faculty did not like educating women. But I am glad I ignored the many people who told me that I could not be an astronomer. I have had a wonderful career in a field that I love.

As for luck, in my late 20s, when I was working as an instructor at the University of Chicago, I observed a star that had unusual and completely unexpected emission spectra. I published a two-page note about it, then continued with my attempt to determine whether the composition of stars depends on their location in the galaxy.

I realized that, as a woman, I had little chance of getting tenure in an astronomy research department. So, to stay in astronomical research, I changed my specialization and accepted a position in the Naval Research Laboratory (NRL). Three years later, I was one of three Americans invited to the dedication of an observatory in Armenia. It turned out that I had been invited because the director of the new observatory was intrigued by my note



“I am glad I ignored the ... people who told me that I could not be an astronomer.”

about the anomalous star. I was a replacement for another invitee, so I had only 4 weeks to get permission from the naval hierarchy to go on the trip. As I carried my papers from office to office, many people ended up hearing that I was going. After my return, NRL leaders asked me to give a talk about my trip and later to give a series of astronomy lectures. As a result, I became widely known.

When NASA was formed 2 years later, most of the science section came from NRL. The leaders of this group, who knew me because of my trip, asked whether I knew anyone who wanted to set up a program in space astronomy, which I interpreted as an invitation to apply. I was hesitant to leave research, but the possibility of setting up a program that I thought would influence astronomy for decades to come was more than I could resist. I got the job and began to develop a program of 20 satellites, culminating in the Hubble Space Telescope, as well as many rockets and instruments on manned missions, all of which are sources of pride.

We now know that the star that changed my life is in the unusual state in which I found it for just about 100 days every 10 or 15 years. So, in some ways, much of my success can be traced back to my luck in seeing it when I did. But equally important was that I recognized that it was interesting, and that I took advantage of the opportunities that my stroke of luck brought my way. ■

Nancy Grace Roman is the retired chief of NASA’s Astronomy and Relativity Programs. Send your career story to SciCareerEditor@aaas.org.